THREE DIMENSIONAL FLUX BOUNDARY CONDITIONS FOR SOIL COVERS

By

BJÖRN WEEKS

B.Sc., University of Manitoba, 1992
M.Sc., University of Manitoba, 1994

A THESIS SUBMITTED IN PARTIAL FULFILMENT OF
THE REQUIREMENTS FOR THE DEGREE OF

DOCTOR OF PHILOSOPHY

in

THE FACULTY OF GRADUATE STUDIES

(Mining Engineering)

UNIVERSITY OF BRITISH COLUMBIA

February 2006

Abstract

Soil covers are commonly used to isolate waste materials from the surrounding environment. The flux of moisture through a soil cover is one of the key parameters defining its performance. While the flux of moisture through soil covers has been well investigated for horizontal soil surfaces, there has been relatively little research on applications to sloped surfaces. This thesis examines moisture fluxes through soil covers in three dimensions, with a particular focus on the variations that occur in evaporation over a three dimensional (sloped) surface. A model for the prediction of net radiation over a three dimensional surface was developed, and verified with field experiments. Statistical analysis of the field data showed that the model could predict net radiation on sloped surfaces with good accuracy for engineering applications. A sensitivity study was also conducted to evaluate model parameters.

The new model for net radiation over a three dimensional surface was designed for engineering application, and for simple integration with existing models of evaporation and flux boundaries on soil covers. The use of the new model, integrated with existing evaporative models, was demonstrated by comparison to field measured actual evaporation data. Applications have also been demonstrated for mapping net radiation and potential evaporation over three dimensional surfaces, with the mapping of actual evaporation also demonstrated for a case study meeting specific constraints.

Table of Contents

List of Tables

List of Figures

List of Symbols and Abbreviations

a_B	fitting coefficient (from Brunt's 1932 longwave equation)
a_o	empirical coefficient which reflects the amount of dust in the atmosphere (Idso, 1980)
a_1	a factor to account for the fact that $S\downarrow$ is not zero when the sky is completely cloud covered
A	inverse of relative humidity at soil surface
AE	actual evaporation
b	a shape factor for the calculation of wind speed on hills
b_B	fitting coefficient (from Brunt's 1932 longwave equation)
B	maximum clear-sky transmissivity
B_h	inverse of air relative humidity
CCBE	covers with capillary barrier effects
C (h)	specific moisture capacity function, $\partial\theta_w/\partial h$
C_h	volumetric specific heat of soil as a function of water content
C_v	specific heat of the soil
$C_W{}^1$	coefficient of consolidation with respect to the liquid water phase
$C_W{}^2$	coefficient of consolidation with respect to the water vapour phase
$D(\theta_w)$	unsaturated diffusivity, $K(\theta_w)/C(\theta_w)$
D_v	diffusion coefficient for water vapour through soil
e_a	vapour pressure of the air above the evaporating surface
e_o	vapour pressure
e_{sa}	saturation vapour pressure of the air at mean air temperature
e_s	vapour pressure at the soil surface
E	evaporation or evapotranspiration
E_a	$f(u)(e_{sa}-e_a)$
f	sky-view factor
f_c	fraction of the sky that is clear
f_L	cloudiness factor
f(u)	a wind mixing function
F	slope factor
g	acceleration due to gravity
G	Soil heat flux
G_{on}	extraterrestrial radiation, on a plane normal to the beam.
h	pressure head (water)
h_r	relative humidity at the soil surface
h_s	half-day length (in radians)
H	Sensible heat flux (heat to the air)
I	infiltration (percolation through the cover)
k_w	hydraulic conductivity

$K(h)$	unsaturated hydraulic conductivity function
L_e	latent heat flux of evaporation
L_{net}	net longwave radiation
$L_{netslope}$	net longwave incident on the slope
$L\downarrow$	longwave radiation incident on the horizontal surface
$L\downarrow_{slope}$	longwave radiation incident on the sloped surface
$L\uparrow$	longwave radiation emitted by the surface
$m_2{}^w$	slope of the moisture retention curve
n	actual hours of sunshine
n_c	cloud cover
N	possible hours of sunshine
P	precipitation
P_{sv}	saturation vapour pressure of the soil at its current temperature
P_t	total gas pressure in the air phase
P_v	Partial pressure due to water vapour
Q_{net}	Net all-wave radiation
R	runoff
R_g	universal gas constant
S_b	beam shortwave radiation
S_{bo}	beam solar radiation on a plane oriented normal to the sun
S_{bs}	the beam solar radiation on a sloped plane
S_d	diffuse shortwave radiation
S_{ds}	the diffuse shortwave radiation incident on the slope
S_{net}	net shortwave radiation
$S_{netslope}$	net shortwave incident on the slope
S_o	maximum potential clear-sky radiation
$S\downarrow$	shortwave radiation incident on the horizontal surface
$S\downarrow_r$	the shortwave radiation incident on the slope due to reflection from adjacent areas.
$S\downarrow_{slope}$	shortwave radiation incident on the sloped surface
$S\uparrow$	shorwave radiation reflected by the surface
t	time
t_e	temperature
t_j	day of the year (julian day)
T	sunrise and sunset times, measured as an angle from solar noon
T_o	surface temperature (in Kelvins)
T_T	total daily transmittance
T_D	total diffuse transmittance
u	wind speed

u_{up}	upstream wind speed
u_{max}	maximum wind speed
W_v	molecular weight of water
x	horizontal distance
z	vertical dimension, positive upwards
α	surface albedo
α_s	albedo of the ground facing the slope
β	slope of the surface under consideration
Γ	slope of the saturation versus vapour pressure curve at the mean air temperature
δ	solar declination
ΔS	the change in soil moisture (water stored in the cover)
ΔT_{cl}	the difference in degrees (Celsius or Kelvin) between the temperature at the screen height and the temperature at the cloud base
ε	surface emissivity
ε_{ac}	clear-sky emissivity
ζ	zenith angle
θ	the angle between the solar beam and a normal to the plane being evaluated
θ_w	volumetric water content
θ_z	zenith angle of the sun
κ	a constant that depends on cloud type
λ	thermal conductivity of soil
ν	psychrometric constant
ρ_s	mass density of the soil
ρ_w	mass density of water
σ	the Stefan-Boltzmann constant = 5.67×10^{-8} W m^{-2} K^{-4}
ϕ	latitude
ψ	azimuth (downslope direction)
ψ_s	azimuth angle
ψ_u	total suction in the soil
ω	hour angle, the angular displacement of the sun through the sky at 15° per hour, zero at solar noon, positive in the afternoon, negative in the morning
Ω	solar azimuth angle is the location of the sun in the sky relative to true north, measured in degrees clockwise from north

Acknowledgements

This thesis was made possible with the assistance of many people. I would like to thank in particular Dr. Ward Wilson, for his constant enthusiasm and guidance through the process. Field work for this thesis was conducted at the Equity Silver Mine site, and I would also thank Mr. Mike Aziz and the staff of the site for their ongoing assistance throughout the project.

Financial support for this thesis was provided in part by the support of Placer Dome Incorporated, the National Science and Engineering Research Council (NSERC) and by the BC Science Council. I thank all of these groups for the financial support that made this research possible.

Finally, I would like to thank my friends and family for their support and encouragement throughout the process. I would particularly like to thank my parents for their unfailing love and support as I completed this degree.

1 Introduction

The key importance of accurately characterizing flux boundary conditions is now well established for a variety of geotechnical applications, particularly for the design of soil covers over waste disposal sites. Accurate characterization of these processes is critical in the design of any soil cover. Several different software packages, based on coupled solutions to heat and mass transfer equations, are now commonly used by geotechnical engineers to characterize flux boundaries. These programs are used to predict key aspects of the interaction between soil covers and the atmosphere, such as evaporation, infiltration, and changes in soil moisture - all components of the surface water balance.

One-dimensional models for the calculation of flux boundary conditions, such as SoilCover (Unsaturated Soils Group, 1997), are now well-established in the literature, and commonly used in geotechnical applications. Implicit in the use of a one-dimensional model is the assumption that the surface modelled is either horizontal, or that deviations from the horizontal do not significantly affect the performance of the surface. This thesis presents an investigation of this assumption, with a study of the factors that affect flux boundaries for sloped soil surfaces in three-dimensional space. The work is focused on the impact that variations in slope steepness and direction of exposure have on the rate of evaporation.

As will be shown in this thesis, changes in net radiation with slope and direction of exposure have a particularly important effect on the rate of evaporation from sloped

surfaces. Swanson (1995) demonstrated the relative importance of net radiation as a control on evaporation rate by using an actual evaporation model to evaluate the sensitivity of evaporation to a variety of climatic variables, and showing that actual evaporation was most sensitive to variations in net radiation.

While it is well known that net radiation can vary significantly with slope, variations in net radiation are not normally quantified in the design of soil covers. On-site measurements of net radiation are typically made on a horizontal surface at a weather station. While it would be useful to have net radiation data on the sloped surfaces of a site, it is not necessarily practical to instrument slopes to measure net radiation. Hay (1979) pointed out that given the variety of possible slope orientations, it would be more useful to have a method to predict radiation on slopes than to have radiation measurements directly on slopes. There do not appear to be any cases presented in the literature where variations in net radiation have been considered or quantified in the design of a soil cover.

The main objective for the present study was to develop and verify a model for the prediction of net radiation on sloped surfaces. The model was needed in a form that could be integrated with existing models for actual evaporation, and could be used with such models to predict the impact that radiation variations would have on actual evaporation. A key criteria in the design of the model was that it use the weather data typically collected at existing cover sites, and avoid the need for additional instrumentation.

The specific objectives of the thesis are described in point form below.

1. To develop an appropriate theoretical framework to describe the energy balance and net radiation for any slope and aspect combination of a ground surface in three dimensional space, and to provide a numerical solution for the mathematical model.

2. To verify and validate in natural environments the numerical model for the prediction of net radiation on cover systems.

3. To demonstrate the integration of the verified radiation model with existing one- and two-dimensional models for actual evaporation. Net radiation is a key input for actual evaporation models, and there is the potential to improve the accuracy of existing models for actual evaporation by incorporating net radiation predictions that correspond to surface variations at the site.

4. To use the verified model to map net radiation and potential evaporation over fully three-dimensional surfaces. Ideally, it should be possible to generate three-dimensional contour maps that illustrate how net radiation and potential evaporation vary over the surface of a given site.

5. To investigate how the combined net radiation and actual evaporations models could be used to map variations in actual evaporation (not just potential evaporation) over a three-dimensional surface.

6. To demonstrate that field-measured differences in actual evaporation on different slopes can be approximated by combining the new net radiation model with existing models for actual evaporation.

7. To use the coupled models to illustrate the impact of different slope angles and orientations on both the net radiation and evaporation for various soil covers and climates. The intent is to show how these properties may vary at a given site as a function of two variables (slope angle and aspect)

8. To use the coupled net radiation and two-dimensional actual evaporation model to illustrate variations in actual evaporation along the length of slopes of various orientation. The intent of this is to show how actual evaporation rates may vary along the length of the slope (typically as a function of moisture distribution), and how these variations relate to the effect that slope direction has on evaporation rates.

9. To identify the types of cases where variations in slope angle and orientation are expected to have the greatest impact on actual evaporation. It is expected that for some slope orientations and locations, the impact of slope variations will have a greater impact on evaporation rates. Identifying the type of cases where

evaporation variations are likely to be greatest would assist in practical application of the model.

10. To develop and illustrate a simple approach for using the combined net radiation and actual evaporation models in the design of sloped covers. The approach in this work has been to design a model that can be used in practical engineering applications. Representative applications will show how the model can be used in design problems.

11. To review other factors that may affect the flux boundaries for a sloped surface, which could be the basis for further research in this area.

In order to accomplish these objectives, an extensive literature review was conducted to integrate the relevant current knowledge on flux boundaries for soil covers, and particularly on factors that affect how soil covers perform when sloped. This included a review of literature on the components of net radiation, and how these components are affected by slope. The literature on the influence of other factors for sloped soil flux boundaries, such as moisture redistribution and wind variations, was also reviewed.

The review of the literature revealed that no existing model was available that would predict net radiation on a sloped surface, based on the measured net radiation for a horizontal surface, using the minimal data typically recorded at conventional weather stations. As a result, a new model was developed based on a combination of methods for radiation analysis and prediction found in the literature. Field data was subsequently

collected to verify the new model. Further field data was also collected to test the ability of the model to predict actual evaporation from slopes when coupled with existing models for actual evaporation.

Using climate and soil data collected from soil covers at the Kidston Gold Mine in Australia and the Equity Silver Mine in Canada, the model was used to assess the performance of sloped soil covers under a variety of conditions, and to illustrate the possible design applications.

The work presented in this thesis includes the following contributions to geotechnical engineering and the design of soil covers:

1. A new and verified model will be developed for the calculation of net radiation on sloped surfaces. The model is intended to be suitable for engineering application and integration with existing engineering models for the evaluation of soil flux boundaries.
2. An approach will be developed to calculate the impact of slope-based variations of net radiation on actual evaporation, and to use this information in soil cover design.
3. The significance of slope-based variations in net radiation will be illustrated for a variety of cover design cases.

The thesis is directed primarily at the evaluation of net radiation and potential evaporation for natural ground surfaces and soil cover systems. While actual evaporation from a bare soil surface is considered, plant transpiration is not. The influence of

vegetation is included only within the context of evaluating energy budgets and net radiation above the plant canopy. Plants utilize both energy and water for photosynthesis and plant growth. The processes related the distribution of energy, actual transpiration and actual evaporation across soil-plant systems between the root zone, soil surface and leaves are a special topic and are not addressed within the scope of the present study. In the same way, the study does not consider freezing conditions or energy budgets for snow packs.

A review of the relevant literature is provided in Chapter 2 and Chapter 3, and the net radiation model is developed in Chapter 4. Chapter 5 presents the methodology used in the collection of field data for verification and testing of the model, with the data collected presented in Chapter 6. The data is analysed in Chapter 7, including verification of the model developed in Chapter 4. Applications of the verified model are illustrated in Chapter 8, with final conclusions summarized in Chapter 9.

2 Flux Boundaries Conditions for Soil Covers

The following chapter provides a review of the current literature on the use of soil covers for waste disposal sites, and the current state of the art for the flux boundary approach of evaluating the water balance across such covers. Special emphasis is given to the methods for calculating evaporation from soil covers, and the role of radiation in these calculations. Approaches for the calculation of radiation are also discussed. Chapter 3 provides a review of the literature on factors that affect flux boundary conditions as a result of slope and local topography, as well as on evaporation measurement.

Soil covers are a commonly used approach for isolating wastes at disposal sites. A brief overview on the current practice for the use of soil covers is presented in Section 2.1, followed by a detailed review of the flux boundary approach for calculating the water balance over soil covers in Section 2.2.

2.1 Soil Covers for Waste Sites

Engineering practice for the design and construction of soil covers on solid waste sites has undergone considerable development in the past 20 years. Particularly in the mining industry, concerns about acidic leachate from waste rock piles have driven extensive research, leading to new approaches for the design of covers.

Thirty years ago, it was well established that waste disposal sites no longer in operation required some sort of cover. Typical covers at that time included approximately 0.5 meters of locally available soil, placed to promote vegetation growth and reclamation of the site. At hazardous waste sites or more sensitive areas, this was supplemented by a barrier layer, (typically compacted clay with low hydraulic conductivity) designed to limit the infiltration of water to the disposal site (Tchobanoglous et al, 1977). These types of covers are still commonly referred to as barrier covers. By 1984, the original version of the USEPA HELP model was available to assist with the design of barrier covers (Schroeder et al, 1984).

The barrier cover design philosophy became well known, and has been used at many sites. In the United States, prescriptive regulations for barrier covers specified minimum thicknesses of barrier layers and maximum hydraulic conductivities for covers on hazardous waste disposal sites (Suter et al, 1993). Variations on these barrier covers have been used at many other sites. However, there are serious technical challenges associated with maintaining the integrity of a compacted barrier layer of clay to prevent the infiltration of water. Albright et al (2004) have shown that barrier covers without a

geomembrane layer are generally not effective. Suter et al (1993) identified seven key factors that tended to cause barrier layers to fail in long term application. These factors included construction flaws, changes in clay structure and permeability due to shrink-swell and freeze-thaw cycles, erosion, subsidence, root intrusion, and animal intrusion. Suter et al (1993) suggested that due to the combined influence of these factors, barrier covers required monitoring and maintenance to be continued in perpetuity, and also required much thicker protective layers than were typical in current practice. A protective layer of at least 3 m in most areas (greater than both the depth of typical frost penetration and rooting depth) was recommended for protection of the barrier soil. Clearly, a protective layer of such great thickness would be a significant cost for any site.

New design approaches have emerged in response to the problems of barrier covers, and are gaining acceptance. "Store and Release" or evapotranspirative covers have been put in place or are planned for several sites (Williams et al, 2003, Timms and Bennett, 2000; Zornberg et al 2003; etc). In mining applications, covers designed to create barriers to the diffusion of oxygen into the waste material have been studied and applied (Choo and Yanful, 2000; Yanful et al 2003; Weeks and Wilson, in press; and others) with varying degrees of success. Research is also ongoing in the area of capillary barrier effects (discussed later), which use contrasts in material permeability to create hydraulic barriers.

The basic design philosophy behind an evapotranspirative or "Store-and-Release" cover is to minimize infiltration by providing within the cover adequate storage capacity to hold the moisture from precipitation on the site, and promote the evaporation of that precipitation back into the atmosphere (Hauser et al, 2001). The porous soils used to

provide water storage do not generally require the careful placement that is required for an effective compacted clay barrier layer, and are less sensitive to the environmental factors that can adversely affect clay barriers. This design approach is especially attractive for arid climates (Swanson et al, 1997; Albright et al, 2004), where annual potential evaporation exceeds annual precipitation. The design of a store-and-release cover requires tools for the accurate prediction of all aspects of the water balance over the cover soil, particularly interactions between soil and atmosphere that affect the rate of infiltration to the soil, and the rate of evaporation and transpiration back into the atmosphere. Where evapotranspirative covers fail, it is commonly due to there being an inadequate depth of soil present for moisture storage, particularly during the wettest parts of the year (Hauser et al, 2001; Wilson et al, 2003). The design of an evapotranspirative cover generally requires computer modeling of the water balance, incorporating soil, plant and climate impacts on the water balance (Hauser et al, 2001).

Covers designed with the store-and-release philosophy have been applied at several mine sites around the world in both test plots (O'Kane and Waters, 2003; Hockley et al, 2003; Milczarek; 2003; Vermaak and Berzuidenhaut, 2003; and others) and full-scale applications (Kuo et al, 2003, Taylor et al, 2003; Durham et al, 2000). Some of the full-scale covers have been in place for considerable periods of time, such as the 18-year old Australian Rum Jungle site (Taylor et al, 2003), and the 7-year old Kidston Gold site (Williams et al, 2003). Evapotranspirative covers are also gaining acceptance outside of the mining industry, with the US Environmental Protection Agency recently approving the first evapotranspirative cover design for a Superfund site (Zornberg et al, 2003). This site included relatively steeply sloped portions (slopes up to 1.3H:1V). Albright et al

(Albright, 2004) compared the performance of store-and-release covers to conventional covers at a variety of sites throughout the United States.

Covers that are designed to prevent the diffusion of oxygen are particularly suited to application at sites where potentially acid-generating waste rock has been stored. It is well known that acid-rock drainage (ARD) develops when both oxygen from the atmosphere and water react with minerals containing iron sulfides (such as pyrite, FeS_2) to produce H_2SO_4 (sulphuric acid). The acidic leachate and/or runoff is a major environmental concern at many mine sites. While the usual approach for minimizing acid drainage from a site and the associated acid generating potential is to minimize the amount of water that enters the waste rock, an alternative approach is to control the amount of oxygen that can reach this waste. Since the rate of oxygen diffusion through water is approximately 10,000 times lower than in air (Weast, 1985), placing the waste underwater can create the needed barrier. This is often referred to in the mining literature as a wet cover. An alternative approach is to create an oxygen barrier with a soil cover by maintaining a saturated or near-saturated layer through at least a portion of the cover thickness. This saturated layer impedes the movement of oxygen through void space in the soil (Choo and Yanful, 2000; Yanful et al 2003).

Aspects of the design of oxygen-barrier covers have been developed in the literature (see for example Nicholson et al, 1989; Akindunni et al 1991; Yanful 1993; Yanful et al 1993a and 1993b). These covers are particularly well-suited to application at humid sites (Swanson et al, 1997) where precipitation exceeds evaporation. They are usually less

feasible in arid climates (O'Kane and Waters, 2003; Vermaak and Bezuidenhout, 2003). Similar to the design of store-and-release covers, the design of effective oxygen barriers requires accurate predictions of soil-atmosphere interactions. And while full-scale soil covers designed to act as oxygen barriers are less common than store-and-release covers, the oxygen barrier philosophy has been used at some full-scale sites, including the cover at the Equity Silver Mine in north-central British Columbia (O'Kane et al, 1998).

Capillary barrier effects make use of contrasts in the moisture-retaining properties of soils and unsaturated flow effects to generate barriers to moisture flow. In the most basic case, a fine-grained soil is placed over a coarse-grained soil, and the contrast in the unsaturated hydraulic characteristics of the two materials restricts flow across the interface between the two materials. Covers with capillary barrier effects (CCBE) have been the subject of considerable ongoing development in the literature. CCBE can be used to create barriers to moisture flow for a variety of cover designs, including covers designed as store-and-release covers, and covers designed to act as oxygen barriers.

The design of CCBE is affected by the factors that affect unsaturated flow through the cover profile, including the soil-atmosphere interactions, thickness of the soil layers, site geometry, and soil properties (Khire et al, 2000). These factors have been the subject of ongoing research (Stormont and Anderson, 1999; Morris and Stormont, 1998; Bronstert and Plate, 1997; Webb et al, 1997; Stormont 1995; Ross, 1990; Nicholson et al, 1989 and others). Of particular interest is the impacts that slope has on the performance of capillary barriers (Tami et al, 2004; Parent and Cabral, 2004; Brussiere et al 2000a and 2000b; Brussiere et al, 1998; Webb et al, 1997; Stormont, 1996, Nichols and Meyer,

1996). This literature has developed a fairly clear picture of the effect that flow dynamics have on moisture distribution within the slope, and the effects that higher moisture contents near the toe of the slope can have on barrier performance. However, while the effect of slope on water flow within the capillary barrier is now reasonably well understood, there does not appear to be any research to date on the impact that changes in evaporation with slope may have on the performance of capillary barriers. This suggests a need for tools to predict the impact of slope on evaporation and soil-atmosphere interactions.

2.2 Evaporation and Radiation for the Water Balance of Soil Covers

Understanding the water balance of soil covers is a critical aspect of their design. The key design question in the design of a soil cover is typically "how much water will get through this cover?" For a store-and-release cover, one also wants to know how thick a storage layer is needed given a particular combination of soils and climate. In the case of a cover designed as an oxygen barrier, another key question is "will the cover soil stay saturated under the local environmental conditions?"

The water balance equation can be written in many different ways. For a soil cover, the following form, adapted from Thornthwaite and Mather (1955) is useful:

[2.1] $P = R + E + I + \Delta S$

where:

P = Precipitation

R = Runoff

E = Evaporation or Evapotranspiration

I = Infiltration (percolation through the cover)

ΔS = the change in soil moisture (water stored in the cover)

The precipitation term, P, is typically the easiest component of the water balance equation to determine, based on weather data from the site under consideration.

Partitioning P into the other components of the water balance is a complex question that has been the subject of ongoing research by engineers and hydrologists. Depending on the application and field of study, the components of the balance may be analyzed in different ways. While considerable work on runoff and infiltration has been done in the field of hydrology, hydrologists tend to be concerned with relatively short-term events (days or hours) that generate run-off response. A brief review of the literature on runoff and infiltration (mostly from the fields of hydrology and agriculture) is provided in Appendix A. For the design of soil covers, the time scale of greatest concern is longer (infiltration through the cover over years). Evaporation and lower intensity precipitation events, which are more likely to be important for soil cover moisture (Blight and Blight, 1993) are of lesser interest to the hydrologist, a fact reflected in the available hydrology literature. Due to their different needs, hydrological models tend to make assumptions that err on the side of maximizing runoff. In contrast, conservative assumptions for the design of a soil cover generally to minimize runoff and maximize infiltration (except for the case of an oxygen barrier cover).

Hydrologists have several models available for the evaluation infiltration and runoff for hydrologic applications, such as HILLFLOW (Bronstert and Plate, 1997), and the HEC-1, HEC-2 and HEC-HMS group models which were developed to make calculations for flood hydrology and runoff from watershed assessments (US Army Corps of Engineers, 2001). In agriculture, models such as SWIM (CSIRO, 1990) have been also been developed to assess the water balance (Verberg et al, 1996). This model has been used in the analysis of evaporation from soil covers (Bruch, 1993).

Engineers concerned with the design of soil covers for waste disposal systems primarily need to evaluate the infiltration term (I) for most cover designs. For covers designed as an oxygen barrier, the change in storage term (ΔS) also needs to be characterized accurately. For such characterizations, the accurate assessment of daily rates of evaporation, and of smaller intensity, longer duration rainfall events (that may contribute the larger part of annual soil moisture) are very important. Evaporation is also very important for the calculation of water balances and moisture requirements in irrigation and drainage engineering (Pereira et al, 1999).

While some of the existing hydrological models have been adapted for the design of soil covers, there are several models available that have been written specifically for the assessment of the water balance on soil covers. HELP (Schroeder et al, 1994), mentioned earlier, has long been the most widely used model (Noël and Rykaart, 2003). While relatively simple to use, the HELP model has several theoretical and practical shortcomings, particularly the fact that the model cannot account for capillary rise of water in the soil beyond a defined "evaporative depth". In arid and semi-arid environments, this can lead to a significant over-estimation of percolation (Kowalewski, 1999). Further, this means that the model is unable to analyze the performance of a capillary barrier (Boldt-Leppin et al, 1999). Several more sophisticated codes now available for cover design, including HYDRUS-2D, UNSAT-H, SoilCover, and Vadose/W. Of these models, SoilCover (and its 2D formulation, Vadose/W), are "from a theoretical standpoint...the only model[s] that can calculate actual evaporation from a soil profile based on coupled heat and mass flow as governed by meteoric and soil conditions" (Noël and Rykaart, 2003).

Any model used for the design of a soil cover needs to provide tools for the accurate calculation of evaporation. At many sites, evaporation is the dominant sink for precipitation. For instance, Nyhan et al (1997) found in a study of soil covers at a semi-arid site that evaporation dominated the water balance. Between 86% and 96% of precipitation on various test covers was lost to evaporation, with evaporation rates affected by slope angle. In contrast, only 2-3% of precipitation was lost to runoff, with no clear correlation between runoff rates and slope. This suggests that at least for drier climates, accurate prediction of evaporation becomes key in accurately characterizing the water balance. Rykaart et al (2001) studied spatial variations in the water balance for a tailings dam and impoundment in a semi-arid environment, and found that for the water balance the "most important single component is accurate calculation of evaporation". Barbour et al (2001) studied the water balance of peat and till soil covers on sloped covers (5H:1V) for oilsands overburden piles, and found that the water stored in the soils was controlled in large part by the actual evaporation that occurred and precipitation, with runoff and other components of the water balance minimal. In more general terms, approximately 70% of the precipitation striking the earth returns to the atmosphere through evaporation, with as much as 90% evaporating in arid regions (Rosenberg et al, 1983).

There is ample evidence in the literature that the actual evaporation can be of paramount importance in evaluating the water balance (Pereira et al, 1999). For the design of oxygen barrier covers, accurate prediction of evaporative rates is critical (Wilson et al, 1994). Further, evaporation is typically the most difficult part of the water balance to

obtain (Yanful and Mousavi, 2003), and flux through a cover is strongly influenced by the evaporative flux (Yang and Yanful, 2002). Depending on the climate evaluated, just the errors in predicted evaporation can be as large as other individual components of the water balance (Parlange et al, 1995).

This thesis is directed to the question of how a water balance on a sloped cover surface differs from the water balance on a horizontal cover surface. In particular, the work is focused on how the 3D orientation of the ground affects the evaporation (potentially the most important component of the water balance), primarily through the effect that slope has on net radiation receipt. As a secondary consideration, the effects that slope has on the distribution of soil moisture and its impact on evaporation is also evaluated. Given the importance of evaporation and net radiation to the present work, a brief review is provided on techniques for predicting evaporation, and for predicting components of net radiation.

2.2.1 Predicting Evaporation

Evaporation is the transformation of a liquid into a gas. For this thesis, the process that is examined is the movement of liquid water into water vapour. This is examined both in the context of bare soil, and in the context of vegetated soil, where liquid water is transformed into water vapour in the vegetation, and passes to the air around the plant (transpiration). Evaporation is used as a general term, and evapotranspiration is used when referring specifically to vegetated surfaces, following the convention of Brutsaert (1982).

Given the importance of evaporation to soil science, agriculture, hydrology and climatology, it is not surprising that considerable efforts have been made over the years to develop accurate methods for its prediction. When evaluating the available methods for the prediction of evaporation from soil surfaces, clear distinctions should be made between the methods for calculating actual evaporation (AE), which is the evaporation that actually takes place from the ground surface, and potential evaporation (PE), which is the evaporation that could take place, if the soil was adequately wet (ie, moisture is not limiting). Typically, the moisture availability at a given site will at some point limit the possible rate of evaporation, and the actual evaporation rate will be less than the potential. There does not appear to be any general agreement in current practice on the best way to estimate evaporation (Parlange et al, 1995).

Analytical work in this thesis has been conducted using the Penman equation (Penman, 1948) for potential evaporation, and solutions to the modified Penman equation for actual evaporation, as presented by Wilson (1990). A review of these methods is provided in the following section, as well as a brief review for some of the related literature on the prediction of evaporation. A more detailed review of the common approaches to the calculation of evaporation can be found in texts on boundary layer climates (such as Oke, 1987) or hydrology (Tindall and Kunkel, 1999). More detailed reviews of evaporation are provided by Brutsaert (1982), and Burman and Pochop (1994).

2.2.1.1 Potential Evaporation

Evaporation from the surface of the soil requires that the following four conditions be met (Tindall and Kunkel, 1999):

1. A supply of water
2. An energy supply to provide the energy needed to change the phase of water from liquid to vapour.
3. A gradient in vapour pressure – that is, the air above the evaporating surface needs to have less water vapour in it than the saturation value of the air at the current air temperature
4. Air turbulence to move the water vapour away from the surface from which it just evaporated.

The various methods available for the calculation of potential evaporation make the assumption that the first item on this list (the water supply) is not a limiting factor. This can be incorporated into a simple definition of potential evaporation by saying that potential evaporation is the amount of evaporation that can take place assuming there are no limitations on the available moisture.

Evaporation can be calculated with a formulation of the Dalton Equation (Wilson et al, 1994):

[2.2] Evaporation = $f(u)(e_s-e_a)$

where:

$f(u)$ = a wind mixing function

e_s = vapour pressure at the soil surface

e_a = vapour pressure of the air above the evaporating surface

The wind mixing function term in this equation can be assessed directly, through the use of wind profiling, or estimated with any of a variety of wind-speed based empirical equations (Burman and Pochop, 1994). The vapour pressure in the air above the soil surface is relatively easy to assess based on relative humidity and air temperature. However, the vapour pressure right at the soil surface is not simple to measure.

Penman (1948) formulated his equation for evaporation to get around this problem, by incorporating net radiation and the energy balance into the Dalton Equation. This resulted in an equation that could be solved with measurable parameters. The Penman equation is very well known, and many variations on it have been developed over the years (Burman and Pochop, 1994). A basic form of the equation is as follows:

[2.3] $$PE = \frac{\Gamma Q_{net} + \nu E_a}{\Gamma + \nu}$$

where:

Q_{net} = net radiation

Γ = slope of the saturation versus vapour pressure curve at the mean air temperature

ν = psychrometric constant

E_a = $f(u)(e_{sa}-e_a)$

e_{sa} = saturation vapour pressure of the air at mean air temperature

Calculations of potential evaporation in this work are based on the above formulation of the Penman method. Penman originally defined evaporation in this equation as the amount of evaporation that can take place from an open water surface, or with a small correction factor (0.9), from bare soil or grassed surfaces with a plentiful water supply. This corresponds to the definition of potential evaporation adopted in the present work. As written, there is nothing in the original Penman equation to account for reductions in the amount of available water that can be expected over a longer-term drying period.

There are several other commonly used methods for the calculation of potential evaporation, including the Thornthwaite method (Thornthwaite and Mather, 1955) for monthly calculations, and the Priestley-Taylor method (Priestley, 1972). Burman and Pochop (1994) and Wilson (1990) provide a more detailed review of potential evaporation calculation methods.

2.2.1.2 Actual Evaporation

As discussed in the previous section, methods for the calculation of potential evaporation assume that the water supply at the surface of the soil will not be a limiting factor. As shown in Figure 2.1, the actual rate of evaporation will in fact drop over time as moisture becomes limiting. If drying continues for a length of time longer than the stage I evaporation shown on the figure, calculating evaporation rates with a PE method may overestimate evaporation, resulting in potentially significant water balance errors.

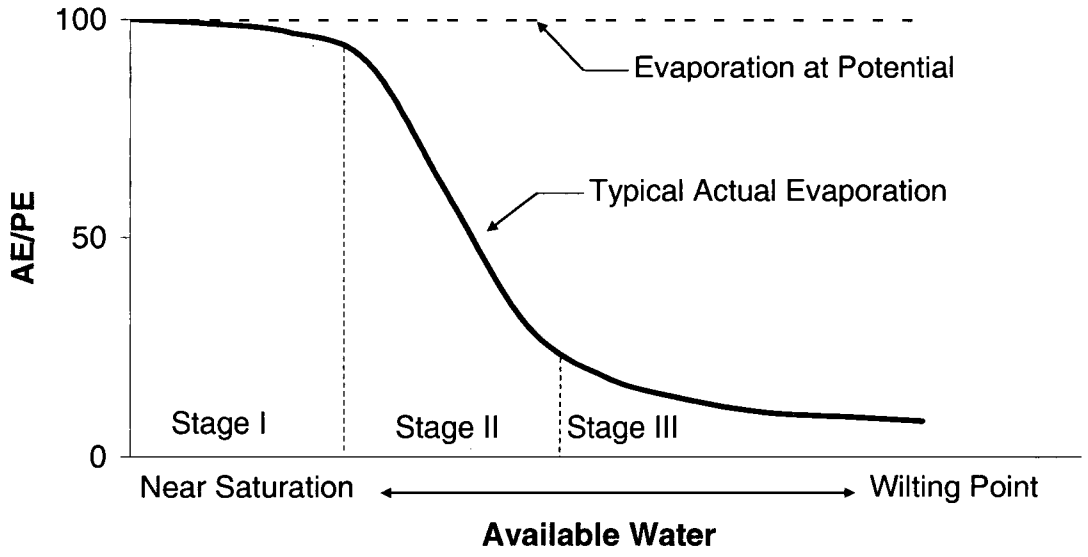

Figure 2.1: The impact of drying on evaporation rate (after Wilson et al, 1994)

The energy balance method (Bowen, 1926) is a commonly used analytic approach to calculating actual evaporation. In this method, it is recognized that the net radiation received at ground surface must go into one of three sinks: heating the ground (soil heat flux, G), heating the air (sensible heat flux, H), or providing the latent heat of evaporation (L_e). If the other components can be measured or estimated (not always simple), the

energy spent on the latent heat of evaporation can be calculated, and converted to an equivalent mass or volume of water. In general, when water is available, most of the net radiation is devoted to evaporation, while limited water supplies focus the energy input on heating the air and ground (Blight, 1997).

The other widely used approach for calculating actual evaporation is the complimentary relationship proposed by Bouchet (1963). This relationship "is based on the assumption that any energy that is not consumed in actual evaporation remains available as a potential" (Wilson, 1990). The complementary relationship has been used in a number of ways, including the formulation by Morton (1983) in the Complementary Relationship Areal Evapotranspiration (CRAE) model, and the Advection-Aridity model (AA) formulated by Brutsaert and Sticker (1979). These are the two most widely known formulations of the complementary relationship, and the CRAE model can provide fairly accurate predictions of regional evapotranspiration on a monthly basis (Hobbins et al, 2001).

Several modifications have been proposed to the Penman method to account for the impact of limited water availability on evaporation rates. Perhaps most widely known is the Penman-Monteith approach (Montieth, 1965), which incorporated a resistance term to account for factors such as the stomatal resistance to transpiration through plants. A major problem with this method is that properties such as stomatal resistance are difficult to measure (Tindall and Kunkel, 1999), and when estimated values are used for stomatal resistance, the Penman-Montieth approach does not necessarily out-perform the original Penman equation (Stannard, 1993), despite the fact that the Penman (1948) equation does

not in any way account for the non-availability of water. Nonetheless, the Penman-Monteith approach is widely used (Samani, 2000). For the calculation of reference crop evaporation rates (similar to potential evaporation), a version of the Penman-Monteith equation has been recommended by the International Commission for Irrigation and Drainage (ICID) and the Food and Agricultural Organization of the United Nations (FAO). This version is commonly called FAO56-PM, and has been widely adopted for reference evaporation calculations (Irmak et al, 2003a).

A more analytical approach to the prediction of actual evaporation was suggested by Granger (1989), who suggested that the actual rate of evaporation from the soil could be determined through the Dalton equation, and the actual vapour pressure at the soil surface. Granger did not present a method for calculation of vapour pressure at the soil surface.

Wilson (1990) provided a fully coupled solution of the heat and mass transfer equations for the prediction of actual evaporation from soils, which has been widely used in the design of soil covers for mine waste sites. This coupled solution allowed prediction of vapour pressure at the soil surface, so that actual evaporation is predicted with the modified Penman equation, as shown:

[2.4] $$AE = \frac{\Gamma Q_{net} + \nu E_a}{\Gamma + A\nu}$$

where:

E_a = $f(u)e_a(B_h-A)$

B_h = inverse of air relative humidity

A = inverse of relative humidity at soil surface

In this equation, the parameter A (inverse of relative humidity at the soil surface) becomes unity in the case of saturated vapour pressure in the soil surface, and the equation simplifies to the original Penman equation. In order to predict the actual evaporation with this equation, it is necessary to solve for the vapour pressure at the soil surface. This is done through the simultaneous solution of equations for water transport (liquid and vapour) in the soil, and heat transport.

Wilson (1990) presented the following equation for the one-dimensional flow of liquid water and water vapour:

[2.5] $$\frac{\partial h}{\partial t} = C_W^1 \frac{\partial}{\partial z}\left(k_w \frac{\partial h}{\partial z}\right) + C_W^2 \frac{\partial}{\partial z}\left(D_V \frac{\partial P_V}{\partial z}\right)$$

where:

h = water pressure head

t = time

z = vertical position (elevation)

k_W = hydraulic conductivity

D_V = Diffusion coefficient for water vapour through soil

P_V = Partial pressure due to water vapour

C_W^1 = Coefficient of consolidation with respect to the liquid water phase

C_W^2 = Coefficient of consolidation with respect to the water vapour phase

The coefficient of consolidation with respect to the liquid water phase and water vapour phases can be calculated as follows (Wilson, 1990):

[2.6] $$C_W^1 = \frac{1}{\rho_w g m_2^w}$$

[2.7] $$C_w^2 = \left(\frac{P_t + P_v}{P_t} \right) \frac{1}{(\rho_w)^2 g m_2^w}$$

where:

ρ_W = mass density of water

g = acceleration due to gravity

m_2^w= slope of the moisture retention curve

P_t = total gas pressure in the air phase

The hydraulic head term (h) and the vapour pressure term (P_v) in Wilson's equation for one dimensional liquid flow may be related with the relation of Edlefson and Anderson (1943), as follows:

[2.8] $P_v = P_{sv} h_r$

where:

P_{sv} = saturation vapour pressure of the soil at its current temperature

h_r = relative humidity at the soil surface;

$$h_r = e^{\left(\frac{\psi_u g W_v}{R_g t_e}\right)}$$

ψ_u = total suction in the soil

W_v = molecular weight of water

R_g= universal gas constant

t_e = temperature

Since the calculation of the vapour pressure in the soil requires knowledge of the temperature in the soil, the temperature in the soil must be evaluated at the same time as

the evaluation of the liquid and vapour flow. The following equation was used by Wilson (1990) for heat flow:

$$[2.9] \quad C_h \frac{\partial t_e}{\partial t} = \frac{\partial}{\partial z}\left(\lambda \frac{\partial t_e}{\partial z}\right) - L_v \left(\frac{P_t + P_v}{P_t}\right) \frac{\partial}{\partial z}\left(D_v \frac{\partial P_v}{\partial z}\right)$$

where:

C_h= Volumetric specific heat of soil as a function of water content = $C_V \rho_S$

C_V = specific heat of the soil

ρ_S = mass density of the soil

λ = Thermal conductivity of soil

L_e = Latent heat of vapourization of water

More rigorous formulations of these equations, accounting for the effects of soil volume change, were also provided by Wilson (1990).

The simultaneous solution of equations [2.4] through [2.9] by finite element methods has been used as the basis for the flux boundary modelling programs SoilCover (Unsaturated Soils Group, 1997) (one-dimensional solution) and Vadose/W (GeoSlope, 2001) (two-dimensional). The solution of the coupled equations with SoilCover is well-established in the literature, and has been shown by several researchers to give reasonably accurate solutions to real-world problems (Noël and Rykaart, 2003; Yanful and Mousavi 2003;

Yanful et al, 2003; Vermaak and Bezuidenhout, 2003; Scanlon et al, 2002; Rykaart et al, 2001).

Both SoilCover and Vadose/W calculate daily evaporation on a site-specific basis, using weather data collected at the site as a boundary condition for the calculation of actual evaporation. The weather data is used in combination with soil characteristics at the site and the calculated changes in soil moisture. This evaporation calculated in the model is part of the overall water balance calculated for the soil profile.

Net radiation is part of the weather data required in the Wilson (1990) method to define boundary conditions. This parameter is typically measured on-site with a net radiometer, and is representative of what would be expected on the horizontal surfaces at a site. Since Q_{net} can vary significantly with surface angle and direction of exposure (Oke, 1987), it is reasonable to expect that evaporation may also vary significantly. The potential impact of these variations in Q_{net} as a function of slope orientation are not routinely considered when applying the data collected from a horizontally oriented measurement system to a site with sloped areas. When large portions of a site under consideration are sloped, this difference could have a significant impact on the predicted evaporation for the entire site. A major component of the present study is to determine if this is in fact the case, and if so, to quantify the effects that may be expected at a typical site.

2.2.2 Net Radiation and Evaporation

Net radiation is well established to be a key parameter in the calculation of evapotranspiration (Irmak, 2003b). Inspection of the equations for potential and actual evaporation presented in Section 2.1.2.1 shows that net radiation, or Q_{net}, is a central term in many of the equations. It is clear from the equations that variations in Q_{net} induced by either temporal or physical changes can result in changes in evaporation.

The shortwave and longwave components of net radiation are affected by slope to different degrees. In developing a method for the calculation of net radiation on slopes, methods for evaluating each component are needed. The shortwave and longwave components of net radiation are discussed in the following sections, as are the approaches used in their calculation.

2.2.2.1 Components of Net Radiation

The net radiation input that drives evaporation consists of radiative fluxes downwards to the surface from solar radiation (or shortwave radiation) and the radiation emitted by the atmosphere due to its heat (longwave radiation). The radiation received by a surface is counterbalanced by the radiation that the surface reflects back to the atmosphere, and the longwave radiation that the surface emits as a function of its own temperature.

For the purposes of this thesis, the shortwave and longwave radiation will be divided following the convention of Oke (1987), with shortwave radiation in the wavelength band from 0.15 to 3 μm, and longwave radiation in the range from 3 to 100 μm. Other

researchers may divide shortwave and longwave slightly differently [Iqbal (1983) puts the division at 4 μm], but this is relatively unimportant as the bulk of the shortwave energy is transmitted by radiation in the band of wavelengths between 0.2 and 1.5 μm, while the bulk of the longwave energy is transmitted in the band between 4 and 30 μm.

The basic components of the net radiation (Q_{net}) are shown schematically on Figure 2.2, and can be expressed as follows:

[2.10] $Q_{net} = L\downarrow - L\uparrow + S\downarrow - S\uparrow$

where:

- $L\downarrow$ the longwave radiation incident on the surface
- $L\uparrow$ the longwave radiation emitted from and reflected by the surface
- $S\downarrow$ the shortwave radiation incident on the surface
- $S\uparrow$ the shortwave radiation reflected by the surface

The shortwave radiation can be further subdivided into beam (S_b) and diffuse (S_d) components, where the beam component is the radiation from the sun that arrives directly at the surface, and the diffuse component is that part of the solar radiation that first has been scattered in the atmosphere, before reaching the surface.

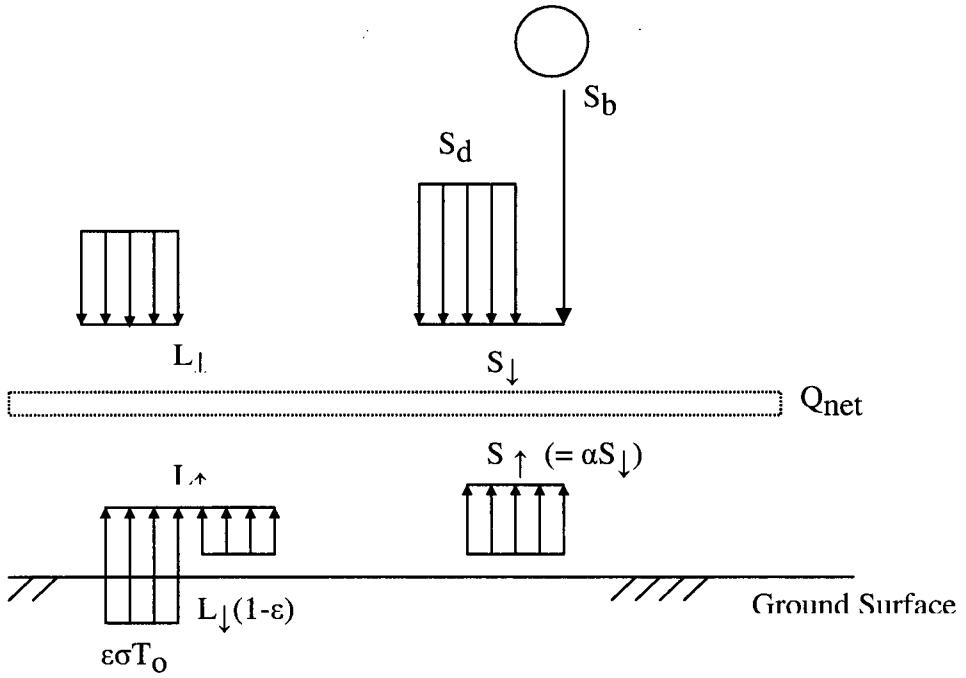

Figure 2.2: Net radiation balance for a ground surface with temperature T_o, emissivity ε and albedo α

Net radiation is commonly measured at soil cover sites (for examples, see Ayres et al, 2003; Williams et al, 2003; Ayres et al 2002; Wels et al, 2001; O'Kane et al, 1998, Wilson et al, 1995; and others) with a net radiometer, a device that records the difference between total incoming and total outgoing radiation (also known as a net pyrradiometer). A pyrradiometer measures total radiation over a hemisphere incident on the instrument surface. Net radiometers are also used at Bowen ratio energy balance measurement stations, which are used for the direct measurement of evaporation in research applications (see for example Blight, 1997; Tindal and Kunkel, 1999; Barbour et al, 2001; Rykaart et al, 2001; O'Kane and Waters, 2003; Williams et al, 2003). Net radiation data is required as a climatic input to programs such as SoilCover (Unsaturated Soils Group, 1997) and Vadose/W (Geo-Slope, 2001). Where net radiation is not

measured, there are methods for the estimation of net radiation based on site location and climatological data (Reddy, 1971; Wright 1982; Dong 1992; Irmak, 2003b).

2.2.2.2 Approaches to Determining Longwave Radiation and its Components

The net longwave radiation at a surface consists of incoming longwave radiation radiated by the atmosphere $L\downarrow$, and the outgoing longwave radiation emitted and reflected by the ground surface, $L\uparrow$. Predicting these two aspects represents two different, but related, problems.

The longwave radiation emitted by any surface is a function of the emissivity (ε) of the surface, and its temperature T_o, as given in the Stefan-Boltzmann law:

[2.11] Energy emitted = $\varepsilon\sigma T_o^4$

where:

σ = Stefan-Boltzmann constant (5.67×10^{-8} W m^{-2} K^{-4})

T_o = surface temperature in degrees Kelvin

Weiss (1982) showed that the outgoing longwave energy from the ground surface is well described by the Stefan-Boltzmann Law.

The emissivity of a ground surface is a function the type of material covering the ground. Oke (1987) provided a summary table of typical emissivity values which is reproduced here in Table 2.1. Table 2.1 also includes albedo values for the reflection of shortwave radiation, which will be discussed in the following section.

Table 2.1: Typical values of albedo and emissivity (after Oke, 1987)

Surface	**Type**	**Albedo**	**Emissivity**
Soils	Dark, wet	0.05	0.98
	Light, dry	0.40	0.90
Grass	Long (1.0 m)	0.16	0.90
	Short (0.02 m)	0.26	0.95
Snow	Old	0.40	0.82
	Fresh	0.95	0.89

Nunez (1980) showed that the total value of $L\uparrow$ is given by:

[2.12] $L\uparrow = \varepsilon\sigma T_o^4 + L\downarrow (1-\varepsilon)$

Where $L\downarrow (1-\varepsilon)$ represents the proportion of the incoming longwave that is reflected from the ground surface.

There are several different approaches to estimating the incoming longwave radiation ($L\downarrow$) at the earth's surface. Ideally, temperature and humidity profiles are measured through the atmosphere, permitting the direct calculation of longwave radiation.

However, such measurements are not always practical, as pointed out by Brutsaert (1975).

There are a number of simplified approaches to estimating longwave radiation under clear skies, based on the Stephan-Boltzmann Law, with terms for emissivity estimated on the basis of temperature, humidity, or both at the point of measurement. These include the models of Brunt (1932), Swinbank (1963), Brutsaert (1975), and several versions by Idso (including Idso and Jackson, 1969; Idso 1981).

Brunt (1932) proposed a model that uses vapour pressure in the calculation of emissivity, such that:

[2.13] $L\downarrow = a_B + b_B\, e_o^{1/2}\, \sigma T_o^4$

a_B, b_B = empirically determined coefficients

T_o = the average daily air temperature near the ground (in degrees Kelvin).

e_o = the vapour pressure in mb

In this equation, the term ($a_B + b_B\, e_o^{1/2}$) is the clear-sky emissivity (ε_{ac}).

Numerous investigations have been done to determine values for the empirical coefficients in this equation (Brutsaert, 1975), which have been shown to vary with

location (Oke, 1987). Brunt (1932) suggested a_B = 0.51 and b_B=0.066 for a northern hemisphere; the values suggested by other authors were similar (Brutsaert, 1975).

The temperature-based model of Swinbank (1963) has found widespread acceptance. The model was empirically developed for clear-sky conditions, and is based on a relationship between the air temperature at screen height and the incoming longwave radiation, as follows:

[2.14] $L\downarrow = 1.22\sigma T_o^4 - 171$

This model can also be expressed as:

$$L\downarrow = (1.22 - 171/\sigma T_o^4)\, \sigma T_o^4$$

Where the term $(1.22 - 171/\sigma T_o^4)$ is the clear-sky emissivity (ε_{ac})

Another significant model for longwave radiation under clear skies was developed by Brutsaert (1975). In this analytically developed model, the clear-sky emissivity was expressed in terms of both temperature and vapour pressure.

[2.15] $L\downarrow = 1.24\, (e_o/T_o)^{1/7} \sigma T_o^4$

The term $(1.24\ (e_o/T_o)^{1/7})$ is the clear-sky emissivity (ε_{ac}) for this formulation

In the model of Idso (1980), the clear-sky emissivity included terms for both temperature and vapour pressure, as well as an empirical coefficient a_o which reflected the amount of dust in the atmosphere and ranged between 0.7 (continental sites) and 0.6 (ocean).

[2.16] $L\downarrow = (a_o + (5.95 \times 10^{-5})1.24\ e_o \exp(1500/T_o))\sigma T_o^4$

The term $(a_o + (5.95 \times 10^{-5})1.24\ e_o \exp(1500/T_o))$ is the clear-sky emissivity (ε_{ac})

Several studies of alternative methods for estimating $L\downarrow$ under clear skies have shown that the method of Brutsaert performed well under a wide variety of conditions at locations throughout the globe (Hatfield, 1983; Weiss 1982; Cluf and Gash 1993). The other methods presented, as well as several methods that have not been reviewed here, are also capable of making reasonable estimates of clear-sky emissivity and longwave radiation under clear-sky conditions, as shown in the original studies.

All of the methods shown thus far for the calculation of longwave radiation assume that the skies are clear. Several approaches are available to account for cloudiness. Paltridge (1975) used an empirical relationship based on the idea that increases in cloud cover resulted in increases of $L_{\downarrow}$. To account for this, $L_{\downarrow}$ was increased by 6 $J/m^2/sec$ for each

tenth of the sky covered by cloud. Weiss (1982) used a cloudiness factor (f_L) in the calculation of net longwave radiation as follows:

[2.17] $L_{net} = f_L(L\downarrow - L\uparrow)$

With the cloudiness factor based on the one given by Linacare (1968):

[2.18] $f_L = [b + (1-b)n/N]$

Where b is a constant and n/N represents the number of actual hours of sunshine to possible. Weiss (1985) reviewed the literature to show that typical values of b are in the range of 0.1 to 0.2. Jury and Tanner (1975) used the ratio of measured to maximum incoming shortwave radiation to the possible shortwave radiation in place of the n/N ratio above. A variant of this approach was used by Buchan (1982a) and Novak and Black (1985). In their approach, the fraction of the sky that is clear is given by:

[2.19] $f_c = (S\downarrow/S_o)a_1 + (1-a_1)$

where:

$S\downarrow$ = downwards shortwave radiation

S_o = maximum potential shortwave radiation on the ground is estimated

a_1 = a factor to account for the fact that $S\downarrow$ is not zero when the sky is completely cloud covered

This fraction of the sky that is clear (f_c) is then used to calculate an effective atmospheric emissivity (ε_a) that can be used in place of clear-sky atmospheric emissivity in the equations for incident longwave radiation, as follows (Buchan, 1982a):

[2.20] $\varepsilon_a = f_c\varepsilon_{ac} + (1-f_c)(\varepsilon_{ac}+(1-\varepsilon_{ac})(1-4\Delta T_{cl}/T_o))$

Where ΔT_{cl} is the difference in degrees (Celsius or Kelvin) between the temperature at the screen height and the temperature at the cloud base. Buchan (1982b) and Novak and Black (1985) both used a value of 10°C as representative for ΔT_{cl}. All other terms in the equation are as defined previously.

Arnould et al (1996) and Brock and Arnold (2000) modified ε_{ac} with a cloud factor as follows:

[2.21] $\varepsilon_a = (1 + \kappa n_c)\varepsilon_{ac}$

Where κ is a constant that depends on cloud type (average 0.26), and n is the cloud cover. Brock and Arnould (2000) calculated the cloud cover, n_c, based on the ration of $S\downarrow/S_o$, similar to the approach of Buchan (1982).

More accurate approaches to the prediction of longwave radiation are available for use in climatology and geophysical research. However, most of these models require a detailed characterization of the atmosphere that is not practical for engineering application. Recent work in the field, (for example Varghese et al, 2003; Chou et al,1993) has focused on the development of numerical modelling schemes that subdivide the longwave radiation spectrum into subset wavelength bands, that are evaluated separately, with band-dependant variables for factors such as the adsorption coefficient. Varghese et al (2003) indicated that simpler broadband models are still suitable for many applications. A comprehensive review of these models is provided by Ellingson et al (1991).

2.2.2.3 Approaches to Determining Shortwave Radiation and its Components

Shortwave radiation can be either estimated from climatological measurements, or measured directly. Similarly, the components of shortwave radiation (beam and diffuse) may be measured, or estimated based on one of several well-established relationships that are available in the literature. The pyranometer is the usual tool for the measurement of total shortwave radiation, with a shaded pyranometer to measure diffuse solar radiation. Pyranometers measure only incident radiation, so a measurement of net solar radiation requires either an estimate of ground surface albedo, or a direct measurement of reflected radiation, made by a downwards-facing pyranometer.

A variety of theoretical and empirical models are available in the literature for the prediction of shortwave radiation at a site, all based on the site location relative to position of the sun, and measurements of climatological parameters such as temperature, humidity and cloud cover. These models range from those designed to predict monthly average insolation, such as that of Hay (1971), to those designed to simulate hourly values of beam and diffuse radiation, such as that of Hatfield et al (1981) and Gul et al (1998). For the National Solar Radiation Data Base for the United States, the METSTAT model is used to produce hourly values (Maxwell, 1998). Davies and McKay (1989) provided a comparison of eight different models for the prediction of shortwave radiation from climate data.

Given a measured or estimated value of net shortwave radiation (S_{net}) and ground surface albedo (α) for a given site, it is fairly simple to calculate the downwards ($S\downarrow$) and upwards($S\uparrow$) components on shortwave radiation.

[2.22] $S_{net} = S\downarrow - S\uparrow$

[2.23] $S\uparrow = \alpha S\downarrow$

This relationship allows a reasonable approximation to be made, despite the fact that albedo varies through the day (Oke, 1987). The albedo of a surface can be measured directly through the use of paired pyranometers over a given surface (one measuring $S\downarrow$ and one for $S\uparrow$), although such point measurements may lack the spatial representativeness needed for regional models (Hay, 1979). Iqbal (1983) presented

extensive tables of typical albedo values for various ground surfaces. A shorter summary table for typical albedo values was presented in Table 2.1 (after Oke, 1987). Note that exact values of albedo are difficult to specify in a meaningful way, as in addition to varying gradually over the course of a day as the sun angle changes, the same material may also have a different albedo at different latitudes, as a function of the sun angle in the sky (Iqbal, 1983; Oliphant et al, 2003). The daily cycles in albedo have been found to be more or less inverse on sloped versus horizontal terrain (Matzinger et al, 2003). Albedo will also vary over the course of a growing season. In reviewing other studies of albedo, Hanson (2001) showed that albedo may increase, decrease, or stay roughly the same over the course of a growing season. The albedo of ice and snow is particularly complicated, with large fluctuations in albedo occurring as functions of snow freshness, surface dirt, thickness, and underlying water (Iqbal, 1983).

For measured or estimated values of incident shortwave radiation ($S\downarrow$) on a surface, calculating the diffuse (S_d) and beam (S_b) components has become a fairly standard problem in solar radiation studies, and there are several methods available to choose between.

The most well known model for the partitioning of global shortwave radiation to its beam and diffuse components (S_b and S_d) is that of Liu and Jordan (1960). Also available are the models of Bristow and Campbell (1985) and the recent model of Roderick (1999). Many other related approaches are also in the literature (see for example Hay, 1976;

Temps and Coulson, 1977; Klein 1977; Orgill and Hollands, 1977; Bruno, 1978; Barbaro et al 1979, Erbs et al, 1982; Skartveit and Osleth, 1987; Reindl et al 1990).

The empirical methods such as that of Liu and Jordan (1960) for the division of $S\downarrow$ into S_b and S_d generally rely on the use of some type of clearness index, reflecting the fact that on cloudier days, the shortwave radiation received at the ground surface will be predominantly made up of diffuse radiation. Rather than use a direct measure of the degree of cloudiness, the maximum potential shortwave radiation on the ground is estimated (S_o), and the ratio between the measured $S\downarrow$ and the S_o (called the total daily transmittance T_T) is used as an input to the empirical formulae. The maximum potential shortwave radiation can be estimated based on solar geometry (see Appendix B), with the latitude of the site and the day of the year as inputs. Many of the alternatives to the Liu and Jordan (1960) approach attempt to incorporate other atmospheric factors, such as precipitable atmospheric moisture, or dust/turbidity measures.

The Liu and Jordan (1960) model is well established and has been used extensively, but its limitations have also been well documented. Ruth and Chant (1976) showed that for several locations in Canada, the Liu and Jordan (1960) model generally underestimates the ratio between S_d and S_o for a given ratio of $S\downarrow/S_o$. Hay (1976) suggested that this was because the model failed to account for "multiple reflections of shortwave radiation between the earth's surface and the overlying atmosphere", and proposed and alternative model to account for this. The method required a term to account for back-scatterance, expressed in terms of the amount of clear sky, the back-scatterance of clear sky, and the

cloud base albedo. Iqbal (1983) attributed the specific shortcomings of the Liu and Jordan (1960) model to the fact that they had not corrected for shadow-band effects in the measurements made with a shaded pyranometer. Iqbal (1983) demonstrated that for corrected studies (and using models with a similar form to the Liu and Jordan), the effect of latitude on the correlation parameters used was minimal for latitudes between 31° and 53° North (the limits of the range evaluated in the study).

Similarly, in a review of the common approaches for separating diffuse and direct shortwave radiation, Roderick (1999) indicated that for the analysis of daily data, a variety of studies showed that the parameters for an equation of the Liu and Jordan (1960) type tend to be applicable at a wide variety of sites. Roderick (1999) showed that it was only when using monthly average data that accuracy of the model became compromised.

Bristow and Campbell (1985), proposed a modification to the Liu and Jordan (1960) model, that incorporated a single, easily measured and physically based coefficient (B, the maximum clear-sky transmissivity) into the prediction of beam and diffuse solar radiation. In the model, the total daily transmittance (T_T) was used to estimate the total diffuse transmittance (T_D) as follows.

[2.24] $T_T = S{\downarrow}/S_o$

[2.25] $T_D = S_d/S_o = T_T(1-\exp(0.6(1-B/T_T)/(B-0.4)))$

As in the Liu and Jordan (1960) model, the value of S_o used to calculate T_T is calculated on the basis of solar geometry (see Appendix B). The new parameter, maximum clear-sky transmissivity, can be either measured or estimated for a give site. As noted by Bristow and Campbell (1985), B values are typically in the order of 0.75. Becker and Weingarten (1991) found that the Bristow and Campbell (1985) model significantly outperformed the Liu and Jordan (1960) model. The Bristow and Campbell (1985) approach incorporated a greater physical basis to the Liu and Jordan (1960) approach, which resulted in an increased accuracy, without requiring the difficult-to-obtain parameters required in the fully physically based models of direct/diffused solar radiation, such as the models of Montieth (1962) and Nunez (1980).

2.3 Summary of Flux Boundaries for Soil Covers

Soil covers for waste disposal sites have undergone considerable evolution in the past 20 years. While covers are still designed as simple water barriers, a variety of other cover design philosophies have also come into practice, including store-and-release covers, oxygen barriers, and covers designed to make use of capillary barrier effects. For all of these alternative cover designs, the accurate characterization of the water balance is important. Particularly important for many design applications is the accurate characterization of evaporation.

Many different methods have been proposed over the years for the prediction of potential evaporation and actual evaporation. The modified Penman method for the prediction of actual evaporation, as proposed by Wilson (1990) has become widely used in geotechnical application, particularly in the design of soil covers at mine sites. Net radiation is a key input into for the calculation of actual evaporation, and is a parameter that can also vary with slope at a given site. Net radiation is composed of both short and longwave components, which are affected by slope to different degrees. Approaches for the calculation of these components have been reviewed, as will be required for the development of a model for prediction of net radiation on slopes.

3 Literature Review - Slope and Evaporation

As has been discussed so far, there is a considerable body of work on soil covers and flux boundary conditions for horizontal surfaces. The focus of the literature review will now shift to the effect that ground surface slope has on the boundary conditions applied to soil covers (Sections 3.1 through 3.4), as well as evaporation measurement (3.5).

For mining waste rock dumps, placement procedures tend to result in surfaces that are steeply sloped, which may behave in a manner quite different from a horizontal surface (Boldt-Leppin et al, 1999). The emphasis of this review is on the influence that slope has on components of the radiation balance, but the impact of slope on other aspects of the microclimate and on the distribution of moisture in the soil slopes are also discussed, to provide a broader context for the work presented on the effect of slope on evaporation.

In an extensive study of topographical effects on fluxes and surface-atmosphere interactions, Raupach and Finnigan (1997) found that perturbations in flux, as well as in temperature and humidity over variable topography had the following four causes; "radiative effects owing to slope, causing changes in available energy; aerodynamic effects [...]; elevation effects induced by adiabatic cooling on ascent; and changes in moisture availability at the surface". They also noted that these causes might not all be equally important at a given site. Sellers et al (1997) also noted that topography would influence evaporation through impacts on radiation and moisture re-distribution.

For waste disposal sites, differences in radiation and moisture distribution due to slope may be significant. Considerable portions of the actual cover may be sloped. For example, approximately 30% of the 7000 acre waste disposal area at the Phelps Dodge Mornci Inc. mine in Arizona is sloped at 4H:1V (Milczarek et al, 2003). Approximately 30% of the waste rock dump site at the Equity Mine in British Columbia is sloped at 3H:1V or greater.

The available literature on the impact of slope on radiation and on moisture distribution is reviewed below (Section 3.1 and Section 3.2). A brief overview is also provided on topographical impacts on other aspects of the microclimate, such as aerodynamic effects and precipitation (Section 3.3). Studies on the impact of slope on evaporation were also reviewed (Section 3.4). The final section of the literature review, Section 3.5, presents an overview of the two approaches to evaporation measurement that were used in this thesis - the microlysimeter method, and the energy balance method.

3.1 Radiation and Slope

As previously discussed, net radiation and evaporation from soil surfaces are closely linked. The slope of a ground surface will have an impact on the net radiation received by a soil, by affecting both the shortwave and the longwave radiation received. These variations in radiation will result in variations in evaporation rates, which are well documented in the literature in the field of climatology. Hay (1971) pointed out that measurements of net radiation on a horizontal surface may not be appropriate for application to sloped surfaces. This was in the context of using the energy balance method for evaporation calculations. Many researchers have observed significant differences in local environmental conditions such as soil moisture, vegetation, frost, as a result of the different amounts of energy received by different slopes. Galacia et al (1999) showed that even at the low latitudes of Mexico, steep north-facing slopes received considerably less radiation than south-facing slopes, and as a result had higher soil-water contents. At moderate latitudes (40°N), it has been shown that evaporation rates vary proportionally to solar radiation, with higher evaporation rates on south-facing than north-facing slopes (Jiang et al, 1998). Similar results are available for southern latitudes (Jackson, 1967). In more extreme climates with significant snowfall, such as a study of soil moisture in a mid-latitude site (near Montreal, Canada) it has been shown that higher energy influxes on south-facing slopes resulted in lower soil-moisture contents on the south facing slope. The difference in radiation also resulted in snow-cover persisting for longer on the north-facing slope (Rouse and Wilson, 1969). Similar results are well documented at many other northerly sites (see for example Segal et al,

1985; Whiteman et al, 1989a and b; Young et al, 1997; Carey and Woo 1999; Carey and Woo 2001).

The beam component of the shortwave radiation is the radiative element that is most affected by the slope of ground surface, and therefore the subject of the most research. The importance of beam shortwave radiation is such that some researchers who have looked at the effects of slope on evaporation have made explicit or implicit assumptions to neglect the longwave component of radiation (for example, Blight, 2002; Fischer and Hermsmeyer, 1999; Segal 1985; Rouse 1969; Jackson 1967).

3.1.1 Effect of Slope on Shortwave Radiation

Given values for both the beam and diffuse components shortwave radiation on a horizontal surface, the calculation of the shortwave input to a slope has been well developed in the literature. The general form of the equations for calculating shortwave radiation on a slope can be expressed as (Paltridge and Platt, 1976):

[3.1] $S{\downarrow}_{slope} = (S_b)F + S_{ds} + S{\downarrow}_r$

where

$S{\downarrow}_{slope}$ = the shortwave radiation incident on the slope

F = ratio between the potential radiation received on a sloping surface to that on a horizontal surface

S_{ds}= the diffuse shortwave radiation incident on the slope

$S\downarrow_r$= the shortwave radiation incident on the slope due to reflection from adjacent areas.

For the calculation of beam radiation on a sloped plane, one can consider the possible locations of the sun relative to a plane. In all cases, the maximum intensity of beam radiation possible on that plane will occur when the sun is located normal to the plane (directly overhead), as shown on Figure 3.1. As the sun moves away from a position directly overhead, the beam radiation intensity will be diminished. As shown in any basic text on solar radiation (Duffie, 1980; Iqbal, 1983), the cosine law relates the shortwave radiation received by a plane oriented normal to the sun to any other plane orientation.

[3.2] $S_{bs} = S_{bo} \cos \theta,$

where:

S_{bo} = Beam solar radiation on a plane oriented normal to the sun

S_{bs} = The beam solar radiation on a sloped plane

θ = the angle between the solar beam and a normal to the plane being evaluated

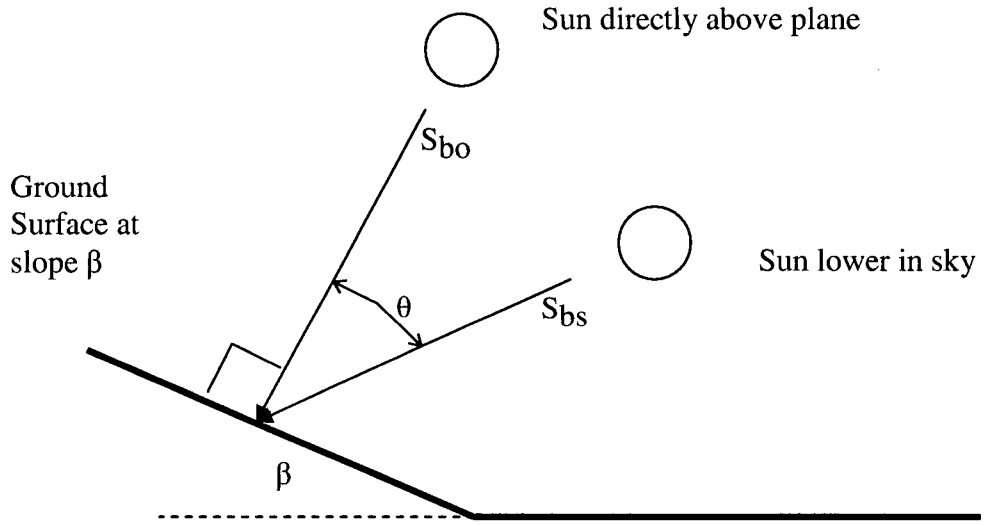

Figure 3.1: Relationship between solar beam and ground at slope β

Following the cosine law, the beam radiation on a plane will be at maximum when the angle θ goes to zero (ie, the sun is directly above, and the solar beam is normal to the plane), and goes to zero as the angle approaches 90° and the beam approaches parallel with the plane. For the situation where one knows the radiation on the horizontal ground surface, and wants to know the radiation on some sloped surface, the zenith angle of the sun (θ_z) can be used. The zenith angle of the sun is the angle that the sun makes with the horizontal ground surface. The beam radiation on a sloped plane (S_{bs}) can be calculated from the beam radiation on a horizontal plane (S_b) as follows:

[3.3] $S_{bs} = S_b (\cos \theta)/(\cos \theta_z)$

The angles θ and θ_Z can be calculated based on the time, date, and site location data, as shown in Appendix B. Most solar radiation models for the calculation of solar radiation on slopes use this basic approach (Gueymard, 1987).

The value of $(\cos \theta / \cos \theta_Z)$ provides a suitable value for F in equation [3.1] to be used in hourly calculation of beam shortwave radiation on inclined surfaces, and is the standard approach to this calculation (Kondratyev, 1969; Duffie, 1980; Iqbal 1983; Oke, 1987). Day totals can by obtained by integrating this equation over the course of a day from sunrise to sunset, through summing the hourly total calculations (Duffie, 1980; Manes and Ianetz, 1983; and others).

Swift (1976) presented a generalized algorithm for calculating F values to be applied to day total solar radiation, using the integrated equations for total potential radiation over the course of a day on sloped surfaces, and an equivalent slope approach (after Lee, 1963). Swift's generalized algorithm extended the equations of Lee (1963) to be valid at all latitudes, and formulated them to be suitable for computer application. In this method, sunrise and sunset times (T, measured as an angle from solar noon) for the slope under consideration are calculated on the basis of solar geometry (see Appendix B) as:

[3.4] $T = \arccos(-\tan\varphi\tan\delta)$

The latitude (φ) used as an input is the equivalent slope, calculated on the basis the original slope's geometry and location:

[3.5] Equivalent Slope =asin (cos(β) * sin (φ) + sin(β)*cos(φ)*cos(ψ))

where

β = Slope angle

φ = site latitude

ψ = Slope azimuth

The algorithm presented by Swift (1976) included error trapping, to handle unusual situations at high latitude, such as days with no sunlight, or no dark periods. With the calculated equivalent slope and day length from Swift's method, potential radiation on the sloped surface can be calculated. The ratio of potential solar radiation on the horizontal surface to potential radiation on the sloped surface gives the slope factor, F.

The total amount of diffuse shortwave radiation on a sloped surface is largely a function of the amount of sky that is exposed to the surface. If diffuse radiation is emitted isotropically by the sky, then it is possible to say that the diffuse radiation received by the surface is proportional to the amount of sky exposed (Oke, 1987). A horizontal surface will be exposed to the full hemisphere (180°), whereas the side of a vertical wall would only be exposed to half (90°). This was expressed mathematically by Kondratyev and Manolova (1960) as a view factor f (not to be confused with the slope factor F), which varied between 0 and 1. The formulation for a simple slope facing relatively flat surrounding terrain is as follows:

[3.6] $f = \cos^2(\beta/2)$

where:

$\beta =$ the slope of the surface

For more complex topographies, the portion of the sky visible to the slope can be further reduced to account for shading effects (Flint and Childs, 1987).

With the view factor f, it follows that the diffuse shortwave radiation incident on the slope S_{ds} for this situation is:

[3.7] $S_{ds} = S_d f$

These equations for diffuse radiation on slopes require an assumption that diffuse radiation is isotropically distributed through the sky. This assumption is relatively common (Duffie, 1980; Oke 1987). In reality, the distribution of diffuse radiation over the sky is only approximately isotropic under completely overcast conditions (Manes and Ianetz, 1983). The actual distribution of diffuse radiation is normally anisotropic, and dependant on the amount and type of cloud cover, factors which are usually not well known (Duffie, 1980). Typically, diffuse radiation is concentrated near the sun location (even on cloudy days), as well as around the horizon (Kondratyev, 1969).

In assessing the use of the isotropic assumption for diffuse radiation on slopes, Hay (1979) pointed out that this assumption of isotropy may underestimate the amount of diffuse radiation that would be received by a sloped surface. Hay (1979) presented an alternative method for estimating the diffuse component of shortwave radiation incident on a sloping surface, which accounted for the anisotropy of diffuse radiation. Other approaches have been developed by Temps and Coulson (1977), Klutcher (1979), and Gueymard (1987), to name a few. Comparative studies of the isotropic and anisotropic approaches typically show that the anisotropic models do have greater accuracy (Ma, 1983; Isard, 1986; Hay and McKay, 1985; Gueymard 1987), although the differences between real measurements and the isotropic models are not necessarily large (Jiménez and Castro, 1982).

The final component of shortwave radiation input to a slope is the radiation that comes from the reflection of facing ground surfaces. As previously discussed, sloped surfaces are exposed to a limited portion of the sky, a factor that can be accounted for with the view factor, f. The slope is also exposed to the surrounding ground surface, and may receive some small amount of shortwave radiation reflected by the facing ground (Oke, 1987). Since the term f indicates the portion of the sky that is viewed by the sloped surface, the remainder (1-f) represents the portion of the ground seen by the sloped surface (Paltridge and Platt, 1976). If the albedo of the surrounding ground surface is α_s, and the incoming radiation is given by $S\downarrow$, then $S\downarrow_r$ (the shortwave radiation incident on the slope due to reflection from adjacent areas) is given as follows.

[3.8] $S{\downarrow}_r = (1\text{-}f)\, S{\downarrow}\alpha_s$

Similar to the diffuse radiation from the sky, this reflected radiation from the facing ground surface is also assumed to be isotropic (Manes and Ianetz, 1983). For some calculations, this assumption may be limiting, since surfaces such as grasslands are anisotropic reflectors (Temps and Coulson, 1977). Snow covered surfaces can also be highly anisotropic reflectors (Gardner and Nadeau, 1988). Corrections for anisotropic reflection have been proposed (Temps and Coulson, 1977; Gardner and Nadeau, 1988).

Other researchers have applied the equations for shortwave radiation to three-dimensional models of shortwave radiation. Rich et al (1994) and Kumar et al (1997) have separately developed programs for use with GIS systems to map shortwave radiation over three-dimensional surfaces. Both of these models use theoretical predictions of solar radiation, rather than site-measured net radiation, modified by user-specified atmospheric parameters such as cloud cover and atmospheric radiation. Dubayah and Rich (1995) presented a review of the approaches for solar radiation modeling in a GIS environment. These approaches have the advantage of allowing more sophisticated calculations of the impact of surrounding topography, particularly in highly mountainous terrain, where the impact of shading from surrounding features may be significant. Courbaud et al (2003) looked at the impacts of shading and slope at the scale of individual trees and stands of trees for forestry applications.

Theoretical predictions of solar radiation are often used in studies of slope effects on radiation. Typically, radiation at the ground surface is predicted on the basis of the solar constant and sun-earth geometry (see Appendix B), combined with measures of atmospheric water, dust, and cloud cover. While such radiation values lack the accuracy of site-specific radiation measurements, many researchers have used them for illustrative purposes (see for example Rich et al 1994; Kumar et al 1997; Nunez 1980; Hatfield et al,1981; Antonić, 1998).

3.1.2 Effect of Slope on Longwave Radiation

While slope has the greatest effect on beam shortwave radiation, longwave radiation is also affected by slope. Longwave radiation is affected by slope primarily as a function of the amount of sky that can be 'seen' by a tilted surface compared that by a horizontal surface, in a manner that is similar to that of diffuse shortwave. In general, it is found that increasing the slope of a surface will increase the net longwave radiation received by the surface, as the surface is exposed to a lesser fraction of the relatively cool sky (Sellers et al, 1997). The skyview factor (f) that was previously calculated for the portion of the sky visible to the slope can also be used for longwave radiation calculations (Kondratyev, 1965). Matzinger et al (2003) illustrated that the measured downward flux of longwave radiation is dependent on the proportions of the sky and ground exposed to steeply facing sites, with the longwave radiation emitted by each element largely a function of temperature.

The total longwave radiation incident on the slope is:

[3.9] $L\downarrow_{slope} = L\downarrow f + L\uparrow(1-f)$

This is similar to the formulation used by Nunez (1980), Oliphant et al (2003), and others. The amount of longwave radiation emitted by a slope is a function of the slope temperature, and is not as greatly influenced by the slope geometry. The term $L\uparrow(1-f)$ represents the amount of radiation that is received on the slope due to reflection from the surrounding ground surfaces. Plüss and Ohmura (1997) found that for steeply sloped surfaces, where a large portion of the sky hemisphere was obstructed by surrounding terrain, this term could be a significant portion of the longwave energy balance. They also found that this term was much less significant for horizontal or nearly horizontal surfaces.

Similar to the case with diffuse shortwave radiation, the use of the sky-view factor implies an assumption that longwave radiation is distributed isotropically through the sky (Oke, 1987). This assumption was examined by Plüss and Ohmura (1997) and was found to introduce only a minimal error to calculated results (less than the error found in the measurement of longwave radiation with typical instrumentation).

The use of a slope factor for the calculation of longwave input to slope represents a simplification of a more complex integration of incident longwave over the hemisphere

of the sky, as developed by Kondratyev and Manolova (1960), and used by Olyphant (1986). In this approach, the double integral over the hemisphere above the surface is used as follows:

$$[3.10] \quad L_{\downarrow Slope} = \int_0^{2\pi} \int_0^{\zeta_s(\psi_s)} L(\zeta, \psi_s)(\cos\theta \sin\zeta)\partial\zeta\partial\psi_s$$

Where the spherical co-ordinates are given by ζ (zenith angle) and ψ_S (azimuth angle), and $\zeta(\psi_S)$ is the zenith angle of the slope in direction ψ_S. The term $L(\zeta,\psi_S)$ is the longwave radiation for a unit of the hemisphere above the ground surface with co-ordinates ζ,ψ_S. The value of $L(\zeta,\psi_S)$ can be calculated with the equations previously presented for longwave radiation, selecting either an equation for radiation emitted by the ground or the sky, depending on the location of the polar co-ordinate relative to the physical surroundings of the slope under consideration. Olyphant (1986) used this approach for the simulation of longwave radiation in rugged terrain. If one wished to avoid the isotropic assumption for the distribution of longwave radiation, this equation could be solved with angle-dependant equations for $L(\zeta,\psi_S)$.

The net longwave to the slope ($L_{netslope}$) is the total of the net longwave radiation to the slope ($L\downarrow_{slope}$), less the net radiation reflected by the slope ($L\downarrow_{slope}(1-\varepsilon)$) and the net radiation emitted by the slope ($L\uparrow$), as given by:

[3.11] $L_{netslope} = L\downarrow_{slope} - L\downarrow_{slope}(1-\varepsilon) - L\uparrow$

3.1.3 Models for Slope Effects on Radiation

As demonstrated in the preceding sections, it has long been recognized that measured radiation values on horizontal surfaces may not be the same as the radiation values on nearby sloped surfaces. As a result, many methods and models have been developed for the prediction of radiation on slopes, typically using the equations that have been presented in the preceding sections, or some variation on them. These include a large number of models that have been developed for shortwave radiation effects only, as well as some models designed for shortwave and longwave radiation. The models vary widely in terms of required input parameters. Some models use no site-specific radiation data, while others require detailed measurements of all components of the radiation balance, as well as of other local climate data.

For models designed to predict shortwave radiation on slopes, many approaches have been suggested which do not involve any type of site-specific radiation data (Fisher and Hermsmeyer, 1999; Antonic, 1998; Kumar et al, 1997; Cazorzi and Fontana, 1996; Rich et al, 1994; Flint and Childs, 1987; Hatfield et al, 1981; and others). These models typically relied on potential radiation values predicted on the basis of the solar constant, modified by sun-earth geometry, and in some cases local climate observations as indicators of cloud cover. Other models for shortwave radiation on slopes made use of

measurements of incident shortwave radiation (Tian et al, 2001; Varley et al, 1996; Gardner and Nadeau, 1988; Gueymard 1987; Isard, 1986; Bristow and Campbell, 1985; Manes and Ianetz, 1982; Jimenez and Castro, 1982; Hay, 1979; Swift 1976, Garnier and Ohmura 1970, and others), typically as made with a pyranometer. These models differed considerably in complexity. All of the models considered the effect of slope on the beam component of radiation, but some neglected the effects on diffuse shortwave radiation. Of those that considered diffuse shortwave radiation, some used sky-view factors while others incorporated GIS calculations and shading factors. There was also considerable variation in whether the diffuse component of the radiation was taken as isotropically distributed through the sky, or anisotropically distributed.

Net radiation models that do not use site-specific measured radiation data included the models of Oliphant et al (2003), Munroe and Huang (1997) and Nunez (1980), and others. These models were generally formulated similarly to the shortwave radiation models. Very few models have been presented in the literature that included site-specific radiation measurements and shortwave/longwave considerations (Matzinger et al, 2003, Brock and Arnold, 2000). The model of Brock and Arnold (2000) was designed to predict radiation on sloped surfaces where shortwave radiation measurements were available for horizontal surfaces. Longwave radiation was predicted on the basis of measured temperature.

The model of Matzinger et al (2003) was designed to address the same problem as is addressed by the net radiation model presented in this thesis: prediction of net radiation on a sloped surface, based on the net radiation measured on a horizontal surface. The

approach taken by Matzinger et al (2003) was semi-empirical, and required the use of several site-specific fitting parameters. The method was based on the assumption that slope impacts on beam shortwave radiation were the most important factor affecting net radiation on slopes, and that as a result variations in net radiation would be proportional to changes in the potential shortwave. The method was only developed for clear-sky conditions, limiting its practical applicability.

3.2 Soil Moisture Distribution, Runoff, and Infiltration for slopes

In addition to the effects that slope will have on the radiation regime over a soil cover, the slope of the soil surface can also affect the distribution of moisture through the soil, and as a result be related to variations in the soil's moisture content. The slope of the soil can also potentially affect the runoff and infiltration behaviour of the soil. The importance of variations in soil moisture for flux boundaries on sloped soils was illustrated by the work of Whiteman et al (1989). In this study, energy budget measurements were used to study evaporation in a deep valley environment, and it was found that actual evaporation rates were more than four times greater from the valley bottom (where soil moisture content was higher) than from the valley sidewalls, which were drier.

This section of the literature review provides a brief overview of the literature documenting the moisture distribution in sloped soils (particularly soil covers) and the variations in infiltration and runoff that develop as a result of precipitation on sloped soil surfaces. A more detailed review of infiltration and runoff theory, as it affects slopes, is provided in Appendix A.

3.2.1 Moisture Distribution in Slopes

Under typical conditions, the water table beneath a horizontal soil surface is at a relatively uniform depth. Where soil surfaces are steeply sloped, there can be considerable variation along the slope in the depth to water table, as illustrated in Figure

3.2. This variation will affect the moisture distribution along the slope length, as will the gravity-driven flow of moisture downslope. Since the moisture content of the soil at any point along the soil slope will affect infiltration/runoff partitioning of runoff (as well as evaporation rates), it becomes important to consider the moisture distribution along the slope. Yang and Yanful (2002) demonstrated for both sand and silt soils that increasing the depth to the water table resulted in decreased evaporation rates by limiting the water supply at the ground surface.

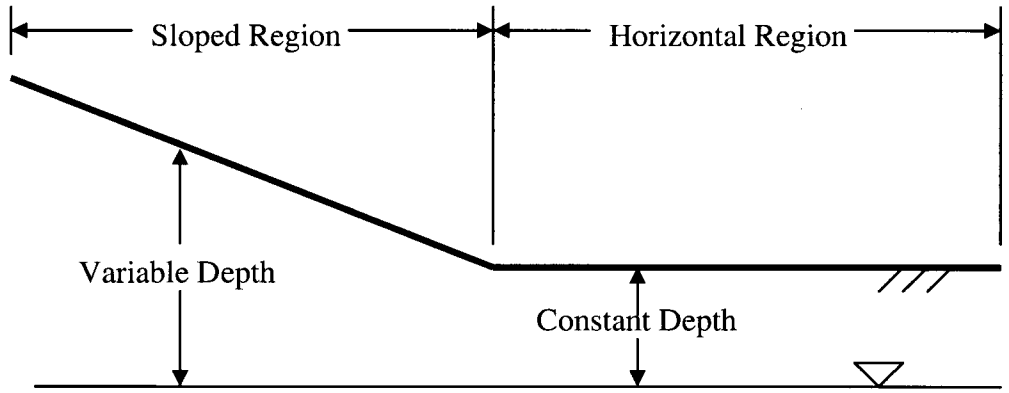

Figure 3.2: Impact of slope on depth to water table.

Where the water table is close to the surface, runoff will tend to be greater from rainfall events, while evaporation will proceed at rates close to potential. When the water table is at greater depth, evaporation tends to be suppressed and the amount of infiltration increased (Salvucci and Entekabi, 1995). At the toe of slopes, moisture is concentrated in part by the downslope flow of moisture, which often creates a near-surface water table and an area that is effectively impermeable to infiltration (Cabral et. al 1992). Higher moisture contents are generally expected in the topographic lows of a region (Dunin,

1976). This is illustrated schematically for natural slopes and cover soil slopes in Figure 3.3.

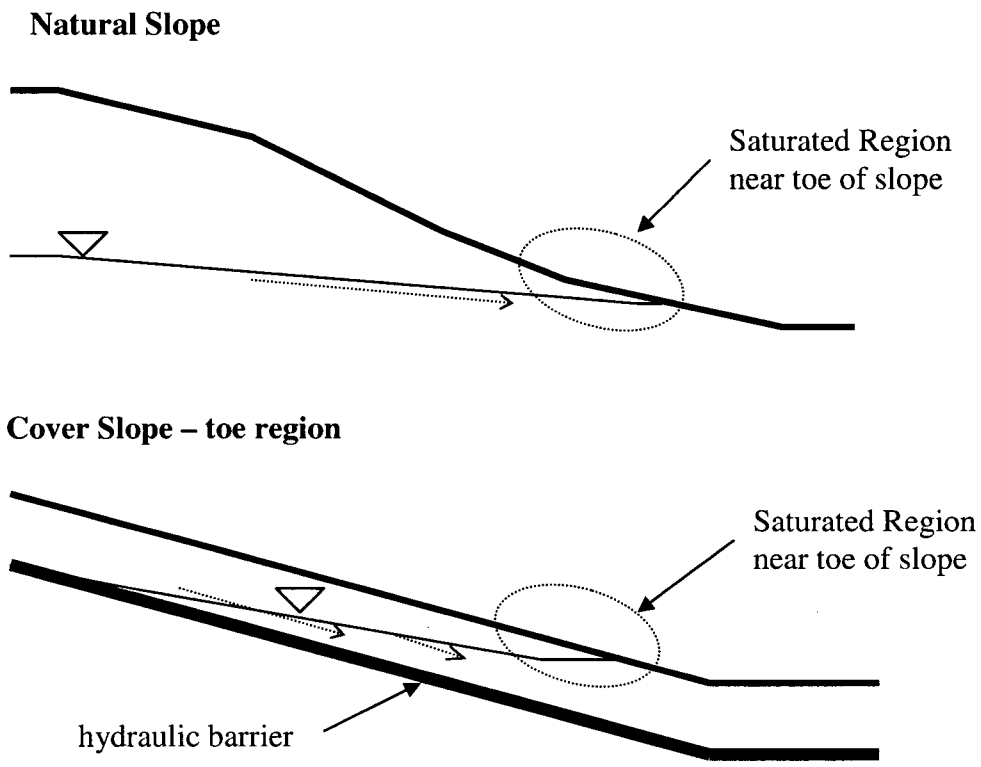

Figure 3.3: Moisture concentration at the toe of natural and cover slopes

The distribution of moisture throughout a soil slope follows certain typical patterns. In topographic lows, the water table is usually located closer to the ground surface, while at topographic highs the water table is deeper (Freeze and Cherry, 1979).

3.2.1.1 Model Studies of Moisture Distributions

Several significant numerical model studies have been conducted on the distribution of moisture through sloping surfaces. These include studies of natural hillsides (studies such as Fipps and Skaggs, 1989; Salvucci and Entekhabi, 1995), and studies of layered soils on natural hillsides, which are comparable to soil covers (Jackson, 1992; Cabral et al, 1992; Meriggi et al, 2002, and others). More recently, research has progressed with studies of the moisture distribution and flux boundaries for sloped covers, such as the work with Vasdose/W (Geo-Slope, 2001) conducted by Newman et al (2003) and Adu-Wusu and Yanful (2004). Research has also progressed on specific applications to the design of covers with capillary barrier effects on sloped surfaces (Webb et al, 1997; Bussiere et al, 1998; Bussiere et al 2000a and 2000b; Parent and Cabral, 2004).

Infiltration to a hill slope tends to generate non-uniform saturated zones, with higher moisture contents near the toe of the slope as a result of down-slope flow. Several numerical studies have demonstrated greater saturation near the toe of a sloped soil surface. For instance, using a 2-dimensional solution of Richards' equation, Fipps and Skaggs (1989) studied the impact of a steady flux applied at the surface of a homogenous natural hillslope. Their study showed that for steeper slopes, the depth of flow in the subsurface drainage pattern varied along the length of the slope, with deeper flow depths near the toe of the slope and shallower flows near the crest. The results of Fipps and Skaggs (1989) fit well with the study by Meriggi et al (2002), where the finite element program Seep/W was used to analyze moisture in slopes of soil over bedrock, for a variety of soil permeabilities. In this study, it was found that the applied infiltration

accumulated at the toe of the slope over time, with a more rapid accumulation at the toe when the soil permeability was high. In a three-dimensional study of cut slopes, Ng et al (2001) found that the groundwater response to rainfall was linked to the depth of the groundwater below the ground surface. Near the toe of the slope, where the groundwater table was close to the ground surface, infiltration resulted in a significant rise in the groundwater table, while near the crest there was some loss of soil suction in the area above the water table, but no change in water table height.

In a numerical study of sloped capillary barriers, Brussiere et al (2000a) demonstrated that the moisture content of the moisture retaining layer in the cover varied with position along the length of the slope, with less water in the soil at the top of the slope. As the steepness of the modeled slope increased from 10 to 18 degrees, the moisture content at the top of the 50 m long slope decreased.

The increase in moisture content towards the toe of a slope can be related to the down-slope component of moisture flow after rainfall infiltration. This down-slope component of flow may not develop until after the end of a rainfall event. Looking at the dynamics of infiltration with a finite element model, Jackson (1992) showed with a 2-dimensional finite element model that during a rainfall, the wetting front initially moved normally into the slope, with flow only gradually becoming vertical. After the rainfall, with the ground surface considered a boundary of practically no flow, a downslope component of flow developed. When the soils were layered or anisotropic, this downslope component became more pronounced. With layered or anisotropic soils, perched water tables may

also develop above the less permeable layers, as was found by Cabral et al (1992) in a study of simulated rainfall events on layered and sloped soils.

Variations in the moisture content along the slope of the soil can have a significant effect on the flux that takes place through the soil surface. Salvucci and Entekhabi (1995) presented a statistical model for the study of hydrological fluxes through soil surfaces to demonstrate that infiltration fluxes could be sensitive to variations in the depth of the water table. They also found that if the water table was located at great depth, small fluctuations in the water table due to infiltration had little impact on the flux rate. The same was true if the water table was located very close to the ground surface.

3.2.1.2 Experimental Observations

Data available from experimental observations of moisture distribution in slopes corresponded well to the numerical studies that have been conducted. Anderson and Sitar (1995) reviewed the literature on the development of saturation in sloping soils over the short term, in response to rainfall events. They found that depending on local conditions, perched water tables may develop anywhere along the slope length, especially where hydraulic conductivities decreased with depth. They also found agreement in the literature that topography had a controlling influence on the development of saturation, with the lower portions of the slope remaining saturated after the upper portions de-saturate. Bronstert and Plate (1997) measured the moisture content at various depths along a hillslope in a natural environment over a period of 18 months. The slope was observed to be typically wet near the toe of the slope, and drier upslope. Interestingly,

higher moisture contents were observed at the crest of the slope. Galicia et al (1999) studied steep slopes in Mexico, and found that areas near the toe of steep slopes typically had higher water contents, while locations near the middle and higher reaches of the slope had lesser water contents.

Tami et al (2004) used a laboratory-scale slope to evaluate a numerical model for moisture movement in a capillary barrier slope, and found that their numerical model predictions matched the physical system very closely. For both, higher moisture contents were present near the toe of the slope than near the crest.

In the past few years, there have been numerous studies on the correlation between moisture contents of soil slopes to topographical indexes such as slope length, steepness and upstream contributing area (Guntner et al, 2004; Hjerdt et al, 2004; Leij et al, 2004; Canton et al, 2004; Hawke and McConchie, 2003, Daws et al, 2002; Qiu et al, 2001; Pachepsky et al, 2001; Gomez-Plaza et al, 2001, van Asch et al, 2001; Western et al, 1999). It has been shown clearly through evaluation of field data that topography is an important control on moisture distribution (Hjerdt et al, 2004; Hawke and McConchie, 2003, Qiu et al, 2001 and others). Daws et al (2002) found that the water regime present on slopes (for their study area) were equivalent to those at plateaus in regions of much higher annual rainfall. Researchers have shown that elevation is an important contributor to soil water content, with lower locations tending to have a higher water content (Leij et al, 2004). Contributing area, which is the amount of land surface upstream of a given point within a catchment has also been identified as an important factor (Guntner et al, 2004; Gomez-Plaza et al, 2001, van Asch et al, 2001; Western et al, 1999). Western et al

(1999) showed that during wet periods, the upstream area was the most important factor correlating to soil moisture, while during dry periods, the slope/radiation receipt was the most important factor.

3.2.2 Runoff from Slopes

During a rainfall event, and in the short term immediately after the rainfall, the water that impacts a soil surface is distributed between infiltration, runoff, and (depending on topography) surface storage. To define the flux of water through a soil surface, it is necessary to be able to determine how much of a given rainfall is absorbed by the surface as infiltration, and how much of the rainfall is repelled as runoff.

Much of the literature available on runoff and infiltration processes and reviewed in Appendix A has been developed in the field of hydrology. While this information is relevant, it is worth noting again that the hydrologist is most concerned with the runoff from an area as it affects peak flows downstream. There is a strong emphasis on the rainfall during storm events and its effect on peak rates of runoff downstream, rather than the smaller typical rainfalls that contribute more to moisture in soil covers (Blight and Blight, 1993). There is also a tendency in hydrology applications to make assumptions that will maximize the runoff rate. In the field of hydrology, this is perfectly reasonable, as it will result in conservative design. However, for cover design, such assumptions are the exact opposite of what would typically be conservative.

The simplest approach to runoff calculation commonly used in geotechnical applications is infiltration excess. In this approach, the proportion of precipitation that can physically infiltrate the soil is calculated (by any of a variety of methods), and the amount of precipitation in excess of this is considered to either go into surface storage (ponding) for later infiltration, or runoff. A common assumption for geotechnical studies of sloped surfaces is that on a sloped surface, all precipitation in excess of the immediate infiltration capacity becomes runoff, and surface storage is assumed to be negligible. Field work, such as that by O'Kane et al (2000), supports this assumption, to the extent that for soil covers, the measured or observed runoff is enhanced on sloped surfaces and infiltration minimized. In a numerical model, this condition is simulated by setting the boundary conditions along a slope as pressure equal to zero for the duration of rainfall in excess of the infiltrative capacity of the soil. The infiltrative capacity of soil at a given time-step is a function of the saturation-dependent hydraulic conductivity at that time. This approach has been used recently with some success in the work of Zhang et al (2004), Collins and Znidarcic (2004), Tsaparas and Toll (2002), Smith et al (2002); Gasmo (2000), Alonso et al (1995), Pradel and Raad (1993), and others.

Setting the boundary conditions along a slope as pressure equal to zero for the duration of rainfall in excess of the soils infiltrative capacity is a simple approach to incorporate numerically, and is attractive for use in geotechnical applications. The main shortcoming of the approach is that it implies that there is no slope effect on runoff – that is, varying the steepness of the slope will not affect the amount of runoff that occurs. As is reviewed in Appendix A, there is a considerable body of laboratory (Goczan 1972; Fox et al 1997; Helming et al, 1998; and others) and field (Evett and Dutt, 1985; Weeks et al, 1992; El-

Hassanin et al,1993; Nyhan et al, 1997; O'Kane and Waters, 2003; and others) data that suggests that this is not the case, and that runoff increases with increases in slope angle, for an equal footprint area. O'Kane and Waters (2003) compared percolation through an evapotranspirative cover in an arid climate, and found that percolation was strongly affected by slope. On horizontal surfaces, runoff was near zero, while on sloped surfaces, the rainfall was partitioned between runoff and infiltration. O'Kane and Waters (2003) also found that antecedent rainfall conditions had a large effect on how much runoff was generated, with more runoff occurring when rain fell on already moist soil.

While some approaches have been suggested for modelling slope effects on runoff (such as the empirical SCS curve approach, or the method proposed by Evett and Dutt, 1985), there does not appear to be a well-developed analytical approach available. Further, there is not complete agreement that slope does play an important role in runoff. In an extensive study of the water balances for 11 different soil cover sites, Albright et al (2004) found that for slopes varying in the range of 5 to 25%, there was no statistically significant impact of slope on runoff rates. They also found that runoff formed a small portion of the overall water balance (from 0 to 10%, with an average of 4%). Climate did play a role in runoff rates, with higher runoff rates observed at the more humid sites. Galicia et al (1999) observed that for arid sites (sites with evapotranspirative demand greater than precipitation), runoff tended to be low or zero, and did not correlate well with rainfall.

Runoff from slopes may be affected by factors other than the steepness of the slope. Vegetation, soil type and surface roughness all have documented impacts on runoff from

sloped soils (Battany and Grismer, 2000) on natural hillslopes, where there can be substantial variations in surface conditions over the extent of the site. Variations in these parameters should be of lesser concern for engineering covers, which are typically quite uniform over their extents.

3.3 Slope and Microclimate (Temperature, Wind and Precipitation)

The topography of a given region can impact aspects of the local microclimate such as temperature, wind, and precipitation, resulting in variations of evaporation and other aspects of the water balance.

The local temperature is typically sensitive to changes in elevation. A parcel of air that rises without losing or gaining energy from its surrounding will cool at a rate of approximately 0.01°K/m, which is known as the adiabatic lapse rate. As a result of this, it is typically observed that for a given region, temperatures are cooler at higher elevations. Site-specific conditions may cause the actual lapse rate to be different from the adiabatic lapse rate (or even inverted, with higher temperatures at greater altitude) (Oke, 1987).

The cooling of air that is typically observed as the air rises may induce saturated or near-saturated conditions, potentially resulting in the formation of clouds and precipitation (Raupach and Finnigan, 1997). This is often observed in mountainous terrain, and elevation is a key predictor for precipitation variations (Kyriakidis et al, 2001). While the cooling that could occur over the change in elevation on a typical waste disposal site is unlikely to induce precipitation, the change in temperature could at least potentially affect evaporation rates through the reduction of the saturation deficit in the air.

As discussed in Section 3.2.1.1, wind affects the rate of evaporation rates by providing the mixing energy (air turbulence) needed to transport water vapour away from the

ground surface. The wind effects are expressed by the mixing function f(u), in which u is the wind speed. The topography of a site may impact wind in one of two ways. First, there are the topographically generated winds that develop as a function of topographic temperature differences that develop in a region. Topographically generated winds include phenomena such as katabatic (downslope) winds and valley winds. Secondly, there are winds that encounter the local topography as an obstruction, and are to some degree modified by the topography. (Oke, 1987).

The way in which a topographically modified wind is affected by the local topography depends on the type of air movement that is present. When the size of the obstruction is relatively large compared to the atmospheric boundary layer, turbulent or non-stratified flows develop (Raupach and Finnigan, 1997). Such flows are complex and difficult to model (Oke, 1997). Over low hills (such as most waste disposal sites), flows tend to remain stratified (Raupach and Finnigan, 1997). Oke (1987) suggests that wind can typically flow over slopes up to 17° without separation. Assuming no separation, the constriction of hill will result in an increased airflow rate over and around the hill, with a subsequent drop in flow velocity after the hill.

For conditions where flow remains stratified, Taylor and Lee (1984) presented a wind correction factor, which can be used to indicate the approximate impact of simple hills on windspeed. If u_{up} is the windspeed upstream of the hill shown in Figure 3.4, the maximum wind speed, u_{max}, which should occur on the crest of the hill is given by:

[3.12] $$u_{\max} = u_{up}\left(1 + b\left(\frac{z}{x}\right)\right)$$

In this equation, b is a shape factor that depends on the type of feature (1.6 for a 3D hill), and z and x are as shown on Figure 3.4. Note that x is taken between the crest of the hill (at elevation z) and the point on the slope where z = z/2.

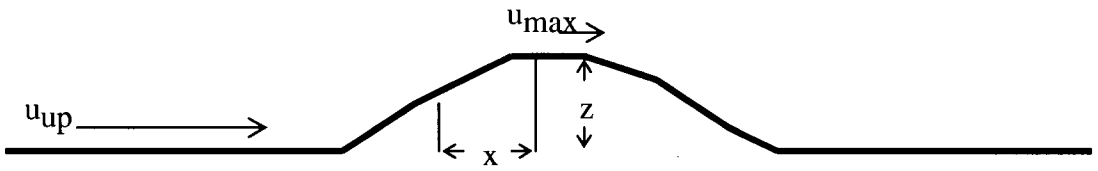

Figure 3.4: Wind flow over a simple hill (after Oke, 1987)

In addition to affecting the water balance through an impact on mixing, wind can also affect the distribution of precipitation. Rainfall per unit of map area is normally considered independent of slope angle, except when strongly directed by wind (Jackson, 1967). Ragab et al (2003) showed that for sloped surfaces facing the prevailing wind direction, the rainfall intercepted was consistently greater. Slope and aspect can also both affect the regional distribution of rainfall (Kyriakidis et al, 2001). Wind can have the most dramatic effect on the distribution of precipitation in cold climates, through the re-distribution of snowfall. In general, wind redistributes snow from exposed areas to more

sheltered areas (Woo et al, 2000), resulting in a significant inhomogeneity for water distribution during spring melt. Unfortunately, such redistributions are difficult to quantify in a predictive manner, as there are no simple relationships between topography and the depth of snow accumulated.

In considering the microclimate over local topography, it is clear that processes affecting wind and temperature have at least the potential to impact flux boundary conditions. The magnitude of these effects for features on the scale of waste disposal sites has not yet been thoroughly studied. While these factors are acknowledged, the focus of the work presented in this thesis is on the impact of variations in radiation receipt and moisture distribution. Munro and Huang (1997) found that for relatively small areas (areas less than 1 km^2), differences in evaporation between slopes are driven primarily by differences in solar radiation receipt, rather than being the result of local boundary-layer climatology. Air temperatures differences between slopes of relatively small extent tend to be minimal due to heat advection between the slopes. Jackson (1967) points out that potential evaporation is greatest when net radiation is greatest, and as a result, characterizing net radiation becomes more important than characterizing other factors.

3.4 Slope and Evaporation

As has been demonstrated, there is considerable literature available on the impact that slope has on the distribution of radiation and on other parameters such as soil moisture. Much less work has been done integrating these areas of study, into an evaluation of evaporation from sloped soil surfaces. Much of the work that has been done is limited, involving only potential evaporation and an incomplete characterization of the radiative climate.

Jackson (1967) characterized variations in potential evapotranspiration for a hillside located at a latitude of 40°S. Calculating potential evaporation with the Penman method, Jackson varied the net radiation input to the equation to predict variations in potential evaporation. Variations in net radiation on slopes were calculated based on the impact that slopes had on beam and diffuse shortwave radiation, following the work of Lee (1963) and Liu and Jordan (1960). Jackson (1967) found that the "differences in energy regime may lead to differences in potential evapotranspiration that are too large to be ignored in considering the water balance of slopes or of catchments having an effective slope of 10° or more..."

Rouse and Wilson (1969) studied the climate and water balance of a hill located at latitude 45° North, with direct measurement of evaporation through monitoring of the water balance components. While the total evaporation from north and south faces of the hill was found to be similar over the course of the year, differences in the radiative climate did lead to the two faces having considerable differences in the moisture regime

over the year, with soils having much higher moisture contents on the northern face throughout the year.

Segal et al (1985) used numerical modeling techniques to predict differences in transpiration during the dry season (summer) for vegetated slopes of various angles in sub-tropical Israel (Latitude 32°North). They found that for north-facing slopes, the rate of transpiration decreased with increases in slope angle, while south-facing slopes reached a maximum transpiration rate around a steepness of 22.5°.

Whiteman et al (1989) used the energy balance to measure evaporation from the base, sidewalls, and crest of a deep valley located in Colorado (Latitude 39° North). In this study, they found that the evaporation rates were dependent on both the amount of radiation received by the surfaces (a function of slope and aspect), and on the moisture that was available, with more evaporation occurring where more moisture was available.

Munro and Huang (1997) developed a theoretical model that incorporated rainfall measurements to predict the variations in evaporation, runoff and rainfall for north and south facing slopes in the Shenchong basin of China (approximate latitude 23° North). Using theoretically predicted solar radiation values and a version of the Penman-Montieth equation to predict evaporation, they found that evaporation rates on south facing slopes were typically 1 mm/day greater, leading to considerable differences in moisture storage on the two slopes.

Sellers et al (1997) evaluated the energy balance for each element of a 30 m x 30 m grid overlaid on a 2 km x 15 km study area, for which extensive field data had been collected. They accounted for the impact of element slope on net radiation, and variations in soil moisture and vegetation (estimated from satellite and airborne microwave measurements). Fluxes for each element were calculated using a version of the Penman-Montieth equation. The study was conducted to evaluate the impact of using area-averaged land surface properties in models, and the results suggested that averaged properties would give a reasonable indication of overall fluxes since the relationships describing the influence of moderate topography on radiation are approximately linear. The non-linear nature of soil drying and moisture distribution did mean that soil moisture effects may turn out to be scale dependent.

Taken together, these studies point towards the importance of slope and variations in net radiation for the accurate calculation of evaporation. However, all of the studies were made using methodologies that have limited practical application for engineering use. Actual evaporation rates were not typically evaluated, nor were all of the components of the radiation balance. None of the studies presented an approach to calculating actual evaporation on slopes that could be applied to sites at any location.

3.5 Evaporation Measurement

Two methods of measuring evaporation from soil covers were considered in this research – the direct measurement of evaporation with microlysimeters, and estimation of evaporation through the energy balance. A detailed review of microlysimeters and their use is provided below, followed by a brief review of the energy balance method. The energy balance method has been developed fully in other literature (see for example Blight 1997).

3.5.1 The Microlysimeter Method

A microlysimeter is a container of soil that is left exposed to the air, and weighed regularly. The weight loss measured over time represents the quantity of evaporation from the soil. The difficulty lies in ensuring that the rate of evaporation from a given microlysimeter is representative of what is happening in an undisturbed soil profile. A schematic illustrating a typical microlysimeter design is shown in Figure 3.5.

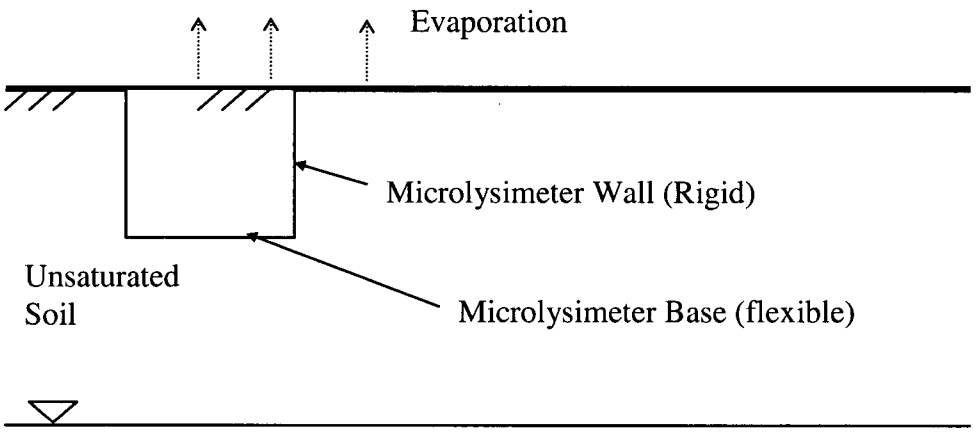

Figure 3.5: Microlysimeter schematic

Initial developments in the use of microlysimeters came from the field of soil science. Boast and Robertson (1982) introduced the concept, with the evaluation of 76 mm diameter microlysimeters of varying length, driven into the soil (to take a core). Boast and Robertson (1982) pointed out the basic assumption of the microlysimeter method, which is that an infinitely long microlysimeter should behave like an undisturbed soil, and that for at least some period of time after installation, the microlysimeter of finite length will behave like one of infinite length. Capping the base of the microlysimeter will cut the soil column off from the water available in the underlying soil, and within a range of practical lengths will eventually limit the moisture available for evaporation.

The fundamental problem in using microlysimeters is to judge for how long a microlysimeter of a given size will give representative results. Boast and Robertson (1982) approached this problem by using a series of microlysimeters with lengths between 20 and 146 mm, and observed how long it took for evaporation from the shorter microlysimeters to deviate from that measured in the longer. The authors developed empirical relations to estimate how long a given length of microlysimeter would be

accurate, but recognized that these relations would change with microlysimeter design and soil type. Evett et al (1995) also used multiple lengths of microlysimeter (100, 200 and 300 mm) and found that for a 9-day study in a clay loam soil, lengths between 200 and 300 mm gave adequate results. Evett et al (1995) pointed out that one could make new microlysimeters on a daily basis to avoid the question of how long the microlysimeter would be effective, a relatively labour intensive approach that was followed by Fujiyasu et al (2000). The microlysimeters used by Fujiyasu et al (2000) were 100 mm diameter by 100 mm long, and installed in highly plastic clay tailings. Tyler et al (1997) indicated that numerical simulations showed their microlysimeter would give valid results for a week, but gave no details on the type on simulations that were run. Their microlysimeter was 100 mm diameter by 305 mm long, and was installed in lacustrine sediments at an arid site. Weeks and Wilson (2001) used the program SoilCover to model the length of time that a microlysimeter would be expected to perform comparably to an undisturbed soil column. Weeks and Wilson (2001) showed that the required length of soil column is a predictable function of the soil properties and the length of time for the experiment.

Construction materials used for the microlysimeter also affect boundary conditions, and thus the measured evaporation. PVC is a good material for the sidewalls of the microlysimeter, as it has a thermal conductivity similar to that of a dry soil. The much higher thermal conductivity of metal sidewalls can result in significant deviations in the heat flux from top to bottom of the microlysimeter (Evett et al 1995), although this effect has not been noted by all researchers (Chen and Novak, 1997). It is important to avoid disrupting the heat flow into the underlying soil at the base of the microlysimeter. Evett

et al (1995) suggested that a thin, flexible membrane that conformed to the underlying soil profile while blocking water flow would give the best results.

Many of the studies with microlysimeters reported in the literature stress the importance of careful installation to ensure accurate results. Where soil conditions permit, the microlysimeter should be driven into the soil to obtain an intact core. It has been noted that where the soils are relatively soft, driving the microlysimeter may partially compact the surface soils, and reduce the measured evaporation rate (Bonachela et al 1999). In contrast, the surface crust on dry soils may be disturbed by the driving process, leading to a short-term increase in evaporation rate (Tyler et al 1997). Where the soil is not amenable to driving the microlysimeter, it is necessary to install the microlysimeter by carefully excavating around the microlysimeter tube, and lowering it gradually around the soil. Once the soil has been excavated and base cap placed, one can either backfill around the completed unit (Blight G.E. and Kreuiter A. 2000), or create a new hole at an adjacent site for the newly completed microlysimeter (Tyler et al 1997; Bonachela et al 1999) to minimize potential disturbances in the surrounding soil that could affect local evaporation. A thin plastic sleeve that remains in the hole can be used to minimize sloughing when the microlysimeter is removed for weighing (Bonachela et al 1999).

3.5.2 Energy Balance Measurements

As discussed in Section 2.2, the net radiation available at a given location on the earth must do one of three things: (i) heat the earth, (ii) heat the air immediately above the

earth, or (iii) evaporate water. This relationship can be expressed mathematically as follows (Blight, 1997):

[3.13] $Q_{net} = G + H + L_e$

where

Q_{net} = Net radiation

G = Soil heat flux

H = Sensible heat flux (heat to the air)

L_e = latent heat flux of evaporation

As it is possible to measure the fluxes of net radiation, soil heat, and sensible heat, the remaining component, latent heat flux, can be calculated, and converted to an equivalent mass of water evaporated. This is usually accomplished with a weather station modified to measure and log each of the heat flux components, commonly called a Bowen station (after the Bowen ratio, H/L_e). A net radiometer is used to measure the net radiation directly, while soil heat flux is measured with a buried heat flux plate, and the sensible heat flux is calculated based on the measurement of temperature and humidity gradients above the ground surface. Blight (1997) provided a detailed explanation of the energy balance method, and the factors affecting it. The Bowen ratio can be determined from temperature and humidity gradients as follows:

$$[3.14] \quad \frac{H}{L_e} = \nu \frac{(T_1 - T_2)}{(e_1 - e_2)}$$

Where T_1 and e_1 are the temperature and vapour pressure at the lower elevation, and T_2 and e_2 are the temperature and vapour pressure at the upper elevation.

Blight (1997) suggested that it was not necessary to use a data-logging station to make the required measurements for calculating evaporation by the energy balance method. Blight outlined an approach for measuring components of the energy balance throughout the day, by making spot measurements with hand-held instruments. The measurements included net radiation, temperature/ humidity gradients, and soil heat fluxes. The soil heat flux was calculated by measuring temperature gradients in the soil and the soil water content, combined with knowledge of the relationship between the specific heat capacity of the soil and its water content. In the same paper, Blight documented close agreement obtained with hand-held and weather station-type measurements of the energy balance. Using the method of Johansen (1975) the thermal conductivity of the soil can be estimated as a function of the soil moisture content, and the ground heat flux becomes:

$$[3.15] \quad G = \lambda \frac{\Delta T}{\Delta z}$$

Where Δz is the distance through the vertical soil profile between the two points over which the temperature difference (ΔT) is measured. The latent heat of evaporation is then simply:

[3.16] $$L_e = \frac{R_n - G}{1 + \left(\frac{H}{Le}\right)}$$

Tyler et al (1997) have pointed out that the Bowen ratio method may not be suitable for very dry environments, where the flux rate is low. In such environments, they had much better results using microlysimeters. Further, measurements made on windy days can be subject to large errors, due to the impact that wind mixing has on temperature and humidity gradients (Blight, 1997). Qiu et al (1998) suggest that Bowen ratio measurements were only really applicable for very large fields, and that measurements taken close to the ground surface are too greatly affected by surface inhomogeneities.

3.6 Summary of Slope and Evaporation Literature

Slope can affect evaporation from a soil cover through its impact on net radiation, moisture distribution, and aspects of the microclimate such as temperature, wind, and precipitation. For the impact of slope on net radiation, the effect is greatest on the shortwave beam component of net radiation, with lesser impacts on the diffuse shortwave radiation and the longwave radiation. If these components are known on a horizontal surface, there are well-established methods available for their prediction on a nearby sloped surface. In Chapter 4, an approach is developed for the calculation of net radiation on any sloped surface, based on the net radiation measured at a horizontal surface. While many approaches to the prediction of radiation on sloped surfaces have been presented in the literature, there have been very few models presented that incorporate both short and longwave effects. No models were found in the literature that would be applicable for predicting in an engineering application the net radiation on sloped surfaces based on the net radiation measured on a horizontal surface.

Experimental and theoretical work in the literature shows clearly that sloped soil surfaces tend to have higher moisture contents near the toe of the slope. Where actual evaporation rates are affected by moisture availability, this indicates that higher evaporation rates may take place near the toe, where there is more moisture. Work presented in Section 8.2 of this thesis show how these effects may be predicted on sloped surfaces using existing models in conjunction with the proposed method of calculating net radiation on sloped surfaces.

Slight variations in wind, precipitation, and temperature may also be expected as a function of slope. These factors have been reviewed as relevant background material, but are not considered as important as the radiation and moisture variations over topographic variations on the scale of waste rock dump sites, and therefore have not been incorporated into the model presented.

Direct measurements of actual evaporation were used in the evaluation of the evaporative approach presented in this thesis. Measurements were made with both the microlyismeter method and by the energy balance method. Both methods have been used by other researchers.

4 Theoretical Development

Presented in this section is the development of a method to estimate the net radiation received on a slope of any orientation, located at any latitude. In this method, the net radiation for the slope is estimated based on the measured net radiation received by a horizontal surface in the same general location. The method has been developed based on several well-established meteorological techniques and relationships, linked in a novel way for the prediction of net radiation on any slope. These techniques have been adapted and modified to produce a practical method that can be used in applications where the estimation of evaporation from a sloping soil cover is the final goal. For general application, the method has been coded as a program (called SunModel) using the MATLAB language. A copy of the program is included in Appendix C. The model has been developed so that it is both generally applicable, and can also be easily integrated with established models for predicting flux boundary conditions on soil covers, such as SoilCover (Unsaturated Soils Group, 1997) and VADOSE/W (GeoSlope, 2001), creating a method of predicting actual evaporation from sloped surfaces.

Other researchers have also observed the need for a model to predict net radiation on sloped surfaces. Matzinger et al (2003) pointed out that while radiation measurements are commonly made with horizontally oriented net radiometers, the actual net radiation balance for a given surface should be evaluated with a net radiometer located parallel to the surface under consideration. Since it is not normally practical to install net radiometers parallel to all of the variously oriented surfaces at a site, a model to predict net radiation on any given sloped surface is potentially useful. Matzinger et al (2003)

approached this problem by developing a model that required site-specific and empirically-fitted parameters for application, and neglected the impact of slope on diffuse and longwave radiation components. The model presented in this thesis is suitable for more general application at a variety of sites, and does not neglect diffuse and longwave components.

A general overview of the theoretical background to the development of this model was presented in Chapter 2 and Chapter 3. The following subsections of this chapter provide a step-by-step description of the computation method used for the prediction of net radiation on sloped surface, and the structure for final version of the model. Major assumptions are also discussed, and a brief description of how to use the coded program is provided in Appendix C.

This model has been developed for typically instrumented sites where net radiation data is available. Where net radiation data is not available, the model can be used with net radiation numbers that have been estimated, using methods such as those proposed by Irmak et al (2003b).

4.1 Partitioning Net Radiation into Its Components

A net radiometer is typically used to collect the radiation data at waste disposal sites. The net radiometer returns an instantaneous reading, which is the net radiation flux (the SI units for the flux are W/m^2). This value can be integrated over a time interval, such as a day, giving a total energy value (such as MJ/m^2), which can be used in the calculation of daily potential or actual evaporation. However, there is no direct way of telling from a net radiation measurement how much of the measured radiation is shortwave and how much is longwave. Knowing the relative proportions of these energy types is necessary if the effect of slope is to be calculated. The components of radiation that make up a net radiation measurement were summarized in Equation 2.10, and illustrated schematically in Figure 2.2.

In this model, partitioning net radiation into its various components required the use of both empirical and analytical relationships. The first step was to determine the proportion of longwave and shortwave radiation in the measured Q_{net} values. This was done by estimating the amount of longwave radiation, based on relationships between air/ground temperature and net longwave radiation. Once the longwave radiation had been subtracted out from the total net radiation measurement, shortwave radiation remained. For the shortwave radiation, proportions of beam and diffuse radiation were estimated based on the empirical relationships that had been established by others for this purpose. These relationships were based on the ratio between the amount of total shortwave *actually* received at a surface to the amount of total shortwave that

theoretically *could* be received by that surface. This ratio indicated the amount of diffuse and beam radiation, as on days when the actual radiation received was low, it is expected that the radiation would be mostly in the form of diffuse shortwave radiation.

An alternative approach to the above methodology for determining the amount of each component of radiation would be direct measurement of the individual radiation components. This could be done with a pyranometer to directly measure the total shortwave radiation, and a shaded pyranometer to measure the diffuse shortwave. Neither of these instruments are typically in place with the weather stations at waste disposal site covers. The methods presented in this thesis were developed to circumvent the use of such instrumentation, allowing data already collected at waste disposal sites to be used in the estimation of evaporation from slope cover surfaces.

As this method was specifically formulated for simple integration with established models for the prediction of actual evaporation, (SoilCover,Unsaturated Soils Group 1997; Vadose/W, GeoSlope, 2001), average daily values were used for parameters such as temperature and vapour pressure. The equations used would also be valid when averaged over smaller time intervals (such as hourly data), although this would require some re-formulation of the model as presented. All radiation values were considered in terms of values that had been integrated over the course of the entire day. For instance, the Q_{net} value used as an input to the model would be specified in $MJ/m^2/day$ for each day evaluated.

4.1.1 Estimating Longwave Components

As shown in the literature review, the longwave radiation emitted by the earth ($L\uparrow$) can be described by the following formula (Nunez, 1980):

[4.1] $$L\uparrow = \varepsilon\sigma T_o^4 + L\downarrow (1-\varepsilon)$$

where:

σ = Stefan-Boltzmann constant (5.67×10^{-8} W m^{-2} K^{-4})

T_o = Average daily ground surface Temperature (degrees Kelvin)

ε = emissivity of the surface

$L\downarrow$ = Longwave radiation incident on the surface

As a result, the net longwave radiation at the ground surface is:

[4.2] $$L_{net} = L\downarrow - \varepsilon\sigma T_o^4 + L\downarrow (1-\varepsilon)$$

For the methodology developed here, it was assumed that the daily average temperature of the ground surface (T_o in the equation) was approximately the same as the daily average air temperature measured at the weather station, an assumption that has been used by others (Nunez, 1980; Weiss, 1982 ; Oke, 1987). The term $L\downarrow (1-\varepsilon)$ in the

equation represented the proportion of the incoming longwave that was reflected from the ground surface.

As discussed Chapter 2, the calculation of downwards longwave radiation, $L\downarrow$, under clear sky conditions required that an atmospheric emissivity ε_{ac} value be determined. There were several alternative methods considered for the calculation of downwelling longwave radiation ($L\downarrow$). Under clear-sky conditions with limited climatic data, the models of Swinbank (1963), Brutsaert (1975) and Idso (1980) have all been commonly used. The method of Swinbank (1963) was relatively simple, requiring only a measurement of atmospheric temperature at screen height in the weather station. The models of Brutsaert (1975) and Idso (1980) required measurements of atmospheric vapour pressure (e_o), and the Idso (1980) approach also required the estimation of an additional parameter (a_0) reflecting the location and expected atmospheric conditions at the site. The models that incorporated vapour pressure were expected to be more accurate at locations throughout the world, based on the research of Hatfield et al (1983), Weiss (1982), and Cluf and Gash (1993). For the applications that will be presented in this work, the differences in results with the different methods were not large (less than 1 $MJ/m^2/day$). Note that none of these models work well below 0°C (Cluf and Gash, 1983). This is not considered unduly restrictive, as most evaporation calculations will be concerned with conditions above freezing. Sublimation is not considered in the present theory.

The method presented in this thesis was formulated so that where data was available, the models of Brutsaert (1975) or Idso (1980) could be used. Otherwise, the simple and robust model of Swinbank (1963) was used by default:

[4.3] $L\downarrow = \varepsilon_{ac} \sigma T_o^4$

where

ε_{ac} = Clear-sky emissivity ($1.22\text{-}171/\sigma T_o^4$)

The Swinbank (1963) model (and the others) were developed with the assumption that skies are clear. To account for cloud, a clearness index was included in the method. While a clearness index may be calculated based on observed cloud, such observations are often not available for remote sites. As a result, the model was formulated to use the ratio of computed incoming shortwave radiation to the theoretical maximum incoming shortwave radiation as an indicator of cloudiness. Jury and Tanner (1975) used this approach, and a variant was used by Buchan (1982) and Novak and Black (1985). In this approach, the fraction of the sky that is clear was given by:

[4.4] $f_c = (S\downarrow/S_o)a_1 + (1\text{-}a_1)$

where:

$S\downarrow$ = downwards shortwave radiation

S_o = maximum potential shortwave radiation on the ground is estimated

a_1 = a factor to account for the fact that $S\downarrow$ is not zero when the sky is completely cloud covered

For the method presented here, f_c was initially set equal to one (clear sky conditions), and then modified iteratively using the calculated values of $S\downarrow$ and S_o. The calculation of the shortwave components will be discussed in a following section. The factor a_1 could be estimated based on the fact that f_c=0 when the sky is totally cloud covered. Substituting f_c=0 and the minimum measured $S\downarrow$ for the site into equation [4.4] allowed a_1 to be calculated for a given site.

Once estimated or calculated, the value f_c was used to calculate an effective atmospheric emissivity (ε_a). This effective emissivity was used in place of the clear-sky atmospheric emissivity term in the equation for incident longwave radiation (Equation 4.3), and was calculated as follows (after Buchan, 1982):

[4.5] $$\varepsilon_a = f_c\varepsilon_{ac} + (1-f_c)(\varepsilon_{ac}+(1-\varepsilon_{ac})(1-4\Delta T_{cl}/T_o))$$

Where ΔT_{cl} was the difference in degrees (Celsius or Kelvin) between the temperature at the screen height and the temperature at the cloud base. Buchan (1982) and Novak and Black (1985) both used a value of 10°C as representative for ΔT_{cl}. All other terms in the equation were as defined previously.

4.1.2 Calculation of Shortwave Components

Once the net longwave radiation (L_{net}) was estimated, it was subtracted from the net all-wave radiation (Q_{net}), with the residual being the net shortwave radiation (S_{net}). S_{net} was divided into its downwards ($S\downarrow$) and upwards ($S\uparrow$) components based on the known or estimated albedo (α) of the ground surface, as:

[4.6] $S_{net} = S\downarrow - S\uparrow$

[4.7] $S\uparrow = \alpha S\downarrow$

As discussed in the literature review, there were several different methods available with which to divide shortwave radiation into its beam and diffuse components. The Bristow and Campbell (1985) model was selected for the work presented here, as it followed the general form of the well-established Liu and Jordan (1960) model, while performing significantly better (Becker, 1991). It also incorporated a greater degree of physical basis than many of the similar available models, and has been demonstrated to work well at a variety of latitudes (Bristow and Campbell, 1985; Becker, 1991). Finally, the relatively simple form of the model was well suited to computer application. The Bristow and Campbell model has also been used extensively by others, including in the MTCLIM and related models for climate predictions (Running et al, 1987; Glassy and Running, 1994; Thornton et al, 1997).

As described in the literature review, the equations put forth by Bristow and Campbell (1985) were:

[4.8] $T_T = S\downarrow/S_o$

[4.9] $T_D = S_d/S_o = T_T(1-\exp(0.6(1-B_c/T_T)/(B_c-0.4)))$

where:

T_T = Total daily transmittance

T_D = Total diffuse transmittance

B_c = Maximum clear-sky transmissivity

S_o = Maximum potential clear-sky radiation

The S_o for a given day was relatively simple to calculate on the basis of solar geometry (see Appendix B). The parameter maximum clear sky transmissivity, B_c, can vary between 0.7 and 0.8, and is typically in the order of 0.75 (Bristow and Campbell, 1985). The value for a given site was estimated from site data by calculating the maximum measured value of T_T.

Equations [4.1] through [4.9] were solved in sequence to provide an initial estimate of the proportions of each type of radiation that made up a daily Q_{net} value for given site location, day of the year, and average daily temperature. The calculated ratio of $S\downarrow/S_o$

was then used to modify the estimated longwave radiation, and the sequence of calculations iterated until good convergence was achieved. The work conducted to date indicated that convergence of better than 0.01 $MJ/m^2/day$ could typically be achieved with fewer than 10 iterations.

4.2 Calculation of the Energy Input to a Slope

Once the net radiation on a horizontal surface had been divided into its various components following the methodology developed in Section 4.1, the input of radiation into a given slope could be determined by applying the appropriate transformation to each component of net radiation. Each component of net radiation needed to be reduced or increased by an appropriate factor, to account for its reduced or increased exposure (functions of slope and aspect). The modified components were then summed to give the net radiation input to the slope.

4.2.1 Calculation of Shortwave input to the slope

For the calculation of the shortwave input to the slope, the following formula was used (Bristow and Campbell, 1985):

[4.10] $S{\downarrow}_{slope} = (S{\downarrow}-S_d)F + S_d\, f + S{\downarrow}(1-f)\alpha_s$

The term f was a sky-view factor, which represented the fraction of the sky visible to the tilted surface.

The term $S\downarrow(1-f)\alpha_s$ in the equation represented the shortwave radiation that was reflected to the slope from the portion of the ground that it faced, where the albedo of the surrounding ground was given by α_s.

For a simple slope facing relatively flat surrounding terrain, f can be calculated with (Bristow and Campbell, 1985):

[4.11] $f = \cos^2(\beta/2)$

where:

$\beta =$ the slope of the surface.

The reduction of S_d by the factor f was made to represent the fact that the tilted surface did not get exposure to the entire sky, from which the diffuse radiation was assumed to come isotropically. While the diffuse radiation was not in fact isotropic through the sky, the error introduced by this assumption was relatively small (Oke, 1987). Note that the method of Hay (Hay, 1979) could be used as an alternative, if one wished to account for the anisotropic distribution of diffuse radiation. However, in the method presented here, total daily values of net radiation were used, which minimized the inaccuracies of the isotropic assumption. On clear days, when the isotropic assumption is least valid, diffuse radiation is a small component of the day total, while the isotropic assumption is more

accurate on cloudy days where the diffuse portion of radiation is going to be more important (Garnier and Ohmura, 1970).

The term F in equation [4.10] was a slope factor, a ratio between the potential radiation received over the course of a day on a sloping surface to that on a horizontal surface (Bristow and Campbell, 1985). Swift (Swift, 1976) provided a generalized algorithm for calculating F at any location on the surface of the planet for any day of the year. The algorithm was based on the geometrical relationships between the surface of the sun and the surface of the earth, and required as inputs the angle of the slope, the aspect of the slope (the compass direction faced by the slope), the latitude of the site under consideration, and the day of the year. The complete algorithm was adapted into the program used for the method presented in this thesis (see Appendix A), and was used for all calculations of F. Calculations for solar declination and extraterrestrial radiation in the algorithm were made as discussed in Appendix B. All other calculations required for F followed the formulation of Swift (1976).

Finally, the net shortwave to the slope is the downward shortwave radiation, less whatever is reflected due to the albedo of the surface.

[4.12] $S_{netslope} = S{\downarrow}_{slope}\,(1-\alpha)$

4.2.2 Calculation of the Longwave Input to the Slope

The input of longwave radiation to the slope was calculated in a manner similar to that of the input of diffuse shortwave radiation. The longwave radiation was assumed to be distributed isotropically from the sky (Oke 1987), and the sky-view factor (f) was used to account for the portion of the sky visible to the slope.

The total longwave radiation incident on the slope was therefore:

[4.13] $$L\downarrow_{slope} = L\downarrow f + L\uparrow(1-f)$$

And the net longwave to the slope was then:

[4.14] $$L_{netslope} = L\downarrow_{slope} - L\downarrow_{slope}(1-\varepsilon) - L\uparrow$$

4.3 Algorithm to Calculate Solar Radiation

The techniques described have been coded into a single model for use with the data collected at weather stations. For each day of data collected by a net radiometer over a horizontal surface, the model can be applied to the original data to estimate what the net radiation would be for a sloped surface at the same location. The required inputs are the net radiation on the horizontal surface (Q_{net}), the average daily temperature, latitude, and the Julian day of measurement. The albedo and emissivity of the original and transformed slopes are also needed.

The full Matlab code for the model is provided in Appendix C, along with a brief description of the main components of the code. A simplified flowchart for the core program is shown in Figure 4.1. In the program, the main calculations for a given slope are done by the subroutine sunfunc.m, which is called by a program that specifies the latitude, slope, azimuth, albedo and emissivity of the slope for which the calculations are to be performed. The function reads daily data for net radiation on a horizontal surface, and transforms it as required for the desired surface.

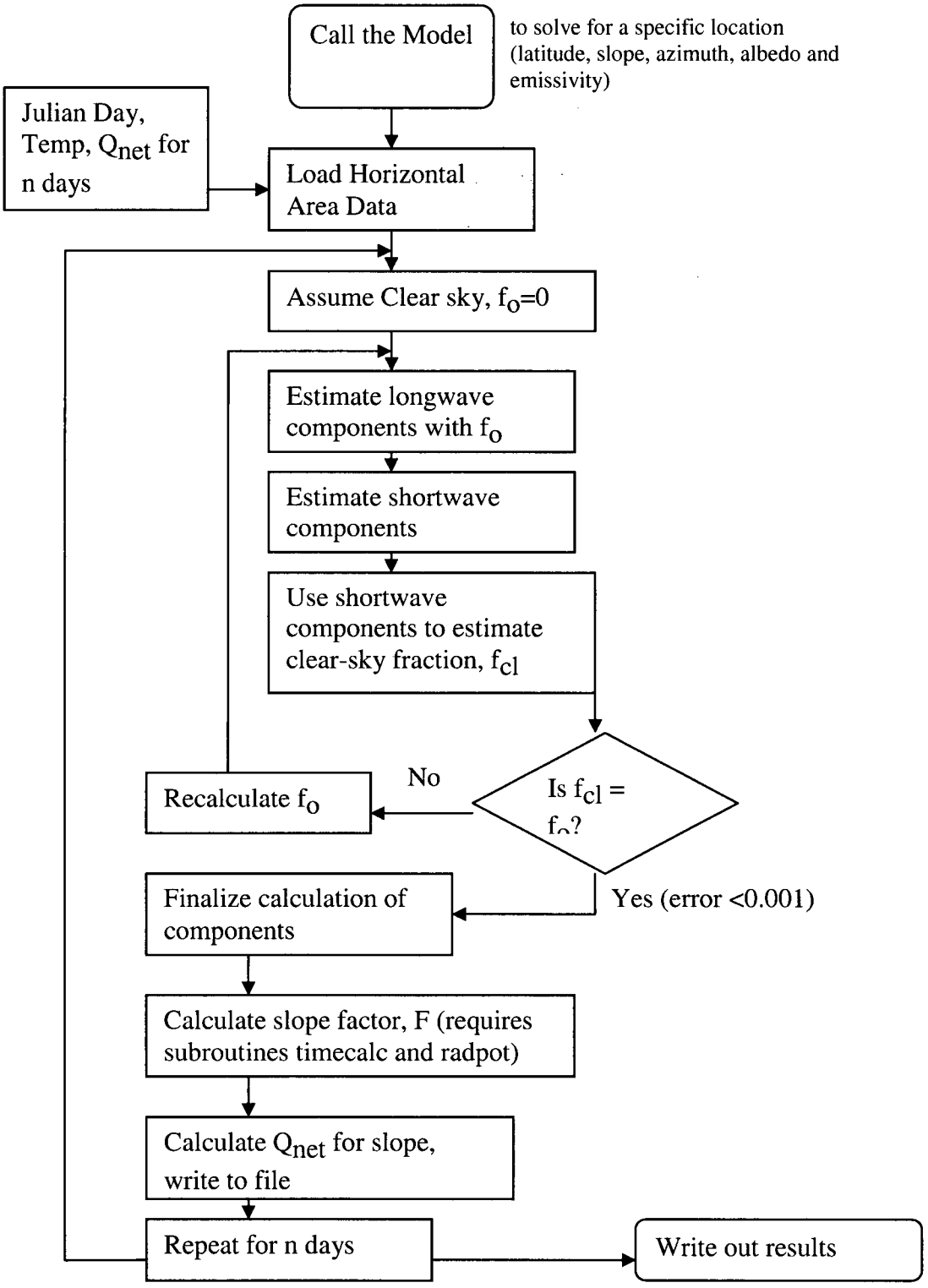

Figure 4.1: Simplified flowchart for model of net radiation on sloped surfaces

4.4 Mapping Results in Three Dimensions

The approach for calculating net radiation on sloped surfaces described in the previous section was suitable for application to uniform slopes, and to single point locations. This approach can also been extended for application to fully three-dimensional ground surfaces, as described in this section. To illustrate a fully three-dimensional approach to mapping net radiation and potential evaporation over a non-uniform ground surface, a simple routine was developed for use with a commercial plotting package (Tecplot 9.2, Tecplot Inc., 2002). The routine was developed to work with survey data describing the topography of a site in terms of data points in three-dimensional space (xyz data).

The basic approach used for mapping radiation in three dimensions is shown schematically in Figure 4.2. A mesh of the site was constructed in the plotting software, based on the survey data. The mesh was created in the program Tecplot, and is a Triangulated Irregular Network (TIN) surface. Most common digital elevation models use either a regular grid surface or a TIN to represent a given topography (Warren et al, 2004).

The TIN data defining the mesh was imported to a program written to calculate for each point in the mesh an average slope and azimuth. A variety of different techniques were available for making such calculations, all of which are prone to some degree of error (Warren et al, 2004). For this application, the slope and azimuth at any given node in the TIN mesh was calculated based on the averaged slope and azimuth for each triangle of surface attached to the node, weighted for the area of the triangle. Calculating slope at a

point in a DEM based on the average of slopes at surrounding areas has been shown to give good results (Warren et al, 2004). Vector math was used to calculate the slope, azimuth and area of each triangle. Vector math approaches are commonly used for calculating slopes with DEMs (see for example Corripio, 2003). Such calculations result in some smoothing of the calculated slopes due to the averaging across several triangles. This was not overly detrimental in a model that was to be used for illustrative purposes. Warren et al (2004) noted that while finer resolution meshes will result in less smoothing, "a grid size that is too small may result in an estimate of slope variation at a much higher level detail than is relevant for the process being modeled".

Once the slope and azimuth was calculated for each node, the radiation model previously described was used by the program to calculate for each point the net radiation expected based on a given day's net radiation on a horizontal surface. At this stage, it was also possible to calculate the potential evaporation at each point, with the addition of some climate data for the site, based on the Penman (1948) method described in Chapter 2. The program generated a data file consisting of all the data points that originally defined the mesh. Each data point had associated with it a calculated net radiation value for each day that the simulation was run, as well as average and total net radiation values for the duration of the run. If potential evaporation was assessed, daily values for this at each point is also included. This data file could be imported back into the plotting software, and the calculated values plotted on the three-dimensional mesh as colour contours. For the sake of simplicity and maintaining reasonable computational times, the effects of shading by surrounding elements were not included in the routine, similar to the simplifying assumptions used by Sellers et al (1997).

Appendix C includes the MATLAB code for the program used to calculate the slope/ azimuth at each node, integrate the data with the net radiation model, calculate potential evaporation, and create data files for use with the plotting software, as shown in Figure 4.2. The majority of the code is devoted to sorting through the data points and finite element mesh, developing for each node a list of the nodes connected to it, and the co-ordinates of the connected nodes. This data is used to perform the vector math required to calculate the average slope at each node, and also calculate the area of triangles associated with each node.

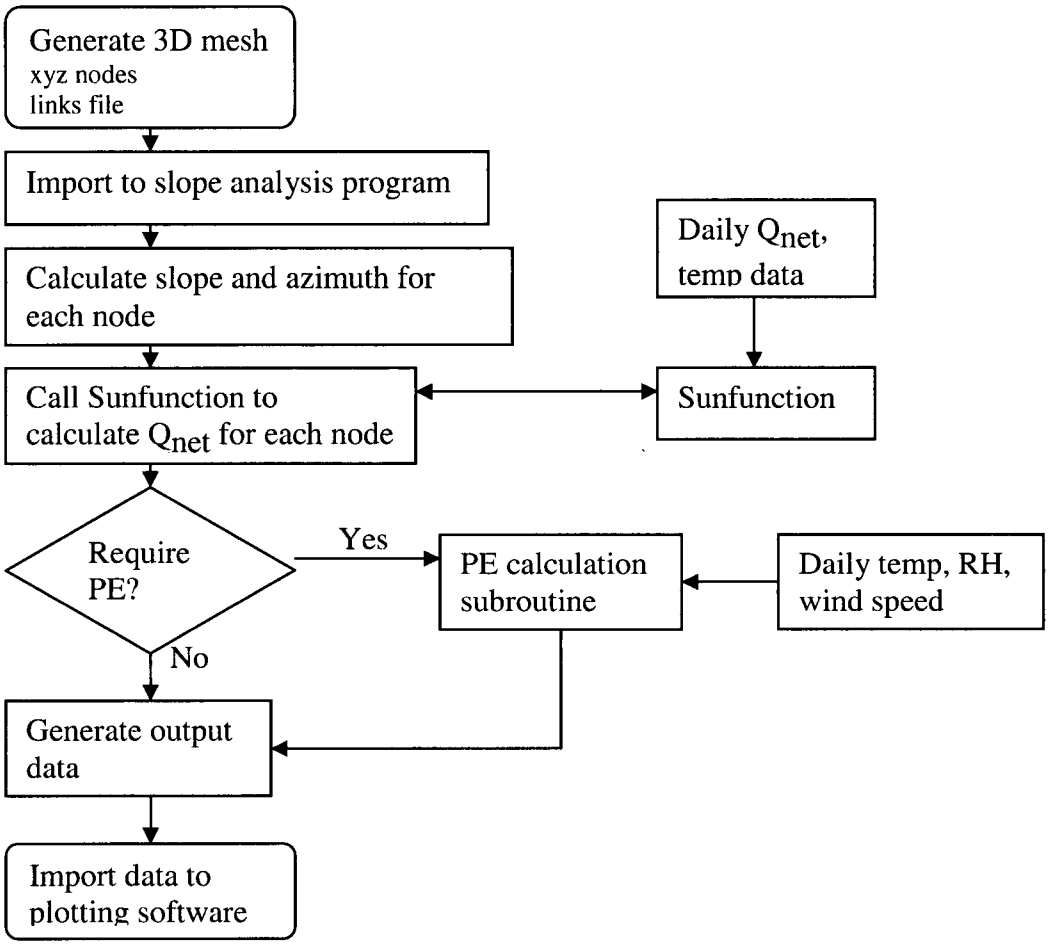

Figure 4.2: Simplified flowchart for mapping in three dimensions

4.5 Summary of Main Assumptions in Method

The development of any theoretical model for practical application requires that simplifying and limiting assumptions be made. It is important to clearly identify these assumptions so that the model is not applied in an inappropriate way, and limitations on the model's potential accuracy are clearly understood. The most important assumptions in the theory used to develop the model in this thesis are summarized in point form below:

1. For the estimation of longwave radiation emitted by the ground, it was assumed that the daily average temperature of the ground surface (T_O in the equation) was approximately the same as the daily average air temperature measured at the weather station.

2. The beam and diffuse portions of the daily shortwave radiation were estimated using the methodology of Bristow and Campbell (1985), which was an empirical method based on the maximum clear sky transmissivity and the potential solar radiation to a horizontal surface.

3. Surface albedo was assumed to be constant at each point of the slope and surrounding locations evaluated.

4. For both longwave radiation and diffuse shortwave radiation, the incoming radiation incident on the ground surface was assumed to be distributed isotropically from the sky.

5. The methods for the calculation of downwelling longwave radiation are accurate only for non-freezing conditions.

6. For three-dimensional mapping, slopes were considered to be relatively simple (similar to those discussed in Section 3.1.1), with skyview factors calculated as a function of the local slope. More sophisticated shading approaches are available in GIS programs such as Arc/Info and Genasys. These programs have been used by others for a more detailed evaluation of shading in shortwave radiation calculations (see for example Kumar et al, 1997). GIS programs were not used for the present work to simplify integration of the net radiation model with flux boundary programs such as SoilCover and VADOSE/W.

4.6 Verification of Model - Evaluation of Subroutines

To determine the validity of the preceding approach to calculate the net radiation on slopes from measured net radiations on horizontal surfaces, the model has been tested against data published in the literature, and against data collected over a soil cover site. Data in the literature was used to test the main algorithm in the model for the prediction of net radiation components, and field data was collected to evaluate the overall performance of the model for predicting net radiation on slopes, based on values measured on horizontal surfaces. The methodology used for the collection of field data is discussed in Chapter 5, with the data presented in Chapter 6 and analysed in Chapter 7.

The algorithm for the calculation of the slope factor (F) and the sky-view factor (f) was tested by comparison of values calculated in the program to those published by Bristow and Campbell (1985). Bristow and Campbell (1985) calculated and tabulated parameters for slopes of 20° and 45°, oriented towards each of the main compass directions (North, South, East, West), and for several days of the year (Julian days 80, 173, 264, 356). The SunModel program was used to calculate both factors for the same conditions, with results virtually identical to those that had been reported. This check confirmed that the coded version of the algorithm had introduced no new errors.

To evaluate the accuracy of the subroutines in the new model for predicting the various components of net radiation, data published by Weiss (1982) was used. The study by Weiss (1982) included field measurements of both net radiation on a horizontal surface,

and the measured shortwave and longwave components of the radiation ($S\uparrow$, $S\downarrow$, $L\uparrow$, $L\downarrow$). The study by Weiss was used as it included necessary information such as the daily average temperature and the daily albedo of the ground surfaces. The measurements were made by Weiss (1982) on a daily basis between August 5 and September 8, over an alfalfa field located at Latitude 41°51' North.

The daily values of the net radiation and average daily air temperature reported by Weiss were used as input for the program SunModel, along with the site latitude, average ground albedo, and an assumed surface emissivity of 0.95 (the emissivity was assumed based on the type of crop cover described by Weiss). The values of $S\uparrow$, $S\downarrow$, $L\uparrow$, and $L\downarrow$ predicted by the model were compared to those measured by Weiss in the field, and excellent agreement was found, as shown on Figure 4.3.

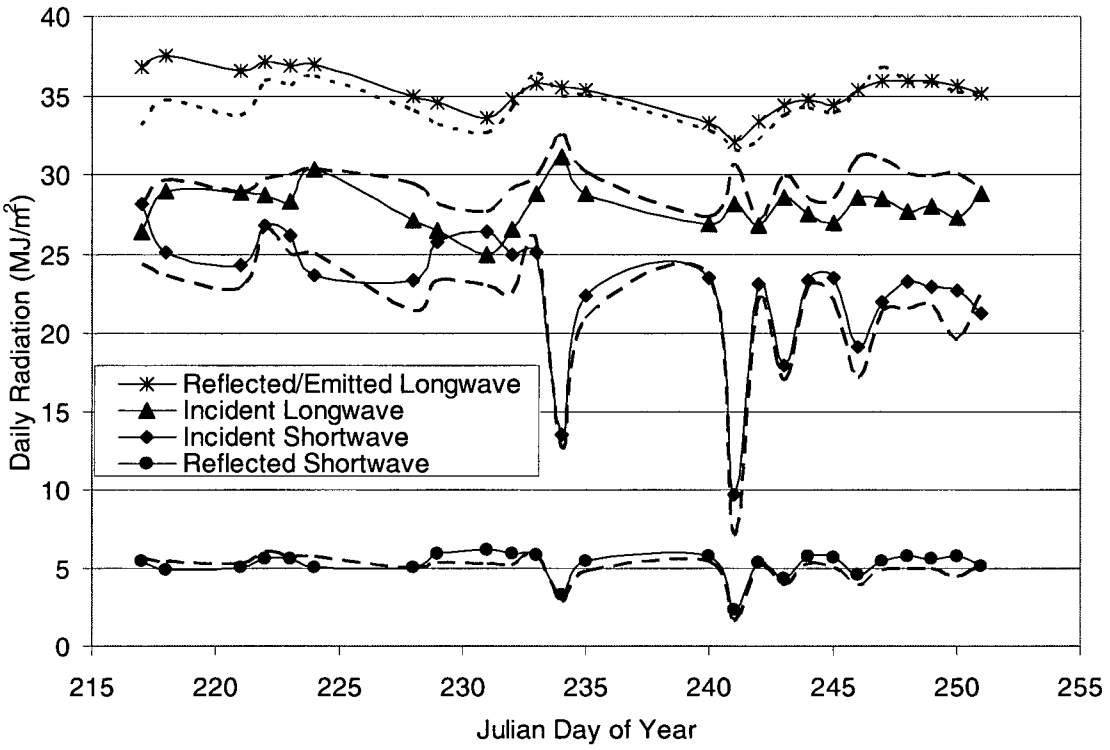

Figure 4.3: Comparison of measured and predicted components of net radiation (Dashed lines show predicted values)

A model has now been developed that allows the calculation of net radiation on any surface, based on the net radiation measured on a horizontal surface and a minimal amount of additional climatic data. Preliminary testing against data in the literature indicated that this new method can predict the various components of radiation contained within a net radiation measurement. Further evaluation of the model with field data is presented in the following sections of this thesis.

4.7 Summary of Theoretical Development

A model has been developed and presented to calculate and show net radiation on any sloped surface, based on the net radiation measured on a horizontal surface. In this model, net radiation data is used along with other basic climate data to estimate the longwave radiation at the site, and the two components of shortwave radiation (diffuse and beam). For any given slope, the components are then modified by the appropriate factors, and re-integrated to give the net radiation input into the slope. This approach has been coded into an algorithm that can be easily incorporated with existing models for actual evaporation, and also as a program that can be used to map net radiation over any three-dimensional ground surface map.

In the following sections of the thesis, the data collection for the experimental verification of this model will be discussed, as will the actual verification of the model, and illustrations of its application.

5 Data Collection – Experimental Methods

For the testing and assessment of the theoretical model for verification of its application, field data was measured at several sites. Related data collected by previous researchers at these sites were also collated. This section provides a brief overview of environmental conditions at the research sites (Section 5.1), followed by a detailed review of climate data (Section 5.2), topographic data (Section 5.3), and radiation measurements (Section 5.4) made at the site. On-site measurements of soil moisture are also reviewed (Section 5.5), as are the methodologies employed for the direct measurement of evaporation (Section 5.6). Finally, key soil properties at the research sites, to be used in models of evaporation at the sites, are reviewed (Section 5.7).

5.1 Research Sites

Data for components of the model verification were collected at sites in British Columbia, Canada (the Equity Silver mine and an overpass in Vancouver), with supplementary data collected at the Kidston Gold Mine in Queensland, Australia. The Kidston site is described briefly below (Section 5.1.1), the Arthur Lang Overpass site in Vancouver is described briefly in Section 5.1.2, and a more detailed description of the Equity Silver site is presented in Section 5.1.3.

5.1.1 Kidston Gold (Australia)

Preliminary measurements of net radiation on slopes and differential evaporation from sloped surfaces were made on the test cover placed at the Kidston Gold mine located in semi-arid North Queensland, Australia, approximately 280 km south west of Cairns. The site was located approximately 540 meters above sea level, at latitude approximately 19° south. The climate at the site was semi-arid and sub-tropical, with a distinct wet season from November to April, during which over 80 percent of the annual rainfall occurred (Williams et al, 2003). Average annual precipitation was approximately 700 mm, considerably less than the 2800 mm potential evaporation (Williams et al, 2003).

Experimental work at the Kidston site took place on the test cover installed at the mine site south dump. The store-and-release cover at this site was constructed over a 23 ha area in late-1995. The upper layer of the cover at this site consisted of an uncompacted layer of oxidized waste rock (a soil-like material), a minimum of 1.5 m thick. This uncompacted layer was end-dumped from trucks to create a hummocky topography and prevent runoff. The hummocks also provided sloped surfaces of various orientations within a relatively small area for use in the current research. More complete details on the design and performance of this test cover can be found in Durham et al (2000), and Williams et al (2003).

For radiation and evaporation measurements, a single hummock was selected near the south end of the test cover. The hummock selected was subject to minimal shading from other hummocks or nearby trees, and was approximately 2 metres in height from its base to crest, with steep side slopes (2H:1V or steeper). The site was minimally vegetated, and all vegetation was cleared from the area to reduce the number of variables affecting net radiation and evaporation measurements.

5.1.2 Arthur Lang Overpass (Canada)

Preliminary net radiation measurements were also collected at the site of the Arthur Lang Overpass, located near the Vancouver International Airport. The location of Vancouver is shown on Figure 5.1. The overpass is located to the immediate north of the intersection between Russ Baker Way and Miller Road, with all measurements taken in the area to the immediate northwest of the intersection. The overpass is located at latitude 49.2° North, just above sea level. Measurements were collected at the overpass in July of 2001, while the overpass was under construction.

Slopes in the areas used varied in steepness from 9° to 19°. At the time of data collection, there was little or no vegetation in the measurement area, and the light grey sandy gravel soil was dry and crusted.

5.1.3 Equity Silver (Canada)

The main portion of the experimental work was conducted at the Equity Silver site, located in central British Columbia, Canada, approximately 575 km north-northwest of Vancouver, as shown in Figure 5.1. The site was located approximately 1300 metres above sea level, at a latitude approximately 54° north. The climate at the site was classified as humid alpine, with an average annual precipitation of 710 mm per year. This precipitation (60% snow, 40% rain) exceeded the annual potential evaporation (500mm) at the site (Swanson et al, 2003). Average monthly temperatures at the site were below zero between November and March, with the majority of the snowmelt and runoff typically occurring in May.

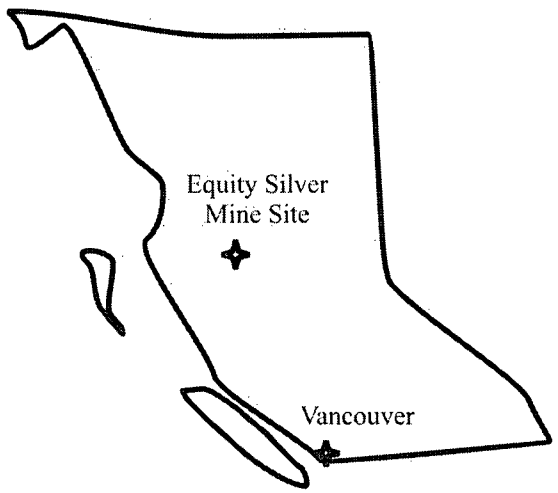

Figure 5.1: Location of Equity Silver Mine in British Columbia

The construction of the soil cover under consideration began in 1991, with progressive completion of cover placement on all three of the waste rock dumps on site by 1994.

During the productive life of the mine (from 1980 to 1994), over 80 Mt of waste rock were generated, and disposed of in three adjacent waste rock dumps. Much of the waste rock disposed of at these dumps had the potential to generate acidic runoff if left exposed to the air and precipitation. In 1981, ARD was discovered at the site. Subsequently, a runoff collection network and lime treatment plant were constructed at the site, to neutralize the ARD. To minimize the exposure of waste rock to oxygen and water, a soil cover was placed over all of the waste rock dumps, with a total cover area of approximately 100 hectares. The size of each of the three dumps is listed in Table 5.1, and the relative locations of the dumps are shown on Figure 5.2.

Table 5.1: Distribution of waste rock between dumps

Dump Name	Volume of Waste Rock (Mt)	Area (ha)	Year of Cover Placement
Bessemer	10	29	1994
Main	52	41	1993-94
Southern Tails	18	31	1991

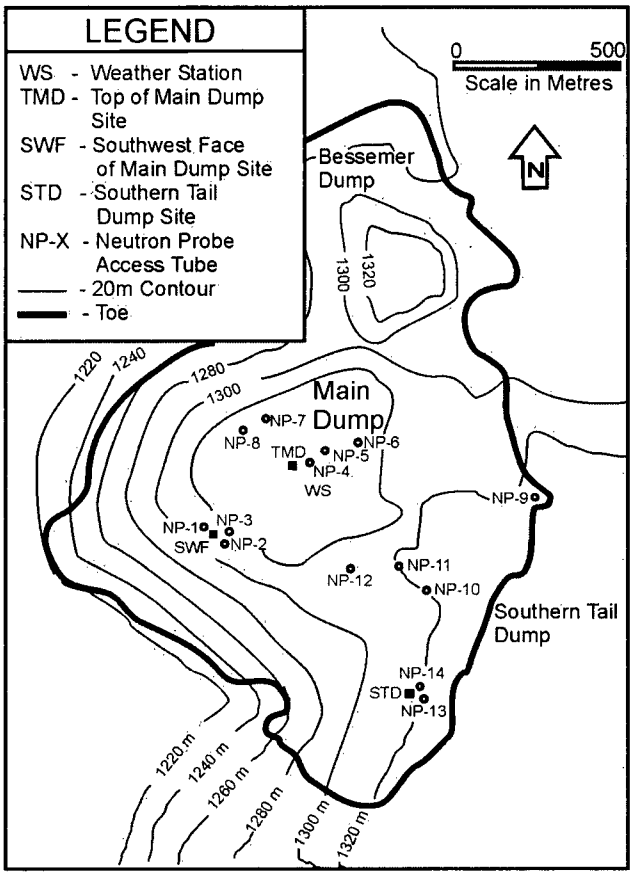

Figure 5.2: Site plan –location of dump and monitoring equipment (after O'Kane, 1995)

The cover was designed to maintain saturation in the lower compacted layer (to limit oxygen diffusion into the waste rock) and also to maximize evaporation from the loose surface till (to minimize the moisture flux through the cover). The till material used in the cover was a locally available material that could be applied to the waste rock dump at a reasonable cost. The cover till consisted of a 0.5 m thick layer of compacted till, overlain by a 0.3 m thick layer of loosely placed till. A summary of the cover material properties is presented in Section 5.7.2. A more detailed description of the cover design rational can be found in O'Kane et al (1998) and O'Kane (1995).

5.2 Climate Data

At both sites, automated weather stations were used to collect relevant climate data, such as temperature, precipitation, humidity, and net radiation. A brief overview of the data collection at the Kidston site is provided in Section 5.2.1, followed by a more detailed review of the data collection at the Equity site (Section 5.2.2). At both sites, data were reviewed on an annual or bi-annual basis, and equipment checked and repaired or replaced when the data results became suspect. Climate data can be screened to assess the quality of the data, and to eliminate obviously erroneous data. Techniques for screening radiation, humidity, and wind data were outlined by Allen (1996).

5.2.1 Kidston Climate Data

Climate data is collected at the Kidston site at a fully automated station for monitoring the Bowen ratio. This weather/Bowen station had been in operation since 1996. Data collected at this station included net radiation, windspeed, rainfall, and daily minimum and maximum values of air temperature and relative humidity. The individual instruments used to make these measurements were similar to those described in the following Section 5.2.2. Additional weather data collected at the station for the calculation of the Bowen ratio and prediction of actual evaporation included soil heat flux (measured with a soil heat flux plate) and upper/lower elevation humidity and temperature values for the determination of sensible heat flux.

5.2.2 Equity Climate Data

Climate data at the Equity site was collected at fully automated weather station located on top of the main dump (TMD location on Figure 5.2). The weather station is shown in Figure 5.3. Climate data collected at the weather station included net radiation, temperature, humidity, windspeed and rainfall data. The weather station had been operational since April of 1993, when it was installed as part of the research conducted by O'Kane (O'Kane, 1995). Since that time, it has been maintained by staff at the mine site and by the author.

Net radiation at the weather station was measured with a net radiometer, sampled every 60 seconds at the data logger. These readings were averaged and stored on an hourly basis. From the original installation of the weather station in April 1993 to the fall of 2001, net radiation was measured with a REBS Q6.1 net radiometer. This net radiometer had a thermopile sensor, shielded from convective cooling with a polyethylene bubble over the sensing surfaces. This type of radiometer was found to be too fragile for reliable operation at the site, with the bubble frequently rupturing or developing condensation problems. On September 27, 2001 the REBS net radiometer was replaced with a Kipp & Zonnen NR-LITE net radiometer. The Teflon-coated thermopile sensors used in this net radiometer does not require a polyethylene bubble for protection. The Kipp & Zonnen net radiometer measures light over a spectral response range of 0-100 μm, compared to the 0.25-60 μm range of the REBS net radiometer. This slight difference in measurement range should not greatly affect the results, as the bulk of shortwave energy is transmitted

by radiation in the band of wavelengths between 0.2 and 1.5 μm, while the bulk of the longwave energy is transmitted in the band between 4 and 30 μm, as discussed in the literature review.

Air temperature and humidity at the weather station were measured with a Vaisala HMP35CF temperature and humidity probe, and wind speed/wind direction were measured with an RM Young 05103 high resolution wind sensor. As with net radiation, hourly average data values for these parameters were stored in the data logger, based on readings taken at 60 second intervals over the course of the hour. Precipitation was measured with a RIMCO siphon tipping bucket rain gauge with a resolution of 0.2 mm, sampled every minute.

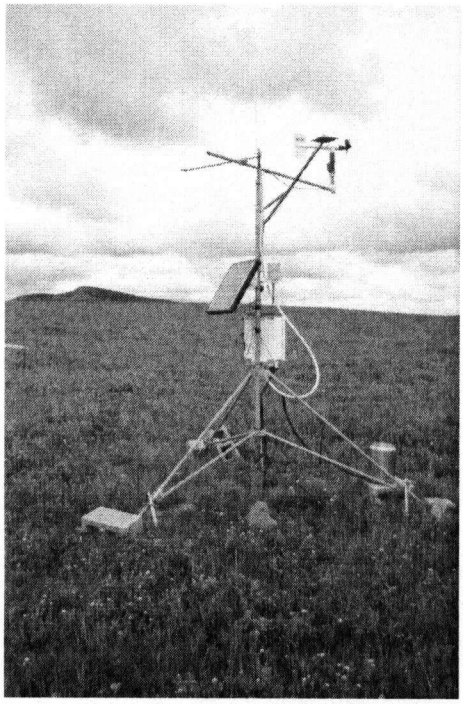

Figure 5.3: Weather station located in the crest area of the main dump

5.3 Topographic Data

Topographic data for the Equity site was collected through site surveys prior to the initiation of this project. Over 2,000 survey data points have been collected to define the topography of the cover over the three dumps on site. The survey data was used to generate the topographic map of the site shown in Figure 5.2. These data were also imported into Tecplot, to generate a three-dimensional mesh defining the surface of the site, as shown in Figure 5.4. Supplementary data points along the relatively flat crest area of the main dump were interpolated from the contour map and input to the meshing program to reduce the size of the TIN elements generated over the crest of the waste rock pile.

Figure 5.5 shows the frequency distribution for the element slopes generated in the finite element mesh. Note that element slopes in excess of 45 degrees were a function of the limited number of data points, rather than an accurate representation of site conditions. Further refinement of the mesh with additional data points would reduce the number of elements generated with excessively steep slopes. Figure 5.6 shows the frequency distribution for element slope directions (azimuth). Zero degrees in north, with values increasing to the east (clockwise).

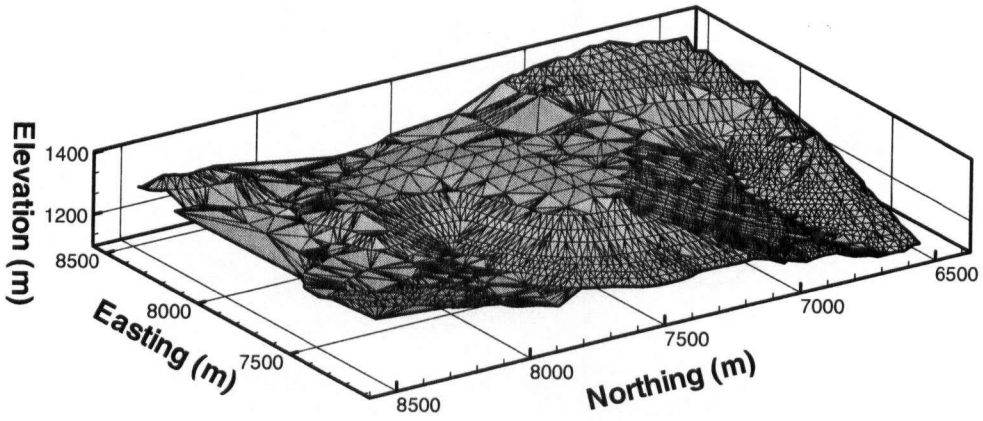

Figure 5.4: Three-dimensional finite element mesh representing the surface of the Equity site.

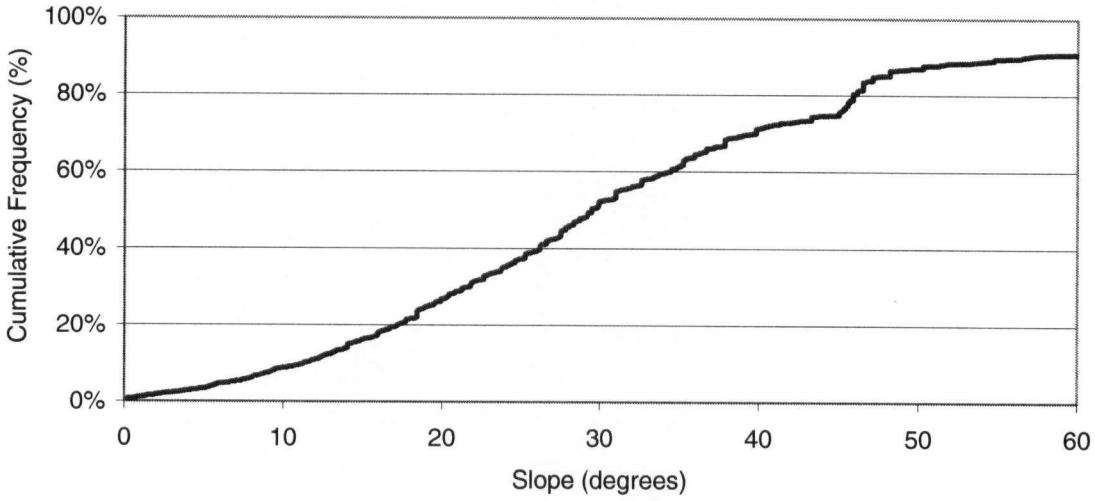

Figure 5.5: Cumulative frequency distribution for slope of elements on Equity site mesh.

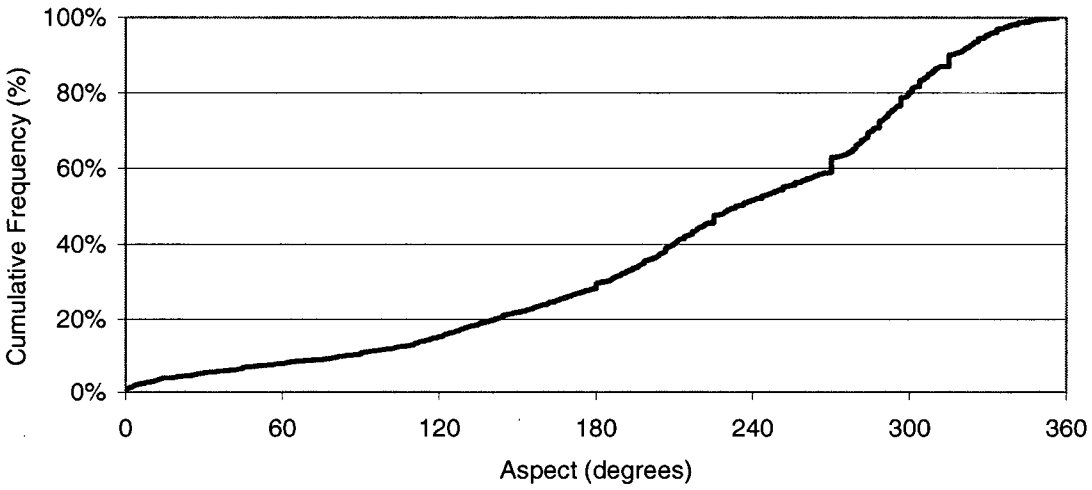

Figure 5.6: Cumulative frequency distribution for azimuth of elements on Equity site mesh.

For the preliminary measurements collected at sites other than Equity, only limited topographic data was required. At the Kidston research site, measurements were confined to a single hummock of limited extent. The hummock was approximately 2 meters high, and side slopes of the hummock were estimated at 1H:1V. For the preliminary measurements made at a third site in Vancouver, Canada (Section 5.4.2), slope angles were measured at data collection locations with a clinometer, and slope bearings were made with a compass. This data is presented in Section 5.4.2.

5.4 Radiation on Slopes

In all cases, net radiation values on sloped surfaces were measured with a net radiometer oriented parallel to the ground surface, as the net radiation budget for a ground surface is defined through a plane parallel to the ground surface (Whiteman et al 1989, part I). This approach to measurement was used by Matzinger et al (2003) for the comparison of net radiation measurements on sloped and horizontal surfaces. A clinometer was used to measure slope angles at all measurement locations, and ensure that the net radiometer was mounted parallel to the ground surface.

5.4.1 Preliminary Measurements Kidston Gold Mine, Australia

Preliminary experimental measurements of net radiation on sloped surfaces were made at the Kidston site between November 30 and December 4, 2000. These measurements were made with Kipp & Zonnen NR-LITE net radiometer, which has a spectral response range of 0-100 μm. This net radiometer was mounted on a tripod (as shown in Figure 5.7) and moved around the surface of the hummock over the course of the day. Measurements were taken on the crest of the hummock, to represent the net radiation on a horizontal surface, and on the slopes of the hummock facing each of the cardinal compass directions (north, south, east and west).

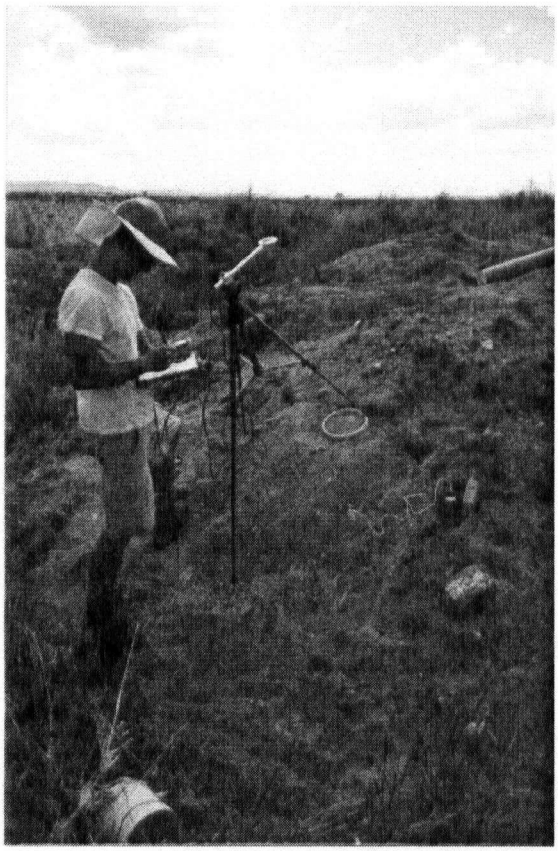

Figure 5.7: Tripod-mounted net radiometer for spot measurements

Spot measurements of net radiation were made using a high quality digital voltmeter (reading to 0.01 mV) to directly measure the potential difference at the radiometer. For each net radiometer reading, 10 readings of potential difference were taken at 5 second intervals and averaged, to minimize error due to small short term variations in voltage. Voltages were converted to net radiation in W/m^2 based on the calibration conversion factor for the net radiometer. On November 30, 2000, measurements were taken six times per day to characterize the variability of net radiation over the hummock. On December 2, 3 and 4, 2000, measurements were taken three times per day at each location (morning, midday and evening) as part of an attempt to characterize the Bowen Ratio on site with hand-held instruments.

5.4.2 Spot Measurements – Arthur Lang Overpass, Vancouver, BC

On July 26, 2001 net radiation measurements were made on the sloped surfaces of the Arthur Lang Overpass (Latitude 49.2° North). Measurements were made with a portable net radiometer set up identically to the tripod-mounted system used at the Kidston Gold Mine site (Section 5.4.1). These measurements were initially made for evaluation of a preliminary version of the net radiation model.

Seven separate measurement locations (Summarized in Table 5.2) were marked at the site, representative of a variety of slope angles and exposure directions. All locations were located to the immediate northwest of the intersection between Miller Road and Russ Baker Way. Little or no vegetation was present in the areas at which measurements were made, and the light grey sandy gravel soil at ground surface was dry and crusted.

Table 5.2: Vancouver Overpass Measurement Location Summary (July 26, 2001)

Location Number	Slope	Slope Bearing	Approximate direction faced by slope
1	18°	340°	North
2	19°	157°	South
3	0°	NA	Horizontal surface
4	15°	70°	East
5	18°	250°	West
6	18°	144°	Southeast
7	9°	214°	Southwest

To characterize the distribution of net radiation over the course of the day, spot measurements were made at each of the seven locations in succession over the course of

the day, following the general approach used by Blight (1997) for characterizing net radiation with hand-held instruments. Measurements were made at each location approximately hourly for 12 hours, starting at 7:30 am (approximately 2 hours after the 5:34 am sunrise that day). Temperature and relative humidity were measured at the same time as net radiation, using a hand-held Vaisala Temperature/Humidity meter. Conditions were warm and almost completely cloudless for the entire day.

5.4.3 Solar Energy Profile – Equity Silver Mine, Houston, BC

Measurements of net radiation on the sloped surfaces of the cover were taken using a net radiometer fitted with a portable data logger. The net radiometer was of an identical type to that used on the weather station (a Kipp & Zonnen NR-LITE with a spectral response range of 0-100 μm). The portable set-up was moved around the site, with net radiation measured on slopes facing approximately to each of the cardinal compass directions (north, south, east and west), and on slopes of different steepness. A typical installation of the portable system is shown on Figure 5.8. Measurement locations are shown on Figure 5.9 and summarized on Table 5.3, with the exact slope direction for each measurement location indicated by the compass bearing of the down-slope direction. Measurements were made in 2002 and 2003. The net radiation measured at the permanent weather station described in Section 5.2.2 was representative of the radiation on the horizontal crest area of the cover. Daily average temperatures used in the model were calculated based on measured temperatures from the weather station, collected at 15 minute intervals.

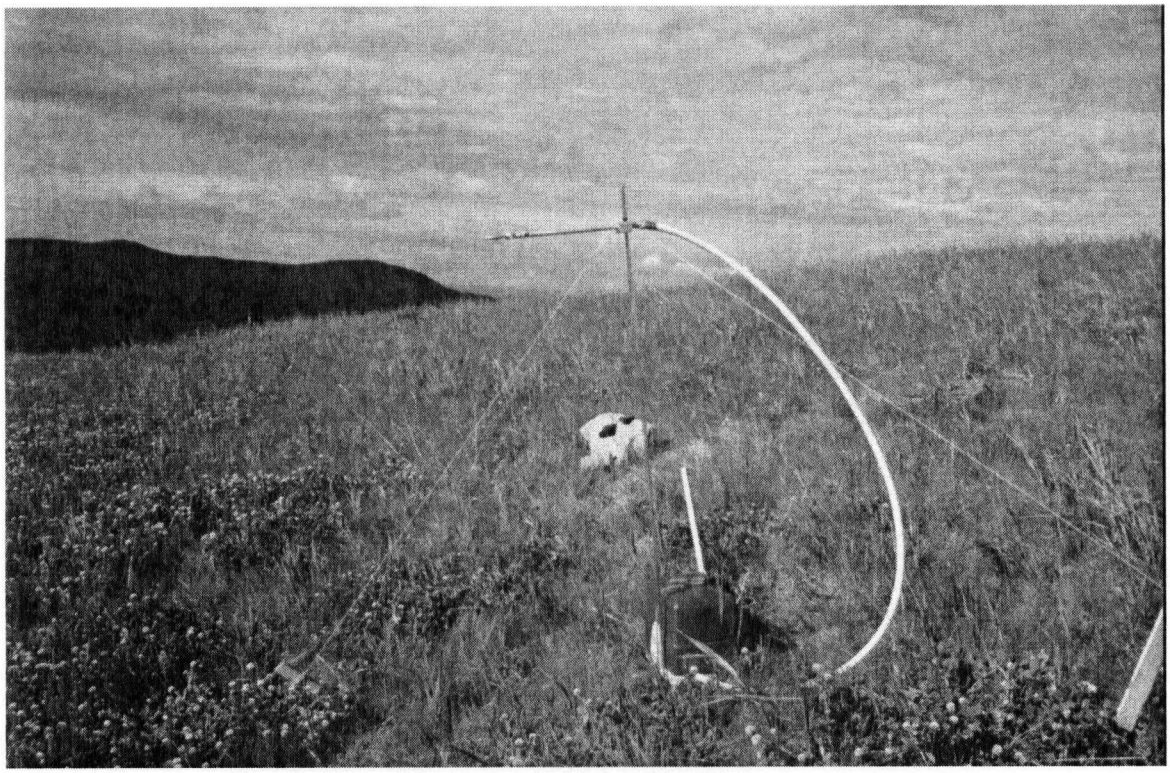

Figure 5.8: A portable net radiometer on the slope of the cover

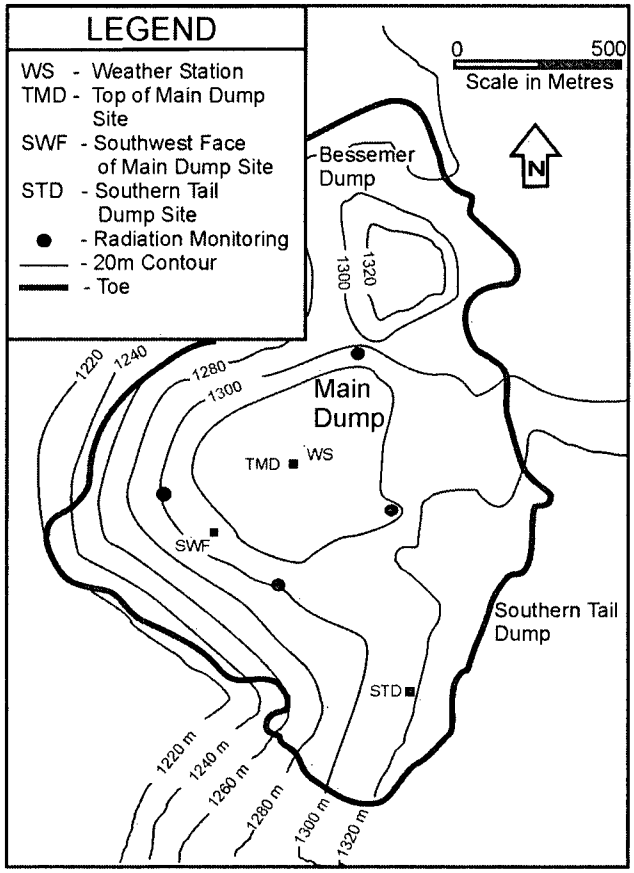

Figure 5.9: Equity site plan showing approximate monitoring locations

Table 5.3: Equity Measurement Location Summary

Location	Year	Slope	Slope Bearing	Days Measured
North	2003	19°	320°	Aug 6-10; Sept 11-Oct 14
South	2002	22°	183°	Aug 13-23
	2003	18°	175°	Aug 15-Sept 10
East	2002	11°	113°	Aug 4-11
West	2002	25°	239°	Aug 25-29
	2003	16°	276°	Aug 11-14

5.5 Soil Moisture Measurements

Soil moisture measurements at the Equity site were made with neutron probes (Section 5.5.1) and with TC Sensors (Section 5.5.2).

5.5.1 Neutron Probes

A total of 14 neutron probe (NP) access tubes were installed in the soil cover at the Equity site, distributed over the Main Dump and the Southern Tails Dump, as shown in Figure 5.2. The elevation and slope direction (that is, the compass bearing of the slope fall line at the probe location) for each of the neutron probes is summarized in Table 5.4. Each access tube consisted of a 50 mm diameter aluminium pipe, pushed through the cover thickness into a void created with a split spoon sampler. The access tubes were sealed at the bottom with a welded plate, and at the top with a removable stopper.

Table 5.4 Neutron probe location details

NP#	Slope Angle (degrees)	Slope Direction[1] (degrees)	Approximate Compass Direction[2]	elevation (m)
1	22	197	South	1324
2	22	197	South	1326
3	none	none	None	1330
4	3 (nominal)	none	East	1332
5	3 (nominal)	none	East	1331
6	3 (nominal)	none	East	1330
7	3	0	North	1338
8	14	333	North	1340
9	none	none	None	1330
10	none	none	None	1321
11	16	230	Southwest	1321
12	none	none	None	1313
13	none	none	None	1333
14	12	256	West	1320

[1] Slope direction indicates azimuth of down slope direction in degrees (clockwise from north, 0°).

[2] Approximate compass direction indicates equivalent cardinal compass direction to the indicated down slope direction.

A Campbell Pacific Nuclear Corporation CPN 503/503DR Hydroprobe was used for all moisture measurements at the site. The Hydroprobe included an Americium-241 neutron source, which emitted fast neutrons. When the fast neutrons encountered the hydrogen atoms of water molecules, they were slowed by elastic collisions with the atom (Silvestri, 1991). These slowed neutrons were detected by a Boron-10 counter, which was used to generate a count proportional to the number of slow neutrons detected. Higher counts were generated by greater numbers of slow neutrons, which in turn indicated higher water (hydrogen) concentrations.

The hydroprobe used at this site was calibrated based on the gravimetric water contents of soil samples taken from a location adjacent to the neutron probes access tube locations. Soil samples were taken at 10 cm depth intervals, and separate calibration curves were prepared for soils in the compacted and non-compacted regions of the cover, as described in O'Kane (1995).

At each of the access tube locations, measurements were taken by lowering the probe into the access tube in 10 cm increments. At each depth the readings (neutron counts) were recorded, and later converted to moisture contents based on the appropriate calibration curve. The moisture contents were measured between one and five times per year at key locations (more frequent readings were made in the early years of the program) and other locations were sampled on an annual or semi-annual basis. Soils in the vicinity of the tubes showed no evidence of shrinkage, cracking or other forms of macropore development that would affect the performance of the neutron probes.

5.5.2 Moisture Profiles (TC Sensors)

Thermal conductivity (TC) sensor strings were installed through the cover profile of the Equity at three locations, for the continual measurement of moisture content profiles in terms of soil suction. At each location, two sensors were installed in the upper loose layer, four sensors in the compacted soil, and two sensors in the underlying waste rock. Sensors were connected to solar-cell powered data acquisition systems, for the daily collection of soil suction data (O'Kane, 1995). The three locations are shown on Figure

5.2, and include the top of the main dump (TMD), the southwest face of the main dump (SWF) and the west-facing slope of the southern tails dump (STD). The location at the top of the main dump is in an area with a nominal 3 degree slope to the east, the southwest face location is on a short horizontal bench adjacent to slopes that are approximately 22 degrees (sloped to the southwest), and the southern tails dump location is located on an area sloped approximately 12 degrees to the west.

5.6 Direct Evaporation Measurements

Direct measurements of evaporation were made at both research sites. The microlysimeter method was used for the measurement of evaporation at both the Kidston and Equity. The general principals of the microlysimeter method were outlined in Section 3.5.1. Additional measurements with hand-held instruments were made at the Kidston site for the calculation of evaporation by the energy balance method, roughly following the method of Blight (1997).

5.6.1 Microlysimeter Measurements – Kidston

A total of seven microlysimeters were constructed and installed at the Kidston site. Two were installed on the vegetated tailings near the Bowen ratio-measuring weather station, and another five were installed on the test hummock. A photograph shows the main components of a typical microlysimeter in Figure 5.10. The microlysimeters used at Kidston were constructed of PVC pipe sections, each with an approximate internal diameter of 208 mm and a wall thickness of 19 mm. Each microlysimeter was approximately 200 mm deep. As discussed in Section 3.5.1, PVC has a thermal conductivity similar to that of dry soil. The microlysimeter sections were used to take cores from each slope of the hummock. Care was taken to disturb the soil profile as little as possible, although some disruption was unavoidable due to the relatively coarse nature of the oxidized waste rock. A flexible membrane base made of water-resistant

polyethylene sheeting was put on each microlysimeter after the core had been taken, following the suggested methodology of Evett et al (1995).

The two microlysimeters on the vegetated tailings were installed November 28, 2000. Five microlysimeters were installed on the test hummock on December 1, 2000. At the hummock, one microlysimeter was installed on the relatively horizontal crest area, with the remainder installed on slopes facing each of the cardinal compass directions (north, south, east, west). A typical slope installation is pictured in Figure 5.11.

Initial weights were measured for the microlysimeters on a laboratory scale. Microlysimeters were weighed each morning on the same laboratory scale for the duration of the experiment, which required that they be removed from the hummock and transported to the lab once per day. The process of extracting the microlysimeters, transporting them to the laboratory for weighing, and re-installation in the soil took approximately 90 minutes each day. The microlysimeters were tightly covered during this period with a water resistant membrane, and the excavated hole left in the hummock was also covered. As a check on the microlysimeter performance, soil temperatures were measured at 50 mm depth during the day using a soil thermistor. This was done at locations both inside the microlysimeter and immediately outside, to help identify any significant differences in the temperature regime. Soil temperatures were consistently within 0.5 $^{\circ}$C at a given depth, and typically within 0.1 $^{\circ}$C, suggesting the microlysimeters were not greatly affecting the temperature profile in the soil. The microlysimeters were removed permanently on the morning of December 6, 2000 for

final weighing. Four samples were taken from each microlysimeter to determine the final moisture content profile.

Figure 5.10: Microlysimeter used at Kidston

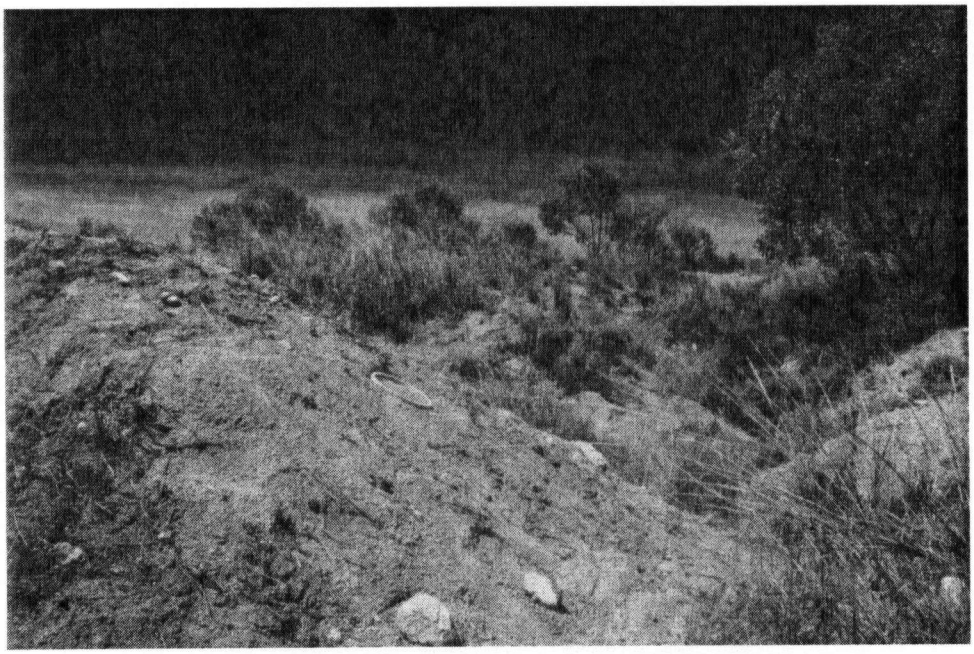

Figure 5.11: Microlysimeter installed in hummock slope

5.6.2 Microlysimeter Measurements – Equity

The methodology for the microlysimeter measurements at the Equity site differed from that at the Kidston site, based on both difference in site conditions, and experience gained at Kidston.

Due to difficult site access to the desired measurement locations, the five microlysimeters were constructed to be placed above-ground. Each microlysimeters consisted of a 270 mm long section of 100 mm diameter PVC pipe, surrounded by a minimum of 150 mm of Styrofoam insulation, protected with a plastic crate for transportation. The microlysimeters are shown in Figure 5.12. Two of the microlysimeters are shown with the plastic cap that was used to minimize evaporation during daily transport of the microlysimeters.

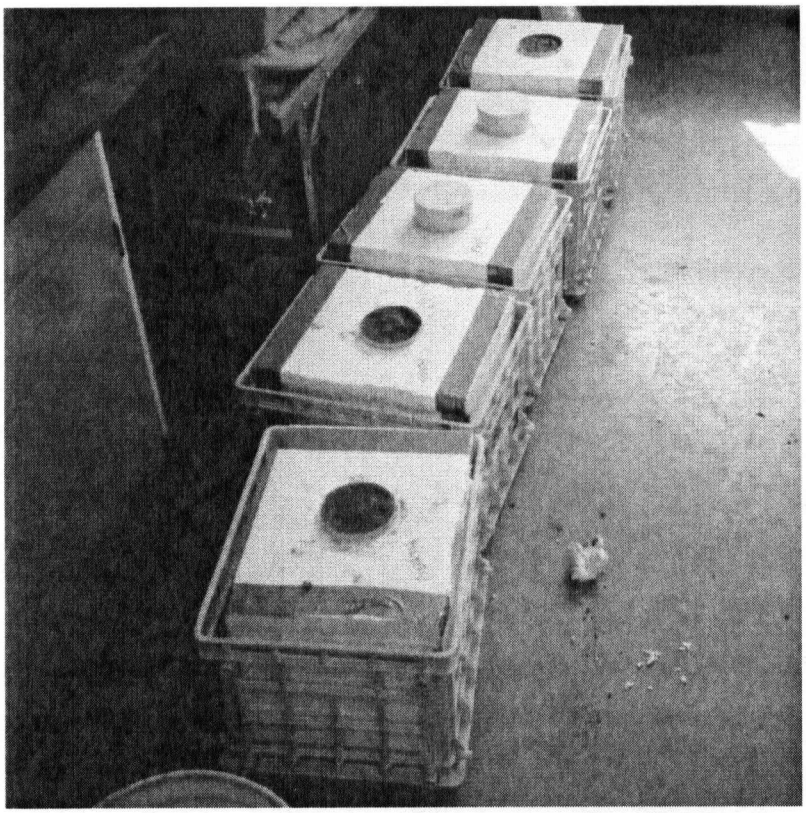

Figure 5.12: Equity Microlysimeters

In order to ensure comparable initial moisture conditions, the microlysimeters were not used to take cores from the cover at this site. Instead, a sample of the cover till was collected and mixed with water to prepare a stockpile of soil that was relatively uniform, and nearly saturated. Cobbles over 3-inch were removed during the mixing process. Each microlysimeter was filled by hand with the mixed soil, and initial weights determined. The microlysimeters were placed in the field locations early morning on August 6, 2003. One microlysimeter was placed on the crest of the cover, near the weather station. The remainder were distributed on the north, east, west and south facing slopes, near the locations at which net radiation on the slopes had previously been measured with the portable net radiometer (See Figure 5.9). Details of the microlysimeter locations are summarized on Table 5.5.

Table 5.5: Equity microlysimeter measurement location summary

Location	Slope	Slope Bearing
North	19°	312°
South	22°	183°
East	11°	113°
West	25°	239°
Crest	0°	NA

Daily early morning weighing of the microlysimeters commenced April 7, 2003. Some localized showers may have occurred overnight from April 7 to 8, 2003, although nothing was detected at the on-site monitoring locations. On April 9, 2003 heavy rains prevented access to the microlysimeters. From April 10 to April 13, 2003 there were good drying conditions on site. Due to the high probability of precipitation overnight on April 13, the experiment was discontinued so that the microlysimeters could be sectioned in the laboratory to determine the moisture profile after a period of drying. Final weights for each microlysimeter were taken, and the soil from each extruded in six sections for the final moisture profile. A typical section is shown in Figure 5.13.

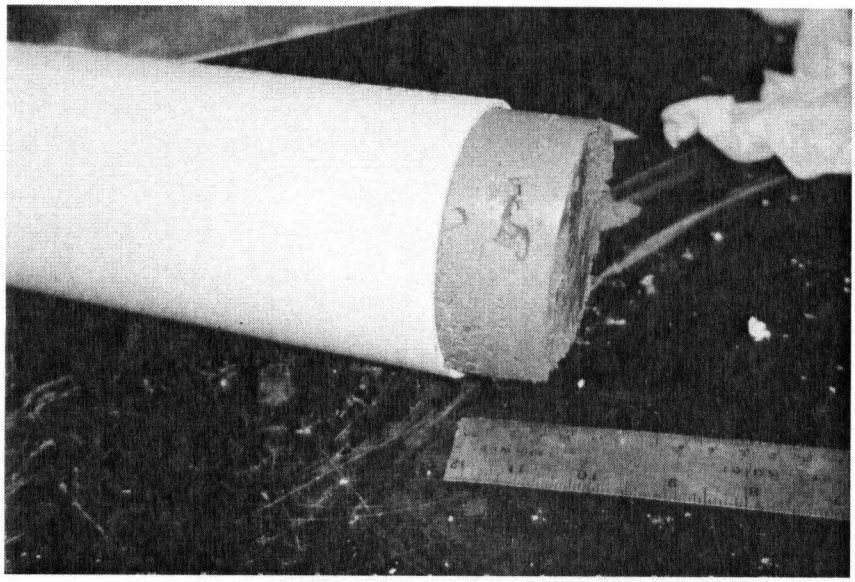

Figure 5.13: Typical soil section from Equity microlysimeter

5.6.3 Energy Balance Measurements

Measurement of evaporation through the energy balance method was attempted at the Kidston site, following the general methodology outlined by Blight (1997), discussed in Section 3.5.2. This approach involved the measurement of components of the energy balance with portable, hand-held equipment. Net radiation was measured with a portable net radiometer (as described in Section 5.4.1). Soil heat flux was calculated by measuring soil temperature at two depths within the soil and the moisture content of the soil between those depths. Latent heat flux was calculated based on temperature and humidity measurements taken at two different elevations above the soil.

For the measurement of soil heat flux, soil temperature was measured at two depths (50 m and 150 mm) with a Hanna Industries 762 thermistor-based penetration probe (accurate to +/- 0.2˚C). For each measurement, the soil between 50 mm and 150 mm was

sampled and its average moisture content measured, so that the specific heat capacity of the soil could be determined as a function of its water content. The method of Johansen (Johansen, 1975) as coded in SoilCover was used to calculate the relationship between the specific heat capacity of the soil (in W/m^2 C) and the gravimetric moisture content.

Air temperature and relative humidity for each location was measured at an elevation of 100 mm and 1500 mm above the ground surface, with a Vaisala HM34 temperature and humidity meter. A simple cardboard shield was used on the sensor tip to minimize wind effects on the probe tip. Each parameter was measured 12 times at each height and averaged to obtain each data point

Measurements of evaporation rates with the portable equipment were made on the test hummock at Kidston three times per day between December 2 and December 4, 2000. Measurements were taken in the general area of each of the microlysimeters on the hummock (crest, north, south, east and west). Supplementary measurements were made in the immediate area of the data-logging Bowen station located on the vegetated tailings area.

5.7 Soil Characterization

The cover soils at both the Kidston and Equity sites have been fully characterized by other researchers. The characteristics of the Kidston cover soils are summarized in Section 5.7.1, with the characteristics of the Equity cover soils summarized in Section 5.7.2. This data is used in the demonstrations of evaporation calculations from slopes using the solar model and flux boundary models.

5.7.1 Kidston Cover Soils

All experimental measurements at the Kidston site were conducted on or in the loosely-placed oxidized waste rock that constituted the upper layer of the test cover on the south dumps. Material properties of the both the loosely-placed oxidized waste rock, and the underlying compacted waste rock, are summarized on Table 5.6. This material has been characterized by Durham et al (2000) as a well-graded gravely sand with a small clay fraction, SW-SC in the USCS classifications. Typical particle size distributions for the loosely placed material are 2 percent silt, 26 percent sand, and 72 percent gravel-sized or larger.

Durham et al (2000) measured the saturated hydraulic conductivity of the uncompacted waste rock to be between 1 and 4 x 10^{-6} m/sec (laboratory falling head tests). The average hydraulic conductivity for the compacted material was 3.8 x 10^{-9} m/sec, with

values as high as 2 x 10^{-8} measured. As shown on Figure 5.14, the air entry value of the uncompacted material was approximately 10 kPa, similar to that of the compacted. The soil water characteristic curves shown in Figure 5.14 are based on laboratory and field measurements, as well as calibration of a numerical model, as described by Durham et al (2000).

Table 5.6: Characteristics of Oxidized Waste Rock Cover at Kidston Mine (after Durham et al, 2000)

Properties	Uncompacted	Compacted
K_{sat} (m/sec)	1 x 10^{-6}	3.8 x 10^{-9}
Porosity	0.2	0.16
Sg	2.72	2.72
Air Entry Value (kPa)	10	10
Classification	SW-SC	SW-SC

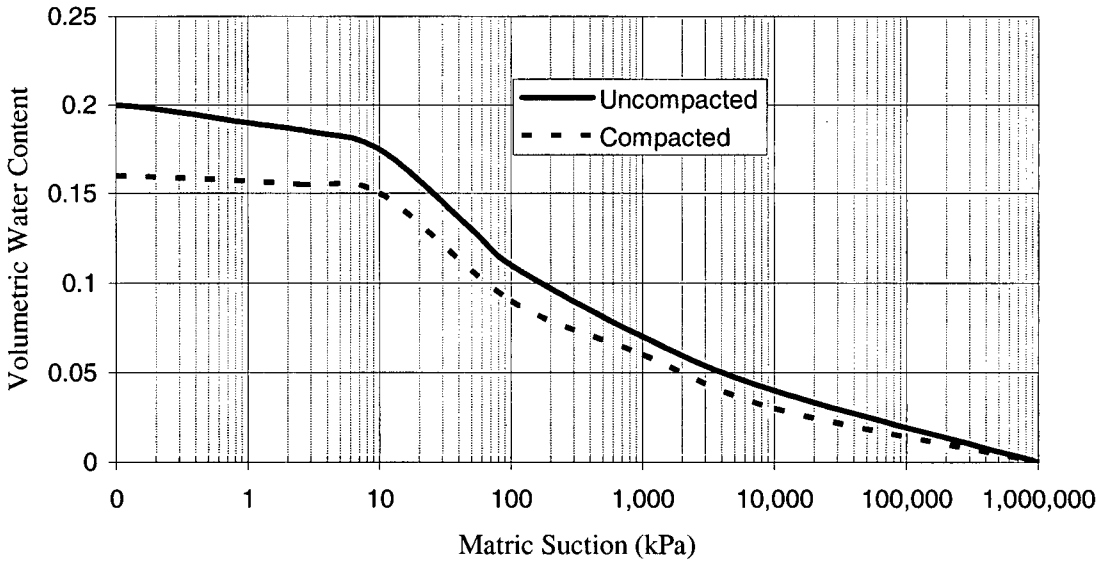

Figure 5.14: Soil Water Characteristic Curve for oxidized waste rock in Kidston cover (after Durham et al, 2000)

5.7.2 Equity Cover Soils

The cover at the Equity site was constructed from a locally available till material, with properties as summarized in Table 5.6. The till was gravel and cobble rich, with a clayey silt matrix, and was classed as CL (Clay Low Plastic) in the Unified Soils Classification method. The cover consisted of two layers of the till - a lower compacted layer approximately 0.5 m thick, and an upper loosely placed layer 0.3 m thick. The compacted lower layer had been designed to act as a barrier to infiltration, and to maintain saturation even under strong drying (high suction) conditions, while the uncompacted upper layer acted as a growth medium for vegetation and a water storage layer (Weeks and Wilson, 2006).

The cover was placed with the lower layer compacted to 95% of Standard Proctor Maximum Dry Density. The compaction quality was monitored using a portable nuclear density gauge, with areas that did not meet compaction criteria excavated and recompacted or replaced, as required (Wilson et al, 1995). As shown in Table 5.7, compaction of the till reduced the hydraulic conductivity and porosity of the till significantly, creating a barrier layer from the compacted material. Porosity values shown on Table 5.7 are based on those measured in-situ with a nuclear densometer by Swanson et al (2003). The air entry values shown on Table 5.7 were interpreted from soil water characteristic curves developed for both the compacted and non-compacted materials by O'Kane (1995), and shown in Figure 5.15. Soil water characteristic curves were obtained by O'Kane (1995) through a combination of modified pressure plate tests (ASTM Designation D 698 Method A) and vapour equilibrium tests. Laboratory tests

were conducted by O'Kane (1995) on compacted and non-compacted samples of the Equity Till, with compacted samples subjected to the same degree of compaction as the field specification. Hydraulic conductivity values for the compacted and non-compacted till are based on values reported by SENES (1991), and agree well with values obtained by O'Kane (1995) through consolidation-conductivity tests conducted with a modified oedometer apparatus. Grain size distributions curves reported by O'Kane et al (1998) indicated that the till is well graded and 9% clay, 40% silt, 28% sand, and 23% cobble/gravel sized. The liquid limit of the till was 39.6% and the plastic limit 17.4%.

Table 5.7: Characteristics of Till Cover Soils at Equity

Properties	Uncompacted	Compacted
K_{sat} (m/sec)	3×10^{-8}	5×10^{-10}
Porosity	0.33	0.31
Sg	2.77	2.77
Air Entry Value (kPa)	100	1000
Classification	SC-CL	SC-CL

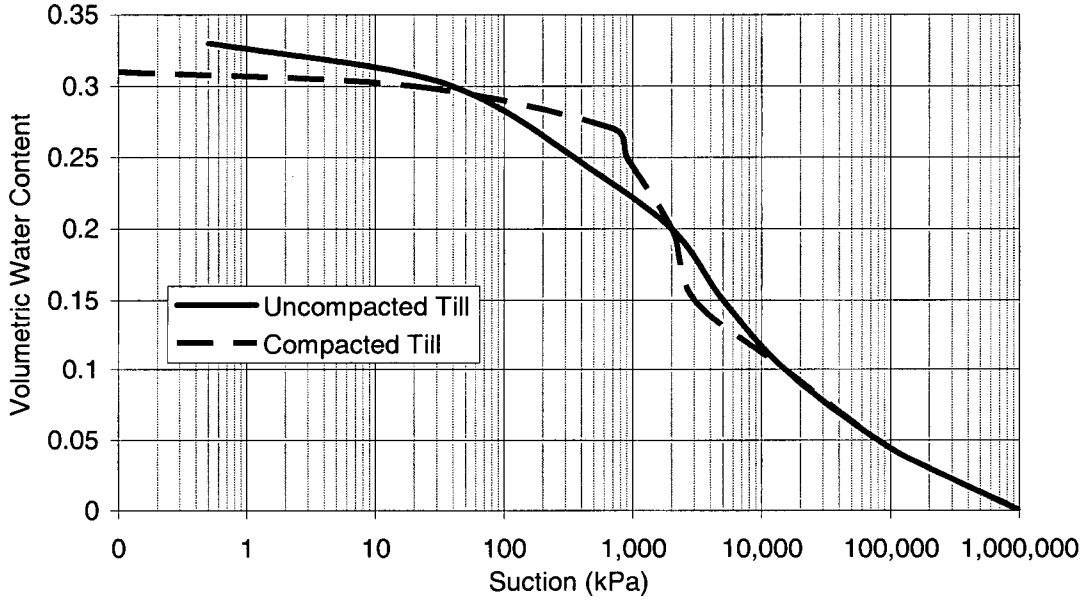

Figure 5.15: Soil Water Characteristic Curve for Equity cover till (after O'Kane, 1995)

5.8 Summary of Data Collection and Experimental Methods

Two main sites were used for collecting the data that was used to evaluate the new model. The Equity Silver site in North Central British Columbia was used to provide data from a site in a humid alpine climate in a northern latitude, while the Kidston Goldmine in Queensland, Australia was used to provide data from an arid site in the southern hemisphere. At both sites, weather data was collected at an automated weather station, with supplemental net radiation data collected with a portable net radiometer. Soil moisture values were monitored with TC sensors and neutron probes, with direct evaporation measurements made with microlysimeters, and with the energy balance method. Additional preliminary data was collected with handheld equipment at a site in Vancouver, British Columbia.

Topographic data was collected at all sites to define the slope and aspect of all measurement locations. Extensive survey data was collected at the Equity Silver site, allowing a 3D surface map of the site topography to be developed. Soils at both the Equity and Kidston sites had been extensively characterized, and key soils data for both sites were summarized in Section 5.7.

6 Experimental Results

The experimental work conducted resulted in data for all research sites. Measured radiation from the research sites was key for the development and verification of the radiation model discussed in Chapter 4. The measured radiation data collected is summarized in Section 6.1. Direct measurements of evaporation, used to evaluate the combined application of the new radiation model and the existing evaporative models are summarized in Section 6.2. The soil moisture measurements made at Equity to provide supplementary data for evaluation of the sloped cover performance is summarized in Section 6.3. And the climate data collected for input to numerical models of the site is described in Section 6.4.

6.1 Radiation Measurements

Radiation measurements included initial measurements conducted at the Kidston site (Section 6.1.1), followed by measurements at the Arthur Lang Overpass site in Vancouver (Section 6.1.2). This data was used for the initial development of the radiation model. Data collected at the Equity site (Section 6.1.3) was used for refinement and verification of the model.

6.1.1 Kidston Radiation

Preliminary radiation measurements taken at Kidston showed that to fully characterize net radiation over the course of a day, measurement times needed to be well chosen. The initial measurements take over the hummock on November 30, 2000 were clustered early morning and late afternoon, and failed to fully resolve the distribution of radiation over the course of the day. The data collected did show that net-radiation on the east-facing slope decreased over the course of the day, and the net radiation on the west-facing slope increased, as would be expected with the movement of the sun over the sky. The average net radiation measurements were higher on the south-facing slope (498 W/m^2) than on either the crest area (471 W/m^2) or on the north facing slope (379 W/m^2). While the site is located in the southern hemisphere, it is at a relatively low latitude, and at this time of year, the south-facing slope was actually the sunward slope.

Net radiation was also measured on the test hummocks as part of the attempt to measure the Bowen ratio on site with hand-held instruments. These measurements are

summarized on Figure 6.1. While three measurements per day at each measurement location was insufficient to characterize the daily distribution of radiation, it did provide a general indication of the radiation variability.

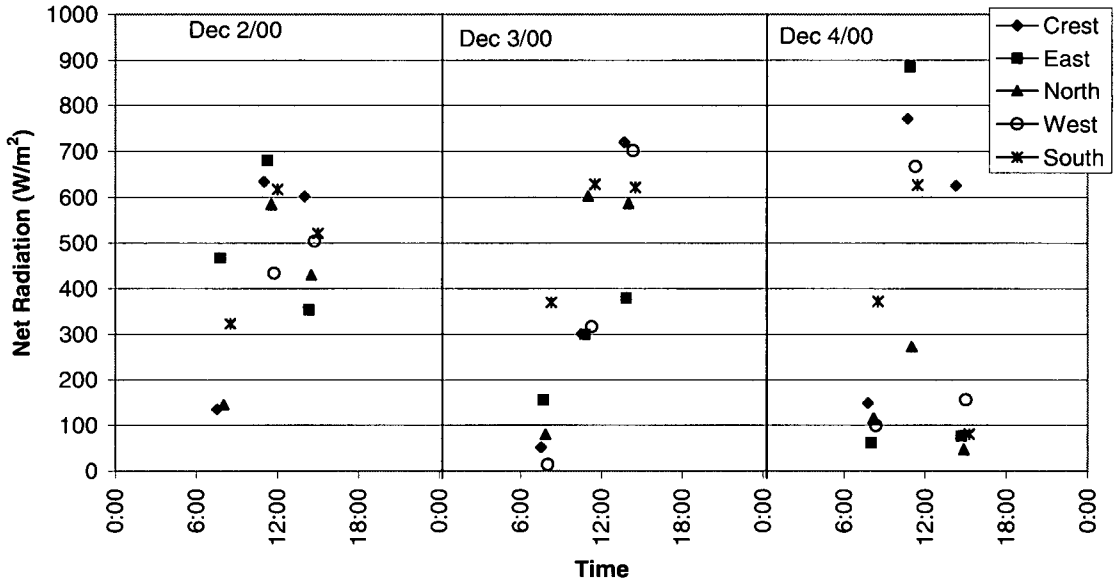

Figure 6.1: Net radiation spot measurements taken at Kidston test hummock

Net radiation at the Kidston site was also measured at the on-site weather station. During the experimental work conducted on site, there was an error in the datalogger, which caused maximum net radiation values to be set to zero whenever the measured net radiation exceeded 500 W/m^2. These readings are evident on the data points shown on Figure 6.2. For assessment of the site date, interpreted values for the net radiation at this time were developed, based on a sine curve fit to the lower range of the available data, and daily maximum net radiation values for each day that were estimated based on readings taken on-site with the hand-held equipment on corresponding days. These interpreted values are shown with the solid lines on Figure 6.2. It is well known that

daily net radiation values vary in an approximately sinusoidal pattern on clear days (such as the days during which the measurements were made). Since peak daily net radiation values had been measured on site, the sine curve was a reasonable approach to estimating the daily pattern of net radiation.

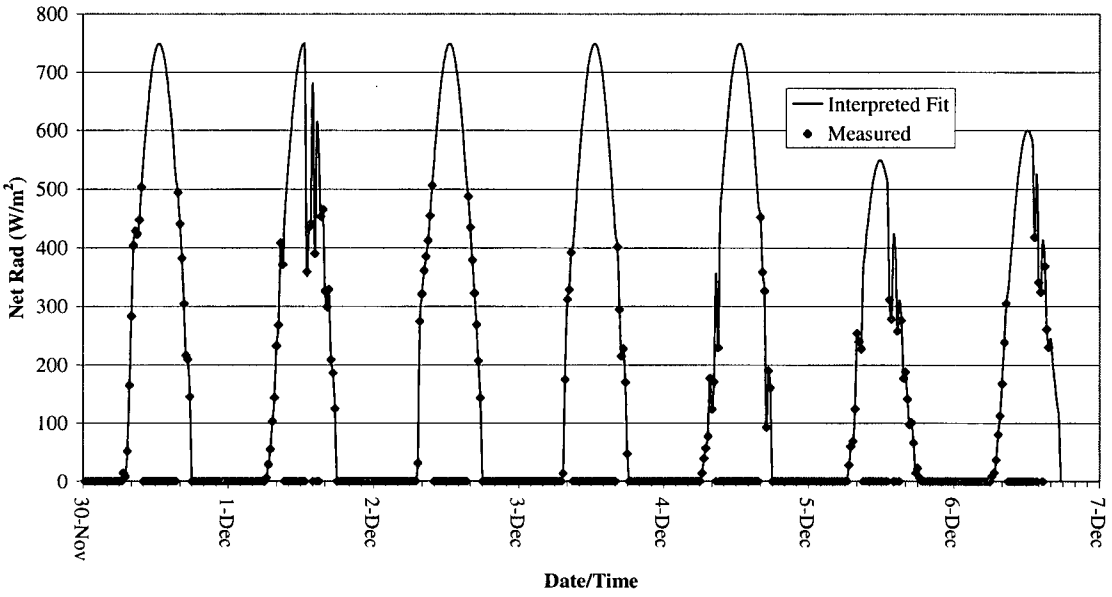

Figure 6.2: Measured and interpreted net radiation values for the weather station at the Kidston site

6.1.2 Arthur Lang Overpass Radiation

As shown in Figure 6.3, measurements taken at approximately hourly intervals over the course of a day characterized the distribution of radiation over the day at the Arthur Lang Overpass measurement locations. These hourly measurements provided a far better characterization of the radiation distribution than the less frequent measurements made at the Kidston site (presented in Section 6.1.1). Radiation distributions over the course of the day match expected distributions, with southerly slopes receiving more net radiation

than horizontal or north-slope surfaces, and easterly slopes receiving peak radiation values earlier in the day than westerly slopes.

Sufficient data was available for each location that the area under the net radiation curve could be integrated to obtain total net radiation values for the day at each location (in MJ/m^2), as presented on Figure 6.4. The net radiation values shown on Figure 6.4 are presented as a function of slope direction (azimuth), and show that the south-facing slopes receive more total net radiation over the course of the day than more northerly-facing slopes of comparable slope. The impact of slope steepness is also indicated on this Figure, with the 9° slope receiving considerably less total net radiation over the day than the steeper slopes with comparable azimuth.

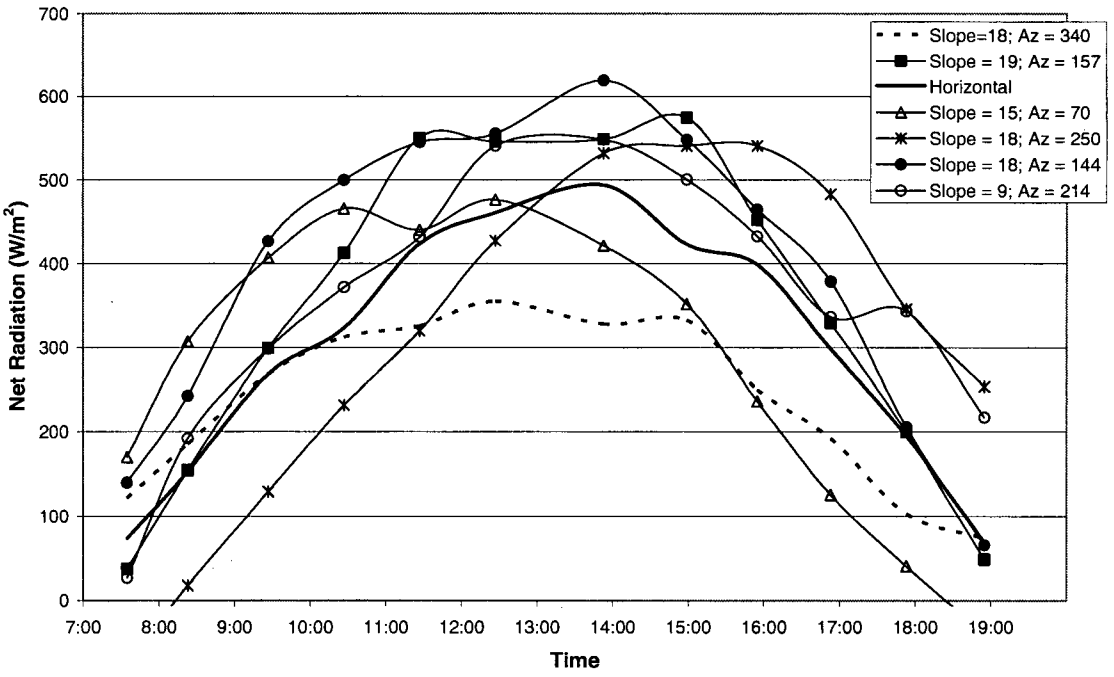

Figure 6.3: Daily radiation profile at the Arthur Lang Bridge measurement locations, July 26, 2001. (Slope angle and azimuth from North in degrees)

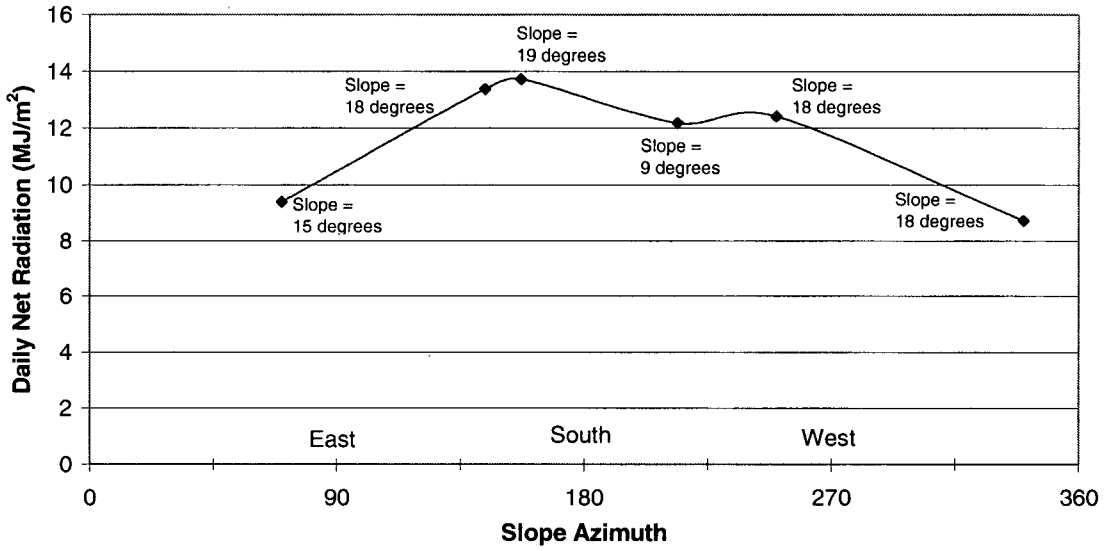

Figure 6.4: Daily net radiation at Arthur Lang Bridge as a function of slope direction (July 26, 2001)

6.1.3 Equity Radiation

As discussed in Section 5.4.3, net radiation measurements made at the Equity site included both ongoing measurements made at the weather station, and measurements made with the portable net radiometer and a data-logger. Day total net radiation values for both were calculated by integrating the measured radiation data (collected at 60 second intervals and averaged over each hour) over the course of the entire day, to obtain the day total value.

The radiation measured on various slopes around the site with the portable setup over 24 days in 2002 and 69 days in 2003. These radiation values are summarized on Figure 6.5 for 2002 and on Figure 5.5 for 2003. On both of these figures, the total net radiation

values for the corresponding days as measured at the weather station are also shown. At the end of the 2003 measurements, the portable net radiometer was placed on the crest of the main waste rock dump for 23 days, near the weather station. This was done to compare the two net radiometers. As shown on Figure 6.6, similar net radiation values were measured at both, with no discernable trend in the slight differences observed between the readings at the two net radiometers. The average difference in daily net radiation as measured by the two net radiometers on a horizontal surface over 23 days was 0.09 MJ/m^2.

Net radiation data at the weather station has been collected for more than 10 years. Net radiation values on the horizontal peak during the summer (typically in July) at around 16 MJ/m^2/day, and are at a minimum in the winter. Figure 6.7 shows the daily net radiation measured at the weather station for a typical year (2002). Note that the period of zero net radiation from Julian day 129 to 142 (mid-May) was due to a malfunction at the weather station. Figure 6.7 shows clearly the variability of net radiation data on a day-to-day basis, as well as the overall seasonal trend. The day-to-day variability of net radiation data is typically a result of variations in cloud cover.

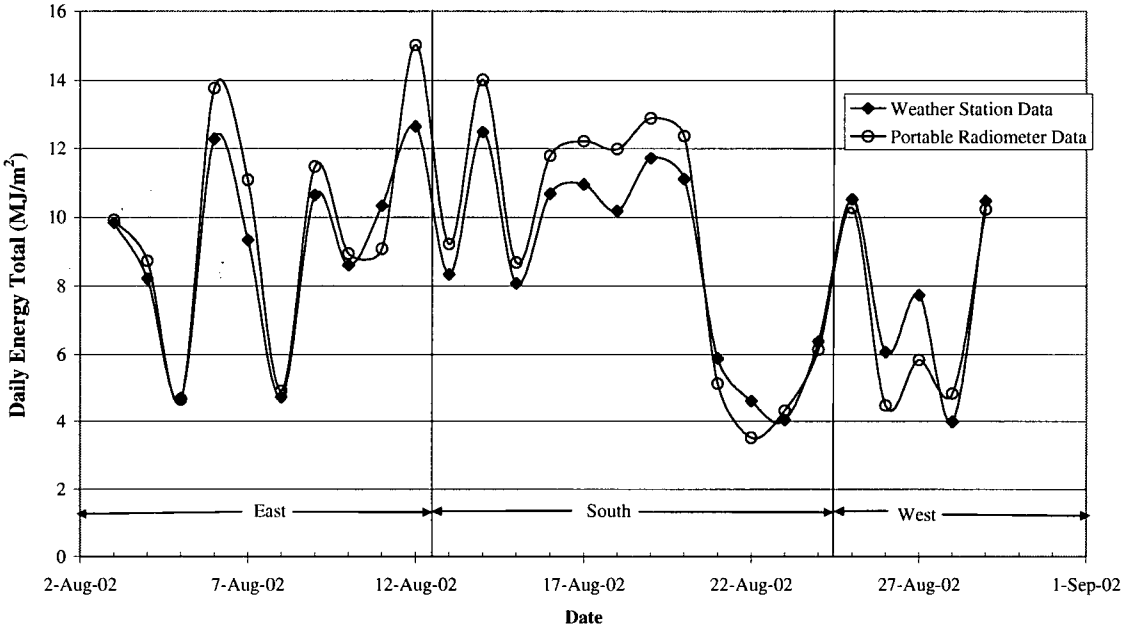

Figure 6.5: Net radiation measured at the Equity site in 2002 with the portable net radiometer

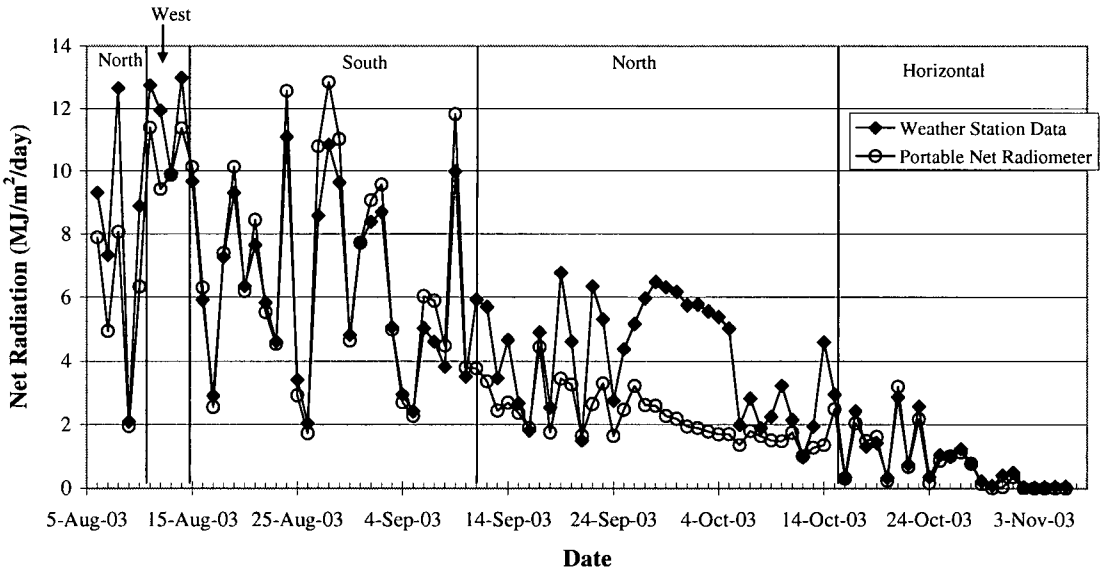

Figure 6.6: Net radiation measured at the Equity site in 2003 with the portable net radiometer

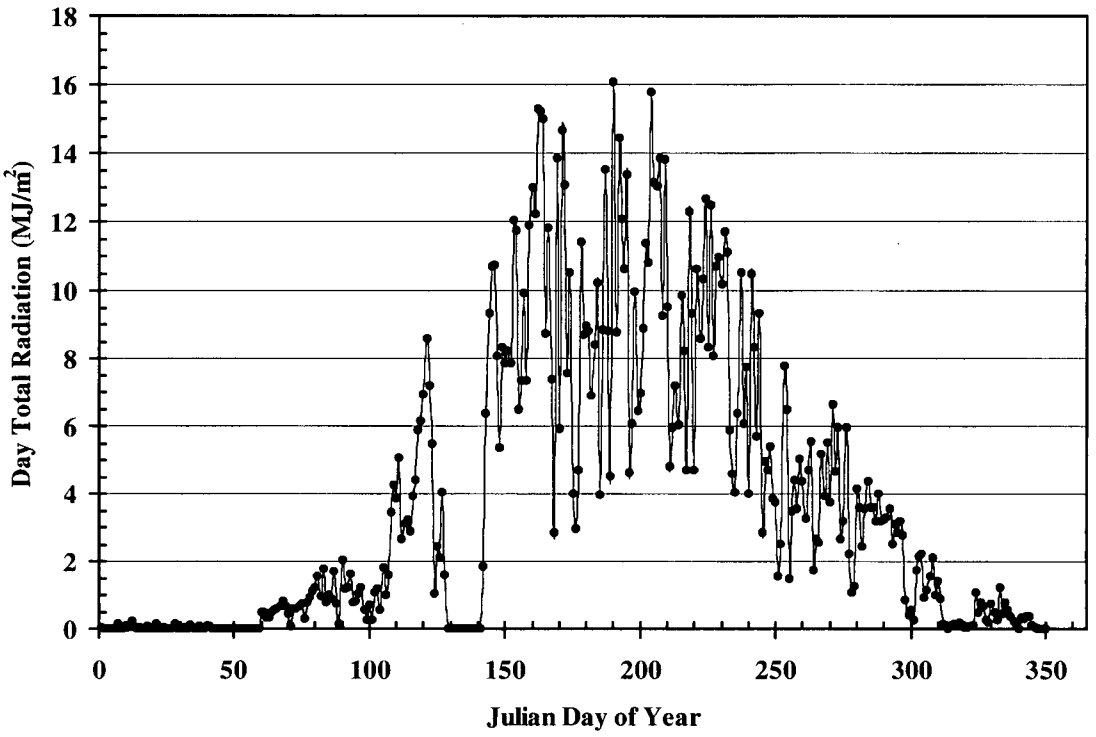

Figure 6.7: Daily net radiation at the Equity Weather station for a typical full year (2002)

6.2 Evaporation Measurements

Direct measurements of evaporation were undertaken at the Kidston site using microlysimeters (Section 6.2.1) and measurements of the energy balance with hand-held equipment (Section 6.2.2). Direct measurements of evaporation at Equity were conducted with microlysimeters (Section 6.2.3).

6.2.1 Microlysimeter Results – Kidston

Microlysimeter data was collected at both the tailings area and on the test hummock. Figure 6.8 shows the cumulative evaporation measured on the tailings at each microlysimeter, as well as the cumulative evaporation as measured based on the energy balance determined with the data-logging weather station. As shown in Figure 6.8, the trend in evaporation is very similar in all three curves, with the main observed difference between the measurement devices occurring on the first day of measurement. Overall, the lowest average evaporation rate was measured with the Bowen station (1.2 mm per day), with slightly higher rates at the two microlysimeters (1.9 and 2.3 mm per day). Note that the lower evaporation rate at the Bowen station is at least partly a function of an error in the data logger during this period that limited net radiation readings to 500 W/m^2, when peak mid-day net radiation values were closer to 750 W/m^2 at this site during the experimental work.

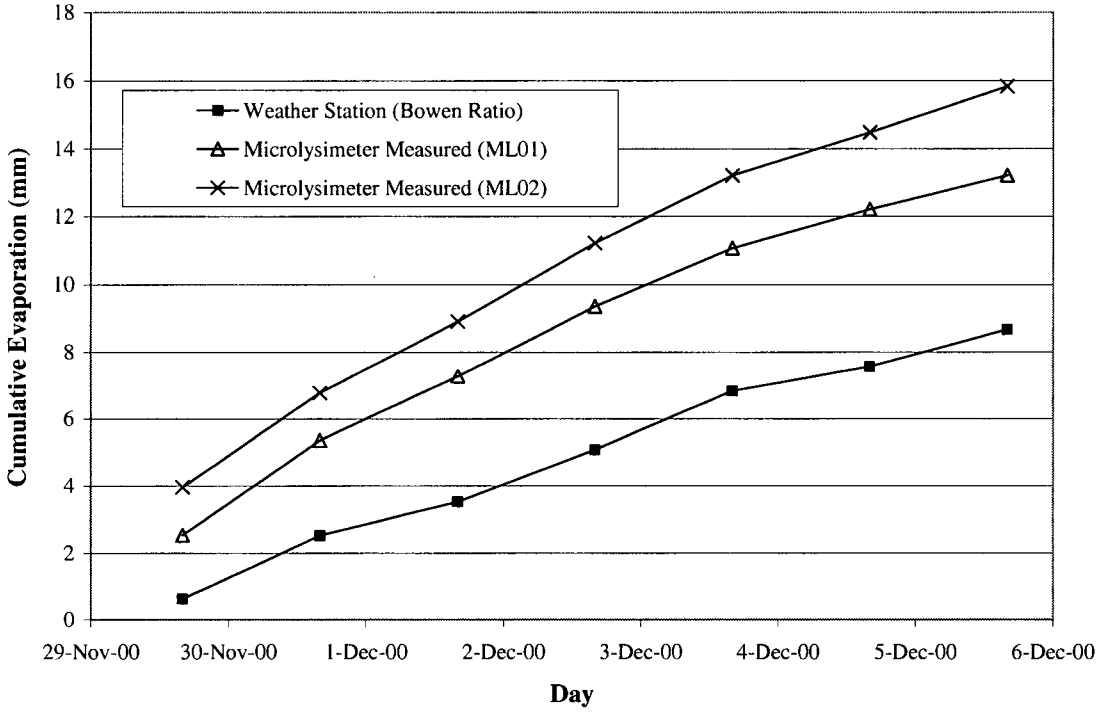

Figure 6.8: Cumulative evaporation rates measured at Kidston tailings

Figure 6.9 shows the cumulative evaporation measured at each microlysimeter in the test hummock over the course of the experimental work in the hummock. Interestingly, while the evaporation amounts from the north slope were less than the south slope (corresponding to the north slope getting less net radiation at this time of year), the greatest amount of evaporation was observed at microlysimeters on the crest and west-facing slope. This is a function of differences in initial moisture content, as shown in Figure 6.10, where the initial average water content in the soil profiles within the north-facing and west-facing slopes was higher than in the samples from slopes facing other directions. Final moisture profiles in each of the microlysimeters showed that by the end of the 5-day experiment, near surface gravimetric moisture contents were in the range of 3-5 %, while moisture contents at depth were in the range of 9-15 %, as shown in Figure 6.11.

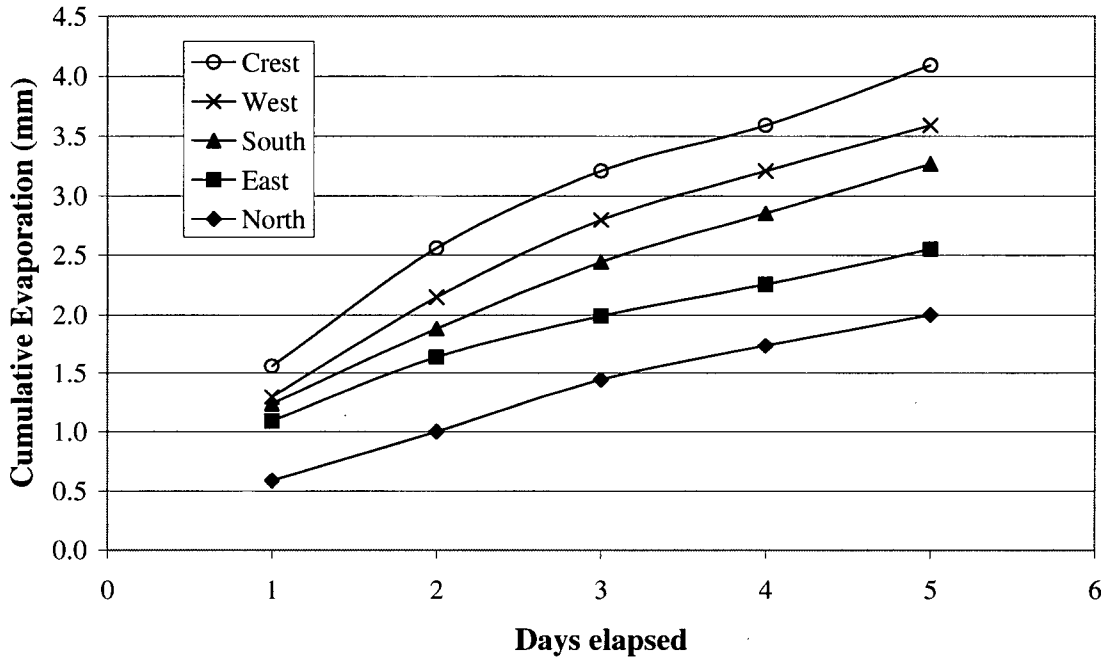

Figure 6.9: Cumulative evaporation rates measured at Kidston test hummock (December 1 to 6, 2000)

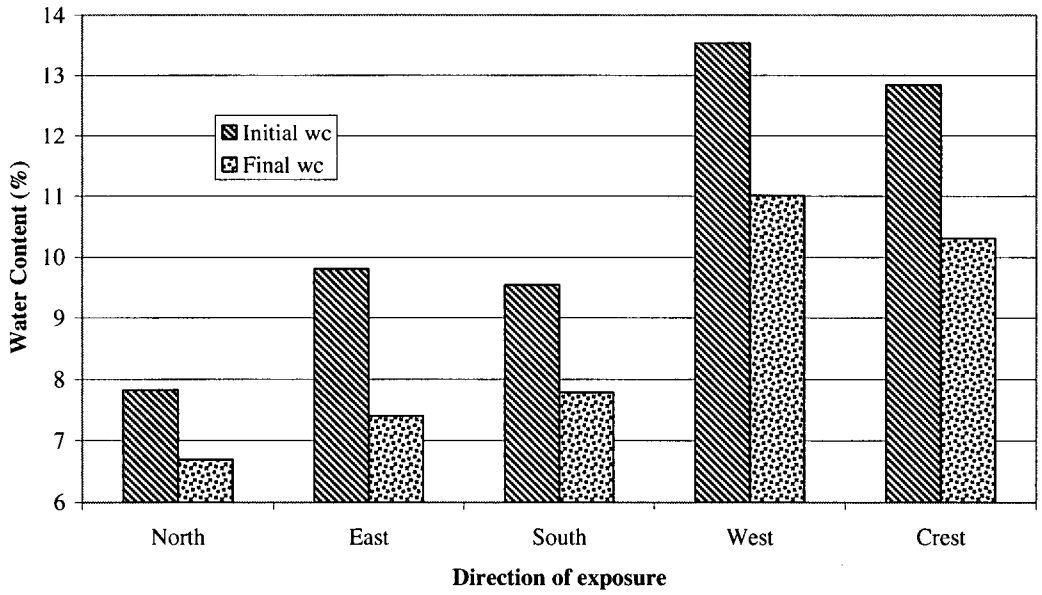

Figure 6.10: Change in microlysimeter moisture content - Microlysimeters on Kidston test hummock

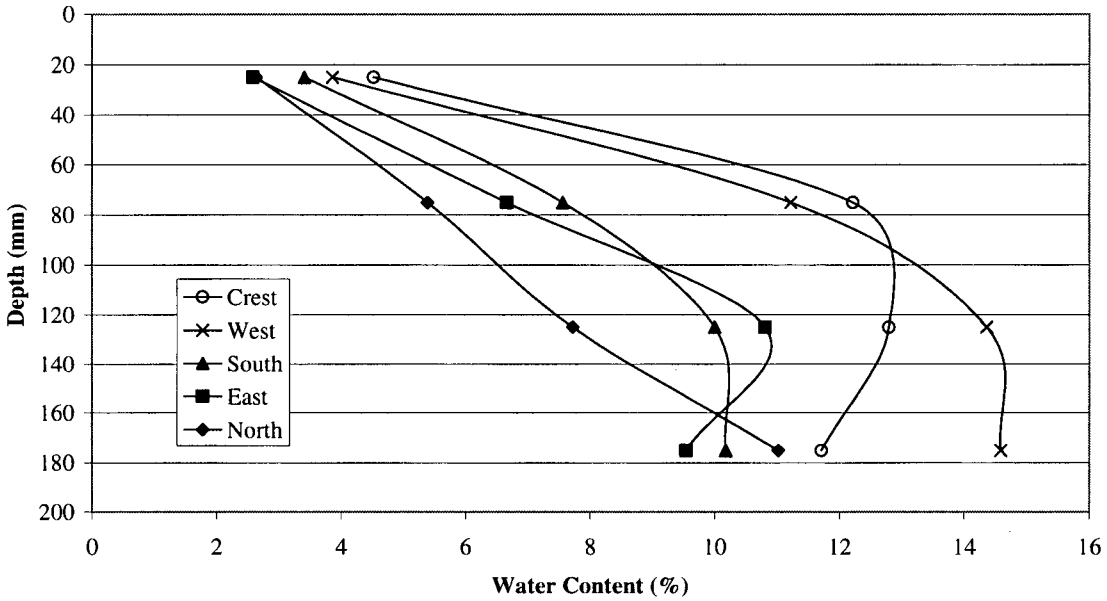

Figure 6.11: Final moisture profiles – Microlysimeters on Kidston test hummock

6.2.2 Microlysimeter Results – Equity

The cumulative evaporation rates from the five microlysimeters used at the Equity site are summarized in Figure 6.12. Note that due to rainfall during the experiment, no data was available for day 3 of the experiment, and a drop in cumulative evaporation (indicating net infiltration) was obtained on day 4. During the first two days of the experiment, there is little difference in evaporation rates between the microlysimeters, reflecting the overcast conditions on these days, and the uniform initial moisture contents. Despite this, evaporation is slightly greater for the microlysimeter on the south face during the first two days.

Following the period of rainfall evaporation from the south-facing microlysimeter is the greatest, as would be expected based on the greater radiation receipt of the south face.

Also matching expectations is that evaporation from the north face is generally the least, with evaporation from the microlysimeter on the crest occurring at a rate between the two extremes. Evaporation from the microlysimeters on the east and west faces fell between the extremes of the north and south face (except for the last days of measurement on the east face), with higher evaporation rates occurring from the microlysimeter on the west face, as shown on Figure 6.12.

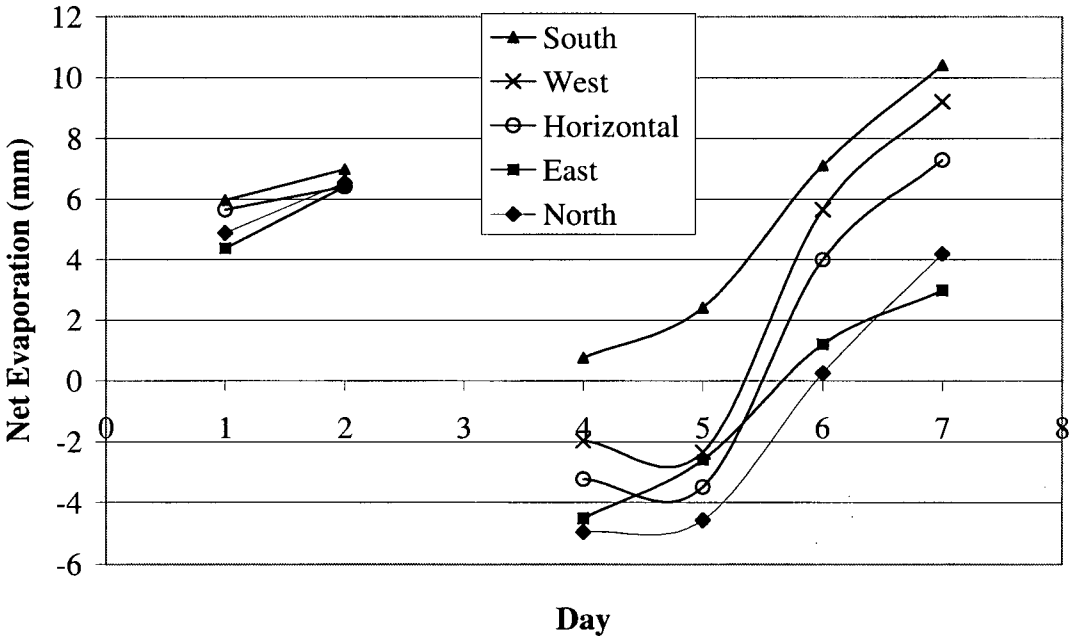

Figure 6.12: Cumulative infiltration for the Equity microlysimeters

Moisture content profiles were obtained for each microlysimeter at the end of the experimental run, with results as shown in Figure 6.13. After the experiment, the average moisture content in the south-facing microlysimeter was 17.9%, while the average moisture content in the north-facing microlysimeters was 18.9%. As would be expected from the evaporation rates on Figure 6.12 and the equal initial moisture contents in the

microlysimeters, the remaining moisture contents were between these extremes, with the west-facing microlysimeter (18.0%) drier than either the crest (18.3%) or the east (18.6%). These trends are not as clear looking at all of the moisture profile data as shown in Figure 6.13, although it can been seen that the south- and west-facing profiles were more dry near the microlysimeter surface.

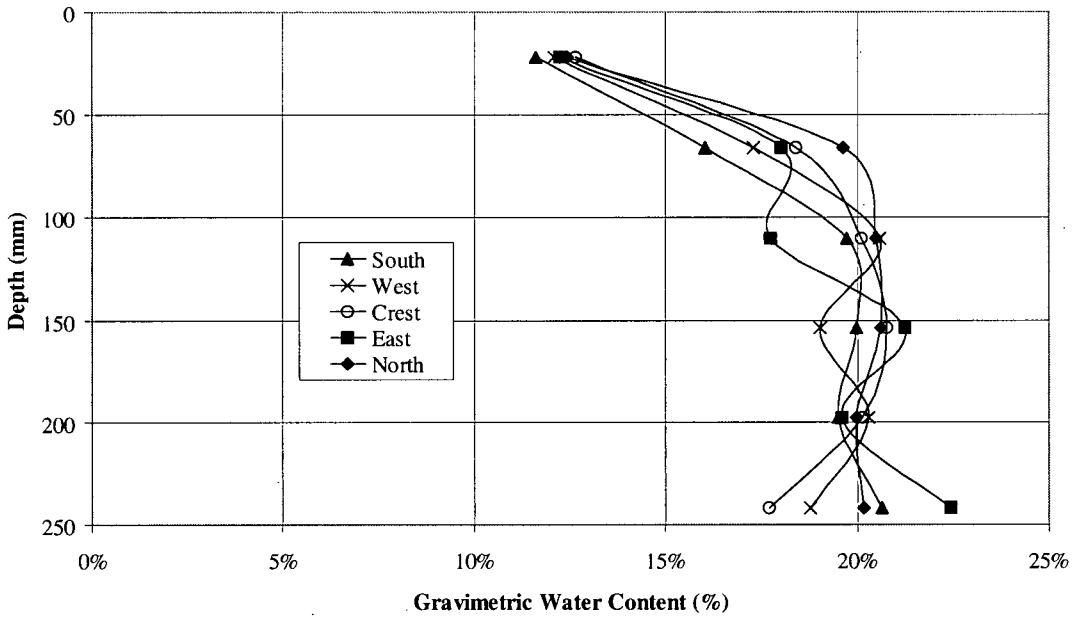

Figure 6.13: Final moisture content profiles – Equity microlysimeters

6.2.3 Kidston Energy Balance Results

An attempt was made to measure the components of the energy balance from the Kidston tailings using hand-held equipment. While the measured values of net radiation and ground heat flux appeared reasonable, a negative sensible heat flux was calculated during the hottest part of the day, based on the measured temperature and humidity gradients. This was not considered reasonable, and it appears from the data that the equipment used

did not have the precision needed to resolve the very small temperature and humidity gradients that occurred under the arid conditions at site.

Further efforts to measure the energy balance with the hand-held equipment were made at the oxidized waste rock over a period of three days. Evaporation rates calculated based on the energy balance measurements varied between 0.4 and 5.1 mm/day, which is in the same order of magnitude as those determined by the microlysimeter. However, the evaporation rates calculated with the energy balance methods were erratic, and did not correlate well with the microlysimeter results. Cumulative evaporation rates as determined with the energy balance method over the hummock (Figure 6.14) did show the least evaporation taking place from the north face of the hummock, comparable to the microlysimeter results. However, the greatest evaporation rate took place on the south-facing slope, in contrast to the microlysimeter results.

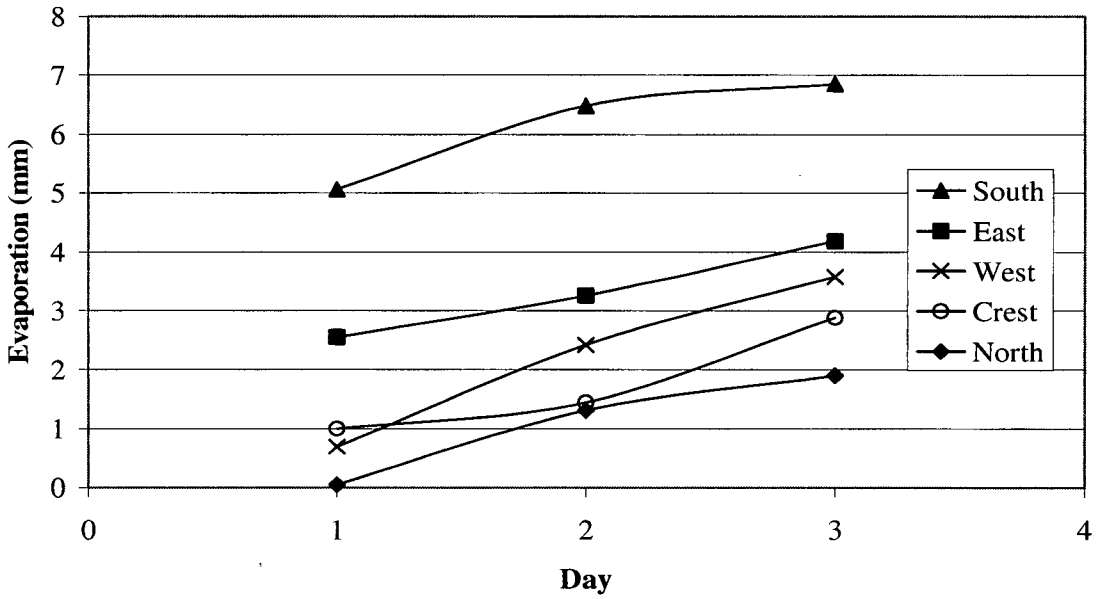

Figure 6.14: Cumulative evaporation determined by the microlysimeter method, Kidston test hummock

There is some evidence in the literature that energy balance methods are not well suited to the measurement of evaporation where the evaporative flux rate is low. In a comparison of methods for the measurement of evaporation at an arid site, Tyler et al (1997) found that measurements of energy balances under low flux conditions tended to be inaccurate, as very small gradients had to be measured in the atmosphere (this same study found that microlysimeters gave very good results). Blight and Lufu (2000) also noted that when measuring evaporation from tailings, energy balance methods were best in the early part of the measurements, when the surface was relatively wet, and that the method lost accuracy as the surface dried out. Oke (1987) has pointed out that temperature gradients in the order of $0.01^{\circ}C$ are often important for flux gradient calculations, and such fine gradients may be difficult to resolve, even with a split thermopile (such as was used in our data-logging Bowen station). The hand-held instrument used for measuring temperature and humidity gradients had a resolution of only $\pm 0.1^{\circ}C$.

6.3 Soil Moisture Measurements

Soil moisture was monitored at the Equity site in the soil cover with neutron probes and TC sensors. A brief summary of the results from these measurements is given below, with a more detailed set of results included in Appendix D.

6.3.1 Neutron Probe Data

Data collection at the neutron probe locations began in June 1993, and has continued to the present day. The neutron probe data collected at representative locations throughout the site is summarized in Appendix D (this data was also presented in Weeks and Wilson, 2006). The neutron probe data collected showed that the average degree of saturation in the compacted layer was maintained at over 90%, with 100% saturation not uncommon. This contrasted with the average degree of saturation in the upper, uncompacted soil layer, which typically varied in the range of 50% to 85%. It also appeared that while the moisture content of the lower compacted layer had been fairly stable, there was a slight drying trend in the upper, uncompacted soils over the past ten years.

A review of the moisture content profiles generated based on the neutron probe data showed that moisture contents typically increased with depth through the cover. While the degree of saturation in the near-surface zone often showed significant variation, the variations were much less pronounced at depth. This suggested that the upper layer of the cover was performing as a store-and-release system for moisture, while the lower

layer was relatively unaffected by variations in the climate. This performance matched the original design of the cover. Between 1992 and 1999, moisture contents were evaluated several times per year at six of the 14 neutron probes (NP1, NP2, NP4, NP5, NP13, and NP14). As show in Appendix D Figure D-1, there was a clear seasonal pattern to variations in the average moisture content of the upper layer. The minimum moisture contents occurred in July or August, following the period of maximum drying. The difference in moisture content between the seasonal highs and lows was in the order of 15 to 20%. In the lower compacted layer (Appendix D, Figure D-2), the degree of saturation was much less variable, although some change in moisture content (in the range of 5%) was evident, with the timing and direction of the changes in lower layers corresponding with the changes in the upper. The reduced monitoring frequency used on site after 1999 does not provide sufficient resolution to illustrate the seasonal variations that likely also occurred in this period.

6.3.2 TC Sensor Data

The neutron probes appear to have worked better than the thermal conductivity sensors in terms of giving stable, consistent data on moisture conditions in the cover soil. Soil suction measurements were highly erratic, and many of the sensors installed gave only intermittent results (see for example Appendix D, Figure D-10). The main problem with the TC sensors appears to have been that the sensors decayed over time. It is now well documented that older sensors such as these (installed in the early 1990s) are subject to decay under environmental stress (wet-dry and freeze-thaw cycles), with poor durability

and reliability resulting over the longer term (Fredlund et al 2000; Shuai et al, 2000; Shuai et al, 2002). By the time data was compiled for this study, several of the sensors had stopped functioning completely. For example the TMD sensor at 49 cm depth had not responded since 1997, and the STD sensor at 68 cm depth had not responded since 1995. Exhumation and replacement of select sensors in 2003 showed that several of the older sensors had almost completely disintegrated. Several of sensors that remained intact functioned erratically, providing usable signals to the data logger only on occasion. The new sensors placed in 2003 are expected to have a longer operational life.

The suction data showed that peak suction values for the sensors in the upper portions of the cover occurred in the July/August period, corresponding to the results from the neutron probes. In the compacted soil (sensors at 49, 69, and 87 cm below the ground surface) there were no discernable seasonal trends, and the data was much more erratic.

6.4 Climate Data Summary

Climate data was collected at both the Kidston and Equity sites with weather logging data stations. A brief overview of the data collected at Kidston is provided in Section 6.4.1. A more detailed review of the Equity data is provided in Section 6.4.2.

6.4.1 Kidston Climate Data

Weather data collection at the Kidston on-site weather station has continued since March 1996. Regional climate data going back nearly 50 years is also available (Rykaart et al, 2001). Figure 6.15 summarizes the maximum daily temperatures recorded at the weather station on-site, up to the time of the experimental work conducted. Figure 6.16 summarizes the daily precipitation as recorded on-site. Based on site data and historical records, the average annual precipitation at the site is approximately 700 mm (Rykaart et al, 2001).

Key climate data collected during the on-site evaporation measurements is summarized on Table 6.1. Total daily net radiation values shown on the table are based on the net radiation data interpreted from the available site data, as was discussed in Section 6.1.1.

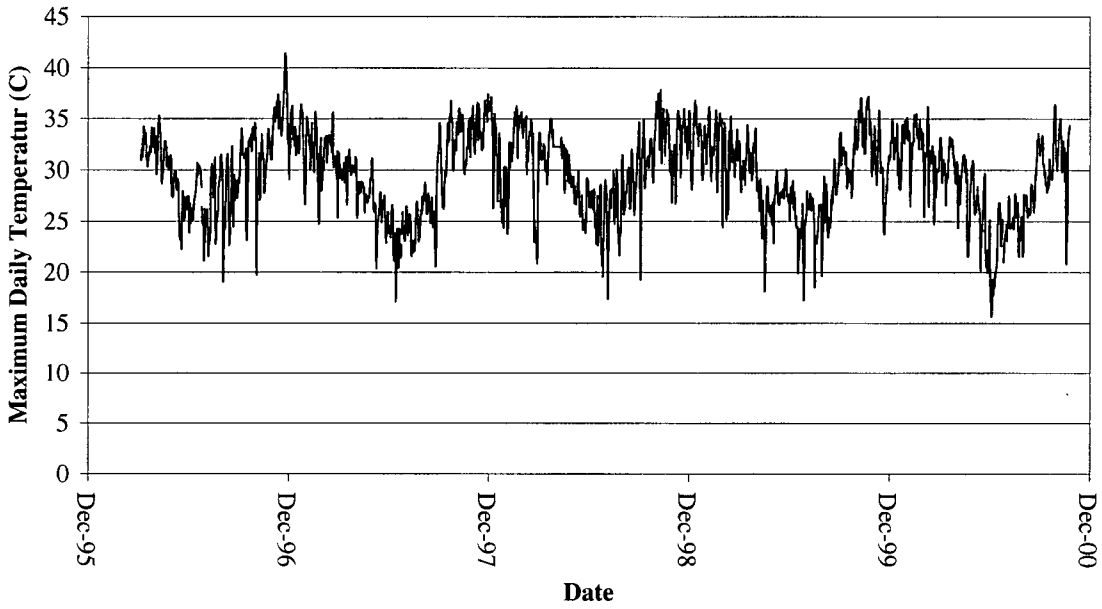

Figure 6.15: Daily maximum temperatures at the Kidston weather station

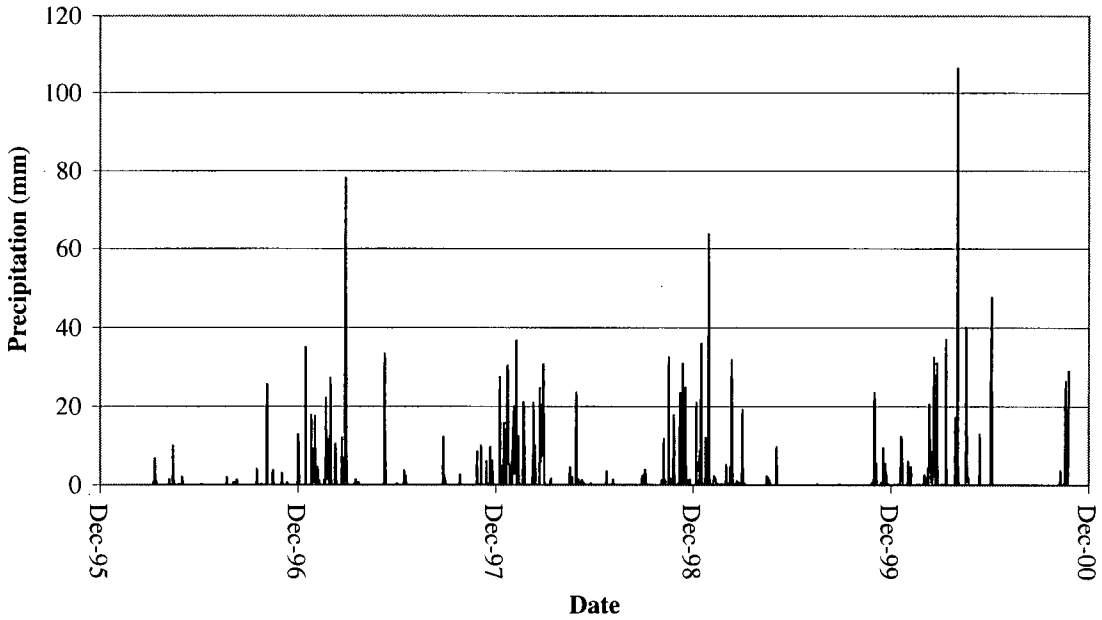

Figure 6.16: Daily precipitation at the Kidston weather station

Table 6.1: Kidston Daily Climate Data, November 30 – December 6, 2000

Date	Daily Average Vapour Pressure (kPa)	Net Radiation ($MJ/m^2/day$)	Temperature (°C)	Air Temp (°C) Max	Min
30-Nov-00	2.01	19.47	23.7	33.4	13.4
1-Dec-00	2.13	17.45	24.5	32.7	18.0
2-Dec-00	1.96	19.55	24.7	34.0	15.9
3-Dec-00	2.12	19.36	24.0	33.3	14.0
4-Dec-00	2.26	18.67	24.6	32.7	18.4
5-Dec-00	2.36	12.56	25.3	32.9	20.1
6-Dec-00	3.78	13.68	25.8	32.0	21.7

6.4.2 Equity Climate Data

Weather data collected from the site included hourly measurements of parameters such as temperature, humidity, net radiation, wind (speed and direction), and precipitation. These parameters were monitored due to their potential impact on the water balance over the soil cover. A full data set is available for these parameters from April of 1993 to the present day, with some gaps due to malfunctions of the data logger or measurement equipment. Weather data for selected parameters are summarized in Figures 6.17 through 6.20. Maximum daily temperatures for the entire period are shown on Figure 6.17. Daily precipitation data (for rainfall) is shown on Figure 6.18. Figures 6.19 and 6.20 show frequency distributions for the humidity and wind direction data collected, respectively.

The precipitation data collected at this site included only the precipitation that was in the form of rainfall. Rainfall at the site was distributed from late April to November, and

peak rainfalls typically occurred in June or July, as shown in Figure 6.18. The greatest single day of rainfall measured at the site was 41.8 mm (July 3, 1994). Over the entire period measured, the average rainfall precipitation was 339 mm of rainfall per year.

Hourly humidity values measured at the site varied from 100% to less than 20%, with the lowest humidity measurements typically recorded in the summer between June and August. As shown on Figure 6.19, the humidity measurements were generally high. The average measured humidity was 82%, with over 63% of the measured humidity values falling in the range from 80 to 100% RH, and only 3% of the measured values falling in the 0 to 40% RH range. This indicated that humid conditions predominated at the site, as was expected based on the regional climate.

The averaged windspeed at the site, based on hourly measurements, was 8.0 km/hr. The wind direction at the site was predominantly southerly, with 63% of the hourly measured wind directions being from the south, southwest, or southeast, as shown on Figure 6.20. Only 17% of the time was the measured wind direction from the north, northwest, or northeast.

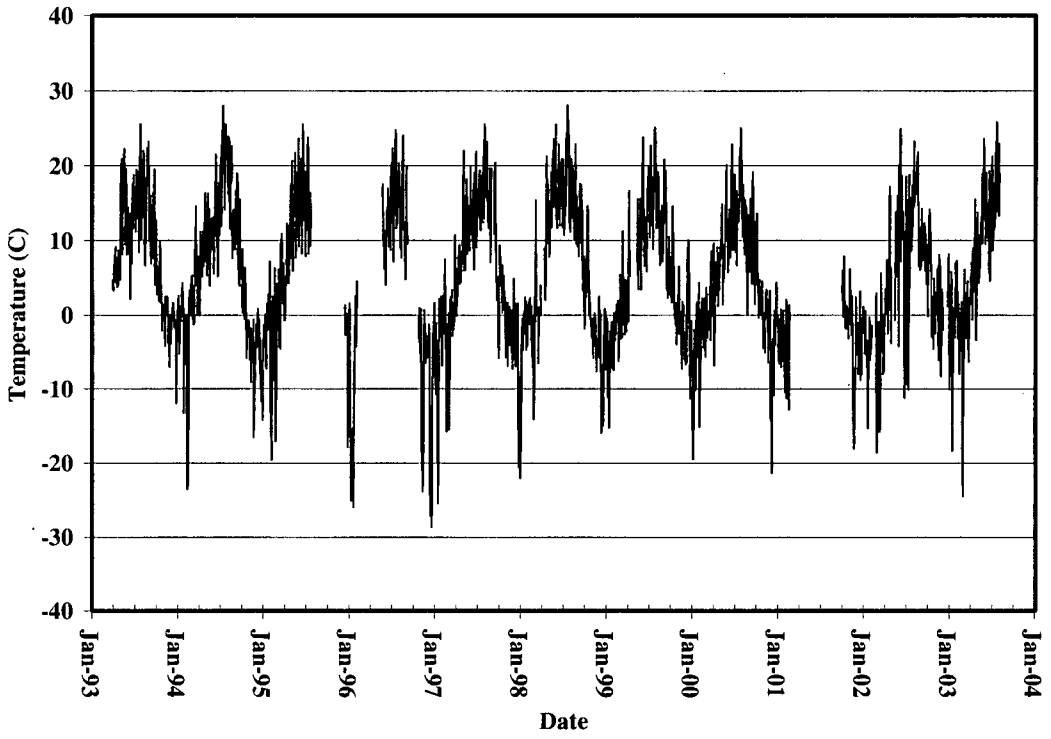

Figure 6.17: Maximum daily temperature data

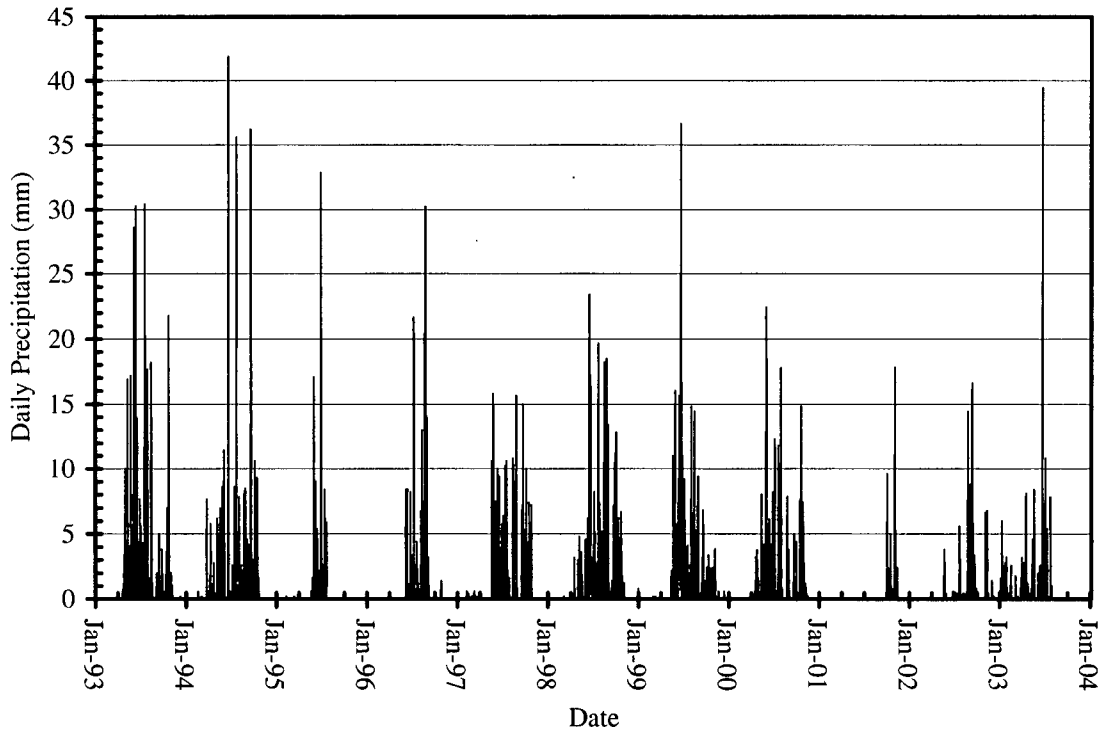

Figure 6.18: Daily precipitation data, 1993 to 2003

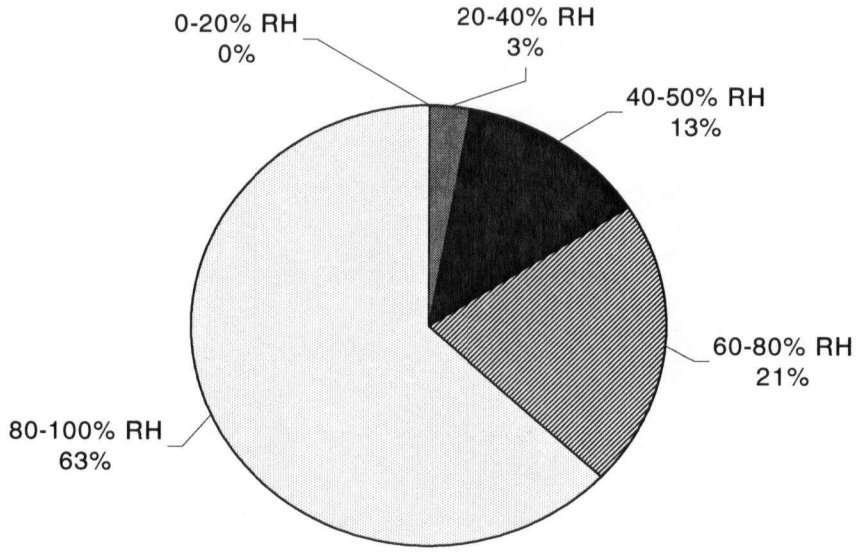

Figure 6.19: Distribution of atmospheric humidity measurements

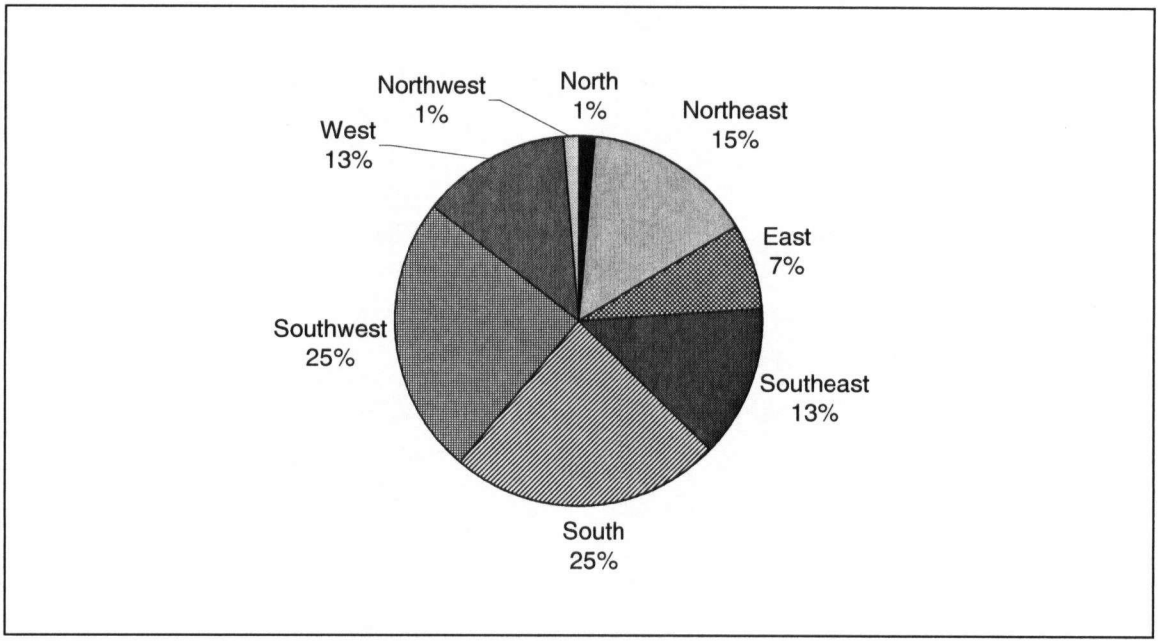

Figure 6.20: Distribution of wind direction measurements

6.5 Summary of Experimental Results

Net radiation was measured on sloped and horizontal surfaces at three separate sites, including the Arthur Lang overpass in Vancouver, British Columbia, the Equity Silver Mine in North-Central British Columbia, and the Kidston Gold Mine in Queensland, Australia. These data will be used to evaluate the net radiation model, by comparison of the net radiation values measured on various slopes to the net radiation values predicted by the model for those slopes (as a function of the net radiation measured on the horizontal). In support of these evaluations, climate data were collected at the Equity and Kidston sites. These climate data, including precipitation, humidity, temperature and windspeed measurements, will also be used in the demonstrations of how the verified predictive model can be applied.

In addition to the net radiation and climate data, supplementary data were collected to characterize evaporation and soil moisture at the Equity and Kidston sites. In general, attempts to measure evaporation with the energy balance method did not work well, and much more reasonable results were obtained with the microlysimeters. Soil moisture data was collected at the Equity site with both neutron probes and TC sensors. The neutron probes typically provided more reliable results, although the functioning TC sensors did corroborate the data from the neutron probes.

7 Data Analysis and Discussion

The theoretical model developed for net radiation on slopes was evaluated with the experimental work described in chapter 5 and chapter 6 of this thesis. This experimental work also provided data for evaluating application of this model to actual evaporation calculations for sloped surfaces. The main component of this work was the gathering of net radiation data on sloped surfaces, to be compared to net radiation amounts predicted with the theoretical model. Details for the comparison are presented in Section 7.1, including a statistical evaluation of the match between the predicted and measured radiation values. A sensitivity analysis of the model, for quantifying the impact of key variables on predicted net radiation values, is also included.

Analyses of direct evaporation measurements are presented in Section 7.2. The net radiation model verified in Section 7.1 was coupled with SoilCover (the 1-D flux boundary model) to compare the measured microlysimeter evaporation rates (presented in Chapter 6) to predicted values. In Section 7.3, the impact of net radiation on the observed moisture distribution in the Equity cover is briefly reviewed.

7.1 Evaluation of Predictive Model for Net Radiation

As discussed in Section 4.1.4, the subroutines in the predictive model for net radiation on sloped surfaces were verified using data available in the literature. A more comprehensive validation of the model has been undertaken through comparison of the model with field data collected expressly for the purpose of model evaluation. Validation was conducted primarily with solar radiation data collected at the Equity silver site specifically for this purpose. A preliminary evaluation of the model was also conducted with data collected in Vancouver at the Arthur Lang connector bridge. Evaluation of the final model with this Vancouver data is also presented.

In terms of the general approach to verification of the net radiation model, the net radiation data measured on slopes was compared to the net radiation values that would be predicted for the slopes using the radiation model. The quality of the fit between the model and reality was evaluated statistically. A sensitivity study was also conducted to examine how significantly the quality of the model fit was affected by changes in key model variables.

7.1.1 Comparison of Measured and Predicted Data - Equity

As presented in Section 6.1.3, net radiation data was measured on various slopes at the Equity site for a total of 93 days in 2002 and 2003. Simultaneously, net radiation was also measured at a weather station located on the horizontal portion of the cover.

Using the net radiation model developed in Chapter 4 of this thesis, the net radiation for each slope was predicted. For each measured data point on a slope, the net radiation measured on the horizontal was used to predict the net radiation on that slope, based on the measured slope angle and bearing for the measurement location (locations are summarized on Table 5.1).

Figure 7.1 shows in summary form the correlation between the net radiation measured on the slope, and the net radiation predicted for the same slope based on the net radiation measured on the horizontal. A total of 93 data points are shown, representing all of the data collected at Equity in 2002 and 2003. Note that this graph shows data for all the different slopes measured.

For a perfect model fit, all of the data points would plot along a straight line, with a slope of 1 and an intercept on the axis of zero. The best-fit straight-line regression shown had an R^2 value of 0.952, which indicated a good fit. The slope of the best-fit line was 1.016, which was not statistically different from a slope of 1 at the 95% confidence level. Similarly, the intercept on the y-axis for the best-fit regression line was at 0.0475, which was not statistically different from an intercept of 0 at the 95% confidence level. A more detailed evaluation of the quality of this fit is provided in Sections 7.1.1.1 through 7.1.1.5.

The fit shown in Figure 7.1 was based on predictions with the net radiation model using a uniform estimated average surface albedo of 0.16, and a corresponding emissivity of 0.9.

This estimate was based on typical albedo values that corresponded to the tall grasses that covered the site (see Table 2.1). In an analysis of shortwave solar radiation data for British Columbia and estimation of radiation on slopes, Hay (1979) indicated that single measurements of albedo "are normally made in specialized instrument enclosures and hence tend to lack spatial representativeness." As a result, he suggested the use of regionally representative albedos, which has been done here. The sensitivity of the model to variations in albedo and emissivity is evaluated in Section 7.1.3.

The parameters a_1 (in Equation 4.4) and B (in Equation 4.9) used in the model were functions of the minimum and maximum total daily transmittance (T_T), respectively. From the field net radiation data collected at Equity, the calculated value of a_1 was 1.1, and B was 0.74. The sensitivity of the model to variations in these parameters is examined in the sensitivity study in Section 7.1.3.

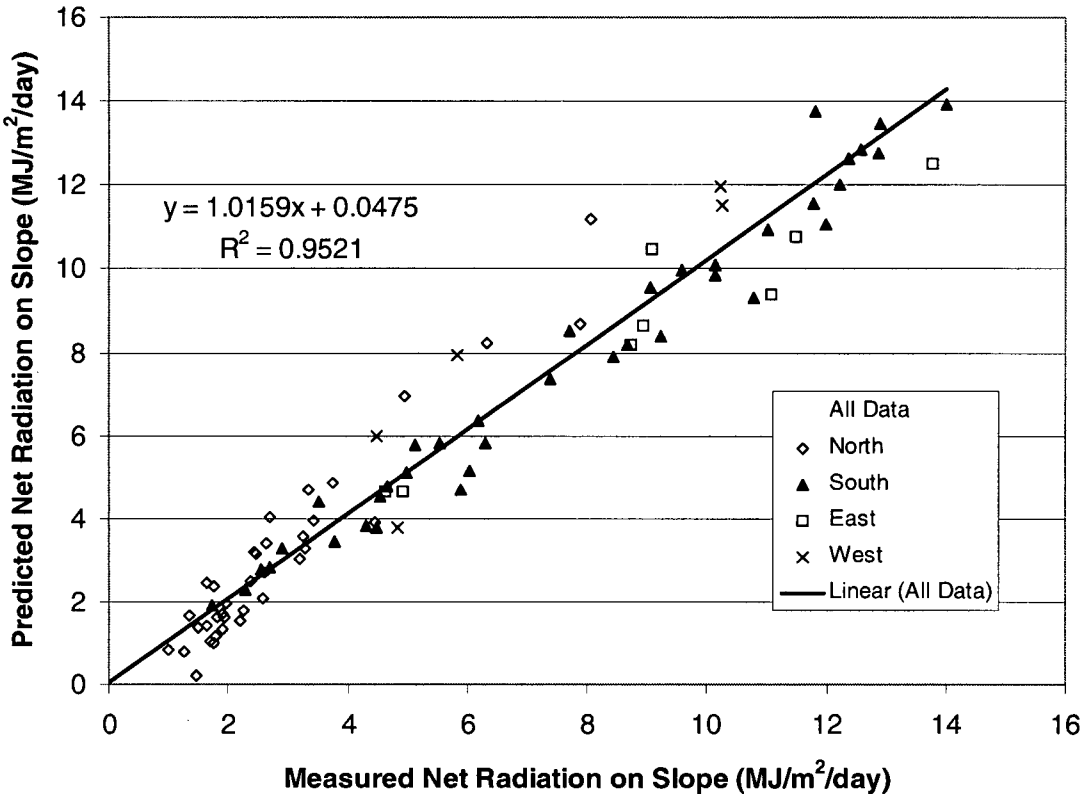

Figure 7.1 Predicted and measured values of net radiation for Equity Silver (2002 and 2003)

7.1.1.1 Model Error Analysis

While the R^2 value for the regression line gave a preliminary indication of the quality of model fit, additional parameters were needed to fully characterize the quality of the model predictions. For evaluating the prediction quality, the following three parameters were used:

- The residual: The difference between the predicted and the measured values (predicted less measured)
- Absolute residual: the absolute value of the above

- The absolute percent error: The absolute residual divided by the measured value.

Clearly, residuals and percent error should be minimized. In addition, random behaviour of residuals indicates that the errors that are inevitably present in any model are due to random processes, rather than systemic biases in the model.

In Table 7.1, the average values of the absolute residuals are summarized for both the total experimental run, and the breakdown for the averages calculated on each slope. Table 7.2 shows a similar summary of the absolute percent error values. Note that the 95% confidence limits on these and following tables are calculated on the basis of Student's t distribution, with the number of degrees of freedom one less than the number of measurements (Snedecor and Cochran, 1989).

Table 7.1: Summary of Absolute Residual Values ($MJ/m^2/day$)

	Total	North	South	East	West
Mean Absolute Residual	**0.66**	0.67	0.46	0.77	1.39
Estimated Standard Deviation	**0.60**	0.62	0.42	0.61	0.63
95% confidence value (+/-)	**0.12**	0.20	0.14	0.51	0.48
upper 95% bound	**0.78**	0.87	0.59	1.28	1.88
lower 95% bound	**0.54**	0.47	0.32	0.26	0.91
Number of measurements	**93**	38	38	8	9

Table 7.2: Summary of the Absolute Percent Error Values

	Total	North	South	East	West
Mean Absolute Percent Error	**15.6%**	25.3%	7.0%	7.6%	18.6%
Estimated Standard Deviation	**15.0%**	17.3%	6.1%	5.4%	11.4%
95% confidence value (+/-)	**3%**	6%	2%	5%	9%
upper 95% bound	**18.7%**	31%	9%	12%	27%
lower 95% bound	**12.5%**	20%	5%	3%	10%
Number of measurements	**93**	38	38	8	9

As shown in Table 7.1, the mean absolute residual in the model prediction error was 0.66 $MJ/m^2/day$, which was equivalent to the latent heat of evaporation for less than 0.5 mm of water. Table 7.2 shows that the mean absolute percentage error in the daily model prediction was 15.6%.

7.1.1.2 Interslope Comparison

In addition to mean errors for predictions based on the complete Equity data set, Table 7.1 and Table 7.2 also present a summary for the errors in the individual slopes at which measurements were made. As part of the full evaluation of the model, the mean errors at each slope were compared to the overall mean error of the prediction, and significant deviations evaluated.

The 95% confidence limits placed the mean residual error between 0.54 and 0.78 $MJ/m^2/day$ for the full experimental run. The mean residual error for the north and east slopes were within this 95% confidence limit, suggesting that there was no significant differences in the accuracy of the model for these slopes. The mean residual error for the south slope (0.46 $MJ/m^2/day$) was actually slightly lower than the range for the total data set, suggesting that the prediction was slightly more accurate on the south slope. In contrast, the average error on the west slope was slightly higher at 1.39 $MJ/m^2/day$. The higher error on the west slope was not readily explicable, suggesting that there may have been some experimental error affecting measurements from the west slope (such as a slight inaccuracy in the measurement of slope angle or aspect).

The mean absolute percentage error in the daily model prediction was 15.6% for the whole data set, with 95% confidence limit range for the mean between 12.5% and 18.7%. The mean error for the south, east and west slopes are all within or below this range. The mean absolute error for the north slope data (25.3%) was above this range. The relatively high error on the north slope is a function of the low net radiation values that were measured on the north slope, as the mean absolute residual values measured on the north slope were not significantly larger than those measured on other slopes. When daily net radiation values were low (in the order of 1-2 $MJ/m^2/day$), the impact of even small residual errors was exaggerated. For instance, a residual error of 0.5 $MJ/m^2/day$ would result in an error of 25% if the daily net radiation on the slope was 2 $MJ/m^2/day$, but if the radiation on the slope was 8 $MJ/m^2/day$ (a more typical value on other slopes), the same residual error would result in a percent error of approximately 6%.

7.1.1.3 Year-to-year comparison

For both the south-facing and west-facing slopes, data were collected in both 2002 and 2003. Comparison of the mean residual errors and mean percentage errors from the two years showed that there were no significant changes in the model prediction error between the years.

Table 7.3: Yearly comparison of errors on West and South Slopes

		Year	Mean	Standard Deviation	Number of Measurements	Lower 95 % bound	Upper 95% bound
South	Absolute Residual	2002	0.50	0.29	11		
		2003	0.44	0.47	27	0.25	0.62
	Absolute Percent Error	2002	7.4%	7.2%	11		
		2003	6.8%	5.7%	27	5%	9%
West	Absolute Residual	2002	1.53	0.42	5	1.01	2.05
		2003	1.22	0.86	4		
	Absolute Percent Error	2002	24%	10%	5	11%	37%
		2003	12%	9%	4		

On the south-facing slope, there were 27 data points collected in 2003 to evaluate the prediction of net radiation on slopes by the model. With the 95% confidence bounds, the mean absolute residual was 0.44 +/- 0.19 $MJ/m^2/day$, and the mean percent error was 6.8 +/- 2%. Both the mean absolute residual error and the absolute percent error for the 2002 data fell in this range, indicating that the mean errors on the south slope were not significantly different at the 95% confidence level.

On the west-facing slope, more data was collected in 2002, so the confidence limits were calculated on the means for the 2002 data. The mean absolute residual error was 1.53 +/- 0.52 MJ/m^2, and the mean absolute percent error was 24 +/- 10%. Both the mean absolute residual error and the absolute percent error for the 2003 data fell in this range, again indicating that the mean errors on the slope were not significantly different at the 95% confidence level.

7.1.1.4 Outlier Analysis

Visual inspection of the errors data for the Equity calculations indicated that there were several data points that had relatively high errors, and may have been outliers. To evaluate the absolute residual data and the percent error data for outliers that could be discarded from the data set, Grubbs' test was used. The Grubbs' test is an iterative mathematical method for the detection of outliers (Nevilly, 1999; Grubbs, 1950). The United States Environmental Protection Agency recommends the Grubbs' test for the detection of outliers (Environmental Protection Agency, 1992). Use of the Grubbs' test implies an assumption that the data can be adequately described with a normal distribution. This assumption is addressed in Section 7.1.1.5.

A Grubbs' test of the residual data indicated that there were no outliers in the error data set. The Grubbs' test applied to the percent error data indicated that there was a single data point that could be considered an outlier (the error value of 87% calculated for North Slope data on Julian day 283 of 2003).

While it could be argued that it would be statistically valid to discard the data from this day, it was retained in the data set for all analyses. The corresponding residual error for that day (1.28 $MJ/m^2/day$) was not excessively large. Rather than being completely spurious, the 87% error was an example of how relatively large errors (in terms of percentage of the total daily radiation) could occur on days where the total daily radiation was particularly low. While an error in the prediction of 87% was clearly not desirable, errors in this order of magnitude were not in fact very significant when the total daily net

radiation on the surface was less than 2 MJ/m^2/day. If such an error occurred on a day of higher actual net radiation (say, greater than 10 MJ/m^2/day), the implications would be of much greater concern. No such errors occurred. A scatter plot in Figure 7.2 shows that the absolute percent error in the predictions decreased with an increase in daily net radiation.

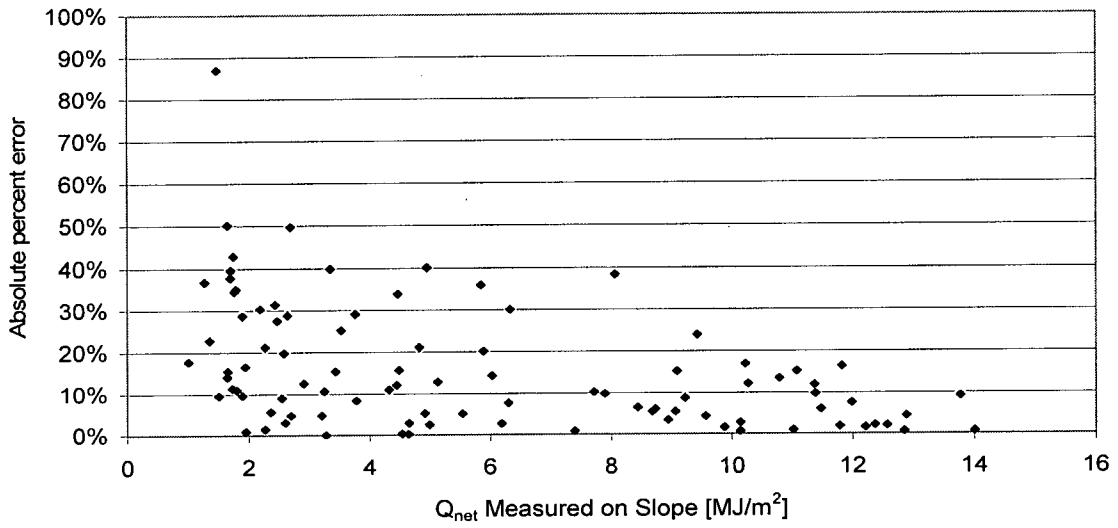

Figure 7.2: Absolute percent error in predicted slope radiation as a function of net radiation measured on slope

7.1.1.5 Graphical Residual Analysis

Graphical analyses of residuals are commonly used for the assessment of regression models (Montgomery and Runger, 2003). Residuals from the 2002/2003 Equity predictions have been graphed in several different ways, to evaluate the normalcy and randomness of the error distribution, and to inspect the data for trends in the error generation. The graphical analysis of the residuals generated suggested that the residuals were random, and at least approximately normal in distribution.

Ideally, the residual errors should be normally distributed. Figure 7.3 shows a frequency histogram for the residual errors, grouped in bins of 0.25 MJ/m^2/day. The distribution of the errors roughly approximated the bell-shaped curve of a normal distribution, with a mean close to zero (the calculated mean for the data set was 0.14 MJ/m^2/day).

Figure 7.4 shows the results of a normal distribution plot constructed for the same data set, in accordance with the method outlined by Rawlings et al (1998). For a perfect normal distribution, all of the data points would plot on a straight line. As can be seen on Figure 7.4, a straight-line regression could be fit to the data with an R^2 value of 0.96, indicating that the error distribution could be considered approximately normal. Further, the intercept of the regression line was approximately the same as mean of the residual errors, with a slope approximately equal to the standard deviation

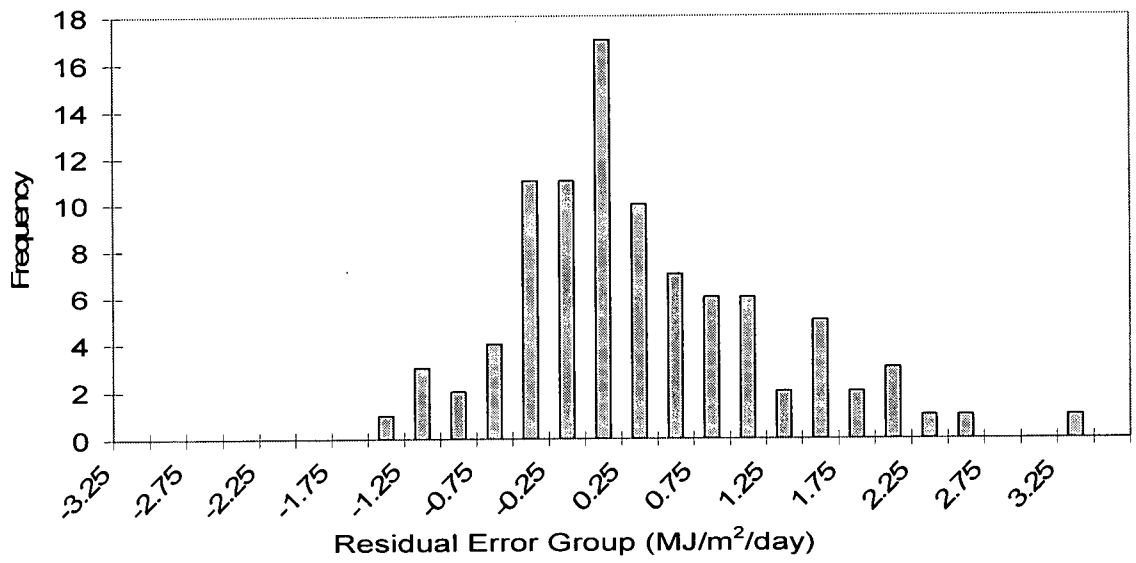

Figure 7.3: Histogram for frequency distribution of residual error (Equity 2002/2003 predictions)

Figure 7.3: Histogram for frequency distribution of residual error (Equity 2002/2003 predictions)

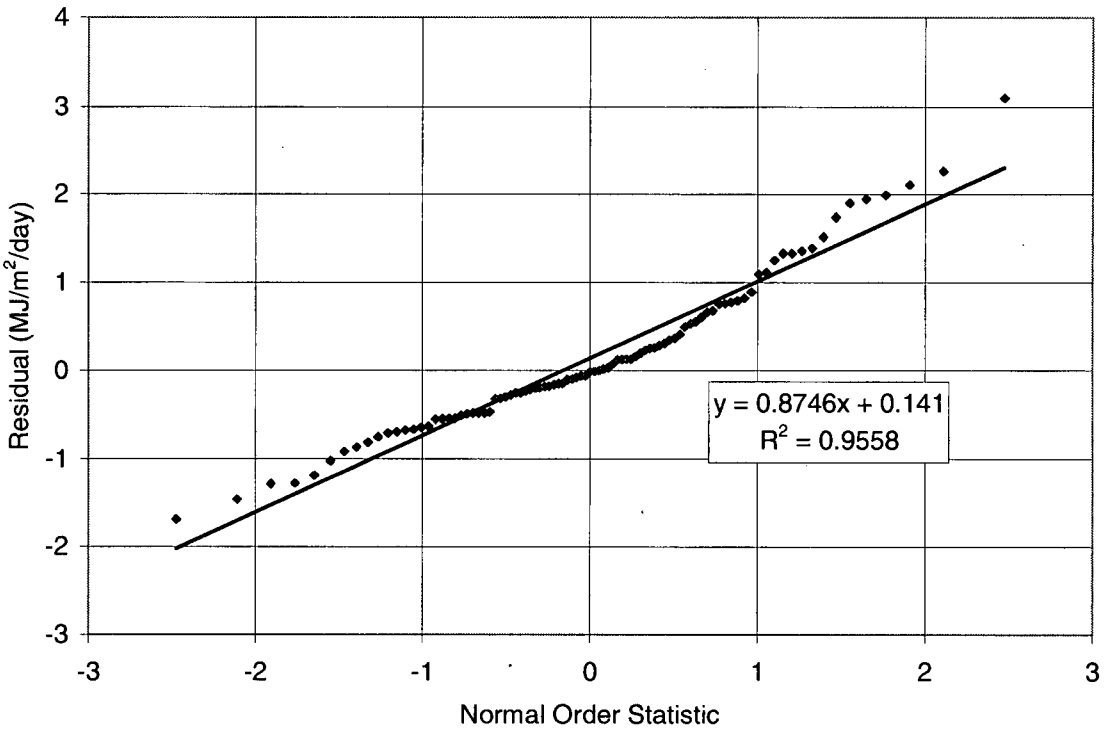

Figure 7.4: Plot of Normal Distribution Test result for residual errors (Equity 2002/2003 predictions)

The previous two plots demonstrated that the residual errors were normally distributed. The lag plot shown in Figure 7.5 was used to demonstrate that the data was randomly distributed. In the lag plot, each data point was plotted against the data point that immediately preceded it in time. There was no identifiable structure in the plot, which indicated that the errors were randomly distributed. A scatter plot with a discernable slope would indicate a correlation (Rawlings et al, 1998).

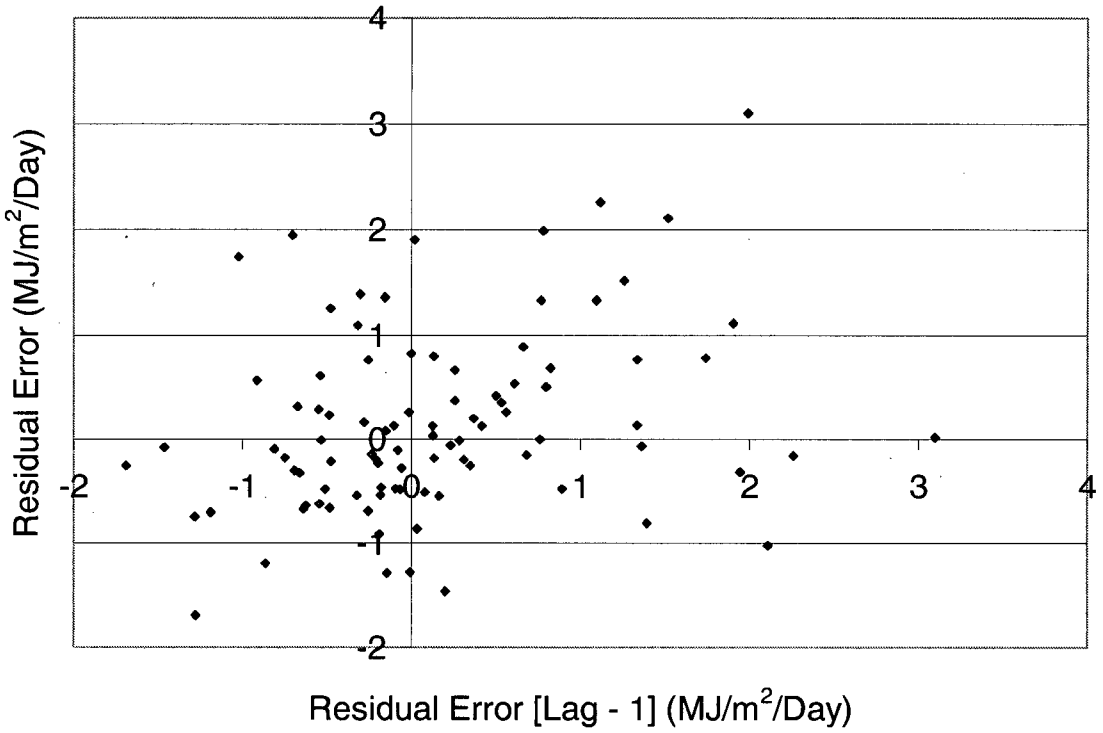

Figure 7.5: Lag plot for residual Error data. (Equity 2002/2003)

The impact on the residual error of net radiation (as measured on the horizontal and used in the prediction of the slope radiation), is shown in Figure 7.6. Ideally, the error magnitude would be independent of the net radiation on the horizontal. Clearly, however, there was some relationship, as the absolute error magnitude increased slightly with increased net radiation on the slope. This increase was quite small, and when considered as a percent of the net radiation (rather than a straight residual), the error actually decreased with increased net radiation (see Figure 7.2).

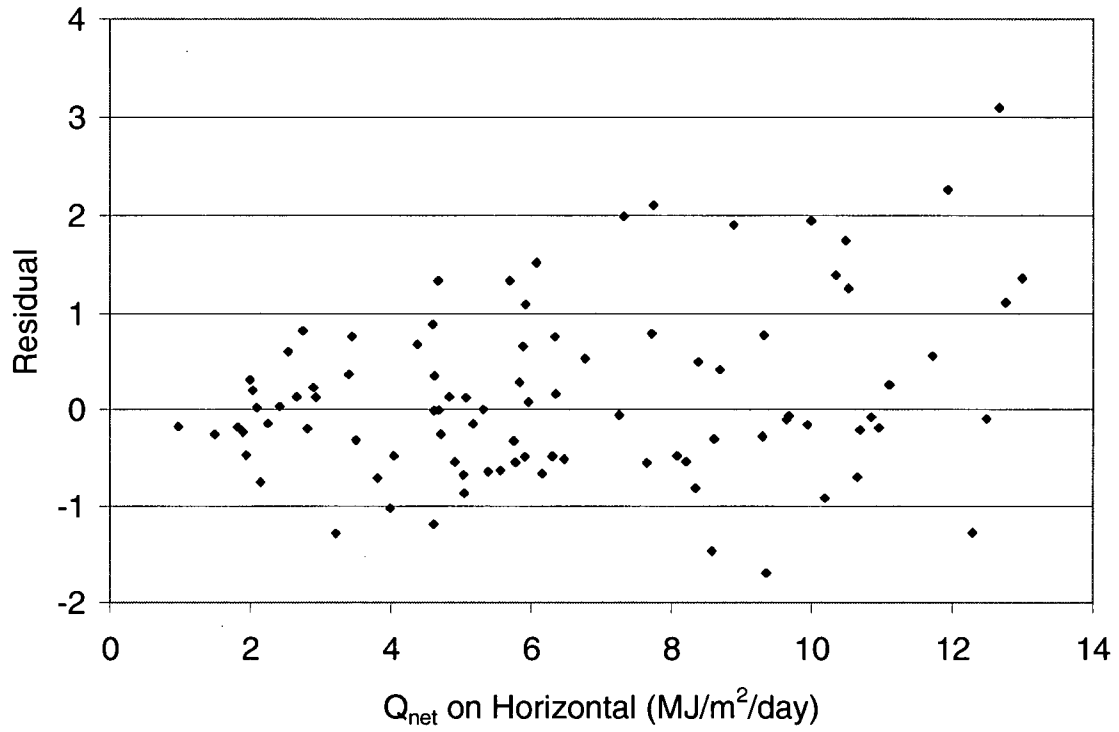

Figure 7.6: Residual errors as a function of net radiation measured on the horizontal surface (Equity 2002/2003)

7.1.1.6 Check on Shortwave Radiation

In addition to the statistical analysis of the Equity data, the general reasonableness of the shortwave radiation as predicted by the model was evaluated by comparing the model predictions against the limited historical data set available.

McKay and Morris (1985) prepared tables of shortwave radiation incident on tilted surfaces at various latitudes throughout Canada, based on measured shortwave radiation on horizontal surfaces, and model-based predictions of radiation on tilted surfaces. A database collected from 1967 to 1976 was used in preparation of the tables. McKay and

Morris (1985) presented data based on measurements taken at the Prince George, BC weather station, which was located approximately 260 km east of the Equity site, and was at a latitude of 53.88°N, comparable to the Equity site latitude.

Using the radiation model to assess the net radiation data gathered during September 2003 (the only full calendar month during which radiation was measured on both the slopes and the horizontal), the average shortwave radiation for the month was 9.9 MJ/m^2, comparable to the average value in the McKay and Morris (1985) tables of 10.9 MJ/m^2. These values are compared graphically with the first paired columns of Figure 7.7. The purpose of this comparison is to show that the calculated shortwave radiation in the model is in the same order of magnitude as the historically measured shortwave radiation values in the region.

Also shown on Figure 7.7 are the values calculated by McKay and Morris (1985) for shortwave radiation incident on slopes titled at angles of 30° and 60°, and oriented to the cardinal compass directions, based on the average daily shortwave radiation of 10.9 MJ/m^2. These values were compared to the shortwave radiation calculated in the net radiation model developed in the current for the same slopes, starting with the 9.9 MJ/m^2 value calculated for the September 2003 data. As can be seen in the graph, the general trends in the data were quite comparable, suggesting that the shortwave radiation values calculated within the net radiation model presented in this study model agree reasonably well with historic data, and with the shortwave calculation approach used by McKay and Morris (1985). Note that for north-facing slopes the model of McKay and Morris

predicted a more rapid decrease in shortwave radiation with increased slope than was predicted with the net radiation model.

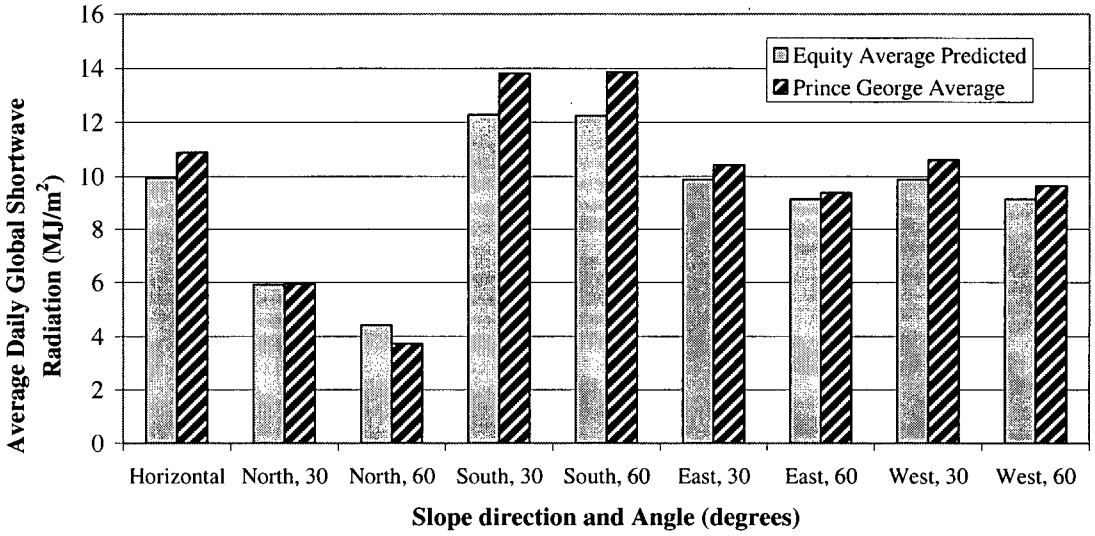

Figure 7.7: Comparison of the September 2003 average daily shortwave radiation predicted for various slopes at the Equity site to predicted shortwave radiation values at Prince George (Prince George calculated values based on September 1967-1976 measured shortwave radiation data, McKay and Morris 1985)

7.1.2 Comparison of Measured and Predicted Data – Airport

As discussed in Section 5, a series of net radiation spot measurements were taken on embankment slopes over the course of a single day at the Arthur Lang Overpass site in Vancouver, British Columbia. As the data collection methodology used at the overpass was substantially different from the methodology that was later adopted at Equity, the limited data collected at the overpass is presented separately.

These measurements were collected for preliminary evaluation of the predictive model, and were analysed here as data that was supplemental to the main model evaluation

experiments conducted at the Equity site. This data also illustrated the model application at a more southerly site (Latitude 49.2° North, compared to Latitude 54.18° for Equity).

The data from the overpass site, as presented in Section 6, included a day total net radiation value estimated from measurements on a level, horizontal surface (11.35 $MJ/m^2/day$), and six day total net radiation values as estimated from measurements at various slopes in the vicinity (presented again on Table 7.4 for reference). The solar radiation model was used to predict the net radiation on the slopes, based on the net radiation that had been measured on the horizontal. As vapour pressure data was available from the humidity measurements, the Brutsaert (1975) formulation of the equation for clearsky emissivity could be used. Table 7.4 shows the model predicted net radiation values at each slope, and the average absolute residual and percent errors associated with each prediction. Three different sets of results are shown, for clear sky emissivity (E_{ac}) as predicted in the model with the Brutsaert method (1975), the Swinbank method (1963) and the Idso and Jackson formulation (1969). For all solutions, the emissivity of the bare, dry soil at the site was estimated to be 0.92, with an albedo of 0.4, and for the Idso and Jackson formulation, the a_o parameter was set to 0.66 as a typical costal region value (Novak and Black, 1985).

Table 7.4: Net radiation predicted for slopes of overpass site, July 26, 2001

Slope Characteristics		Slope Net Radiation (MJ/m^2 - day)			
Angle (degrees)	Azimuth (degrees)	Measured	Predicted		
			Swinbank	Idso	Brutsaert
18	340	8.7	10.0	9.2	9.8
19	157	13.7	12.0	12.6	12.1
15	70	9.4	10.9	10.8	10.9
18	250	12.4	11.7	12.1	11.7
18	144	13.4	12.0	12.5	12.0
9	214	12.2	11.7	12.0	11.8
	Average Absolute Residual Error		1.2	0.7	1.1
	Average Absolute Percent Error		11%	6%	10%

Given the limitations in the methodology used, the predicted values of net radiation on the slopes matched the measured values quite well. Clearly, for this data set, using the Idso and Jackson (1969) formulation to predict ε_{ac} gave the best result, with an average absolute percent error of 6%, but even the Swinbank (1963) results are reasonable at an average absolute percent error of 11%.

The average absolute residual error in the predictions for the overpass site (with the Swinbank method) was 1.2 MJ/m^2, day, with 95% confidence limits placing this average in range of 0.68 to 1.71 MJ/m^2/day. This suggests that the residual error in this limited data was larger than the average residual error in the Equity data set, which was 0.66 MJ/m^2/day for the whole data set. Given the limitations inherent in the measurements made at the overpass site (where all measurements were collected with hand-held instruments), and the smaller total number of measurements, it is reasonable that the error should be higher in this data set.

While the data at the overpass was initially collected for the evaluation of a preliminary version of the net radiation model, the data provided supplemental evidence that the net radiation model could provide reasonable predictions of net radiation on slopes for a site located at a more southerly latitude.

7.1.3 Sensitivity Study for Predictive Model

Any changes in model input parameters will affect the final output from the model. A sensitivity study was conducted for the solar model, to examine the effect of small variations in model input parameters on the predicted values for net radiation on slopes. The sensitivity study was intended to address the following key issues outlined in point form below.

1. To determine if any of the model input parameters have particularly strong effects on the model prediction. Such parameters would require extra care for accurate determination at any sites to be analysed.

2. For parameters that were typically estimated based on observed site conditions (such as the clear-sky transmissivity), the sensitivity analysis should indicate how much error may be introduced to the overall model accuracy with respect to the estimation of these parameters.

3. For parameters that were directly measured during the site characterization (such as slope, azimuth, and latitude), the sensitivity study provides a tool to assess the overall impact of measurement errors on the final predicted results.

4. For the alternative methods used in the calculation of clear-sky emissivity (ε_{ac}) the sensitivity study provides a comparison of the three different methods.

For the sensitivity study, the parameters evaluated were assumed to lie in relatively small ranges, based on the errors in estimation or measurement that might reasonably be expected to occur. For instance, slope angle inputs were varied in the range of ± 2° from the measured slope. The impact of much larger changes in slope was considered separately, under application of the predictive model.

For the majority of the sensitivity analyses conducted, the full data set from Equity was used (93 data points from various slopes in 2002 and 2003). Subsets of the full data set were used for the assessment of slope/azimuth variations and for the assessment of alternative methods of calculating clear-sky emissivity (ε_{ac}), for reasons that will be discussed.

The best estimates or measurements of all input parameters, as previously used in the model assessment, were taken as the base case conditions for sensitivity analysis. For all sensitivity analysis, all input parameters except the one under consideration were held

constant at base case values, while the parameter examined was swept through the range of analyzed values.

For presentation purposes, the mean absolute residual error was used as an index value to show the impact of changes in input values on the overall model results. For each parameter, the mean absolute residual error is shown for the base case conditions and the impact on this value by variations in the parameter under consideration also shown. Use of this value provided a simple tool to summarize the results of numerous sensitivity analyses, while giving a quantitative indication of how much better or worse the change under consideration has made the model fit the real-world data. Appendix E also provides summary tables for all the sensitivity analyses presented that show the mean absolute residual error, the mean absolute percent error, and the 95% confidence intervals for all calculated means.

7.1.3.1 Sensitivity for Estimated Parameters

Figure 7.8 through Figure 7.11 show the effects of small variations in the estimated values of albedo, emissivity, maximum clear-sky transmissivity (B_C), and the a_1 parameter. As discussed in Section 7.1, the values for average albedo and emissivity used for the site were estimated based on observed site conditions and typical values, while the B_C and a_1 parameters were estimated from the site net radiation data.

Figure 7.8 shows the effect of varying albedo (between 0.11 and 0.21) on the mean absolute residual error for the predicted net radiation on slopes. The range of albedo values assessed was chosen to represent a reasonable range of possible values for the grassed slopes at the site. As can be seen on Figure 7.8, varying albedo in this range had a non-linear impact on the mean absolute residual error, with the impact on the best estimated albedo value less than 0.1 $MJ/m^2/day$. The sensitivity analysis suggested that the estimated average albedo for the site (base case value of 0.16) may have been slightly high, as an albedo of 0.14 improved the fit of the model to the observed data.

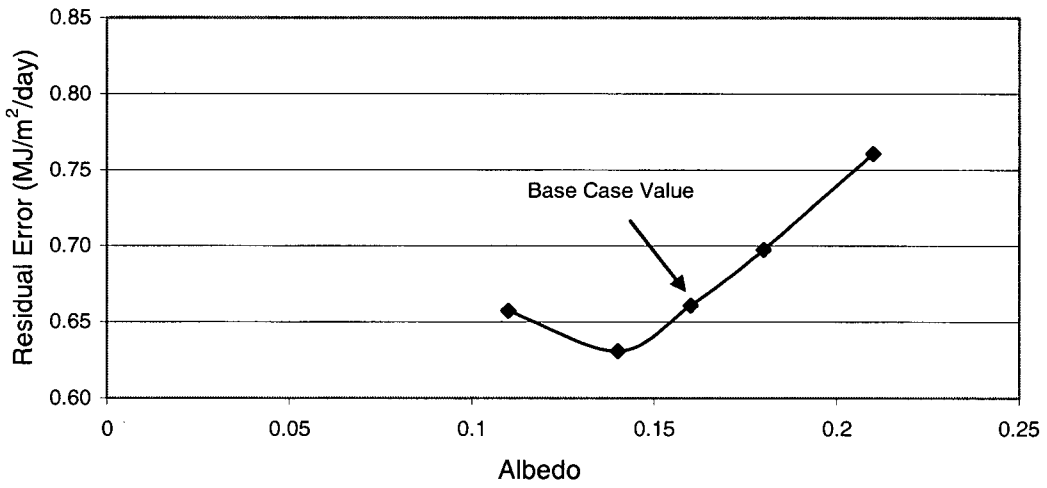

Figure 7.8 : Sensitivity of mean absolute residual error to variations in albedo

Figure 7.9 illustrates the effect on the mean residual error of varying emissivity in the range of 0.87 to 0.94. This range of emissivity values bracketed the estimated average emissivity for the site (0.9) over a reasonable range of possible values. As shown on Figure 7.9, the mean absolute residual error increased linearly with increased emissivity, at least in the range of values tested. The magnitude of the increase in error was

relatively small, with the total change in the mean residual error over the range of emissivity values tested approximately 0.08 MJ/m^2/day.

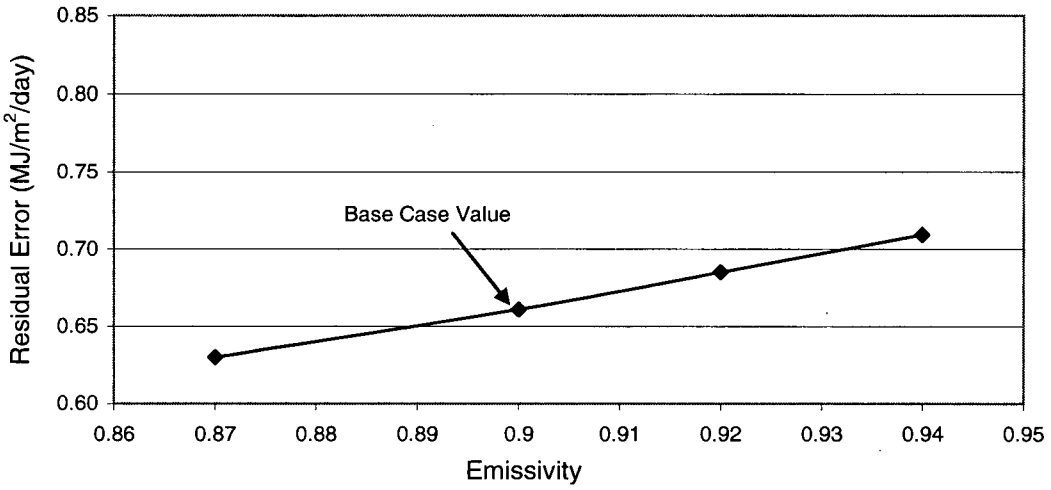

Figure 7.9: Sensitivity of mean absolute residual error to variations in emissivity

The maximum clear-sky transmissivity (B_c) typically varies in the range of 0.7 to 0.8 (Bristow and Campbell 1985, Gates 1980). For the Equity site, the estimated value of B_c was 0.74, based on net radiation data collected at the site (see Section 4.1 for details on the estimation of B). Figure 7.10 shows the effect variations of B_c in this typical range on the calculated mean residual error. The total impact on the mean residual variations through this full this range is again quite moderate, less than 0.07 MJ/m^2/day.

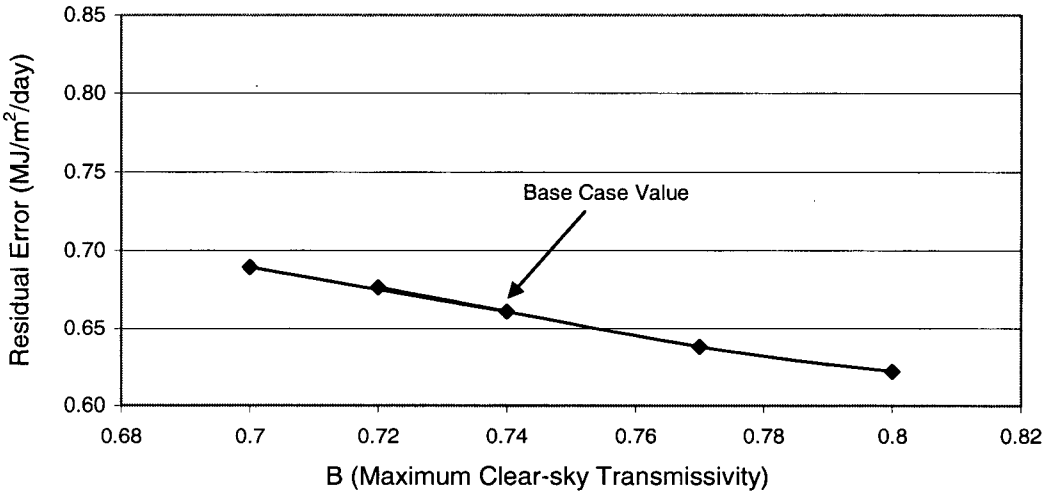

Figure 7.10: Sensitivity of mean absolute residual error to variations in maximum clear-sky transmissivity (B_C)

The a_1 parameter is related to the minimum daily transmittance (T_{Tmin}), as discussed in Section 4.1. For the sensitivity analysis, values of a_1 between 1.05 and 1.3 were assessed, corresponding to T_{Tmin} values between 5% and 23%. The value of a_1 calculated for the site was 1.1, which corresponded to a T_{Tmin} of 9%. Figure 7.11 shows the non-linear variation of the mean absolute residual error in response to changes in a_1, with a maximum variation of less than 0.05 MJ/m^2/day, and a local minimum value occurring near a_1=1.2.

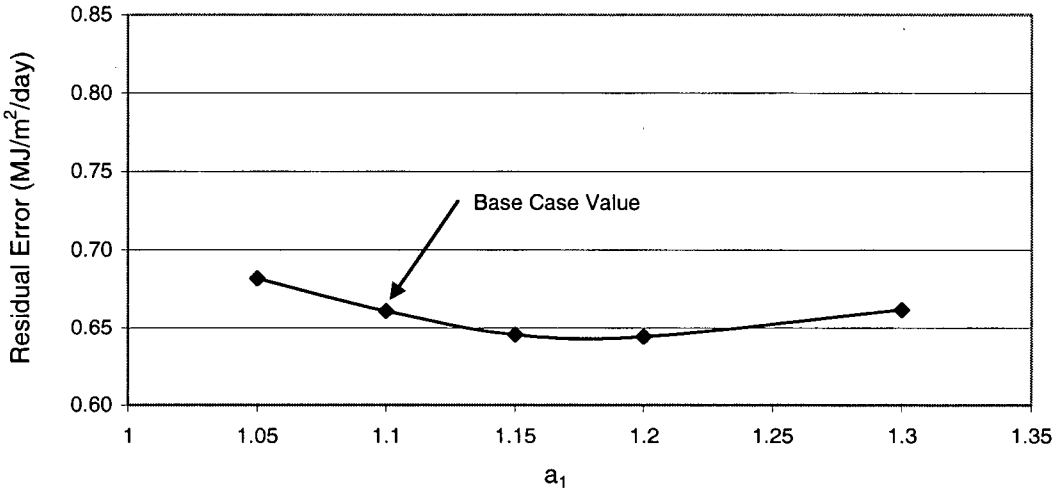

Figure 7.11: Sensitivity of mean absolute residual error to variations in a_1

Varying the estimated parameters within a reasonable range of values clearly has some effect on the model results, as shown by the impact of these variations on the mean absolute residual error. The impact was greatest for variations in albedo, with lesser effects evident (less than 0.1 MJ/m^2/day) from variations in emissivity, B, and a_1.

7.1.3.2 Sensitivity for Directly Measured Parameters

The sensitivity for directly measured parameters was evaluated for the slope azimuth, slope angle, and the site latitude. Figure 7.12 and Figure 7.13 show the impact of small changes in slope azimuth (compass bearing of downslope direction) and slope angle (steepness), respectively. For the analysis of the slopes, a subset of the Equity data was used, consisting of all of the measurements taken on the south-facing slope in 2003 (27 measurements). Analyzing the impact of slope and azimuth variations for a single slope facilitated presentation and interpretation of the sensitivity analysis. The south-facing

slope is the slope for which small changes in slope or azimuth have the potential for the most dramatic results.

Azimuth measurements were taken with a hand-held compass that had measurement divisions of 2 degrees. For the sensitivity analysis, the measured slope azimuth (175°) was bracketed with measurements that would represent an error in measurement of up to two compass divisions (4°) on either side of the field measurement, as shown on Figure 7.12. As shown on Figure 7.12, variation within this range had only a minimal effect on the final mean absolute residual error that was calculated (the total change over this range of measurements was less than 0.001 MJ/m^2/day). Note the inset on Figure 7.12, which shows that the azimuth did impact the error in the prediction, but that overall magnitude of this effect was very small.

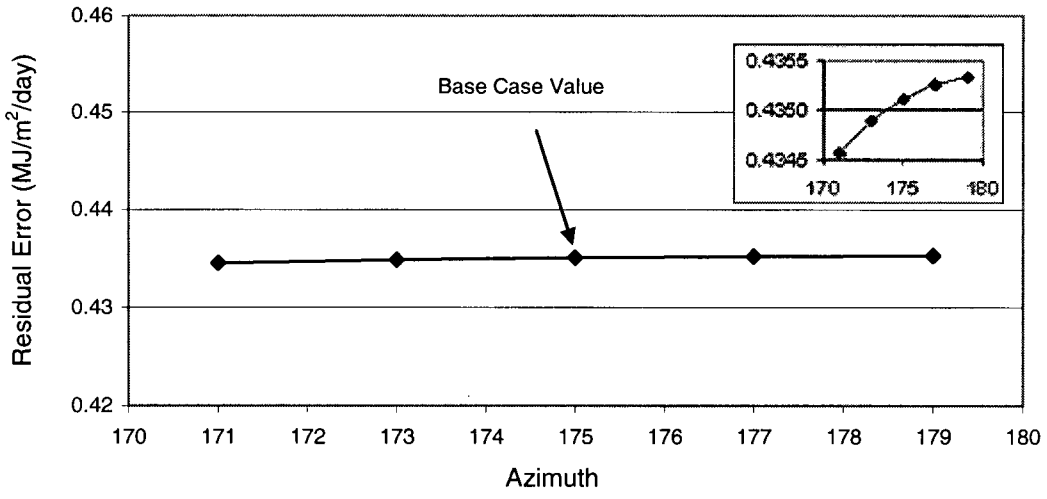

Figure 7.12: Sensitivity of mean absolute residual error to variations in slope azimuth (inset shows line curvature at higher resolution)

Slope angle measurements were taken with a hand-held clinometer that had measurement divisions of 1 degree. For the sensitivity analysis, the measured slope azimuth (18°) was bracketed with measurements that would represent an error in measurement of up to two measurement divisions (2°) on either side of the field measurement, as shown on Figure 7.13. It is clear from the figure that an error in slope measurement could have considerably greater impact than errors in the slope azimuth measurement on the overall mean absolute residual error that is estimated.

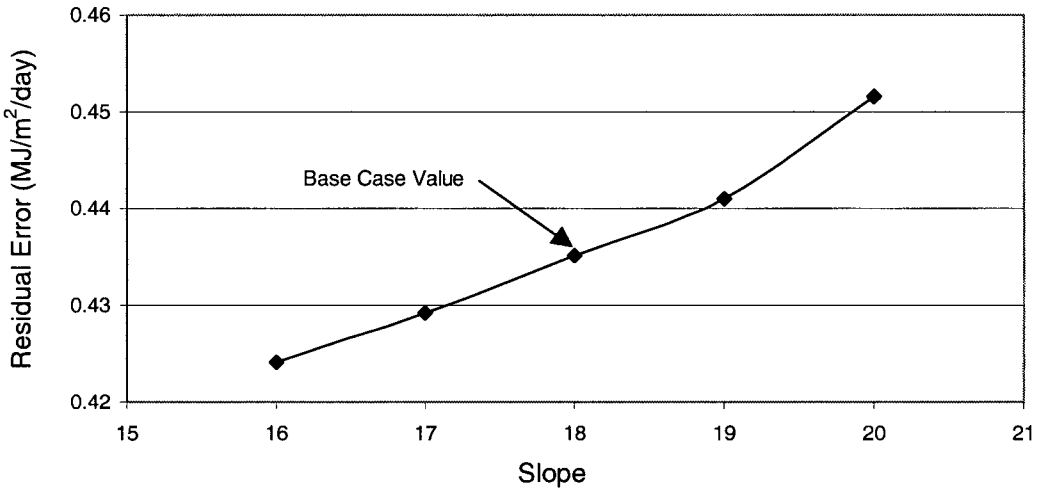

Figure 7.13: Sensitivity of mean absolute residual error to variations in slope angle

The effect of small variations in latitude was evaluated for the full data set. The latitude for the site, as measured from both site maps and GPS co-ordinates was 54.18° North. For the base case conditions (with the full data set), this resulted in a mean absolute residual error of 0.661 MJ/m^2/day. A variation of latitude by +/- 0.1° (corresponding to approximately +/- 10 km in the site location) resulted in a mean absolute residual error range between 0.654 and 0.668 MJ/m^2/day, a relatively small effect.

7.1.3.3 Sensitivity for Clear-sky Emissivity Calculation Methods

As discussed in the theoretical development of the model (Section 4.0), the model has been formulated to include three alternative methods for the calculation of ε_{ac}, the clear-sky emissivity. For base case evaluations, the model of Swinbank (1963), which required a minimal number of input parameters, was used. For the sensitivity study, the results generated with the Swinbank method were compared to the results generated using the method of Brutsaert (1975), which required an input of daily vapour pressure data, and that generated with the method of Idso (1980), which requires an estimated value of a_0 (the factor used to ensure that shortwave radiation does not go to zero under cloud-covered conditions). The a_0 parameter varies in the range of 0.6 (ocean) to 0.7 (inland). As the a_0 parameter was estimated from site conditions, a subset of this sensitivity analysis was conducted to illustrate the sensitivity of the results with the Idso (1980) method to variations in this parameter.

For evaluating the sensitivity of the model to the equations used to calculate ε_{ac}, only the data collected at Equity in 2002 was used. This was done because the vapour pressure data required for solution with the Brutsaert (1975) method was only available in 2002. This data was therefore used for all three methods, to facilitate parallel comparisons of the results.

The bar graph shown in Figure 7.14 summarizes the results of the sensitivity analysis with the three methods (and with the three values of a_0). The error in the predictions

made with the Swinbank (1963) and Brutsaert (1975) methods were almost identical, and comparable to the error obtained using the Idso (1980) method with an a_0 value of 0.7 (reflecting inland conditions at the site). This suggested that at least for this initial data set, all three methods gave reasonable and comparable results. For the Idso (1980) method, it was also evident that selection of an appropriate value of a_0 was important. As a_0 values were decreased from 0.7 to 0.61, the error in the prediction increased considerably, as shown on Figure 7.14.

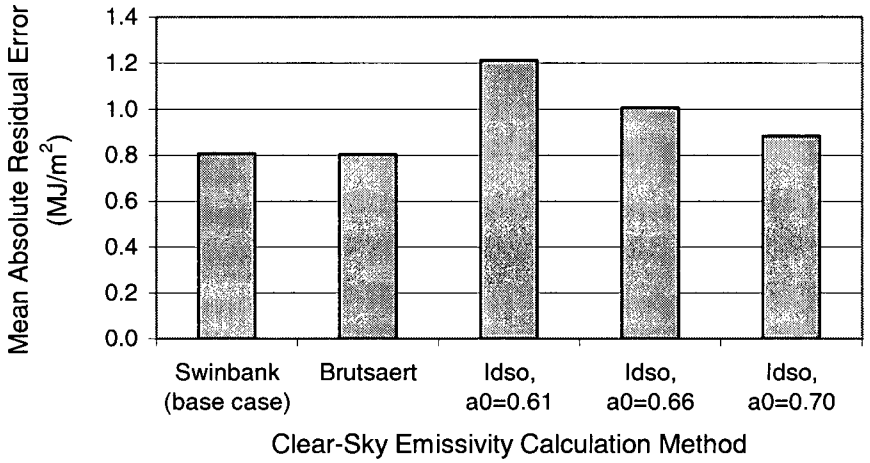

Figure 7.14: Sensitivity of mean absolute residual error to method used for calculation of clear-sky emissivity (ε_{ac}) for 2002 data

7.1.3.4 Summary of Sensitivity Study Results.

The sensitivity study has shown that small changes in any of the measured or estimated model input parameters can have an impact on how well the new model for net radiation on slopes predicts the actual conditions at the site. Within reasonable error bounds, none of the parameters evaluated had disproportionate impacts on the final quality of model fit. This suggests that the model should be reasonably robust in application.

Among the estimated parameters, the quality of the model fit was most strongly affected by the estimated value for average surface albedo. It therefore would be good to have accurately measured values of albedo. Albedo would ideally need to be measured and averaged over the year, as albedo values can easily vary by 0.02 or more over the course of a growing season (Hanson, 2001). Another possibility is to introduce an albedo function to the model that allowed albedo to vary with the day of the year. While such an approach may improve numerical accuracy, it would take the application away from the original intent of having a model that used only readily available site data.

7.1.4 Summary of Net Radiation Model Evaluation

The predictive model for net radiation on slopes has been evaluated against data measured in the field, as well as against available data in the literature. Based on the analysis conducted to date, the new model presented in this thesis can provide a reasonable approximation of the net radiation incident on a sloped surface at a given site,

based on the net radiation that is incident on a horizontal surface at the same site. The quality of the model fit to the measured field data is statistically acceptable, as shown by the analysis presented in Section 7.1.1. The sensitivity of this new model to key input parameters has also been evaluated. The model is now ready to be used with flux boundary models such as SoilCover, Vadose/W and SVFlux (SoilVison Systems Ltd., 2005) that use net radiation as a climate input.

7.2 Evaluation of Flux Measurements

Evaporation at the Kidston and Equity sites has been measured with microlysimeters. Under idealized conditions, evaporation from microlysimeters takes place in one dimension (vertically, through the column). The one-dimensional flux boundary modeling program SoilCover was used to model evaporation from the microlysimeters. The SoilCover analysis was coupled with the radiative model, which was used to modify net radiation weather data as a function of the slope on which the microlysimeters were installed. The evaluation of evaporation measurements made at Kidston is presented in Section 7.2.1, with the evaluation of evaporation measurements made at Equity in Section 7.2.2.

7.2.1 Kidston Evaporation Measurements

The results of microlysimeter measurements conducted at Kidston on the test hummock were presented in Section 6.2.1. These results showed greater evaporation from the microlysimeter placed in the south face of the hummock than the north, corresponding well with the greater net radiation received by that slope at the time of the measurements. Note that for most of the southern hemisphere, north facing slopes will tend to receive more solar radiation than south-facing slopes throughout the year. However, at low latitudes (such as at this site) a reversal occurs in the summer (as a function of the earth's tilt), and the south-facing slopes receive more solar radiation.

To simulate conditions at each of the microlysimeters, the net radiation data collected at the weather station over the duration of the experiment (presented in Section 6.1.1) was used. The radiative model was used to predict the net radiation expected at each microlysimeter, based on the slope angle and aspect of the microlysimeter location. A fairly high albedo was used (0.35), based on the bare, dry soils at the test area.

SoilCover was used to simulate evaporation from the microlysimeters. In addition to the modeled net radiation data, climate data collected on-site during the experiment was used to define the upper boundary of the simulation for the period. The wind gauge at the weather station was not functioning properly during the field work, so average wind speed data for the same period from the previous years (1996-1999) was used. Soil properties used in the microlysimeter were as presented in Section 5.7.1 for the oxidized soil cover. The 200 mm column of soil in the simulation was underlain by a thin (5 mm) layer of very low conductivity soil (10^{-14} cm/sec) to simulate the effect of the plastic membrane at the base of the microlysimeter. For the analysis, the soil at the base of the microlysimeter was taken to have a suction near the air entry value as a lower boundary condition (10 kPa). The soil was taken to be initially at its residual suction (200 kPa) near the ground surface.

Figure 7.15 shows the strong correlation between the measured and predicted cumulative evaporation for the microlysimeters on the north slope and the microlysimeter located on the horizontal crest area. Shown separately for clarity on Figure 7.16 is the correlation between measured and predicted evaporation rates on the south slope. The correlation for the north slope is also shown on this figure for reference. As can be seen on these two

figures, the general trend in the cumulative evaporation from the microlysimeters was well modeled using SoilCover in conjunction with the net radiation model. In all cases, boundary conditions, soils data and climate data were identical in the models. The only variation was in the net radiation used in the climate boundary. As can been seen in the figures, the variation predicted in this one parameter (as a function of slope and direction of exposure) was sufficient to account for much of the difference in evaporation actually measured at the microlysimeters. This strongly suggests that the net radiation model can be a useful tool to aid in the prediction of actual evaporation from slopes.

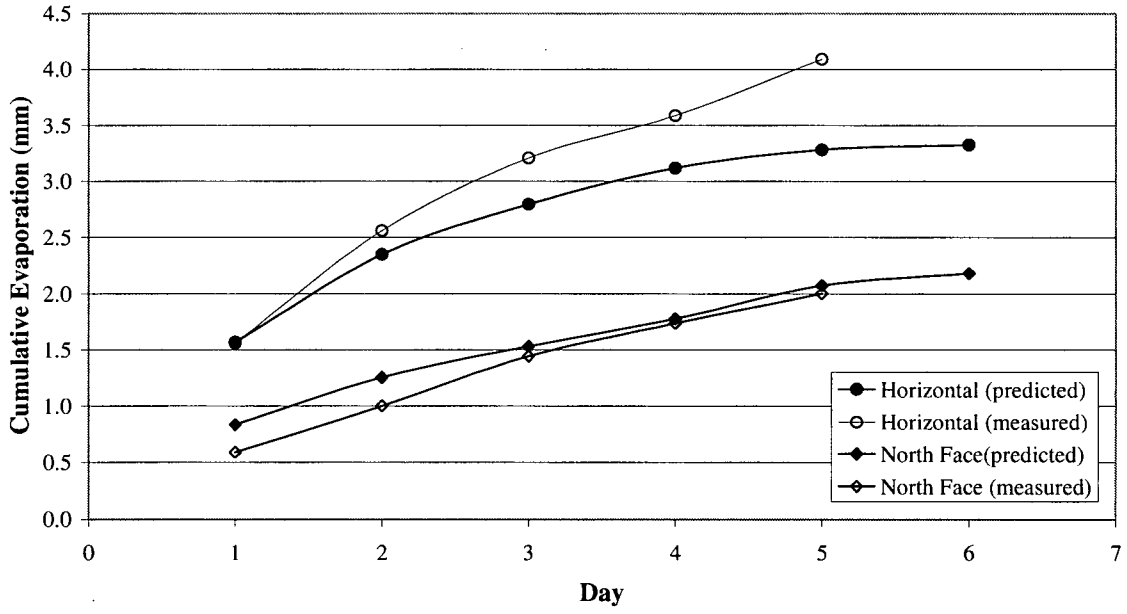

Figure 7.15: Comparison of measured and predicted cumulative evaporation for crest and north slope for Kidston site

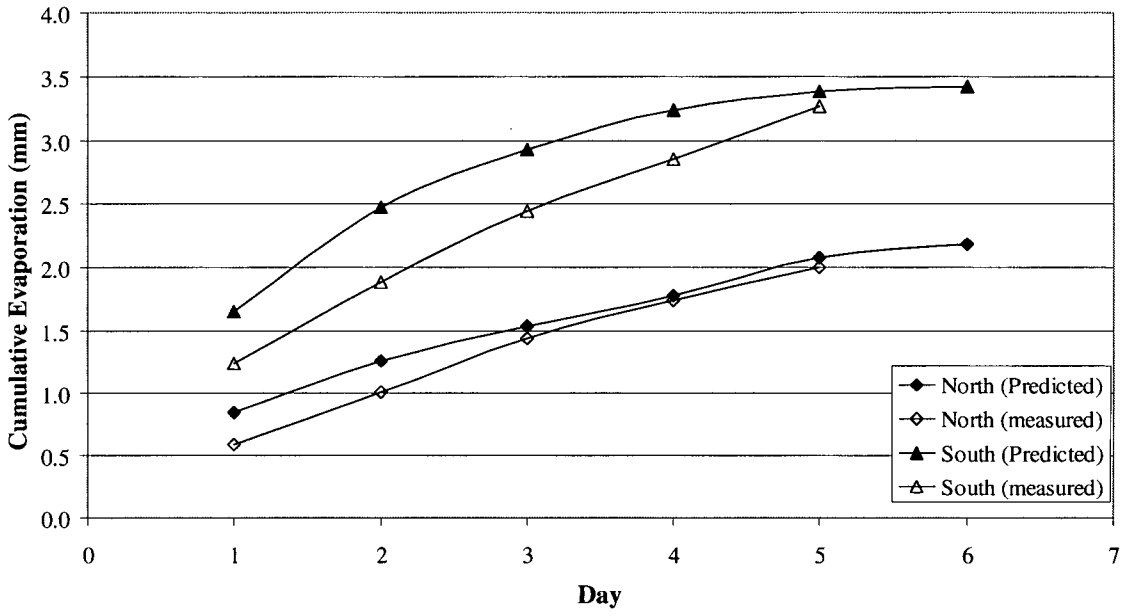

Figure 7.16: Comparison of measured and predicted cumulative evaporation for north and south slopes for Kidston site

At the completion of the field work, moisture profiles were determined in the microlysimeters, as discussed in Chapter 6. Moisture profiles were also calculated for the modeled microlysimeters in SoilCover. As shown in Figure 7.17, the moisture contents measured in the field throughout the profile were higher than predicted with SoilCover. While there is reasonable agreement in the measured and predicted near-surface moisture contents, the actual moisture content observed at depth was consistently greater than that predicted with SoilCover. There are two likely causes for the difference between measured and predicted moisture contents at depth. First, the shape of the predicted moisture content curve at depth is largely a function of the soil's soil water characteristic curve. Accurate predictions of evaporation are possible with soil cover as long as the near-surface suctions are well predicted. Initial moisture conditions through the profile that were input to the SoilCover model were approximations of field conditions. Over

the short duration of the experiment, these initial moisture conditions likely had a controlling effect on the final moisture profile, rather than the final moisture profile being controlled by differences between evaporation rates on the north and south slopes. For instance, the final moisture contents measured in the north face microlysimeter were lower than those measured in the crest microlysimeter contents (as shown on Figure 7.17), reflecting the influence of the lower initial moisture content in this soil. If initial moisture contents were the same, the SoilCover model suggests that the crest microlysimeter would be drier, as a function of the greater net radiation received by the crest, and subsequent evaporation, as shown on the predicted moisture profiles in Figure 7.17.

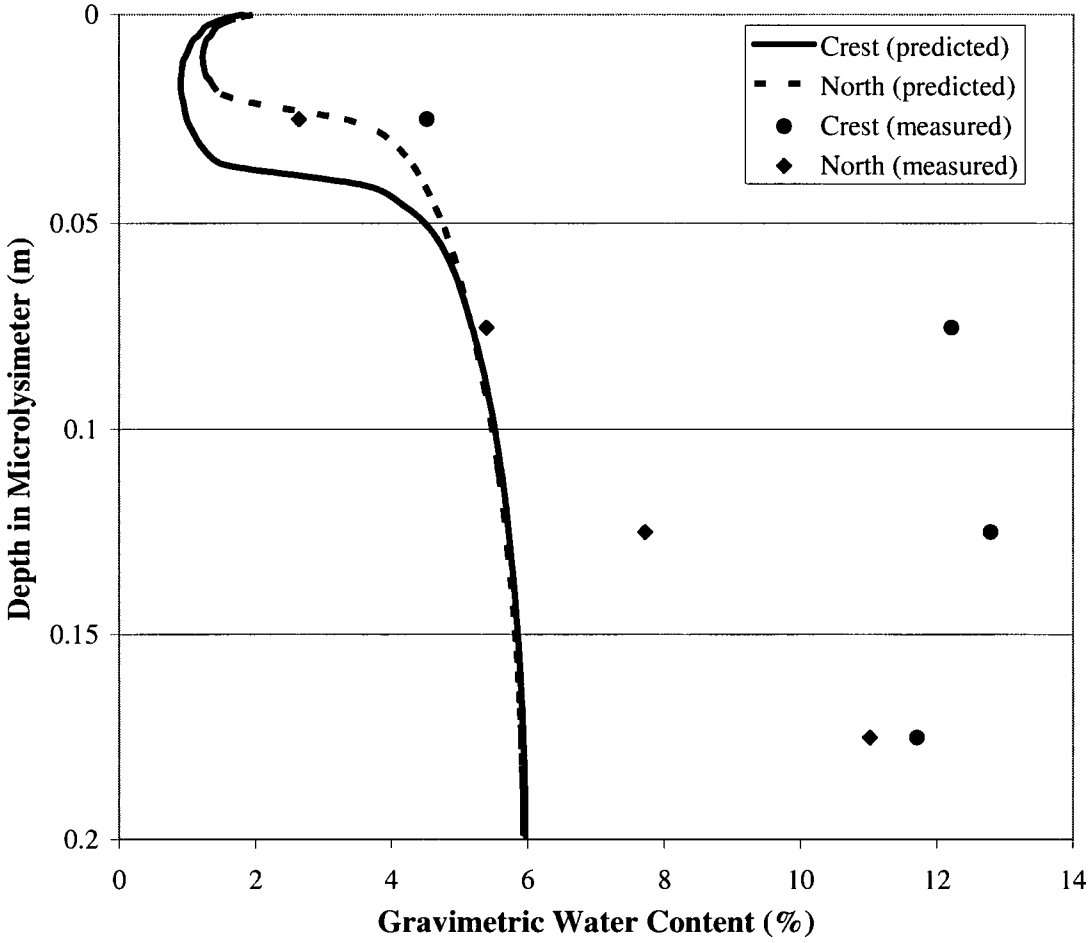

Figure 7.17: Measured and predicted final moisture profiles for Kidston microlysimeters

7.2.2 Equity Evaporation Measurements

The results of the microlysimeter measurements conducted at Equity were presented in Section 6.2.2. While the results from the microlysimeter work did clearly show greater evaporation rates on the south-facing microlysimeters (in response to greater net radiation), rainfall during the experimental period adversely affected the amount of information that could be derived from the experimental work.

Similar to the analysis of the microlysimeter data from Kidston, SoilCover was used to simulate the performance of the microlysimeters at Equity. Climate data measured at the weather station over the period of the experiment was used as an input to the model, with net radiation data transformed using the radiation model as appropriate for the slope angle and direction under consideration. Soil properties used in SoilCover were the properties for the non-compacted Equity till, as described in Section 5.7.2. The soil was taken to be at a uniformly saturated initial moisture content in all microlysimeters (in keeping with the microlysimeter preparation described in Section 5.6.2). Based on the moisture profile observed at the end of the experiment, the lower boundary of the microlysimeters was modeled as a zero pressure boundary.

Following the experimental work, it was found that the humidity was not being measured correctly at the weather station. This seriously impaired the possible accuracy of any actual evaporation modeling attempted for the microlysimeters in this period. As an approximation, a synthetic data set was constructed from past measurements at the site during this time of year, with the daily maximum humidity set to 100% on all days with precipitation or trace precipitation, and the maximum humidity set to 90% on other days. Minimum humidity values were estimated based on days with similar minimum temperatures during the same time period. This synthetic humidity data set was used to allow a conceptual level analysis of the microlysimeter data.

Figure 7.18 shows a comparison between the cumulative evaporation measured at the microlysimeters, and the cumulative evaporation predicted with SoilCover. Decreases in

evaporation reflected infiltration from rainfall during the period. The modelling conducted with SoilCover closely matched the general trends in evaporation, with both the model and the field data showing greater cumulative evaporation from the south-facing microlysimeter than the north-facing one, and with evaporation from the microlysimeter on the crest between the two extremes. In this case, the model did not accurately represent the degree to which slope seems to have affected evaporation rates, underestimating the actual difference between the north and south slopes (a predicted difference in cumulative evaporation between the north and south faces of only 2 mm, compared to a measured difference of 6mm).

Final moisture content profiles in the SoilCover model were almost uniform, indicating that evaporation from the profile did not significantly affect soil moisture storage. The final average moisture content modeled for the north-facing column was 16.6 %, with 16.2 % in the south-facing column. In the field-measured column, the final average moisture content was 18.9 % in the north facing, and 17.9 % in the south facing. The difference in final average moisture contents between north and south microlysimeters for the modeled system was 0.4 %, compared to 1 % for the real system.

Given the limitations of the experimental work, the SoilCover model performed reasonably well. The lack of good humidity data limited the possible accuracy of the analysis. Further, considerable rainfall occurred during the experiment, which the experimental methodology was not designed to accommodate. Finally, there was significant cloud cover during the experiment, which was not ideal for giving results illustrative of the effect of radiation differing on opposite slopes.

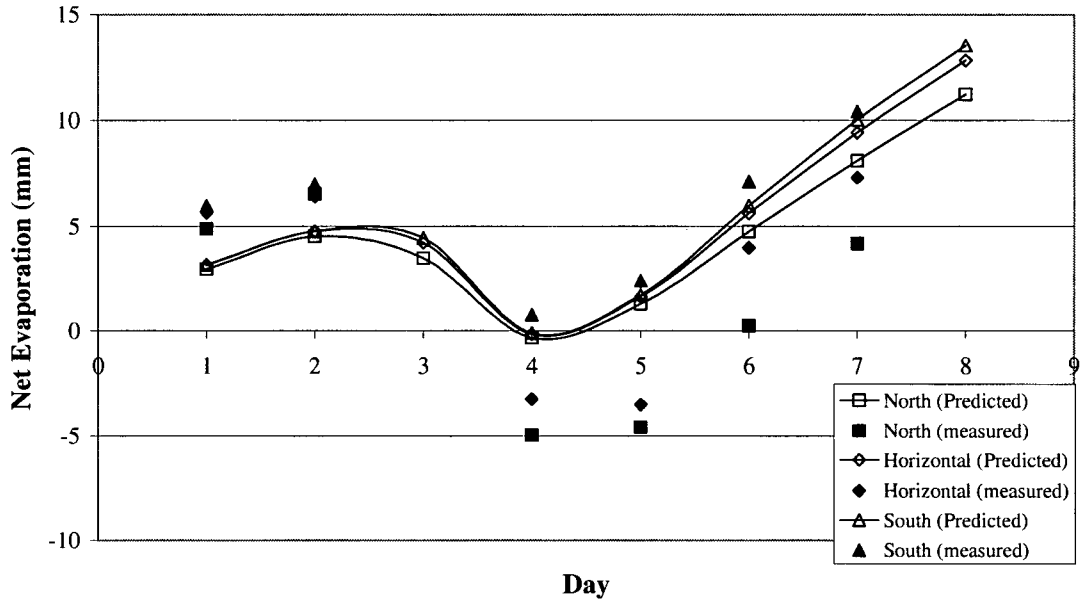

Figure 7.18: Measured and predicted cumulative evaporation from Equity microlysimeters

Considering the results of the microlysimeter experiments conducted at both Kidston (Section 7.2.1) and Equity (Section 7.2.2) it has been shown that using the program SoilCover in combination with the net radiation model can provide a reasonable approximation of measured evaporation, and of the differences between evaporation measured on north- and south facing slopes. At the Kidston site, the combined use of SoilCover and the net radiation model provided a good approximation of the different evaporation rates observed. At the Equity site, the combined models provided a bulk representation of the overall evaporation rates and the general trends in their differences.

7.3 Equity Soil Moisture Measurements

With data from 14 neutron probes distributed throughout the cover, there was a unique opportunity to investigate variations in the moisture profile over the cover area, and to evaluate some of the possible effects of slope and exposure on moisture content distribution through the profile thickness. Neutron probes NP1 through NP9 were located on the main dump in very similar cover soils, and are compared in more detail below.

The neutron probes NP1, NP2, and NP3 were located quite closely together (within 10 meters of each other) on the southwest face of the main dump cover, as shown on Figure 7.19. NP1 and NP2 were located at similar points in terms of slope steepness and exposure, while NP3 was located on a small bench slightly higher on the slope. (Representative moisture profiles for NP2 and NP3 are shown in Figure 7.20 and Figures 7.21, respectively). The moisture content conditions at NP1 and NP2 were similar, with the degree of saturation at depth typically between 95% and 100%, with the near-surface degree of saturation varying from 35 to 75%. In contrast, NP3 typically had a greater degree of saturation near the surface, in the range of 50% to 85%.

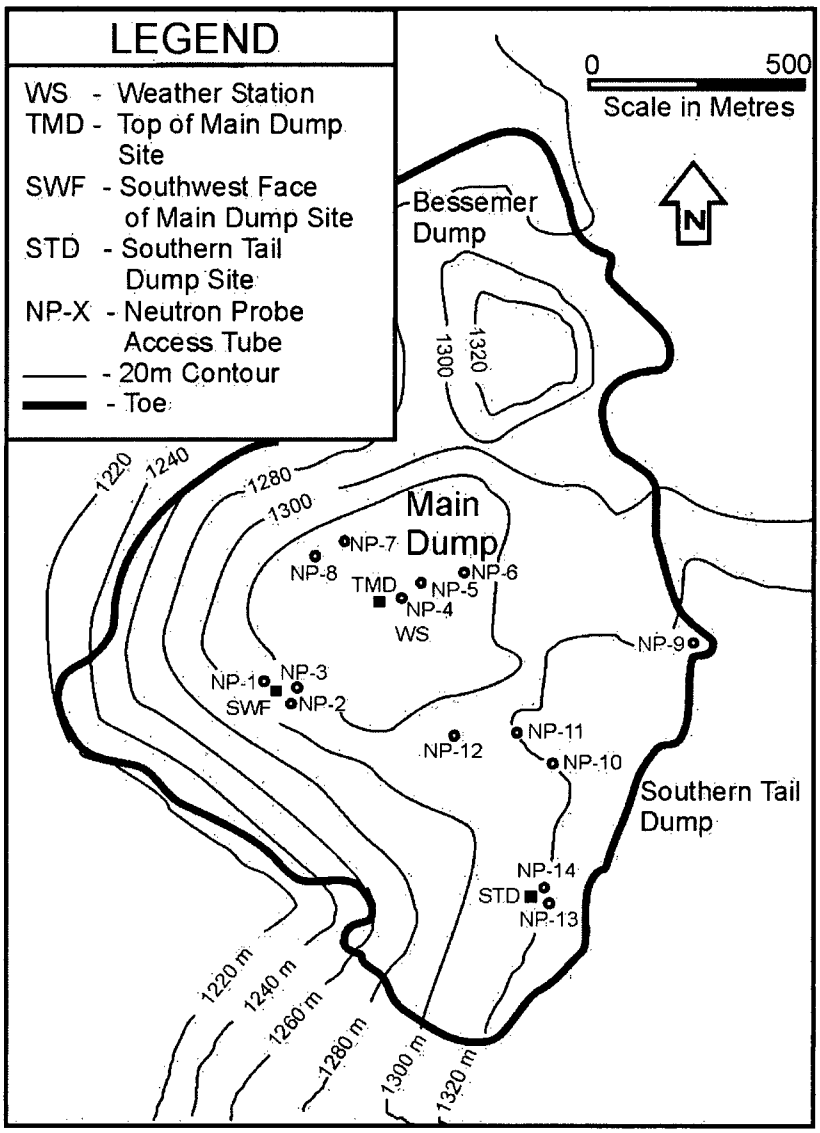

Figure 7.19: Site plan – location of neutron probes (after O'Kane, 1995)

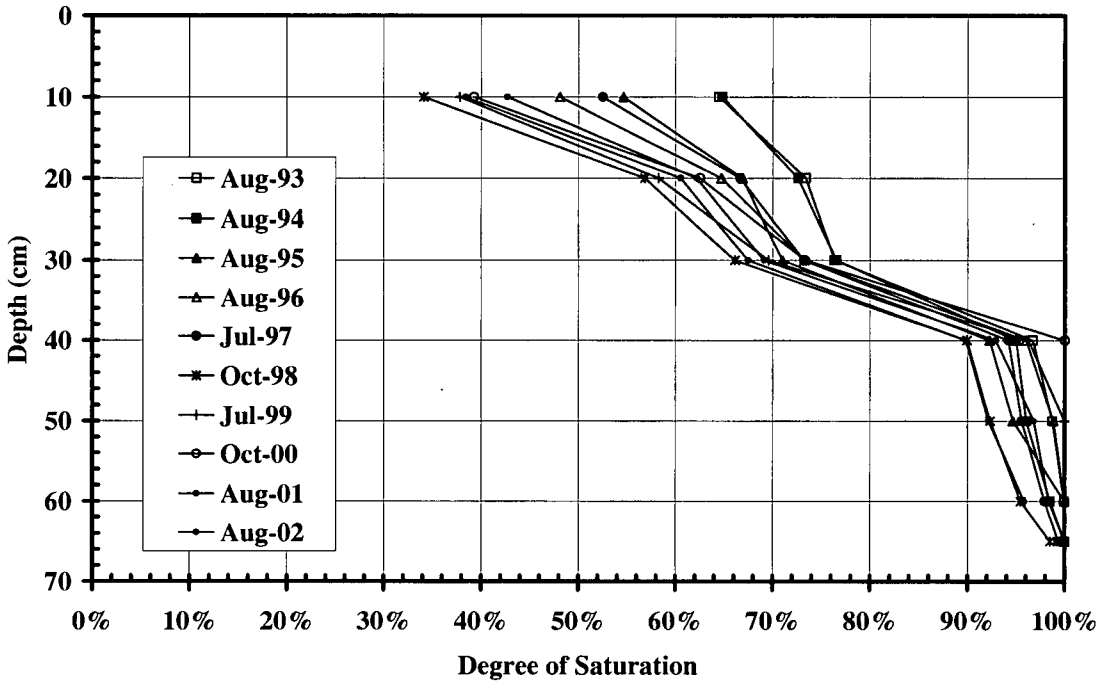

Figure 7.20: Soil moisture profile at neutron probe NP2, Equity

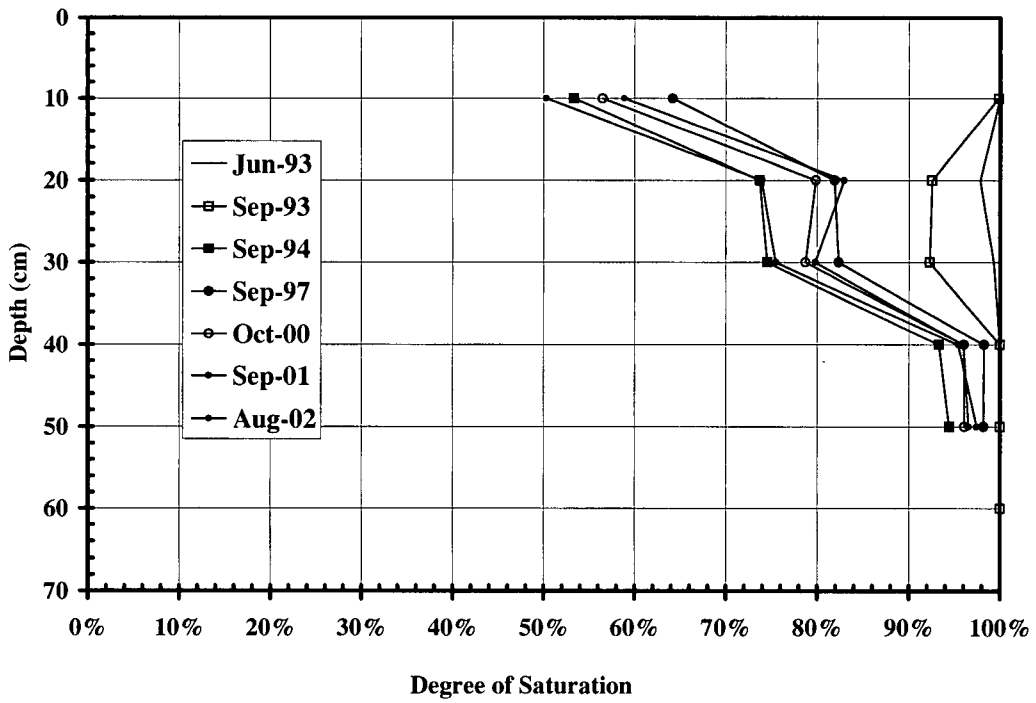

Figure 7.21: Soil moisture profile at neutron probe NP3, Equity

There were two obvious possible explanations for the consistently higher moisture content observed at NP3. The first explanation was that the difference was driven by differences in the radiation received by the soil in the area of NP3. As NP3 was located on a horizontal surface, the soil in the immediate area of this probe received less net radiation over the course of the year that was received at either of the other probes, which were both located on slopes with a southerly exposure. Other factors being equal, this should lead to less evaporation from the soil, and a higher overall moisture content. Differences in potential and actual evaporation with slope for the Equity site are quantified with the theoretical model in Section 8.0.

The second possible explanation for the higher moisture content at NP3 was that that being located on an approximately horizontal slope, the soil at NP3 was subject to a higher rate of infiltration than occurred at the more steeply sloped soil around NP1 and NP2. As indicated by the discussion of the literature on slope effects for infiltration and runoff (Appendix A) there is not a clear consensus on how variations in slope affect infiltration rate, assuming that there is a sufficient gradient to prevent ponding. Since there is a slight gradient at NP3, ponding was not likely to occur. In the context of models such as Vadose/W and SoilCover, where runoff is essentially function of precipitation in excess of infiltrative capacity, there should be little or no difference in the modeled infiltration rates at the two locations. In reality, the runoff rate may have been greater on the more steeply sloped region, but there does not appear to be a widely-accepted predictive model to quantify this difference.

The neutron probes NP4, NP5, and NP6 were all located on top of the main dump, with similar slopes and exposure conditions. Moisture profiles at all three locations were quite similar, with NP6 (Figure 7.22) being the wettest. The other profiles are included in Appendix D. There was a slight surface grade in this area (approximately 3%), with NP6 the neutron probe located furthest down-slope. This position may have impacted the moisture profile at this location.

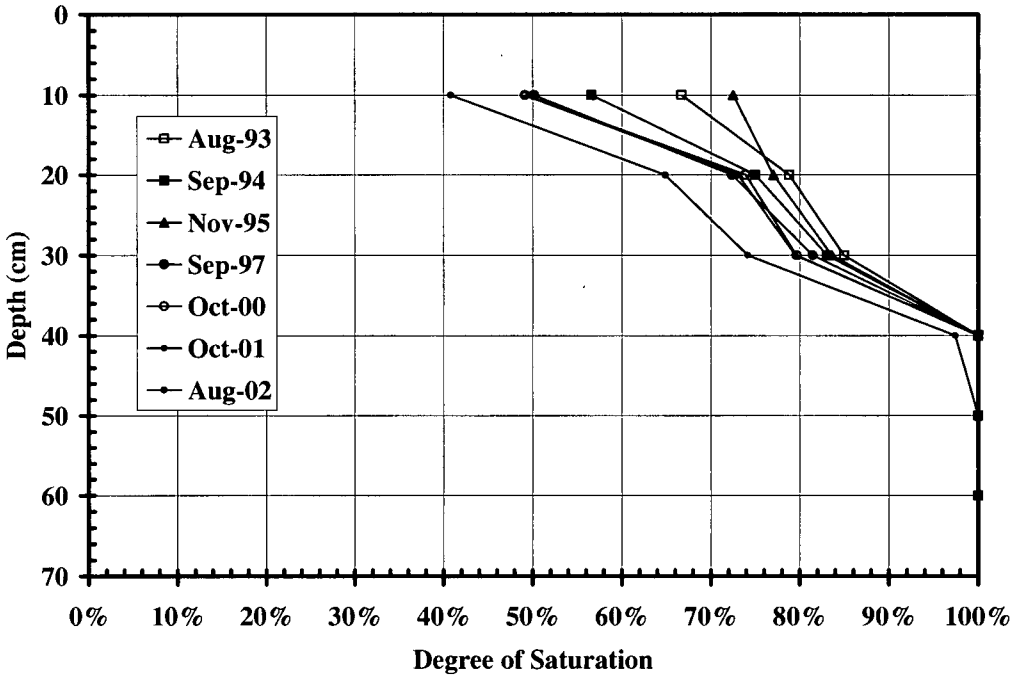

Figure 7.22: Soil moisture profile at neutron probe NP6, Equity

Neutron probes NP7 and NP8 were located quite close together, but NP7 was located well within the relatively flat area of the cover, while NP8 was located at the edge of the cover, near a 14% slope to the north. Moisture profiles differed between the two locations, as can be seen in a comparison of Figure 7.23 and Figure 7.24. At NP7, the degree of saturation in the near-surface profile was typically greater than at NP8. NP7

and NP8 had similar degrees of saturation near the base of the profile. The drier conditions observed at NP8 may have been a function of the greater lateral drainage through the sloped cover soils.

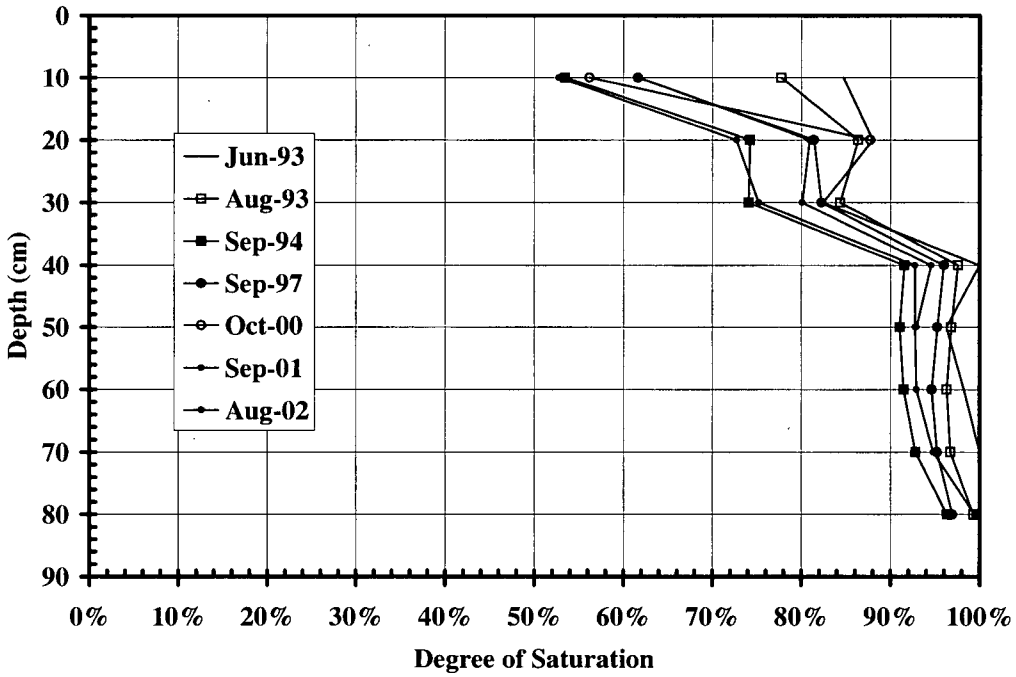

Figure 7.23: Soil moisture profile at neutron probe NP7, Equity

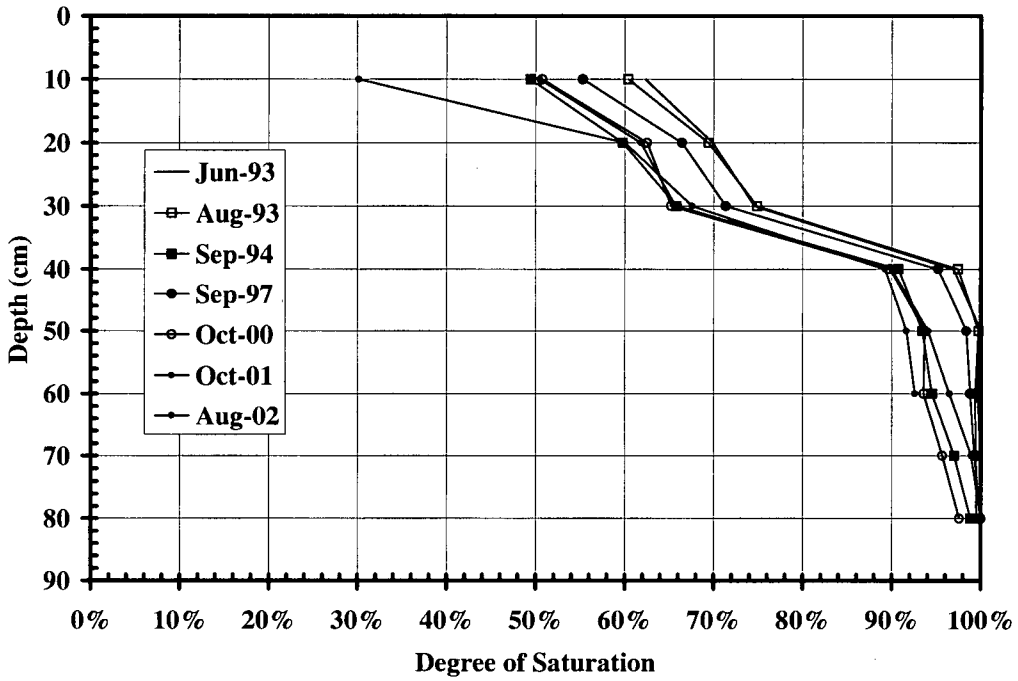

Figure 7.24: Soil moisture profile at neutron probe NP8, Equity

7.4 Summary of Data Analysis

The predictive model for net radiation has been evaluated by comparing the measured values of net radiation on slopes to the net radiation values that would be predicted by the model using the net radiation measured on a corresponding horizontal region. The results showed a very good correlation between measured and predicted values, and the quality of the correlation was confirmed through a statistical analysis of the model error.

To further evaluate the model, a sensitivity study was conducted. In this study, measured input parameters were varied in the range of values that might reasonably occur from errors in measurement, while estimated parameters were varied over their typical ranges. For the measured parameters, variations in the slope angle had the greatest impact; while for the estimated parameters, the results were most sensitive to errors albedo.

The verified net radiation model was coupled with the one-dimensional flux boundary modeling program SoilCover to predict evaporation from the microlysimeters. Using the models together allowed quite good approximations of evaporation rates from the microlysimeters, while final moisture profiles through the microlysimeters were only roughly approximated, most likely as a result of the limited ability to predict the unsaturated hydraulic conductivity function.

Spatial variations in moisture content over the Equity cover were quantified by neutron probe measurements, as presented in Section 7.3.

The model for net radiation on slopes has now been verified, as has its application in conjunction with a model for actual evaporation. The following chapter demonstrates how the model can be used to provide a better understanding of radiation and evaporation over a three-dimensional surface, and also provides applications for some hypothetical design cases.

8 Application of Predictive Model

A predictive model for net radiation on sloped surfaces has been developed and verified. The analysis of the field data presented thus far has suggested ways in which the net radiation model can be used in combination with evaporative models for the analysis of evaporation from sloped surfaces. In the following sections, the applications of the net radiation model will be considered in more detail, including the mapping of net radiation in three dimensions over a soil cover (Section 8.1), the prediction of actual evaporation on sloped surfaces under a variety of conditions (Section 8.2), and mapping potential evaporation over a three dimensional surface (Section 8.3). Certain special cases where actual evaporation can be approximately mapped in three dimensions are also considered (Section 8.4). Finally, some applications for obtaining practical design information with the coupled application of the radiation and evaporation models will be reviewed (Section 8.5).

8.1 Mapping Net Radiation in Three Dimensions

The net radiation model presented in this thesis provides a powerful tool for predicting variations in net radiation over a ground surface, based on limited climate data. The effects of slope on net radiation, for cases in the northern and southern hemisphere, are demonstrated in Section 8.1.1. In Section 8.1.2, this application is expanded to show the three-dimensional map of net radiation that can be generated using topographic site data and the net radiation model.

8.1.1 Slope Impacts on Net Radiation

A key application for the net radiation model is the prediction of how actual evaporation may vary over sloped surfaces, as a function of the variations that occur in net radiation over these same surfaces. Climate data collected at the Equity and Kidston sites were used to simulate the effect of slope on net radiation.

For the Equity site, climate data from 1998 (a typical year) was used in the net radiation model to illustrate the impact of slope angle on Q_{net}, as shown on Figure 8.1. The figure shows how the daily average of the annual net radiation was affected by varying the slope angle from 1:1 North-facing to 1:1 South-facing. Each data point was based on the averaged daily results from running the net radiation model for a full year's growing season for the given combination of slope and aspect. Note that in the context of evaporation from soils at Equity, a full year growing season refers to the period of time in

which there was no snow on the ground (non-freezing conditions). For the 1998 data shown, this was from approximately Julian day 108 to 306. Any slope in three-dimensional space could be evaluated. The slopes shown in Figure 8.1 were taken along a north-south axis to illustrate the most extreme effects of changes in slope. Note that the curve shown is asymmetrical, with increases in slope on the sunward side of the site having a less dramatic impact on net radiation than increases in slope on the far side. This is consistant with the known distribution of solar energy. Since the site is located at relatively high latitude (54° North), it was expected that there would be a considerable difference in the net radiation received by the sunward and shaded sides of the slope, as is shown on the figure.

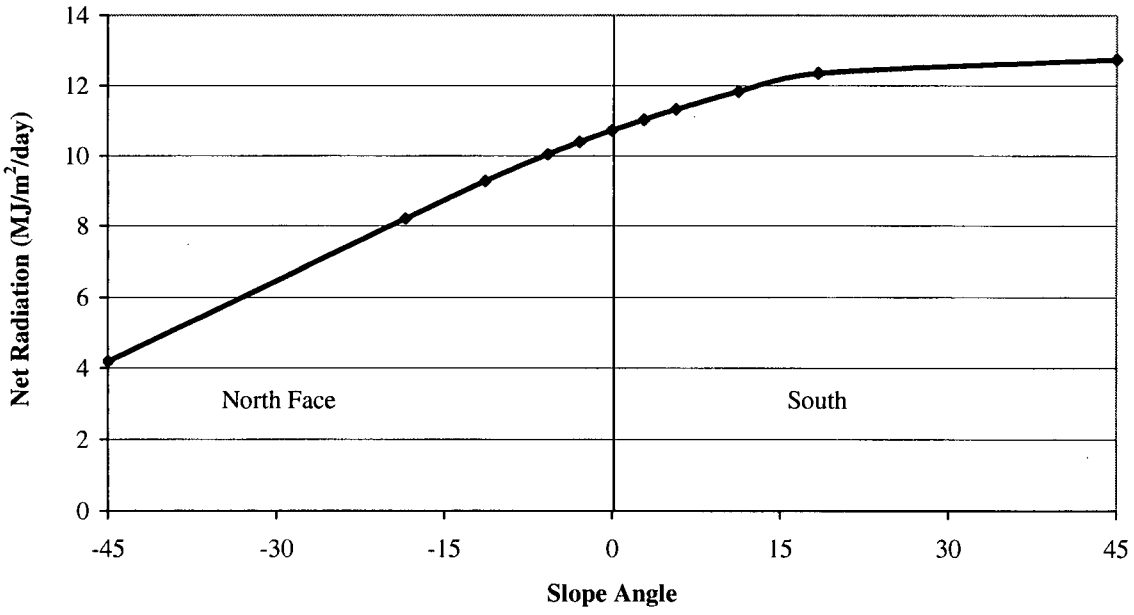

Figure 8.1: Effect of Cover Slope and Direction on Net Radiation at Equity Site (Based on 1998 Climate Data for Horizontal Surface)

Figure 8.2 shows the effect of slope on the predicted net radiation for the Kidston site, over the course of a full year (365 days in the case of Kidston). Note that at Equity, the peak net radiation occurred on the south-facing slopes, as would be expected for a site in the northern hemisphere, whereas at Kidston, the peak net radiation for the year occurred on a north-facing slope.

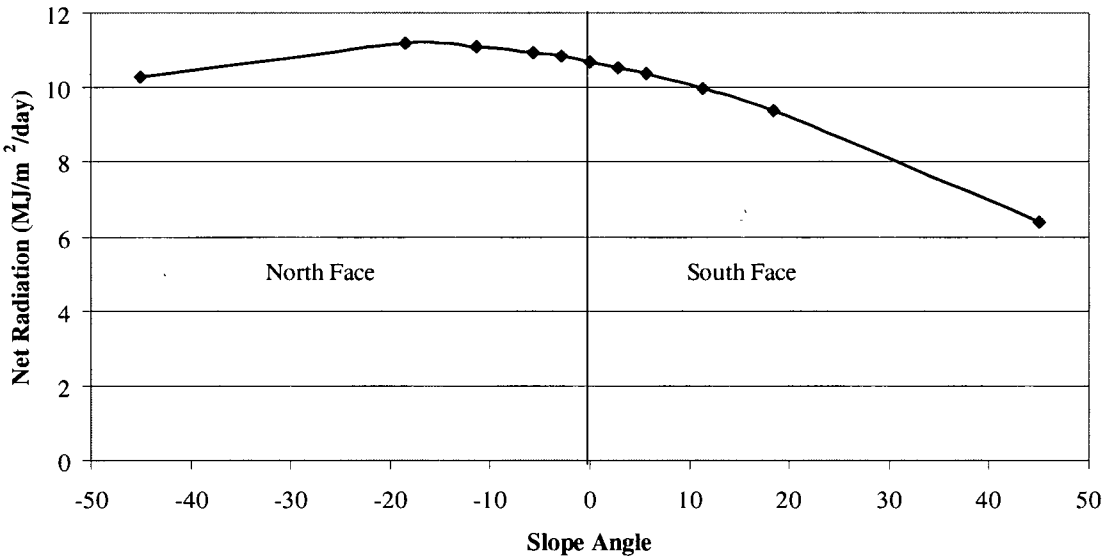

Figure 8.2: Variation in annual daily average net radiation at Kidston as a function of slope

For both sites, the curve created by the net radiation/slope relationship was asymmetrical. Increases of slope on the sunward side of the site had a less dramatic effect on the net radiation than increases of slope on the shaded side. Also note that for the site at a higher latitude (Equity) the impact of slope on the daily net radiation was generally greater than that found on radiation at a more moderate latitude (Kidston). For the Kidston site, there

was a point where increases in slope to the north (within the range of slopes evaluated) actually began to diminish the Q_{net} received over the year.

8.1.2 Net Radiation on a 3D Surface

As discussed in Section 5.3, topographic data was collected for the Equity site, and used to construct a three-dimensional topographic surface that represented the dumps at the site and the surrounding area. Using the net radiation model in conjunction with the topographic data, it was possible to map predicted net radiation for the entire surface in 3D space. The program used to combine the net radiation model with the topographic data was described in Section 4.1.4, with the program code included in Appendix C.

Figure 8.3 shows a colour contour plot of net radiation over the Equity site 3D mesh. Net radiation contours are shown in terms of average daily net radiation in $MJ/m^2/day$. The same 1998 climate data set that was used for Equity in Section 8.1.1 was used in the preparation of this plot. The colour contours illustrate the variation in annual net radiation over the entire dump, providing a more detailed view of the trend that was evident in Section 8.1.1, with more net radiation received over the year by the south facing slopes, and less on the more northerly-oriented ones.

Figure 8.4 shows the net radiation pattern over the site on Julian Day 211 (July 30, 1998) of the data set. On this day, the daily net radiation distribution was quite similar to the annual average shown on Figure 8.3. This contrasts with the distribution shown on

Figure 8.5 for Julian day 216 (August 4, 1998). On this day, the total measured net radiation was much less, corresponding to a much more overcast day. As a result of the overcast conditions, beam shortwave radiation to the site was minimized, which in turn minimized the differences in net radiation between the different slopes. Net radiation maps for additional selected single days in this data set are presented in Appendix F. The detailed net radiation data represented by these colour maps can be used for the calculation of evaporation over complex surfaces, as will be discussed in Section 8.2.

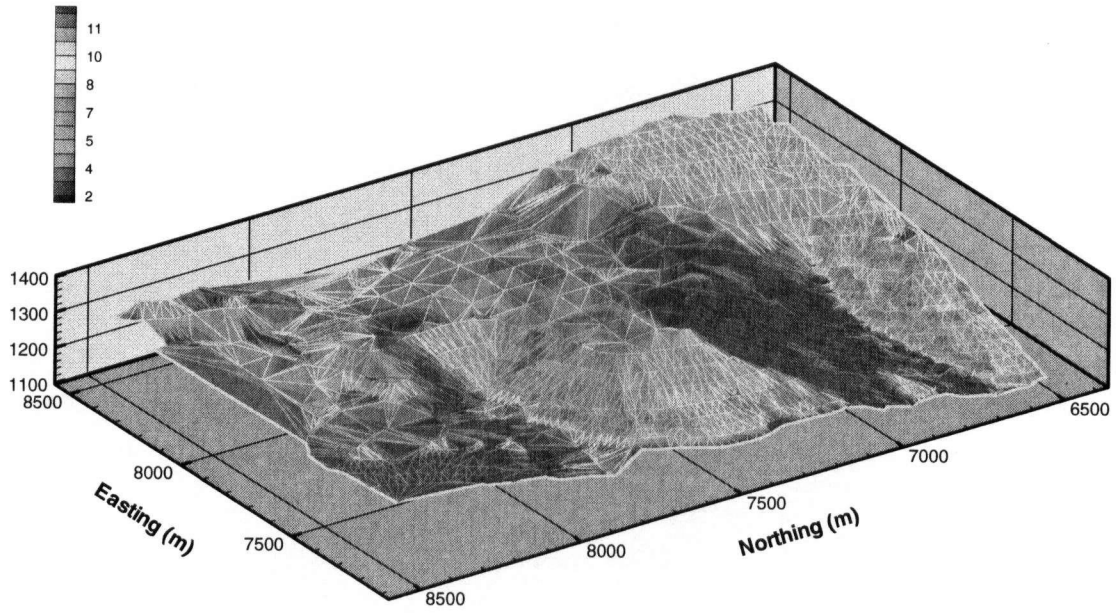

Figure 8.3: Variation in Average Daily Net Radiation over the Topography of the Equity Site (Based on 1998 Climate Data for Horizontal Surface). Contour Intervals shown in $MJ/m^2/day$.

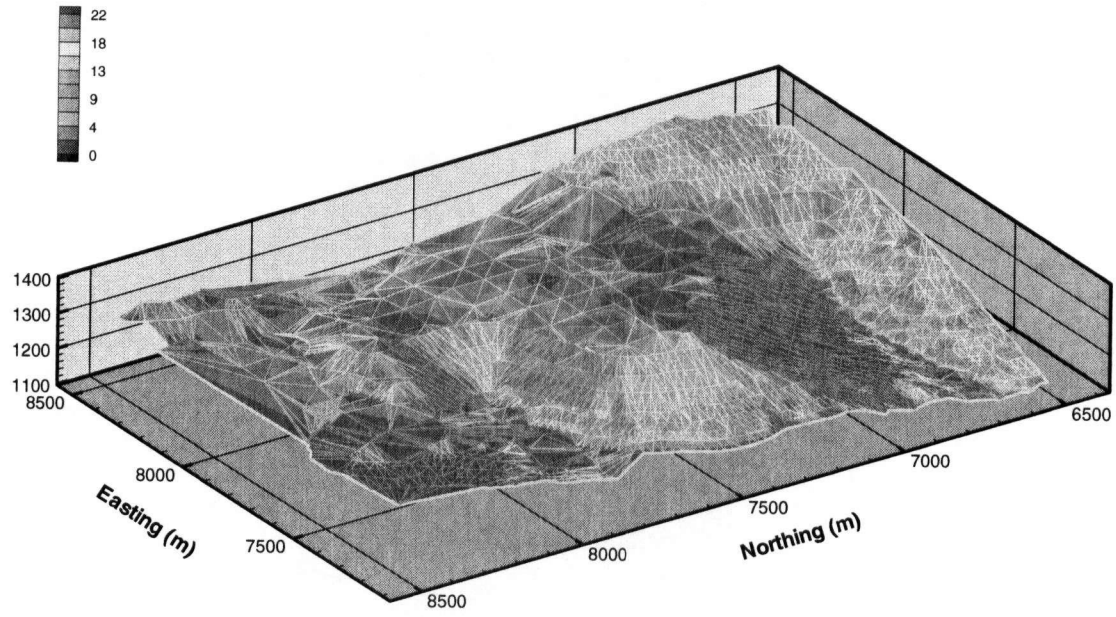

Figure 8.4: Variation in Daily Net Radiation over the Topography of the Equity Site for Julian day 211 (July 30, 1998). Contour Intervals shown in MJ/m^2/day.

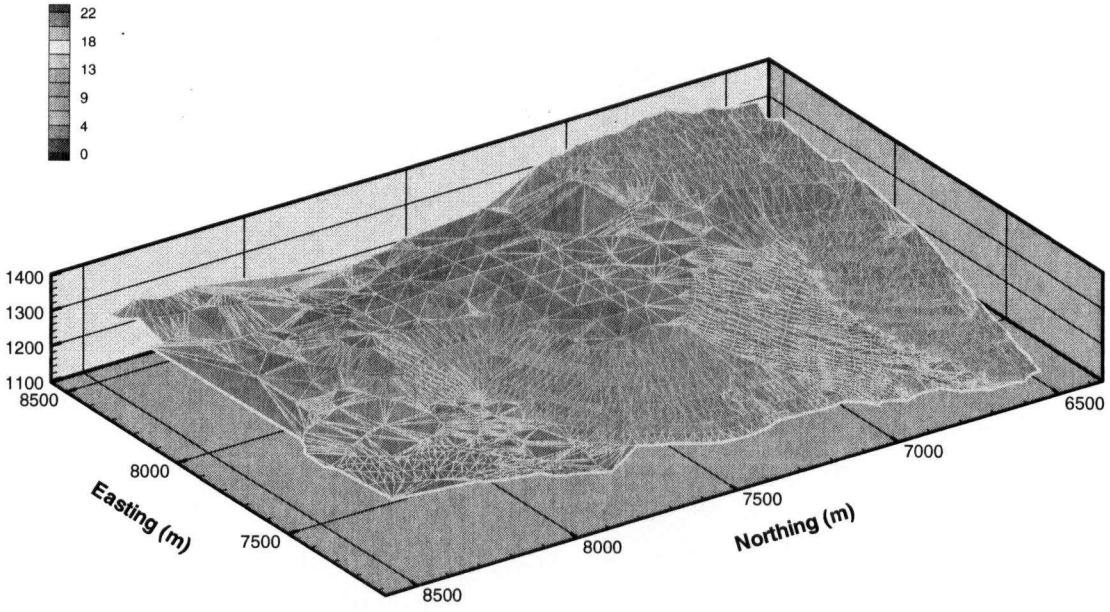

Figure 8.5: Variation in Daily Net Radiation over the Topography of the Equity Site for Julian day 216 (August 4, 1998). Contour Intervals shown in MJ/m^2/day.

8.2 Actual Evaporation Prediction on Slopes

The net radiation model can be combined with existing models for the prediction of actual evaporation to provide predictions of the effect that slope will have on actual evaporation. In Section 8.2.1, a one-dimensional model for actual evaporation was coupled with the net radiation model, to illustrate in simple terms the effect that changes of radiation with slope will have on actual evaporation for different sites. In Section 8.2.2, the effect of latitude on the net radiation model was used to illustrate differences in the sensitivity of actual evaporation to latitude. In Section 8.2.3, a commonly used and commercially available two-dimensional model for actual evaporation is incorporated with the net radiation model, to illustrate the effect of slope direction on evaporation for a fully two-dimensional case, giving particular attention to the effect of two-dimensional variations in moisture distribution on actual evaporation.

The potential evaporation rate for free water, saturated soil surfaces and well-watered plant canopies generally represents the maximum rate of evaporation and evapotranspiration that can take place, and is most strongly influenced by energy availability (net radiation). Alternatively, the evaporation rate from a bare soil surface, while approximately equal to potential evaporation when water is freely available, is often water limited and typically represents the lower limit of actual evaporation. Evaporation is therefore evaluated in terms of potential evaporation (the energy limited case) and actual evaporation from bare soil surfaces for the water limited case.

8.2.1 Impact of Slope Orientation and Angle on AE

To illustrate the degree to which slope angle and orientation can affect evaporation rates from soil covers, the Q_{net} values calculated for sloped surfaces in Section 8.1.1 with the net radiation model were used as inputs in potential evaporation (PE) and actual evaporation (AE) calculations. These calculations required climate and soils data for the sites evaluated. The calculation of actual evaporation for these sites with the modified Penman Equation (Wilson 1990) required solution of the coupled heat and mass transfer equations, as discussion in Section 2.2.1.2 of this thesis. This was done with the program SoilCover (Unsaturated Soils Group, 1993).

To illustrate the effects of slope on actual evaporation, fluxes were calculated for a soil column based on the cover profile at the site under consideration, with energy input varied as a function of slope and aspect. Initial moisture conditions were constant for the various slope/aspect configurations modeled. At the Equity site, the cover profile was modeled with pressure = 0 kPa set as the boundary condition at the lower limit of the cover profile, to simulate the saturated conditions that were typically observed at the base of the cover profile in the field. This was intended as a simplified approximation to actual conditions, for the purpose of illustrating the impact of radiation changes in isolation. For actual site conditions, variations in soil moisture content with topography were likely to have been significant, as will be discussed in Section 8.2.3.

The Equity cover profile was modeled in SoilCover as a 0.3 m thick layer of uncompacted till, underlain by a 0.5 m thick layer of compacted till, as per the cover design. Material properties for the till layers in the model were as discussed in Section 5.7.2. Daily values of Q_{net} used as input for each run of the model were calculated with the radiation model, based on the slope angle and direction under consideration, as well as the local climatic data. A similar approach was used for the Kidston cover, with material properties as discussed in Section 5.7.1, and a cover profile consisting of 1.5 m of the uncompacted oxidized waste rock, over 0.5 m of the compacted oxidized waste rock.

Vegetation effects were not included in the SoilCover analyses. For the water balance of real cover systems, plant transpiration is an important component. Plant transpiration can be expected to increase the total evaporation from the cover above what would take place without vegetation. However, vegetation effects were not included for the present study in order to model the simplest possible case for actual evaporation from sloping soils. Further, by predicting potential and actual evaporation for a non-vegetated soil surface, the two extremes of moisture-limited and soil-limited evaporation were illustrated. Potential evaporation calculations illustrated the amount of evaporation that would take place if the moisture supply at the soil surface was unlimited. Actual evaporation calculated from the bare soil illustrated the case of maximum evaporation suppression due to moisture-limited conditions at the soil surface. Transpiration by surface vegetation can be expected to increase total evapotranspiration above what would be expected from bare soil to some level closer to potential evaporation. Vegetation is an

important component of soil cover systems, and the performance of an actual soil cover is heavily influenced by the type and quality of vegetation, but is not evaluated herein.

Figure 8.6 shows the potential evaporation rates calculated for the Equity site as a function of slope, as well as the actual evaporation rates calculated in SoilCover. All evaporation totals are given for the part of the year in which there was no snow on the ground, as in the radiation analysis.

As shown on Figure 8.6, the calculated value of PE can vary dramatically as a function of slope. For the steepest slopes shown (45 degree, or 1H:1V), potential evaporation more than doubled from the north-facing slope (330 mm) to the extreme south-facing slope (730 mm). Even the more moderate slopes (18 degree, or 3H:1V) showed over a 30% difference in PE between the north and south-facing slopes, from 520 mm to 715 mm.

For all slopes the annual actual evaporation was considerably less than the potential, reflecting the impact of limited moisture availability on evaporation. There was still clearly however an impact of slope on the calculated AE. For the extreme (1H:1V) slopes, AE on the south facing slope was more than 75% greater than evaporation on the north facing slope (310 mm on the south face, versus 174 on the north).

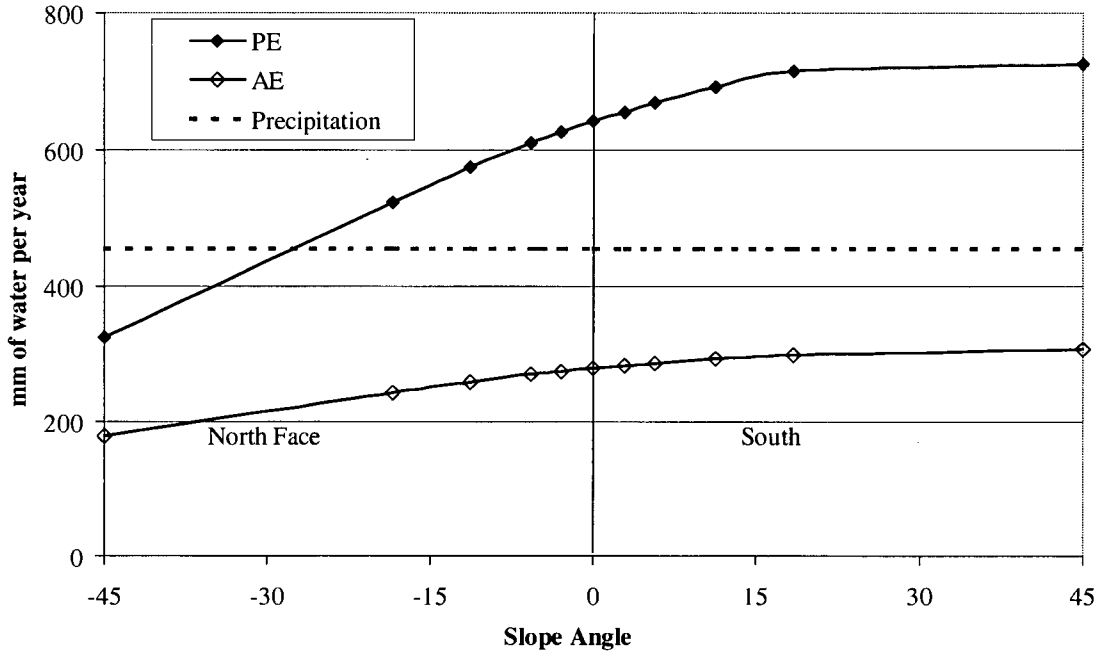

Figure 8.6: Effect of Cover Slope and Direction on Potential and Actual Evaporation at Equity Site (Based on 1998 Climate Data for Horizontal Surface)

Figure 8.7 illustrates the impact of slope on annual average potential and actual evaporation for the Kidston site. As can be seen on the Figure, potential evaporation is still significantly affected by the variations in net radiation, while the effect on actual evaporation at this site is much smaller. Potential evaporation was not as greatly affected by slope at Kidston as it was at Equity, which was expected for a site located at a more moderate latitude. The total amount of potential evaporation at Kidston for all slopes was much greater, as a function of the hotter, drier climate.

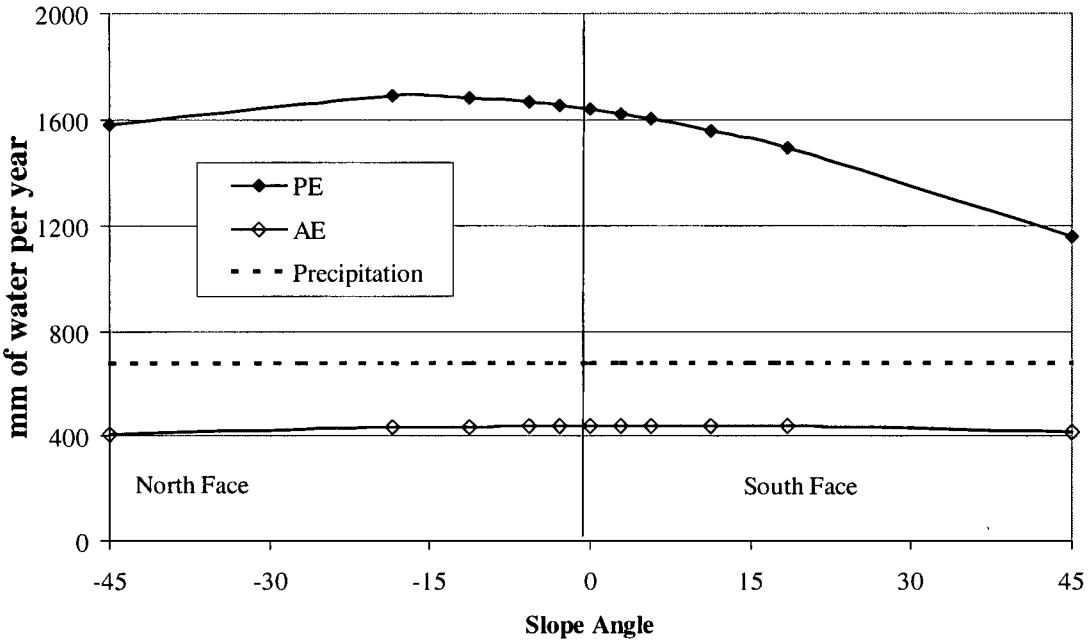

Figure 8.7: Effect of slope on calculated evaporation at Kidston

For both sites, the annual actual evaporation was considerably less than the potential. This was expected, as limited moisture availability in the soils typically results in AE that is less than PE. At the Equity site, there was still clearly an impact of slope on AE. For the extreme (1H:1V) slopes, AE on the south facing slope was more than 75% greater than evaporation on the north facing slope.

At Kidston, there was almost no impact of slope on AE. This was attributed to the fact that site was located in an extremely arid region, where on an annual basis, the potential evaporation greatly exceeded the moisture availability. As a result, surface soils spent much of the year with low moisture conditions. In such conditions, there is relatively little moisture for the soil to give up to the atmosphere, and variations in the moisture demand over a comparatively small range (represented by variations in Q_{net} or in the

potential evaporation) have little impact on the limited amount of moisture that is available for evaporation. Evaporation at such a site can be considered moisture limited, rather than energy limited. This suggests that at arid sites, variations in Q_{net} with slope may be less important on an annual basis than at more humid sites, where evaporation is more energy limited. At energy limited sites, the variations in Q_{net} with slope have a larger impact on actual evaporation.

8.2.2 Impact of Latitude and Climate on AE

For sites that are located at high latitude (either far south or far north), the sun is typically lower in the sky. As a result, the difference in energy interception between north and south slopes tends to be more dramatic. As one considers locations closer to the equator, the position of the sun in the sky is closer to directly overhead, and the importance of slope direction along the north-south axis is lessened. The sensitivity of slope/evaporation relationship to latitude is illustrated in Table 8.1. This table summarizes the values of PE and AE on opposing 3H:1V (18°) slopes that were calculated using the Equity data, but transforming radiation data for slope effects as if the data as had been collected at sites with a lower latitude. As shown on the table, the difference between north and south slope evaporation increase dramatically with increasing latitude. The difference in annual potential evaporation between north and south facing slopes was over 190 mm at a latitude of 54°N, compared to almost no difference at a latitude of 30°N. Similarly, for actual evaporation, the difference at 54°N

was 57 mm, with almost no difference in the predicted actual evaporation at 30°N. This suggested that while the effect of slope on evaporation rates can be important at high latitudes, the effects may be negligible closer to the equator.

Table 8.1: Sensitivity of potential evaporation to site latitude for a 3H:1V slope

Site Latitude	Potential Evaporation (mm/year)		Actual Evaporation (mm/year)	
	North Face	South Face	North Face	South Face
54°N	523	714	242	299
45°N	577	659	267	282
30°N	617	619	274	276

8.2.3 Impact of Slope Moisture Distribution on AE

To this point, the net radiation model has been coupled with SoilCover, a one-dimensional model for actual evaporation. To evaluate the impact of a sloped surface on evaporation, the two-dimensional model Vadose/W (GeoSlope, 2001) was coupled with the net radiation model. By coupling the net radiation model with the two-dimensional evaporation model, information about the direction faced by the slope is processed together with the slope geometry, opening the door to a pseudo-three-dimensional analysis approach. Vadose/W is a commonly used commercial software package for the modeling and design of soil covers. The approach shown in this section illustrates how the net radiation model can be incorporated with existing software that uses net radiation as an input.

For the evaluation of slope effects on cover evaporation, a simple finite element mesh was constructed in Vadose/W, representing a 2.5H:1V slope, with a horizontal length of 25 m and a height of 10 m. The mesh is shown in Figure 8.8. The slope was covered with a cover layer of the uncompacted Equity till, placed 80 cm deep. The waste rock was represented with the hydraulic properties of Beaver Creek sand (Wilson, 1990), an approach that was used by Swanson (1995). The 10-year averages for the Equity climate data set (1994-2003) were used as the climate boundary for the model. The water table was set as a boundary condition 1 m below the toe elevation of the slope. Note that this case represents a hypothetical case to illustrate the model, and is not intended to represent the cover at the Equity site. For initial moisture conditions in the model, an initial water table was set with negative porewater pressures above the water table limited to 12 kPa (the suction at residual water content in the waste rock). This initial condition is more realistic than hydrostatic conditions for making initial moisture content profile through the model space that would be representative of long-term average conditions. Following the rational outlined in Section 8.2.1, vegetation effects were not considered in this model of a soil cover. Vegetation would be expected to significantly enhance actual evaporation taking place from the cover.

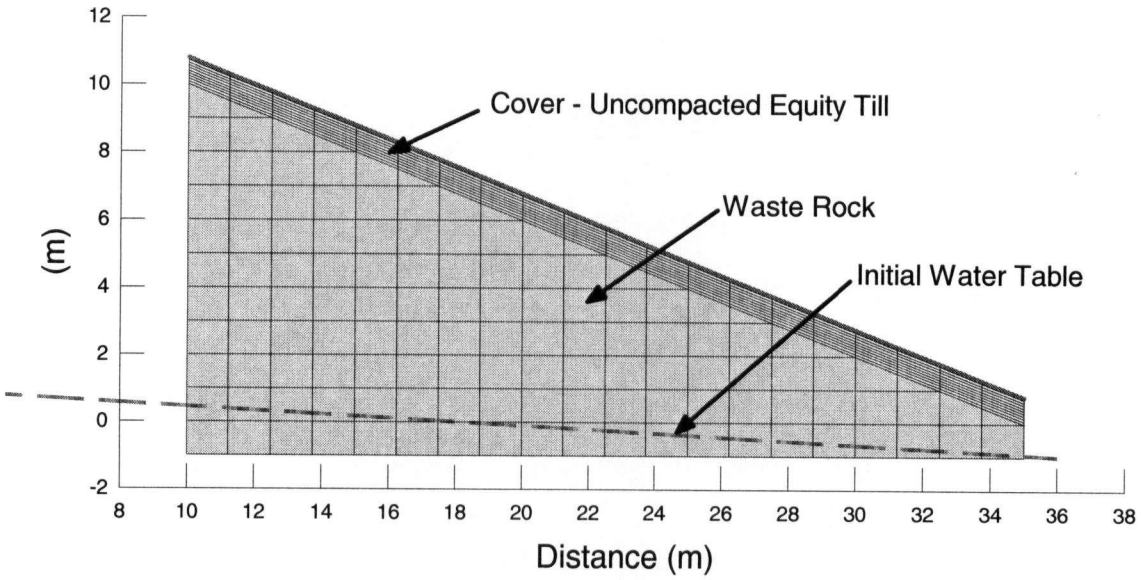

Figure 8.8: Finite element mesh use for the analysis of slope effects

To evaluate north and south facing slopes, the net radiation values in the climate data set were modified with the net radiation model, based on the slope angle, latitude, and daily measured values of temperature and net radiation. Following this approach, the model showed slightly better performance (in terms of infiltration) by the south facing cover, with an annual net infiltration through the cover of 1.81 m^3 (approximately 72 mm), compared to an infiltration of 2.11 m^3 (84 mm) through the north-facing cover.

For the north and south facing slopes, potential evaporation rates were uniform along the length of each slope, equal to 505 mm over the year on the south facing slope, and 445 mm per year on the north-facing slope (a 60 mm difference). Figure 8.9 shows the actual evaporation rates that were predicted along each slope for this base case. The average rate of actual evaporation on the south-facing slope was 373 mm, compared to 342 mm

per year on the north-facing slope, a 31 mm difference. As expected, the higher evaporation rate was found on the south-facing slope, which received more net radiation. For comparison, a 'horizontal' case is also shown on Figure 8.9, illustrating the results obtained if net radiation values as measured on a horizontal surface were used in the model.

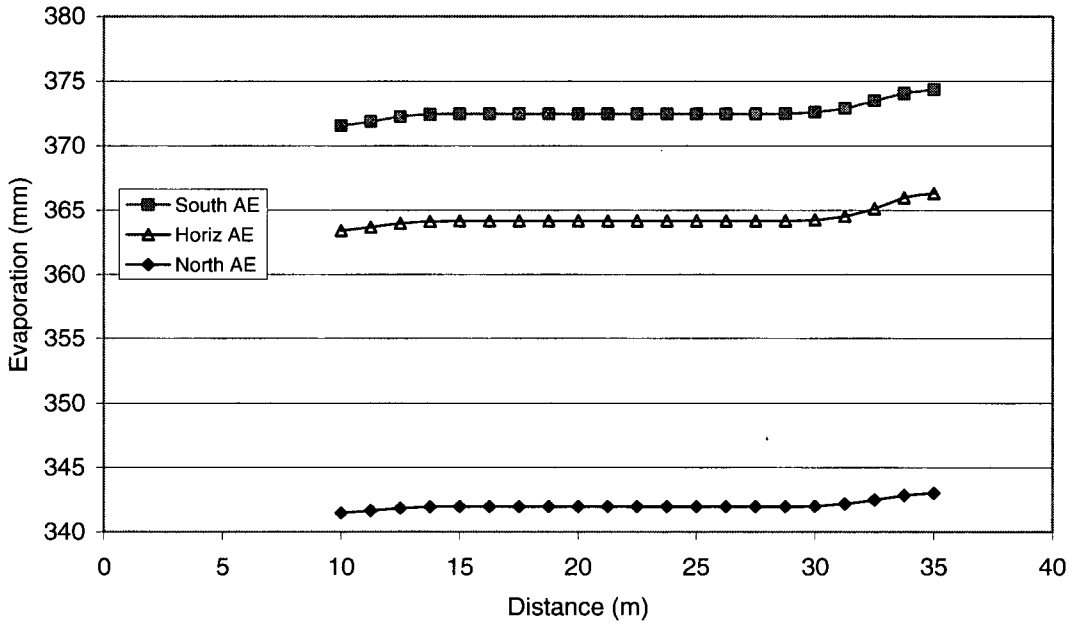

Figure 8.9: Actual evaporation total at the end of simulation for the year modeled along slope for base case (crest of slope located at distance = 10 m)

Figure 8.9 also shows that the total actual evaporation predicted was not uniform along the length of the slope. Near the toe of the slope the rate of evaporation was slightly higher than it was at the crest. This was likely a function of slightly higher moisture contents at the toe. Since soils at the toe were not as high above the water table, there would have been a greater availability of water to evaporate from the soils near the toe. As shown on Figure 8.9, the difference between the evaporation rate at the toe and at the crest was quite small (a 1.5 mm difference on the north face, and a 2.8 mm difference on

the south face). This suggested that for the particular case modeled, the impact of slope on moisture content and water content was not great. In this case differences between the north and south faces were far greater than differences between the crest and the toe. This finding should not however be generalized, as there could be alternative configurations (with different soil properties or water table position) where the impact of slope position on evaporation rate would be greater.

To examine the impact of slope position on moisture content, the modeled volumetric water contents were plotted for nodes located near the crest and near the toe of each slope. At each location, nodes in the cover were evaluated at ground surfaces, at the interface between the cover and the underlying waste rock, and at mid-elevation in the cover between these two points. The results of these evaluations confirmed that water contents at the near-surface nodes were more variable than water contents at the deeper nodes, and that water contents tended to be higher at the toe and at the north face.

Figure 8.10 shows the variations over the course of the year modeled for water contents in all surface nodes. As shown on Figure 8.10, water contents were generally higher on the north side of the slope than the south, as a function of higher evaporation rates on the southern face. This difference was most evident in the latter portion of the year. One can also discern on Figure 8.10 that for both the north and south slope, water contents were slightly higher throughout the year at the toe than at the crest, but that the magnitude of these elevation-induced differences was far less than the magnitude of the slope direction induced differences.

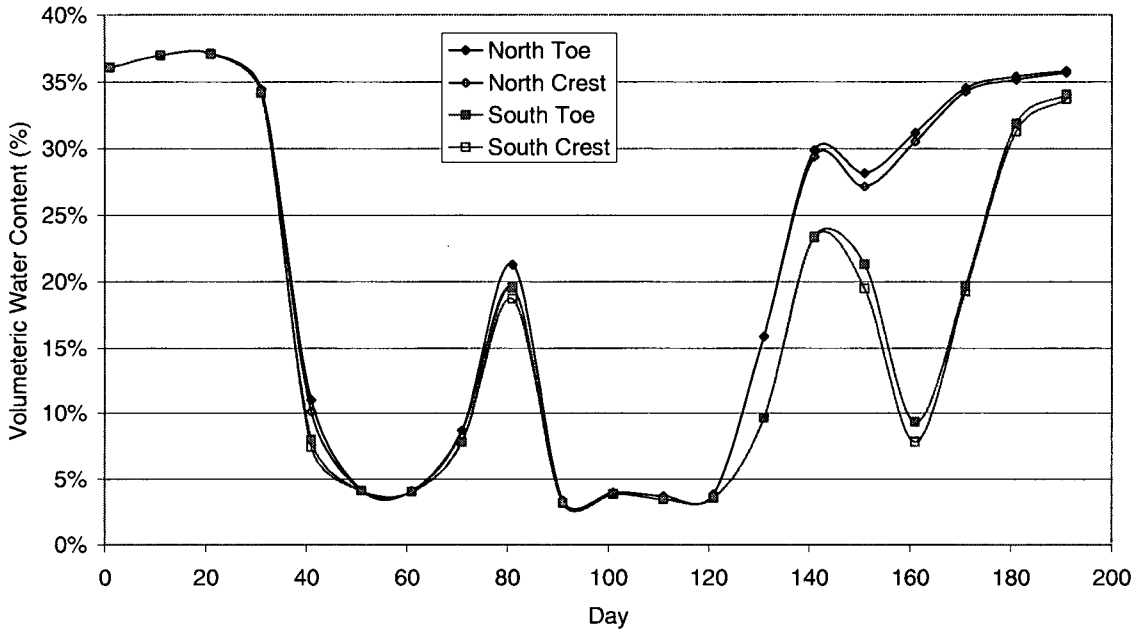

Figure 8.10: Water content variations in nodes at ground surface near toe and near crest of slope

Figure 8.11 shows similar trends for the variation of water content in nodes located at mid-elevation in the soil cover (approximately 40 cm deep). In this case, higher moisture contents again occurred on north face, and at the toe, although the degree of impact is more similar for the two different causes.

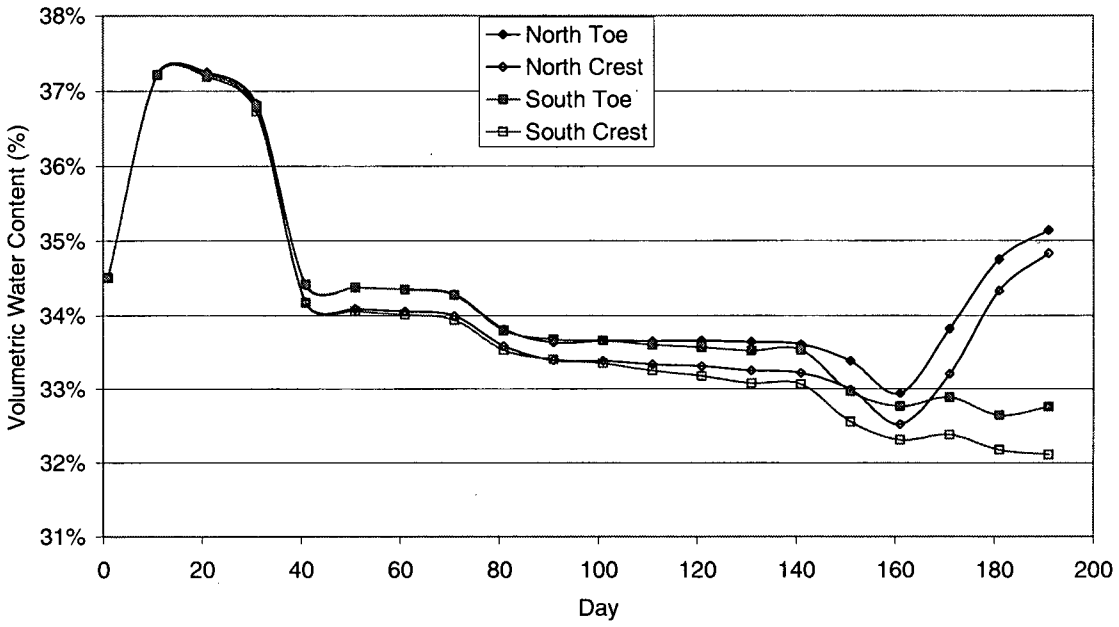

Figure 8.11: Water content variations in mid-cover nodes (40 cm below ground surface)

Figure 8.12 shows the change over time for water contents in the nodes located at the interface between the cover soil and the waste rock. Interestingly, in this case, the impact of location (toe versus crest) was greater on the water content than the direction faced by the slope (north versus south). This was a reversal of the trend at the surface shown in Figure 8.10, and suggested that near the ground surface, the direction faced by the slope had the larger impact on water content, while at depth this impact was muted, and position on the slope (or height above water table) was the more important effect. This trend would likely be affected by factors such as variations in soil properties and climate.

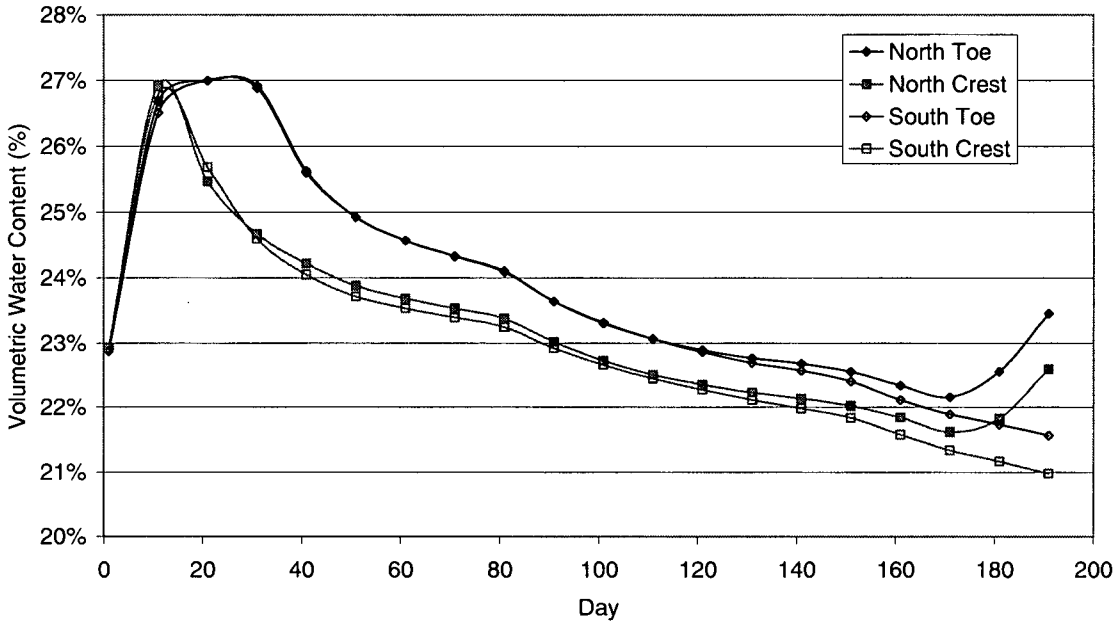

Figure 8.12: Water content variations in nodes at cover/waste interface (80 cm below ground surface)

Figure 8.13 shows the variation in water content for all nodes at the toe of the soil cover. This illustrated that the water content in the near surface nodes underwent a much greater degree of variation in moisture than the nodes located at depth.

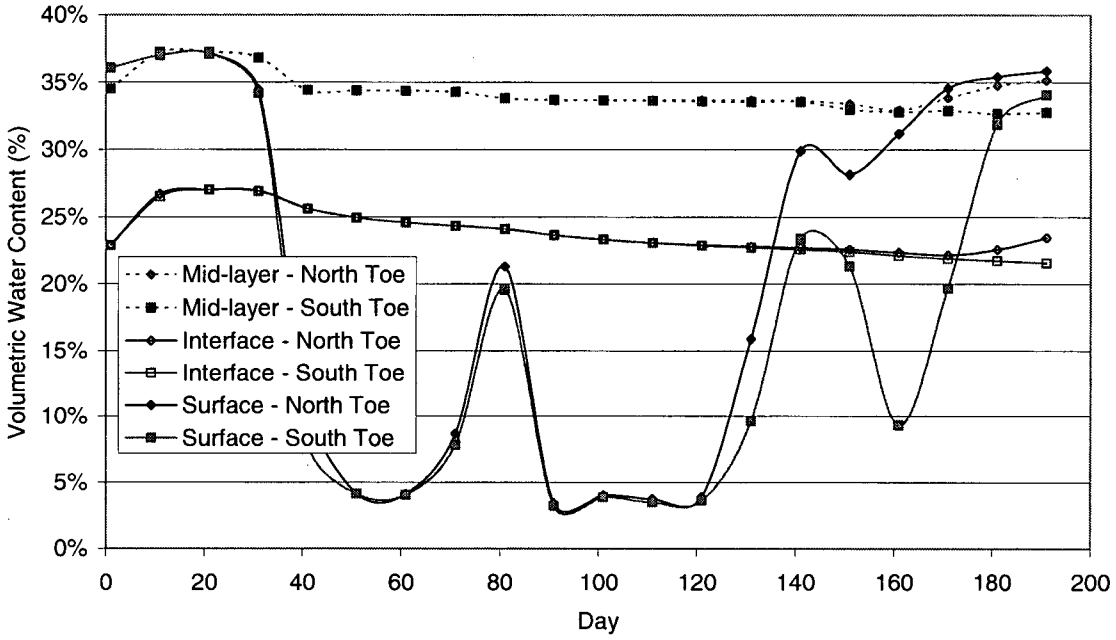

Figure 8.13: Water content variations at surface, mid-layer and interface nodes at toe of cover

To further investigate the effect of slope position on evaporation rates, the base case shown in Figure 8.8 was modified with a slightly elevated water table (raised by two meters), causing the water table to intercept the toe of the cover at the extreme right-hand side of the model space. The impact on actual evaporation rates for this slight change in water table is illustrated in Figure 8.14, which shows the actual evaporation predicted along the slope for the higher water table case, compared to the actual evaporations predicted with the base-case scenario (originally presented in Figure 8.9). As shown on Figure 8.14, the actual evaporation rate on the upslope area is quite similar in both cases. Near the toe however, there is a dramatic rise in the actual evaporation rate, which in the case of the north slope becomes approximately equal to the potential evaporation rate on the north face (445 mm) for the lower meter of the slope (the nodes illustrated on Figure 8.14 at distance = 34 m are located approximately 40 cm above the water table). On the

south face, evaporation at the toe of the slope does not quite reach potential evaporation rates (505 mm).

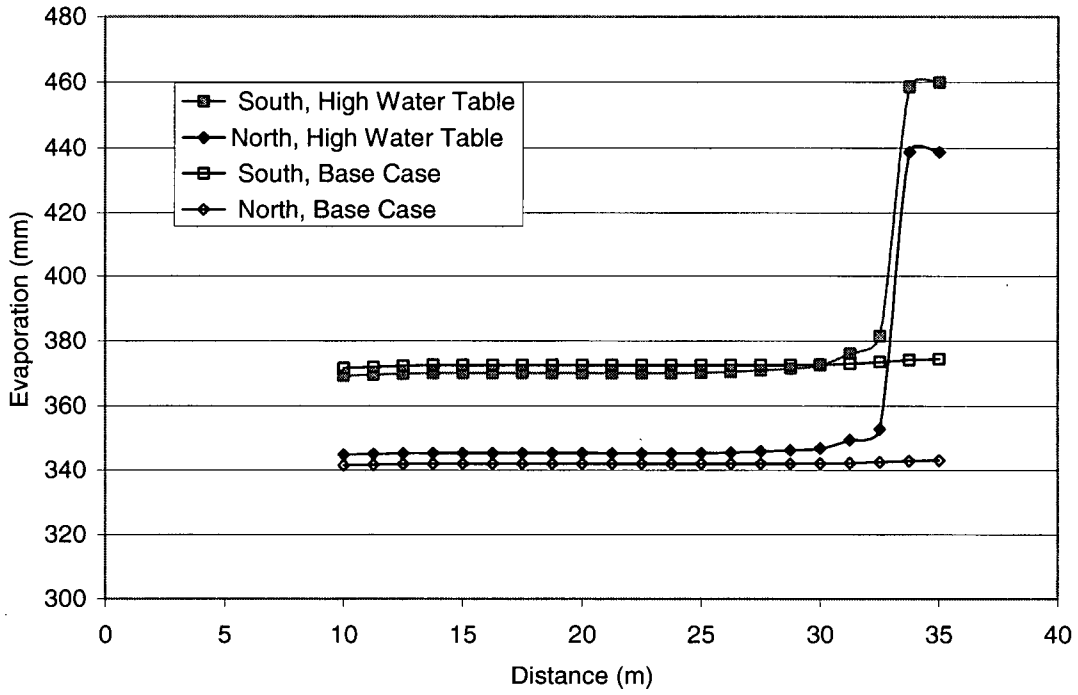

Figure 8.14: Comparisons of annual actual evaporation rates along the slope for the original case and the high water table case

To further evaluate the impact of slope on a soil cover, the cover profile shown in Figure 8.8 was modified to more closely represent the cover at Equity. The mono-layer cover was replace with a two-layer cover (50 cm of compacted Equity till, overlain by 30 cm of loosely placed till). This configuration reduced the flux through the cover from the 1.8 and 2.1 m^3 previously predicted for south and north face of the 80 cm uncompacted profile, to 0.15 m^3 on both faces (approximately 6 mm). Interestingly, introducing the compacted layer not only dramatically reduced infiltration (as expected) it also virtually eliminated the difference between the faces in terms of infiltration. Figure 8.15 shows the flux through the base of the cover over time for both slopes, as well as the flux

through the base of the loose layer. While there was virtually no difference between the flux values predicted for the base of the cover, one can see flux through the base of the loose layer are differentiated slightly, with less infiltration flux through loose layer on the southern face (more negative numbers indicate greater infiltration through the base of the layer under consideration.

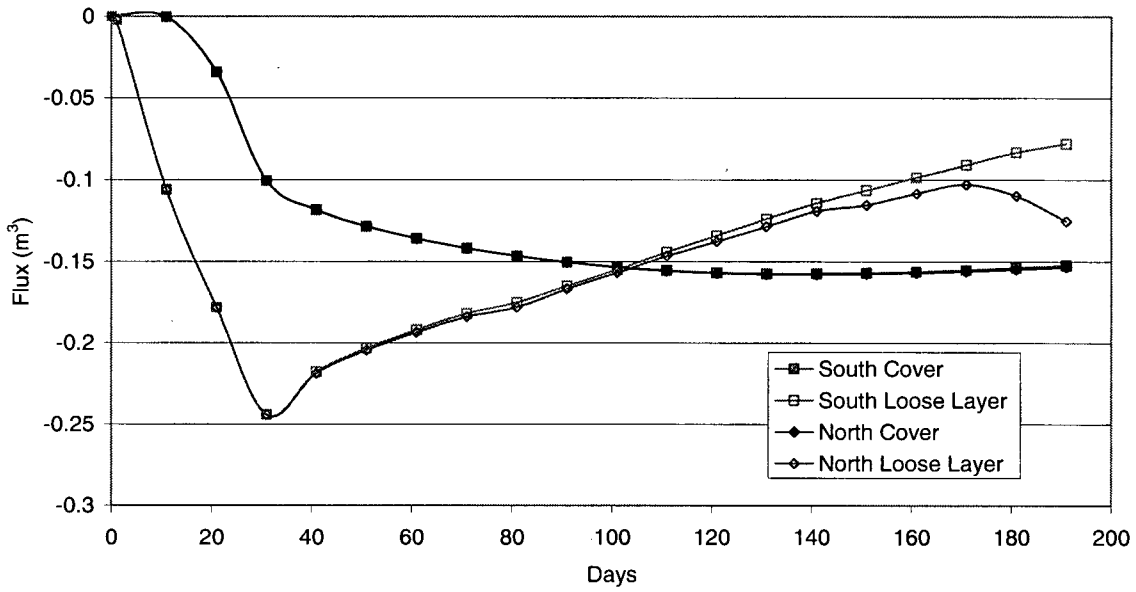

Figure 8.15: Total flux in model of water through base of total cover (loose layer over compacted layer) and total flux through the base of loose layer only

Figure 8.16 shows that there was still a considerable difference between the slopes for actual evaporation, depending on the direction of cover exposure. On the north face, the average actual evaporation was 340 mm, and average actual evaporation along the south face was 366 mm. This was slightly less than the actual evaporation that took place over the same faces for the fully uncompacted cover (365 mm north and 372 mm south). Figure 8.16 also shows that there was a slight impact of slope position on actual evaporation, with more evaporation taking place at the toe of the slope than at the crest.

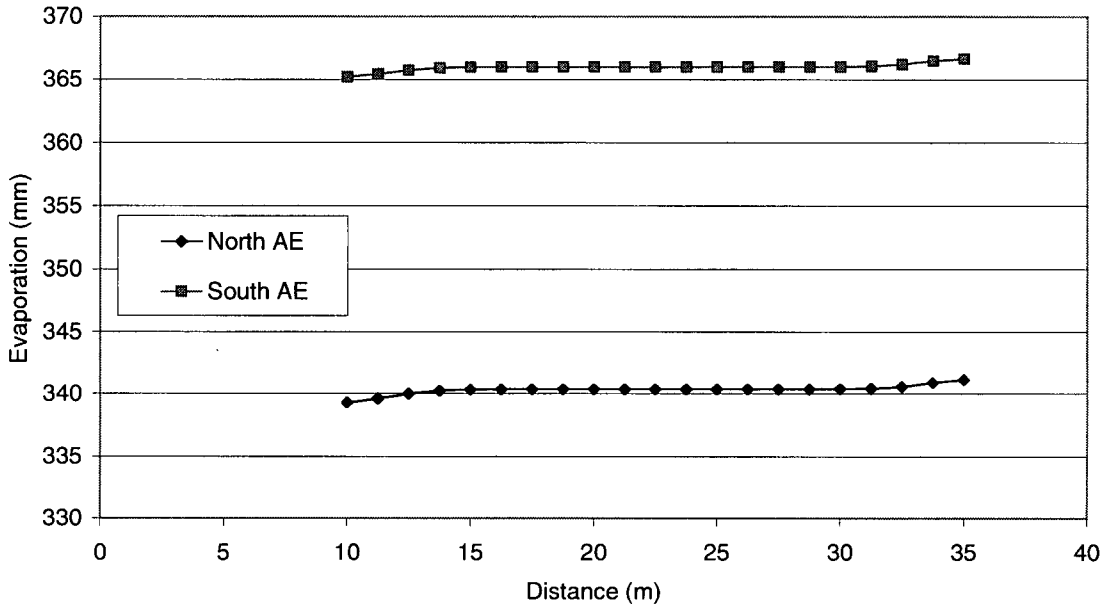

Figure 8.16: Actual evaporation rate along slope for the two-layer cover (crest of slope located at distance = 10 m)

The water content of the two layer cover was in general more stable than the water content of the mono-layer cover. Near the surface, in the uncompacted till, the water content was still subject to significant variations as a result of climate. At depth, the water content was far less variable. Figure 8.17 shows the degree of saturation in nodes located near the base of the cover (approximately 5 cm above the cover/waste interfaces). At all locations, a high degree of saturation (97 % or higher) was maintained throughout the year, with little impact on the water content as a function of season, or location on the slope. This was good performance for a cover intended as an oxygen barrier.

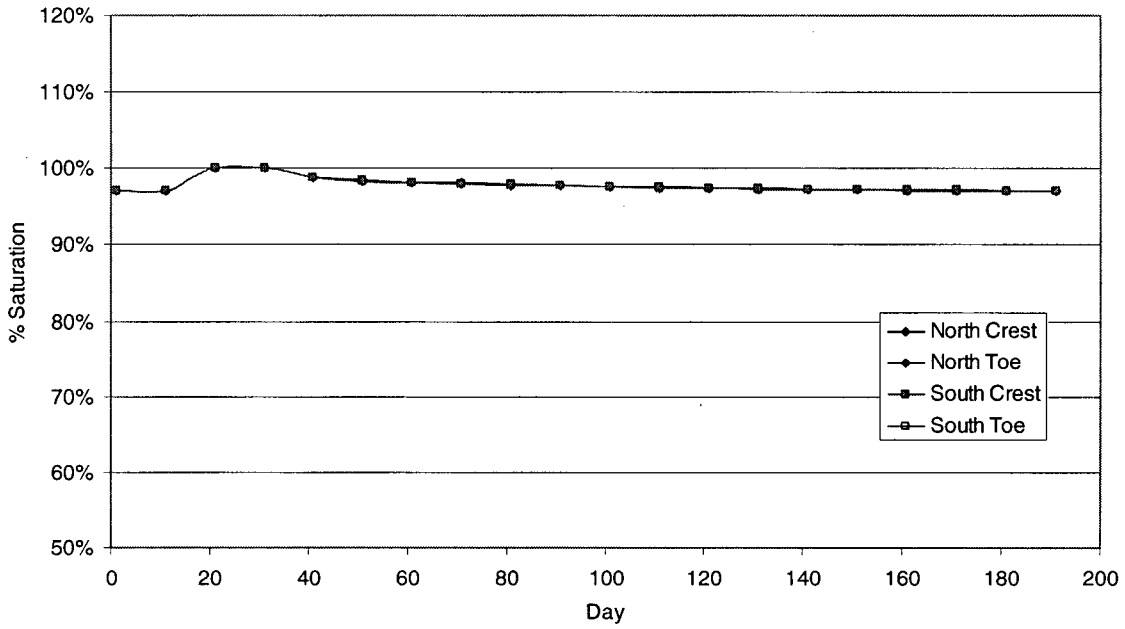

Figure 8.17: Degree of saturation maintained in cover 5 cm above the soil/waste interface

8.3 Mapping PE in Three Dimensions

As shown in Section 8.1.2, the net radiation model can be combined with topographic data and climate data to develop three-dimensional maps of net radiation over a given surface. Where the needed additional climate data is available, this approach can be extended to generate maps of potential evaporation over the surface, based on the variation in net radiation modeled. As discussed in Section 2.2.1.2, the calculation of potential evaporation requires knowledge of the relative humidity at the site on a given day, as well as temperature and net radiation. Assuming temperature, humidity, and windspeed to be approximately constant over the site, the potential evaporation for each element of the site map can be calculated as a function of the variable net radiation, and mapped as shown in Figure 8.18.

Potential evaporation levels shown on Figure 8.18 were calculated using the 1998 Equity climate data set, and the net radiation values mapped on Figure 8.3. The contour levels on Figure 8.18 illustrated that the potential evaporation was greatest on the slopes with southern exposure, and less on the slopes that face a more northerly direction, following the trends observed for net radiation.

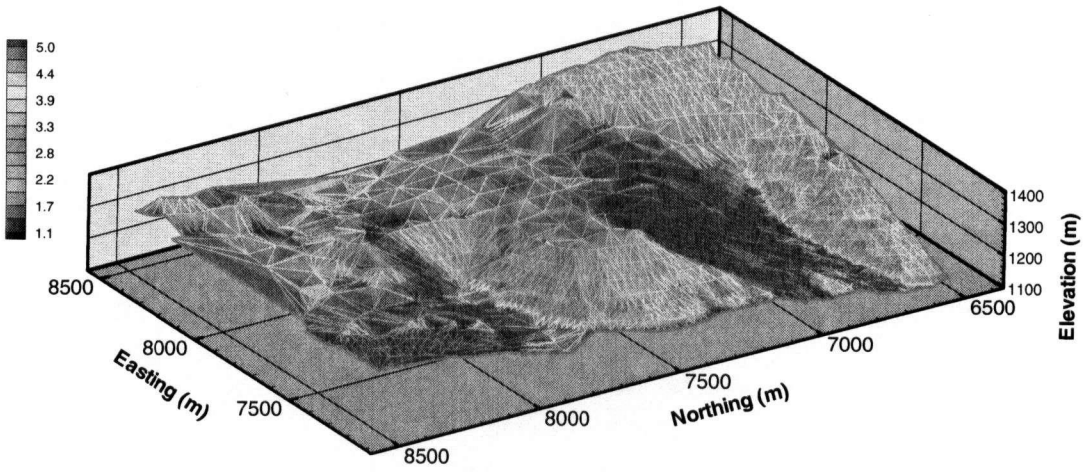

Figure 8.18: Variation in Average Potential Evaporation (mm/day) over the Topography of the Equity Site (Based on 1998 Climate Data for Horizontal Surface)

8.4 Mapping AE in Three Dimensions for Special Cases

In Section 8.2, it was demonstrated how the net radiation model could be integrated with soils data through one and two-dimensional models for actual evaporation, to predict the effect of slope orientation on actual evaporation. Such an approach can be used to provide design data for a wide variety of problems. However, it would be ideal to have a fully three-dimensional model for actual evaporation, which incorporated a 3D solution for the coupled heat and mass transfer equations (Section 2.1.2.1.2) with soils data over a ground surface, climate data, and modeled net radiation. Such a model could be used to generate three-dimensional maps of actual evaporation over a ground surface, comparable to the potential evaporation maps shown in Section 8.3. While developing a fully generalized version of such a model is outside the scope of this thesis, a three-dimensional map of actual evaporation can be constructed with the tools presented thus far for certain special cases.

The relationship between actual evaporation and potential evaporation is normally non-linear. Actual evaporation is a function of soil properties, soil moisture, and climatic conditions, while potential evaporation is a function of climate conditions only. Despite this, there are certain cases where, over a limited range of values and for specific sites, there is a discernable trend in the relationship between the two kinds of evaporation. Where such a relationship exists, potential evaporation maps (such as the one shown in Figure 8.18) can be transformed into maps of actual evaporation.

The process to create such a map is site specific, and requires the following four steps:

1. Select a cover profile to model with a 1D actual evaporation model (such as SoilCover) that is representative of conditions over the entire cover. This approach is most meaningful when soil, vegetation and moisture conditions are fairly similar over the site. Where initial moisture conditions vary widely over the cover, an approximate average needs to be selected.
2. Annual values of actual and potential evaporation need to be calculated with the 1D model for a wide variety of slopes, using the cover profile from step 1 along with the site climate data, and the net radiation program. The net radiation model is used to vary the net radiation input, as a function of slope for each run of the 1D model.
3. The calculated annual AE values are plotted as a function of the PE values, and the relationship between the two assessed.
4. If there is a clearly discernable relationship between the two parameters, this relationship can be applied to the PE map of the site, and a three-dimensional map of AE plotted.

The approach outlined above is inherently highly site specific, requiring multiple runs of a 1D model to evaluate a range of possible actual evaporation cases. There are also several other important limitations to such a method. Representing the entire cover surface as having a uniform initial moisture content generally represents a significant simplification of the real system. As discussed in Section 8.2.3, moisture variations over the cover and along the slope of the cover can have a significant impact on actual

evaporation. However, the assumption of a uniform soil cover is required to approximate AE over the 3D surface with the models available. Another important limitation is that even in considering annual totals (as opposed to the more variable daily values) of potential and actual evaporation, there may not be a clear relationship between the two parameters. This is especially likely to occur at arid sites, where the differences in actual evaporation with slope and aspect are much less dramatic that the differences in potential evaporation. At more humid sites where the two parameters are closer, one is more likely to find a relationship.

The humid site data collected for Equity presented an opportunity to demonstrate this approach to estimating actual evaporation in three dimensions. Using the data that was generated in Section 8.2.1 to illustrate the effect of slope and aspect on actual evaporation based on data collected from the Equity site, Figure 8.19 was developed. Figure 8.19 shows the annual actual evaporation calculated with the 1998 Equity data, as a function of the annual potential evaporation. Each data point was generated with a run of the SoilCover model for a different radiation input (corresponding to a different slope orientation). Each run generated an annual potential evaporation and an annual actual evaporation number, which provided one data point for Figure 8.19. As shown on the Figure, for this site, the relationship between actual and potential evaporation is very nearly linear in the range shown ($R^2 = 0.9984$).

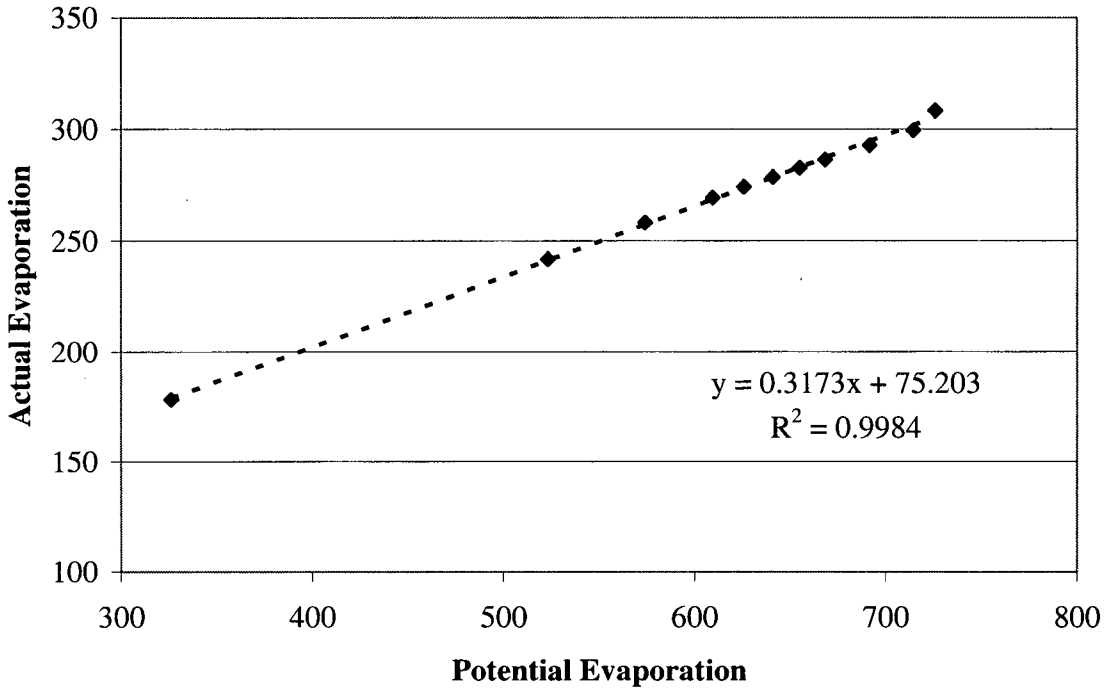

Figure 8.19: Annual actual evaporation as a function of potential evaporation for the Equity site (1998 weather data)

Based on the data shown in Figure 8.19, the site-specific relationship that (AE= 0.317 PE + 75.2) is used in TecPlot to transform the map of annual potential evaporation over the site (this map was shown in Figure 8.18), generating a map of annual actual evaporation, as shown in Figure 8.20. This plot shows the trend over the site for annual actual evaporation, which was directly proportional to the potential evaporation map shown on Figure 8.18, as a function of the linear relationship shown on Figure 8.19. The plot shown in Figure 8.20 is a simplified rendition of the actual evaporation that would occur, due to the assumptions necessary to generate the plot. The plot is essentially an extension of the analysis presented in Section 8.2.1 for a simplified cover profile. It does however provide some indication of the approximate differences in actual evaporation that would

occur at the site, with actual evaporation over 300 mm on the south face of the site, and less than 200 mm on the north face.

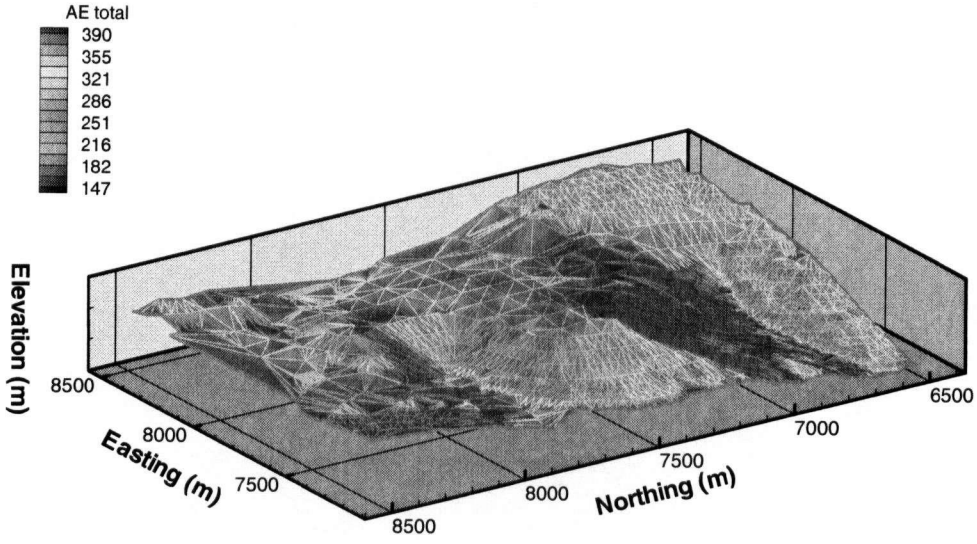

Figure 8.20: Variation in Average Actual Evaporation (mm/day) over the Topography of the Equity Site (Based on 1998 Climate Data for Horizontal Surface)

8.5 Obtaining Design Information with Coupled Models

The work presented to this point has shown in a general way how the net radiation model could be coupled with evaporative models such as SoilCover and Vadose/W to predict evaporation on sloped surfaces. In this section, the application of the net radiation model to a more design-oriented context is considered. Using a soil cover over waste rock as an example, covers with different orientations are compared, and the differences in design thickness of the covers required to obtain equivalent performance are determined.

To illustrate this application, a simple cover profile, consisting of uncompacted Equity till over a waste rock (modeled with Beaver Creek sand) was evaluated with SoilCover and the net radiation model. The soil cover thickness was varied in 20 cm increments between 40 and 80 cm. The underlying waste rock profile was modeled to a two meter depth below the soil cover/waste rock interface. The lower boundary condition in the waste rock was set as a soil suction of 12 kPa, equivalent to the suction in the waste at residual water content. Each case was modeled with net radiation input as if the soil was horizontally oriented (un-modified data) and as if the soil was sloped at a 2.5H:1V side slope to the north or south (data transformed with the net radiation model). For the sake of simplicity and clarity, vegetation effects (transpiration) were not incorporated into the analysis. In general, the presence of vegetation would increase the amount of actual evaporation expected from a given cover design. Predicting evaporation over a non-vegetated surface also illustrates the two extremes of moisture-limited and soil-limited evaporation for a give set of soil and climate data. The effects of vegetation could be

incorporated to future analysis with SoilCover by specifying factors such as a leaf area index for the design vegetation.

Note that these cover profiles were not meant to model a specific cover existing at any of the experimental sites. These simple cover profiles were intended only to illustrate in a hypothetical way a potential design application of the radiation model. The focus of this section is primarily on illustrating design methodology.

These soil cover cases were evaluated with a climate data set based on the growing season climate data collected at Equity. Climate data for the Equity site was summarized in Section 6.4.2. The climate data set used in the analysis was based on averages from 10 years of data collected at the Equity site for each required climate parameter, including temperature, humidity, net radiation, wind speed, and precipitation. For the Equity climate data set, the total annual precipitation was 499 mm, including 204 mm of spring snowmelt evenly distributed over the first thirty days of the 191-day data set. This 204 mm of snowmelt was based on average annual snowfall measured at the nearby Smithers weather station. The 191-day (growing season) climate data set was applied to the cover design to represent the application of the model to this cover in a humid environment. For comparison, the soil profiles were also evaluated with the 365 data set collected at the Kidston mine in Australia, representing climate data from an arid site in the southern hemisphere. The weather data for the Kidston site was based on 1998 data gathered at the site, representative of typical conditions at Kidston. The total precipitation was 680 mm, well below the potential evaporation at the site, which was over 2000 mm. This climate data was used to illustrate the predicted cover performance at the latitude of the

Kidston Site (19° south), as well as the performance at a hypothetical site with the same climate located further south, at latitude 35° south.

8.5.1 Performance with Equity Climate

The criteria by which the performance of a soil cover is evaluated depends on the philosophy behind the design of the cover. For an oxygen barrier cover, the degree of saturation maintained in the cover is important. A high degree of saturation (usually at least 85%) must be maintained year round, to prevent the movement of oxygen through the cover. For a cover that is to act as a barrier to water movement, minimizing the total flux through the cover is of greater importance. In both cases, the actual evaporation from the cover is an important determinant of its behaviour.

Figure 8.21 shows the degree of saturation maintained in the lower 10 cm of the uncompacted cover of Equity till, subjected to the 191-day equity climate data set. As an illustration, one could consider a design requirement to maintain an average degree of saturation in the lower 10 cm of the cover of at least 90%. As shown on Figure 8.21, the modelling suggests that meeting this requirement would take a cover 70 to 74 cm thick on the horizontal and south slopes, but would only require a cover 50 cm thick on the north-facing slope. This is a function of the reduced evaporation that occurs on the north slope, as shown on Figure 8.22. Note also on Figure 8.22 that while actual evaporation from the cover varies considerably as a function of direction of exposure, the thickness of the cover has a much more modest effect on evaporation rates (the slight increase with increased thickness reflects the impact of increased soil moisture storage).

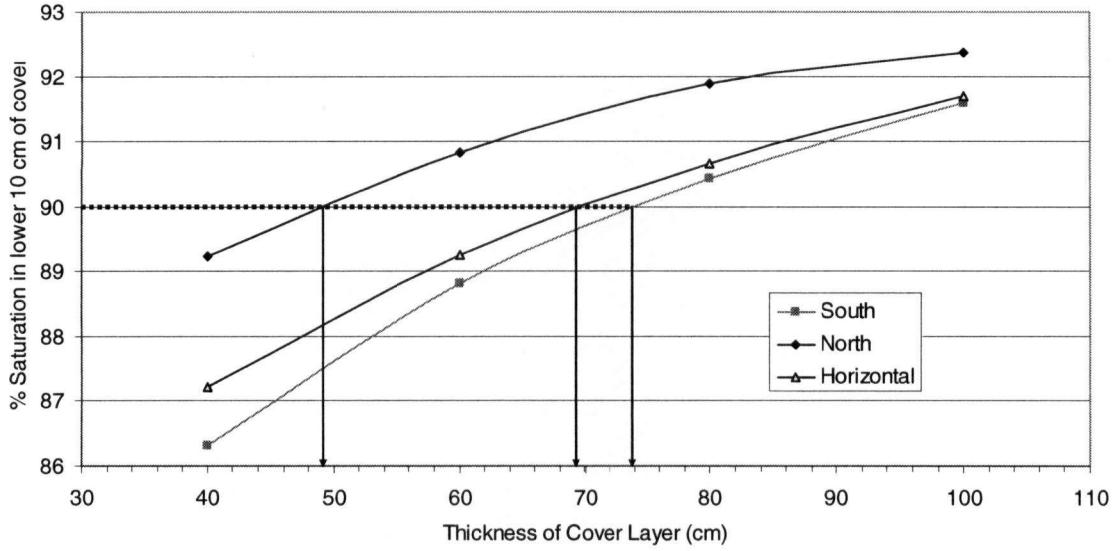

Figure 8.21: Average degree of saturation in the lower 10 cm of the uncompacted store-and-release cover subject to Equity climate. (Arrows indicated thickness of cover required to maintain 90% saturation)

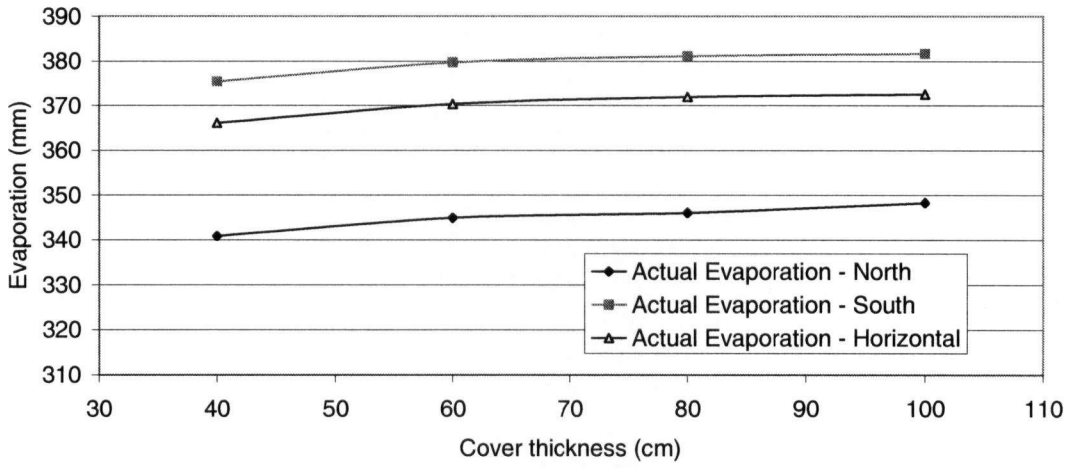

Figure 8.22: Effect of slope and cover thickness on actual evaporation from the uncompacted cover (Equity climate)

Figure 8.23 shows the modeled performance of the various cover thickness in terms of infiltration through the cover, which would be the basis for the evaluation of performance with a barrier cover. As would be expected for a fairly permeable cover configuration without a compacted low-permeability layer, all profiles let through a considerable

portion of the annual precipitation (values shown are approximately 15 to 25% of annual precipitation). However, for the purposes of illustration, one can see from the arrows on Figure 8.23 that if the cover was required to limit annual infiltration to 100 mm, a cover layer approximately 50 cm thick would be required on the south and horizontal faces, while a cover layer at least 62 cm thick would be required on the north face. Also interesting to note is that for this particular configuration, there is very little practical difference between infiltration through the cover on the south face and on the horizontal.

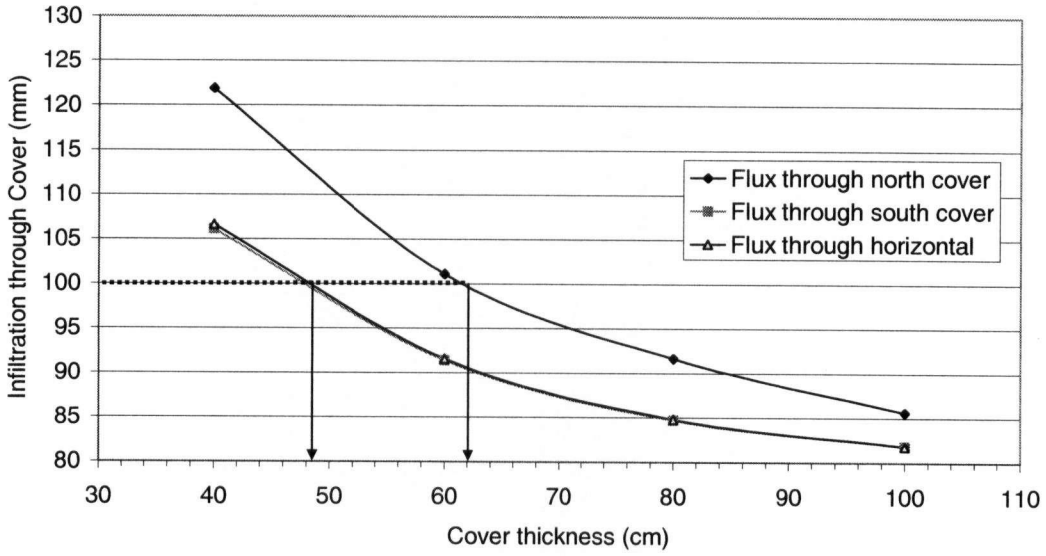

Figure 8.23: Effect of slope and cover thickness on annual infiltration through the uncompacted barrier cover (Equity climate – arrows indicate equivalent cover thicknesses for 100 mm infiltration limit).

These graphs illustrate a general approach that could be used for applying the net radiation model in conjunction with SoilCover to compare the performance of soil covers with different orientations at the same site. This type of approach could be used at any site and for any climate design.

8.5.2 Performance with Kidston Climate

To further illustrate the design application of the coupled models, the exact same set of cover profiles were examined using the Kidston climate data as an input. Again, non-vegetated, non-compacted covers were evaluated for a variety of cover thicknesses. Figure 8.24 shows the average degree of saturation maintained in the lower 10 cm of the cover in this case, comparable to Figure 8.21 for the covers with the Equity climate. As expected, the average degree of saturation maintained is lower in this drier climate, and the south face (which receives less net radiation over the course of the year) has a slightly higher average water content than the north and horizontal surfaces. Interestingly, the increased aridity of the climate also serves to reduce the differences between north and south-facing slopes, such that from a design standpoint, there is no significant slope-based difference in the cover performance – soil cover thickness is the main determinant of the average degree of saturation maintained.

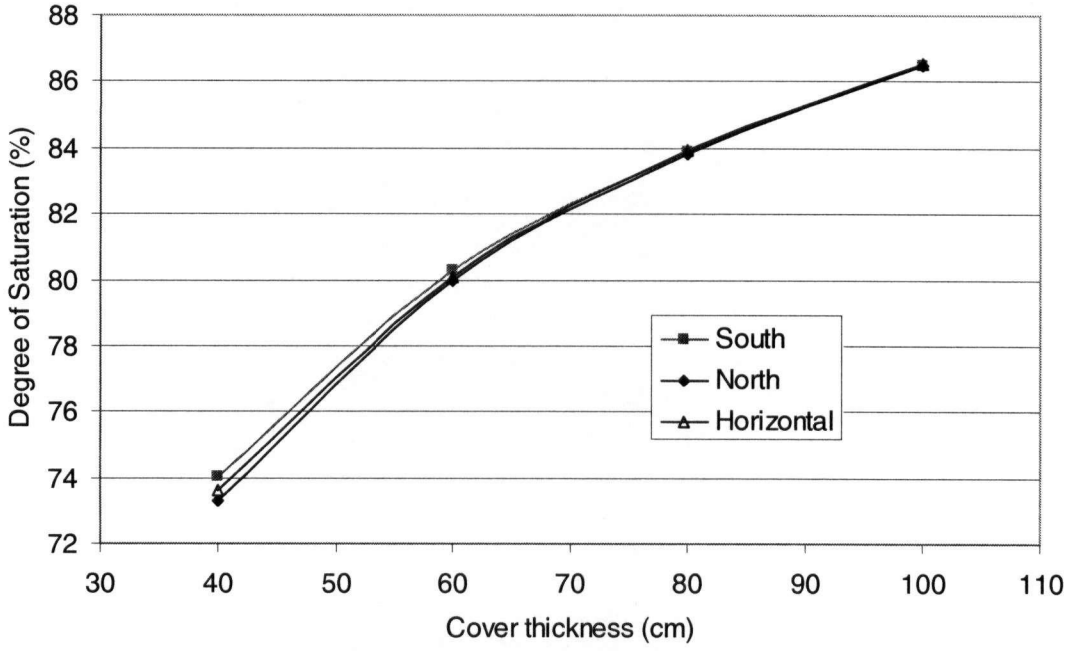

Figure 8.24: Average degree of saturation in the lower 10 cm of the uncompacted cover subject to Kidston climate (Latitude 19° South).

Figure 8.25 shows the predicted actual evaporation from the Kidston cover, and Figure 8.26 shows the predicted flux through the cover. For clarity, only the results from the north and south faces are shown (the horizontal surface performs very close to the south-facing surface). Comparing Figure 8.25 (Kidston) with Figure 8.22 (Equity) one can see that for actual evaporation, changes in cover thickness had a much greater impact on the total actual evaporation from the cover at the more arid site. This likely reflects the increased importance of water storage in the soil at an arid environment, particularly at a site with pronounced wet and dry seasons.

Figure 8.26 shows the effect of slope on getting equivalent performance from the covers. Using a design infiltration limit of 36 mm to illustrate the maximum differences between the cover, it is clear that a cover on the north face would have to be almost 20 cm thicker

than the cover on the south face to provide equivalent performance, in terms of infiltration through the cover.

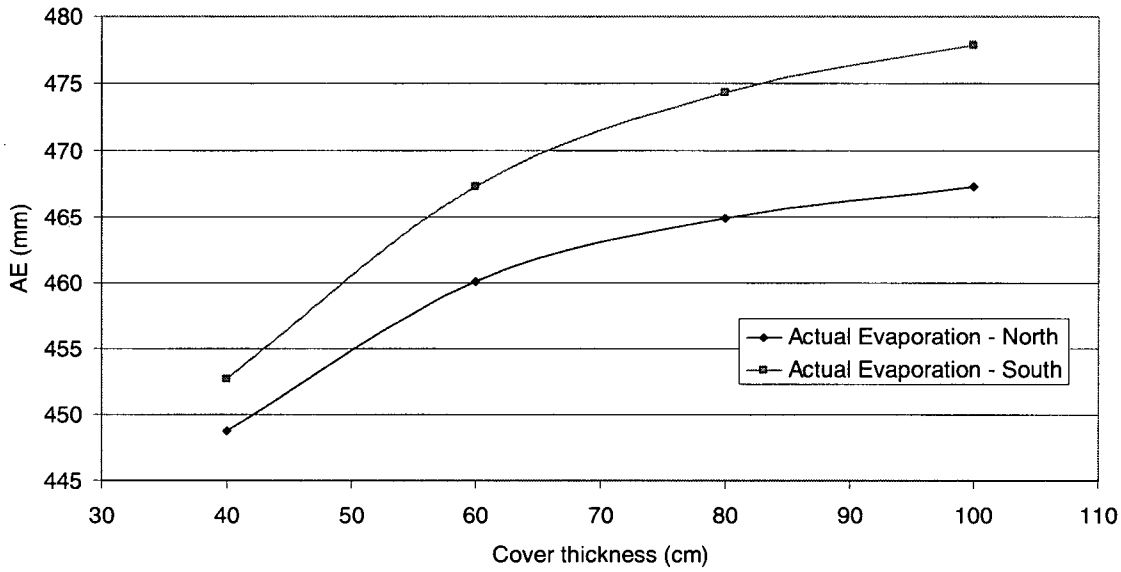

Figure 8.25: Effect of slope and cover thickness on actual evaporation from the uncompacted cover (Kidston climate)

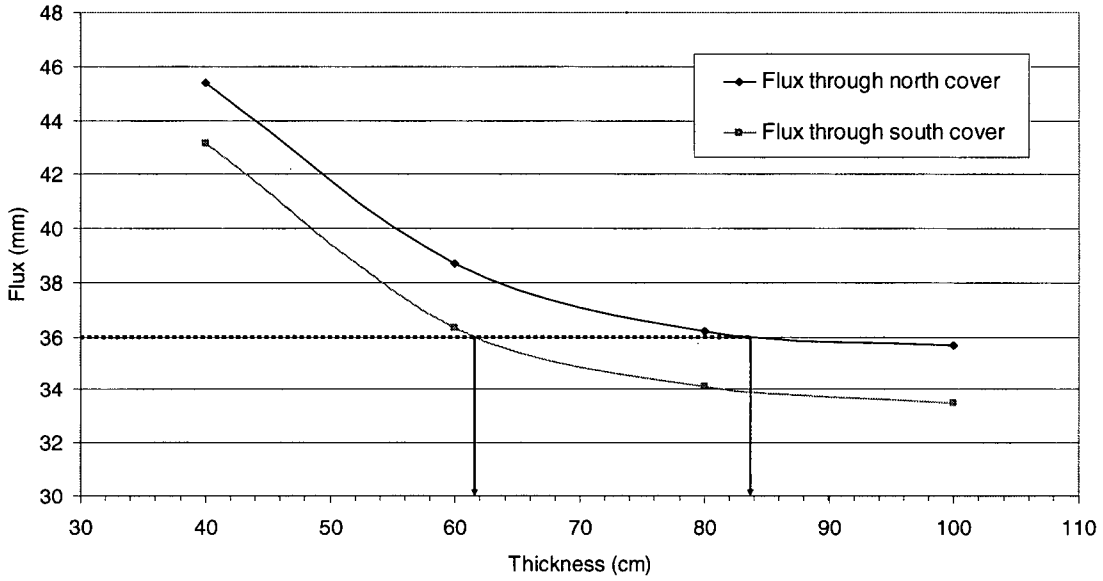

Figure 8.26: Effect of slope and cover thickness on annual infiltration through the uncompacted cover (Kidston climate – arrows indicate equivalent cover thicknesses for 36 mm infiltration limit)

An initially surprising outcome shown on both Figure 8.25 and Figure 8.26 is that the predicted actual evaporation is greater on the south-facing slope than the north-facing, and the corresponding flux through the cover is less. This is despite the fact that the predicted total annual energy input to the south face (3,376 MJ) is less than the total annual energy input to the north face (3,982 MJ). While this result is counter-intuitive, the underlying reason is that the majority of the annual rainfall at the site occurs during a time of year when the south facing slopes are receiving more radiation than the north-facing slopes. The bulk of the annual evaporation therefore takes place at this time of year. When there is more radiation on the north face, there is also less water available, and actual evaporation is correspondingly suppressed.

That greater radiation occurs on the south-facing slope for a portion of the year is a function of the site latitude (19°S). While this latitude puts the site well into the southern hemisphere, it is less than the tilt of the earth's axis (23.5°). As a result, there is a portion of the year (during the summer) when the south-facing slopes are actually more directly exposed to the sun's rays than the north facing slopes. This was observed in the experimental measurements on net radiation on slopes conducted at Kidston during the summer (Section 6.1.1). Figure 8.27 shows the daily net radiation values predicted for the north and south-facing slopes. On this figure it can be seen that during the summer months at this latitude, the net radiation predicted for the south slope is typically greater than that predicted for the north. In addition, precipitation at the Kidston site is distributed between distinct wet and dry seasons, with the wet season occurring during the summer (this is also shown on Figure 8.27). As a result, the majority of the annual precipitation falls at a time when net radiation is greatest on south-facing slopes. The combined effect results in most of the annual actual evaporation taking place during the summer, when evaporation rates are greater on the south facing slope. During the winter months, when potential evaporation rates would be greater on the north-facing slope, there is very little water to evaporate, and the evaporation rates are correspondingly reduced.

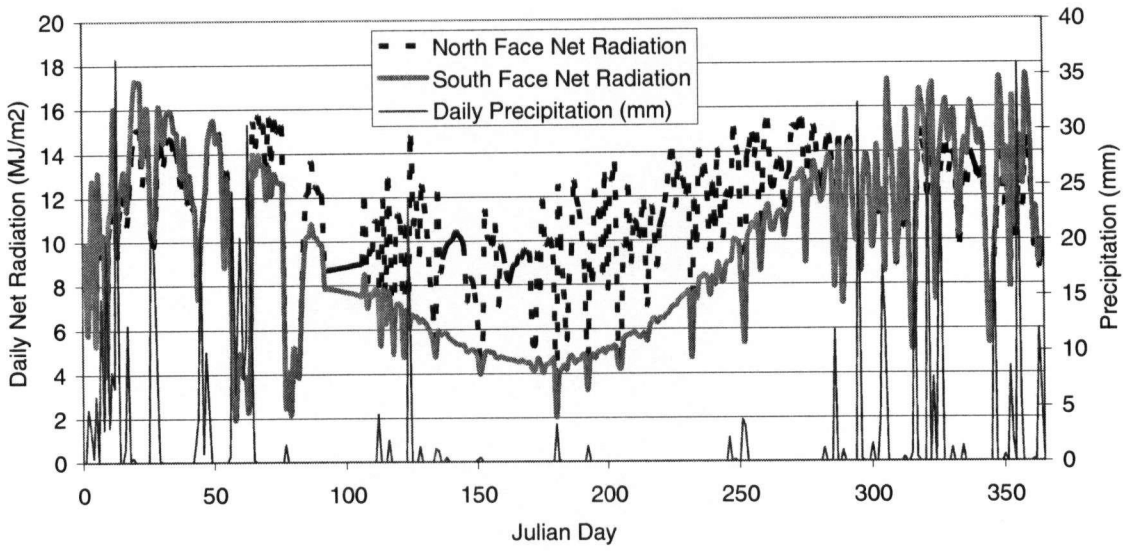

Figure 8.27: Annual precipitation and predicted net radiation patterns for the Kidston site (2.5H:1V slopes)

Figure 8.28 further illustrates how the greater evaporation on the south face was directly linked to the impact of latitude on net radiation. The predicted actual evaporation results plotted in Figure 8.28 were generated using the same modeling approach as in Figure 8.25, but treating all data as if it had been collected at a location further south. A latitude of 35°S was used for the analysis, corresponding to a latitude that would be greater than the tilt of the earth, but still located within Australia. As can be seen in Figure 8.28, the results now correspond to what one would initially have expected, with the greater predicted actual evaporation occurring on the north-facing slope.

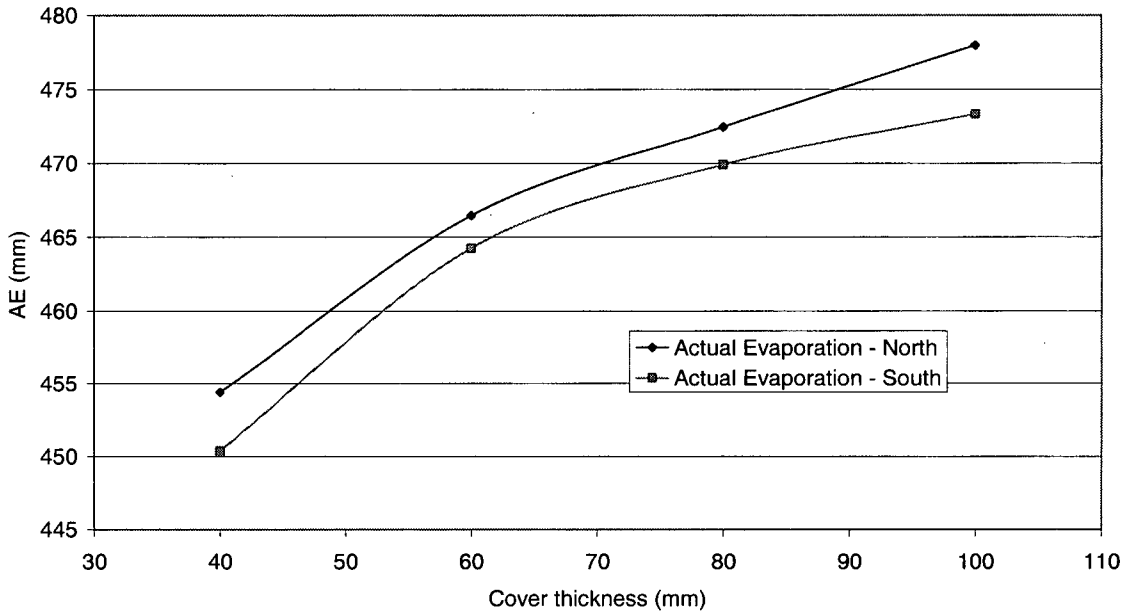

Figure 8.28: Effect of slope and cover thickness on predicted actual evaporation from the uncompacted cover (Kidston climate, modified as if the site was located at a latitude of 35°S)

8.5.3 Design approach summary

The design cases shown here were intended to provide a simple illustration of how the models may be coupled to provide design information, rather than a comprehensive overview of how cover performance may vary as a result of climate, slope, and cover design. The effect of slope on net radiation may or may not have a significant effect on the performance of a cover, based on the interaction of soil properties, climate, and cover design. The approach outlined in this section can be applied to any cover design to quantify the impact of variations in radiation on cover performance. This general

approach is equally applicable to covers designed as either water barriers or oxygen barriers.

The cover designs presented in this section were only intended for illustrative purposes. From an engineering standpoint, a single, non-compacted soil layer with no vegetation would actually represent a very poor cover design for most applications. However, the principles illustrated in this section with the simple cover would apply to a wide variety of cover designs, including multi-layer, vegetated covers.

8.6 Summary of Predictive Model Application

Using the net radiation model in conjunction with field data collected at both the Equity and Kidston sites, variations in net radiation and potential evaporation with slope and aspect have been demonstrated for a wide variety of cover orientations, and in the case of the Equity site, mapped in three dimensions. Soils and climate data have been incorporated from the two sites to demonstrate how the net radiation model can be incorporated with models for actual evaporation (such as SoilCover and Vadose/W) to predict actual evaporation over a variety of differently oriented surfaces. The data for the Equity site was used to demonstrate a simplified approach that can be used at select sites to map actual evaporation over a three dimensional surface.

Finally, several hypothetical design cases were presented to illustrate how the net radiation model coupled with an actual evaporation model could be used in design applications. The application of the two models to the design of oxygen barrier (moisture retaining) and infiltration barrier covers were illustrated, to show how the models could be used to estimate equivalent covers for differently oriented surfaces.

9 Summary and Conclusions

A model for the prediction of net radiation on sloping surfaces has been developed and verified with field-measured net radiation values. The model was developed based on established theory, and verified through field measurements at mine sites. Verification of the model showed very good agreement between predicted and measured net radiation values on sloped ground surfaces. The model was developed to be simple and robust, able to make use of the climate data that would be readily available at any site where net radiation was routinely measured. The model was also developed so that it would integrate well with existing models for the calculation of actual evaporation from soil surfaces. Testing the coupled application of the radiation model with established models for actual evaporation indicated that the coupled models could be used to approximate the differences in evaporation rates that occur on sloped soil surfaces facing different directions.

A review of the related literature showed that flux boundaries from soil covers in three dimensions may be affected by a variety of factors, including differences in wind, soil moisture distribution, infiltration rates, and net radiation. At many sites, the differences in net radiation were the most important of these four factors. The coupled net radiation and actual evaporation models were used to demonstrate the importance of variations in net radiation for a variety of sites. Using a one-dimensional model for actual evaporation, it was shown that the relative importance of Q_{net} variations over slope were at least partly a function of the site climate and latitude. Variations in Q_{net} were more

important at humid sites, where the actual rate of evaporation was closer to the potential. Variations in Q_{net} were also more significant for sites at higher latitudes, where the differences in Q_{net} between north and south slopes were more dramatic.

Using the net radiation model coupled with a 2-dimensional model of actual evaporation, it was shown that evaporation rates varied along the length of the slope, as well as with the direction faced by the slope. For the cases examined, near surface soil moisture conditions in non-vegetated sites were most strongly affected by the direction faced by the slope, while the soil moisture at depth was more strongly affected by the height of the soil above the water table.

The net radiation model developed was extended to include a generalized program for mapping variations in net radiation and potential evaporation over any three-dimensional surface. The radiation and potential evaporation mapping approach was applied to the research site at the Equity Silver mine in British Columbia, and showed that more southerly-facing slopes received the largest amount of net radiation. These maps also showed that on the more overcast days, when the total net radiation receipt was low, there was relatively little variability in the net radiation over the site. On clear days, when the net radiation totals were higher, differences across the site as a function of direction of exposure were more dramatic. The trends shown in maps of potential evaporation over the three-dimensional space closely paralleled the trends shown in maps of net radiation.

An approach to mapping actual evaporation in three dimensions was also demonstrated. This approach was by necessity far less generalized in applicability than the potential evaporation mapping approach presented. The method was based on conducting multiple runs with the actual evaporation model, to determine if a suitable relationship existed between actual and potential evaporation for a given site over the course of the year. Where a strong relationship was found between the annual totals of potential and actual evaporation for the year, this relationship was used to modify the three-dimensional potential evaporation map into a three-dimensional actual evaporation map. While the assumptions necessary in making such a map are limiting, the approach could still provide a useful approximation to actual evaporation variations over the site.

Finally, a design approach was illustrated for combining the net radiation model and a one-dimensional actual evaporation model. The design approach was set up to allow the engineer to evaluate alternative cover profiles for a given site, and compare the variations in cover thickness that would be required to obtain equivalent performance on different slopes. The design approach was illustrated for covers that were designed to limit the flux of oxygen through an uncompacted cover (by maintaining a nearly saturated layer), as well as for more the more traditional cover design concept, where the cover is designed to limit the amount of water that can infiltrate through the cover into the underlying waste.

The work presented in this thesis has thus met all of the objectives as initially stated in the introduction. A theoretical framework has been presented for the estimation of net

radiation on a sloped surface as a function of the net radiation on a horizontal surface, and this approach formulated in a model which as been verified with field experiments.

The work presented in this thesis represents the following contributions to the current state of engineering practice:

1. The main contribution of this work has been to introduce an approach for incorporating the impact of net radiation variations to the calculation of evaporation slopes in a geotechnical application. A new model has been presented for the calculation of net radiation on sloped surfaces, as a function of the net radiation measured on horizontal surfaces. This model has been verified through field-testing, and the sensitivity of the model to all input parameters tested. The modeling approach is suitable for engineering application and integration with existing engineering models for the evaluation of soil flux boundaries.

2. In addition, an approach has been developed and presented for calculating the impact of slope-based variations of net radiation on actual evaporation. This approach showed a potential application of the new model to provide design information for soil covers, illustrated with a sample design application.

3. The significance of slope-based variations in net radiation were also illustrated for a variety of cover design cases.

The work presented in this thesis should serve as a starting point for future research in this area. While preliminary verification of the net radiation model has been presented in this work, additional verification with data collected at other sites around the world would be ideal. An extended program of verification of the net radiation model coupled with evaporation measurements for sloped surfaces would also be an area worthy of future work.

The net radiation model has been presented in a form that can be easily used with existing software for the evaluation of flux boundaries. However, for the maximum ease of application in engineering practice, it would be ideal to code the model in a more user-friendly format, possibly integrated with an existing software package.

This work has been presented in the context of soil covers, particularly for soil covers used in mining applications such as waste rock disposal sites. However, the results of this thesis can be applied to any sloping soil surface where flux boundary conditions are a concern, such as dams and embankments (slope stability problems), or soils placed over other types of waste.

References

Adu-Wusu, C. and Yanful, E. K. (2004). "Comparison of field performance of a silt cover with numerical model simulations." 57th Canadian Geotechnical Conference, Session 8D:23-28.

Agassi, M., Shainberg, I., and Morin, J. (1990). "Slope, aspect, and phosphogypsum effects on runoff and erosion." Soil Science Society of America Journal, 54(4), 1102-1106.

Akindunni, F. F., Gillham, R. W., and Nicholson, R. V. (1991). "Numerical simulations to investigate moisture retention characteristics in the design of oxygen-limiting covers for reactive mine tailings." Canadian Geotechnical Journal, 28, 446-451.

Albright, W. H., Benson, Craig H., Gee, Glendon W. , Roessler Arthur C., Abichoe Tarek, Apiwantragoon Preekcha, Lyles Bradley F., and Rock Steven A. (2004). "Field water balance of landfill final covers." Journal of Environmental Quality, 33, 2317-2332.

Allan, C. J. and Roulet, N. T. (1994). "Runoff Generation in zero-order Precambrian Shield Catchments: the stormflow response of a heterogeneous landscape." Hydrological Processes, 8, 369-388.

Allen, R. G. (1996). "Assessing integrity of weather data for reference evapotranspiration estimation." Journal of Irrigation and Drainage Engineering, 122(2), 97-106.

Alonso, E., Gens, A., Lloret, A., and Delahaye, C. (1995). "Effect of rain infiltration on the stability of slopes." Proceedings of the First International Conference on Unsaturated Soils, A.A. Balkema, Rotterdam, Netherlands, 241-249.

Anderson, S. A. and Sitar, N. (1995). "Analysis of rainfall induced debris flows." Journal of Geotechnical Engineering, 121(7), 544-552.

Antonic, O. (1998). "Modelling daily topographic solar radiation without site-specific hourly radiation data." Ecological Modelling, 113, 31-40.

Arnold, N. S., Willis, I. C., Sharp M.J., Richards, K. S., and Lawson, W. J. (1996). "A distributed surface energy-balance model for a small valley glacier. I. Development for the Haut Glacier d'Arolla, Valais, Switzerland." Journal of Glaciology, 42(140), 77-89.

Ayres, B., Dirom, G., Christensen, D., Januszewski, S., and O'Kane, M. (2003). "Performance of cover system field trials for waste rock at Myra Falls operations." Proceedings Sixth International Conference on Acid Rock Drainage (ICARD), 233-239.

Ayres, B. K., O'Kane, M., Lanteigne, L., and and Christensen, D. (2002). "Construction and field performance monitoring of three experimental dry cover systems for acid-generating waste rock at Whistle Mine, Ontario, Canada." 2002 Tailings and Mine Waste Conference.

Barbaro, S., Coppolino S., Leone, C., and Sinagra, E. (1979). "An atmosphere model for computing direct and diffuse solar radiation." Solar Energy, 22, 225-228.

Barbour, S. L., Tamm, T. A., Lee, N. H., and Wilson, G. W. (1999). "Evaluation of Surface Runoff and Infiltration for a Large Scale Test Facility at Key Lake, Cameco Corporation." 52nd Canadian Geotechnical Conference, 187-193.

Barbour, S. L., Boese, C., and Stolte, B. (2001). "Water balances for reclamation covers on oilsands mining overburden piles." Proceedings of the 54th Annual Canadian Geotechnical Conferences, 313-319.

Battany, M. C. and Grismer, M. E. (2000). "Rainfall runoff and erosion in Napa Valley vineyards: Effects of slope, cover and surface roughness." Hydrological Processes, 14(7), 1289-1304.

Becker, P. and Weingarten, D. S. (1991). "A comparison of several models for separating direct and diffuse components of solar irradiation." Agricultural and Forest Meteorology, 53, 347-353.

Ben-Hur, M. and Wakindiki, I. I. C. (2004). "Slope mineralogy and slope effects on infiltration, interrill erosion, and slope factor." Water Resources Research, 40(W03303).

Blight, G. E. (1997). "Interactions between the atmosphere and the earth." Geotechnique, 47(4), 715-767.

Blight, G. E. (2002). "Solar radiation on surfaces of tailings dams - effects of slope and orientation." Tailings and Mine Waste '02, Swets & Zeitlinger, 333-337.

Blight, G. E. and Blight, J. J. (1993). "Runoff frome landfill surface isolation layers under simulated rainfall." Geoconfine 93, Balkema, Rotterdam, 313-318.

Blight, G. E. and Kreuiter, A. (2000). "Disposal of industrial waste liquids by evaporation and capillary storage in waste dumps ." Tailings and Mine Waste '00, Balkema, Rotterdam, 141-148.

Blight, G. E. and Lufu, L. (2000). "Principles of tailings dewatering by solar evaporation." Tailings and Mine Waste '00, Balkema, Rotterdam, 55-63.

Boast, C. W. and Roberston, T. M. (1982). "A microlysimeter method for determining evaporation from bare soil: description and laboratory evaluation." Soil Science Society of America Journal. 46, 689-696.

Boldt-Leppin, B., O'Kane, M., and Haug, M. D. (1999). "Soil Covers for sloped surfaces of mine waste rock and tailings." Tailings and Mine Waste '99, 393-405.

Bonachela, S., Orgaz, F., Villalobos, F. J., and Ferrers, E. (1999). Measurement and simulation of evaporation from soil in olive orchards. Irrigation Science. 18[4], 205-211.

Bouchet, R. J. (1963). " Evapotranspiration reele et potentielle, signification climatique." Int. Assoc. Sci. Hydrol. Symposium Publication, 62, 134-142.

Bowen, I. S. (1926). "The ratio of heat losses by conduction and by evaporation from any water surface." Physical Review, 27, 779-787.

Bristow, K. L. and Campbell, G. S. (1985). "An equation for separating daily solar irradiation into direct and diffuse components." Agricultural and Forest Meteorology, 35, 123-131.

Brock, B. W. and Arnold, N. S. (2000). Spreadsheet-based (Microsoft Excel) point surface energy balance model for glacier and snow melt studies. Earth Surface Processes and Landforms 25[6], 649-658. John Wiley & Sons Ltd, Chichester, Engl.

Bronstert, A. and Plate, E. J. (1997). "Modelling of runoff generation and soil moisture dynamics for hillslopes and micro-catchments." Journal of Hydrology, 198, 177-195.

Bruch, P. (1993). Evaporative fluxes in homogenous and layered soils. M.Sc Thesis, University of Saskatchewan, Saskatoon, Saskatchewan.

Bruno, R. (1978). "A correction procedure for separating direct and diffuse insolation on a horizontal surface." Solar Energy, 20, 97-100.

Brunt, D. (1932). "Notes on radiation in the atmosphere." Quarterly Journal of the Royal Meteorological Society, 58(389-418).

Brussiere B., Aubertin M., and Chapuis R.P. (2000a). "The use of hydraulic breaks to limit desaturation of inclined capillary barriers." 53rd Canadian Geotechnical Conference, 465-472.

Brussiere, B., Aubertin, M., and Chapuis, R. P. (2000b). " An investigation of slope effects on the efficiency of capillary barriers to control AMD." ICARD 2000 Proceedings From the Fifth International Conference on Acid Rock Drainage, 969-977.

Brussiere, B., Aubertin, M., Morel-Seytoux, H. J., and Chapuis, R. P. (1998). "A laboratory investigation of slope influence on the behaviour of capillary barriers." 51st Canadian Geotechnical Conference, 831-836.

Brutsaert, W. (1975). "On a derivable formula for long-wave radiation from clear skies ." Water Resources Research, 11, 742-744.

Brutsaert, W. and Stricker H. (1979). "An advection-aridity approach to estimate actual regional evapotranspiration." Water Resources Research, 15(2), 443-450.

Brutsaert, W. (1982). Evaporation into the Atmosphere: Theory, History, and Applications, Kluwer Academic Publishers, Boston.

Bryan, R. B. and Peosen, J. (1989). Laboratory experiments on the influence of slope length on runoff, percolation and rill development. Earth Surface Processes and Landforms. 14; 3, Pages 211-231.

Buchan, G. D. (1982a). "Predicting bare-soil temperature. 1. Theory and models for the multi-day mean diurnal-variations." Journal of Soil Science, 33(3), 185-197.

Buchan, G. D. (1982b). "Predicting bare-soil temperature. 2. Experimental testing of multi-day models." Journal of Soil Science, 33(3), 199-209.

Buchan, G. D. (1982c). "Predicting bare-soil temperature. 3. Extension to single day variation." Journal of Soil Science, 33(3), 365-373.

Burman, R. and Pochop, L. O. (1994). Evaporation, Evaportranspiration, and Climatic Data (Developments in Atmospheric Science 22), Elsevier Science, Amsterdam, The Netherlands.

Cabral, M. C., Garrote, L., Bras, R. L., and Entekhabi, D. (1992). "A kinematic model of infiltration and runoff generation in layered and sloped soils." Advances in Water Resouces, 15, 311-324.

Canton, Y., Sole-Benet, A., and Domingo, F. (2004). "Temporal and spatial patterns of soil moisture in semiarid badlands of SE Spain. " Journal of Hydrology, 285(91-4)), 119-214.

Carey, S. K. and Woo, M. (1999). "Hydrology of two slopes in subarctic Yukon, Canada." Hydrological Processes, 13, 2549-2562.

Carey, S. K. and Woo, M. (2001). "Spatial variability of hillslope water balance, Wolf Creek basin, subarctic Yukon." Hydrological Processes, 15, 3113-3132.

Carzorzi, F. and Fontana, G. D. (1996). "Snowmelt modelling by combining air temperature and a distributed radiation index." Journal of Hydrology, 181, 169-187.

Celia, M. A., Bouloutas, E. T., and Zarba, R. L. (1990). "A General Mass-Conservative Numerical Solution for the Unsaturated Flow Equation." Water Resources Research, 26(7), 1483-1496.

Cerda, A. and Garcia, F. P. (1997) The influence of slope angle on sediment, water and seed losses on badland landscapes. Geomorphology. 18[2], 77-90.

Chen W.J. and Novak M.D. (1997). "An improved tension-plate system for measuring first-stage evaporation under straw mulch." Agricultural and Forest Meteorology, 85, 1-17.

Choo, L.-P. and Yanful, E. K. (2000). "Water flow through cover soils using modeling and experimental methods." Journal of Geotechnical and Geoenvironmental Engineering, 126(4), 324-334.

Chou, M. D., Ridgeway, W. L., and Yan, M. M. H. (1993). "One-parameter scaling and exponential-sum fitting for water vapour and CO2 infrared transmission functions." Journal of Atmospheric Science, 50, 2294-2303.

Cluf, A. D. and Gash, H. C. (1993). "Longwave radiation from clear skies in Niger: a comparison of observations with simple formulas." Journal of Applied Meteorology, 32, 539-547.

Collins, B. D. and Znidarcic, D. (2004). "Stability analysis of rainfall induced landslides." Journal of Geotechnical and Geoenvironmental Engineering, 130(4), 362-372.

Corripio, J. G. (2003). "Vector algebra algorithms for calculating terrain parameters from DEMs and solar radiation modelling in mountainous terrain." International Journal of Geographical Information Science, 17(1), 1-23.

Courbaud, B., de Coligny, F., and Cordonnier, T. (2003). "Simulating radiation distribution in a heterogeneous Norway spruce forest on a slope." Agricultural and Forest Meteorology, 116, 1-18.

CSIRO (1990). Soil Water Infiltration and Movement. User's Manual., Division of Soils, Commonwealth Scientific & Industrial Research Organization, Australia.

Davies, J. A. and McKay, D. C. Evaluation of selected models for estimating solar radiation on horizontal surfaces. Solar Energy 43[3], 153-168. 1989.

Daws, M. I., Mullins, C. E., Burslem, D. F. R. P., Paton, S. R., and Dalling, J. W. (2002). "Topographic position affects the water regime in a semideciduous tropical forest in Panama. " Plant and Soil, 238(1), 79-90.

Dingman, S. L. (1994). Physical Hydrogeology, Prentice Hall, Englewood Cliffs, New Jersey.

Dong, A., Grattan, S. R., Carroll, J. J., and Prashar C.R.K. (1992). " Estimation of daytime net radiation over well-watered grass." Journal of Irrigation and Drainage

Engineering, 118(3), 466-479.

Dubayah, R. and Rich, P. M. (1995). "Topographic solar radiation models for GIS." International Journal of Geographic Information Systems, 9, 405-409.

Duffie, J. A. and Beckman, W. A. (1980). Solar Engineering of Themal Processes, John Wiley & Sons, New York.

Dunin, F. X. (1976). "Infiltration: its simulation for field conditions." Facets of Hydrology, J. C. Rodda, ed., John Wiley and Sons, Bristol, 199-227.

Dunne, T. and Black, R. D. (1970). "Partial area contribution to storm runoff in a small New England watershed." Water Resources Research, 6, 1296-1311.

Durham, A. J. P., Wilson, G. W., and Currey, N. (2000). "Field Performance of Two Low Infiltration Cover Systems in a Semi Arid Environment." ICARD 2000 Proceedings From the Fifth International Conference on Acid Rock Drainage, Society for Mining, Metallurgy and Exploration Inc., 1319-1326.

Edlefsen, N. E. and Anderson, A. B. C. (1943). "Thermodynamics of soil moisture." Hilgardia, 15(2), 31-298.

El Hassanin, A. S., Labib, T. M., and Gaber, E. I. (1993) Effect of vegetation cover and land slope on runoff and soil losses from the watersheds of Burundi. Agric-ecosyst-environ 43[3/4], 301-308.

Ellingson, R. G., Ellis, J., and Fels, S. (1991). "The intercomparison of radiation codes used in climate models: Long wave results." Journal of Geophysical Research, 96(D5), 8929-8953.

Environmental Protection Agency (1992). Statistical Training Course for Ground-Water Monitoring Data Analysis, EPA/530-R-93-003, Office of Solid Waste, Washington DC.

Erbs, D. G., Klein, S. A., and Duffie J.A. (1982). "Estimation of the diffuse radiation fraction for hourly, daily and monthly-average global radiation." Solar Energy, 28, 293-302.

Evett, S. R. and Dutt, G. R. (1985) Length and slope effects on runoff from sodium

dispersed, compacted earth microcatchments. Soil Science Society of America Journal 49[3], 734-738.

Evett, S. R., Warrick, A. W., and Matthias, A. D. (1995) Wall materials and capping effects on microlysimeter temperatures and evaporation. Soil Science Society of America Journal. 59[2], 329-336.

Fipps, G. and Skaggs, R. W. Influence of slope on subsurface drainage of hillsides. Water Resources Research. 25[7], 1717-1726. 1989.

Fipps, G. and Skaggs, R. W. (1989) Influence of slope on subsurface drainage of hillsides. Water Resources Journal. 163, 62-71.

Fischer, C. and Hermsmeyer, D. (1999). "Digital photogrammetry and GIS in tailings and mine waste management." Tailings and Mine Waste '99, Balkema, 77-86.

Flint, A. L. and Childs, S. W. (1987). "Calculation of solar radiation in mountainous terrain." Agricultural and Forest Meteorology, 40(3), 233-249.

Fox, D. M., Bryan, R. B., and Price, A. G. (1997). "The influence of slope angle on final infiltration rate for interrill conditions." Geoderma. 80(1-2), 181-194.

Fredlund, D. G. and Rahardjo, H. (1993). Soil Mechanics for Unsaturated Soils, John Wiley & Sons.

Freeze, R. A. and Cherry, J. C. (1979). Groundwater, Prentice Hall, Englewood Cliffs, NJ.

Fujiyasu, Y., Fahey, M., and Newson, T. (2000) Field investigation of evaporation from freshwater tailings. Journal of Geotechnical and Geoenvironmental Engineering 126[6], 556-567.

Galicia, L., Lopez-Blanco, J., Zarco-Arista, A. E., Filips, V., and Garcia-Oliva, F. (1999). "The relationship between solar radiation interception and water content in a tropical deciduous forest in Mexico." Catena, 36, 152-164.

Gandolfi, C. and Savi, F. (2000) A mathematical model for the coupled simulation of surface runoff and infiltration. Journal of Agricultural Engineering Research 75[1], 49-55.

Gardner, C. L. and Nadeau, C. A. (1988). "Estimating south slope irradiance in the Arctic - A comparison of experimental and modeled values." Solar Energy, 41(3), 227-240.

Garnier, B. J. and Ohmura, A. (1970). "The evalutation of surface variations in solar radiation income." Solar Energy, 13, 21-34.

Gasmo, J. M., Rahardjo, H., and Leong, E. C. (2000). "Infiltration effects on stability of a residual soil slope." Computers and Electronics in Agriculture, 26(2), 145-165.

Gates, D. M. (1980). Biophysical Ecology, Springer-Verlag, New York.

Geo-Slope International Ltd. (2001). SEEP/W. Calgary, Alberta, Canada.

Geo-Slope International Ltd (2001). VADOSE/W, Ver 1.16, user's guide, Geo-Slope International Ltd., Calgary Alberta.

Glassy J.M. and Running S.W. (1994). "Validating diurnal climatology logic of the MT-CLIM model across a climate gradient in Oregon." Ecological Applications, 4, 248-257.

Goczan, L. (1972) New methods of mapping the water budget of sloping areas. Geographia Polonica 23, 37-44.

Gomez-Plaza, A., Martinez-Mena, M., Albaladejo, J., and Castillo, V. M. (2001). "Factors regulating spatial distribution of soil water content in small semiarid catchments." Journal of Hydrology, 253((1-4)), 211-226.

Granger, R. J. (1989). " Evaporation from natural non-saturated surfaces." Journal of Hydrology, 111, 21-29.

Green, W. H. and Ampt, G. A. (1911). "Studies on Soil Physics, Part I:Flow of air and water through soils." Journal of Agricultural Science,(4), 1-24.

Grubbs, F. E. (1950). "Sample Criteria for testing outlying observations." Annals of Mathematical Statistics., 21, 27-58.

Gueymard, C. (1987). "An isotropic solar irradiance model for tilted surfaces and its

comparison with selected engineering algorithms." Solar Energy, 38(5), 367-386.

Gul, M. S., Muneer, T., and Kambezidis, H. D. (1998). "Models for obtaining solar radiation from other meteorological data." Solar Energy, 64(1-3), 99-108.

Guntner, A., Seibert, J., and Uhlenbrook, S. (2004). "Modeling spatial patterns of saturated areas: An evaluation of different terrain indices." Water Resources Research, 40(5), art. no.-W05114.

Hanson, C. L. (2001). "Clear-sky albedo measured at seven rangeland sites in southwest Idaho." Journal of Hydrologic Engineering, 6(6), 532-534.

Hatfield, J. L. (1983). "Comparison of long-wave radiation calculation methods over the United States." Water Resources Research, 19, 285-288.

Hatfield, J. L., Giorgis, R. B., and Flocchini, R. G. (1981). "A simple solar radiation model for computing direct and diffuse spectral fluxes." Solar Energy, 27(4), 323-329.

Hauser, V. L., Weand, B. L., and Gill, M. D. (2001). "Natural Covers for Landfills and Buried Waste." Journal of Environmental Engineering, 127(9), 768-775.

Hawke, R. M. and McConchie, J. A. (2003). "Variability of in situ moisture measurements and implications for modeling hillslope processes." Environmental & Engineering Geoscience, 9(3), 213-223.

Hay, J. E. (1971). "Computation model for radiative fluxes." Journal of Hydrology (NZ), 10 (1), 36-48.

Hay, J. E. (1979). An evaluation of solar radiation data for British Columbia. RAB Bulletin 14, Ministry of Environment, Province of British Columbia, Victoria, BC.

Hay, J. E. (1976). "A revised method for determining the direct and diffuse components of the total short-wave radiation." Atmosphere, 14(4), 278-287.

Hay, J. E. and McKay, J. E. (1985). "Estimating solar irradiance on inclined surfaces: A review and assessment of methodologies." International Journal of Solar Energy, 3, 203-240.

Helming, K., Romkens, M. J. M., and Prasad, S. N. (1998) Surface roughness related processes of runoff and soil loss: a flume study. Soil Science Society of America Journal 62[1], 243-250.

Helming, K., Roth, C. H., Wolf, R., and Diestel, H. (1993). "Characterization of rainfall microrelief interactions with runoff using parameters derived from digital elevation models (DEMs)." Soil Technology, 6, 273-286.

Hjerdt, K. N., McDonnell, J. J., Seibert, J., and Rodhe, A. (2004). "A new topographic index to quantify downslope controls on local drainage. " Water Resources Research, 40(5), art. no.-W05602.

Hobbins, M. T., Ramirez, J. A., Brown, T. C., and Claessens, L. H. J. M. (2001). "The complementary relationship in estimation of regional evapotranspiration: The complementary relationship areal evaporation and advection-aridity models." Water Resources Research, 37(5), 1367-1387.

Hockley, D. E., Noel, M., Rykaart, E. M., Jahn, S., and Paul, M. (2003). "Testing of soil covers for waste rock in the Ronneburg WISMUT mine closure." Proceedings Sixth International Conference on Acid Rock Drainage (ICARD), 273-279.

Holtan, H. N. A concept for infiltration estimates in watershed engineering. U.S. Department of Agriculture Bulletin 41-51. 1961. Washington D.C., U.S. Department of Agriculture.

Horton, R. E. (1939). "Analysis of runoff-plot experiments with varying infiltration capacity." Transactions American Geophysical Union, 20, 693-711.

Idso, S. B. (1980). "On the apparent incompatibility of different atmospheric thermal-radiation data sets." Quarterly Journal of the Royal Meteorological Society , 106, 375-376.

Idso, S. B. (1981). "A set of equations for full spectrum and 8-14 um and 10.5-12.5 um thermal radiation from cloudless skies." Water Resources Research, 17, 295-304.

Idso, S. B. and Jackson, R. D. (1969). "Thermal radiation from the atmosphere." Journal of Geophysical Research, 74, 5397-5403.

Iqbal, M. (1983). An introduction to solar radiation, Academic Press, Toronto.

Irmak, S., Irmak, A., Allen, R. G., and Jones, J. W. (2003a). "Solar and net radiation-based equations to estimate reference evapotranspiration in humid climates." Journal of Irrigation and Drainage Engineering, 129 (5), 336-347.

Irmak, S., Irmak, A., Jones, J. W., Howell, T. A., Jacobs, J. M., Allen, R. G., and Hoogenboom, G. (2003b). " Predicting daily net radiation using minimum climatological data." Journal of Irrigation and Drainage Engineering, 129(4), 256-269.

Isard, S. A. (1986). "Evaluation of models for predicting insolation on slopes within the Colorado alpine tundra." Solar Energy, 36(6), 559-564.

Jackson, C. R. (1992). "Hillslope Infiltration and Lateral Downslope Unsaturated Flow ." Water Resources Research, 28(9), 2533-2539.

Jackson, R. J. (1967). " The effect of slope, aspect and albedo on potential evaporation from hillslopes and catchments." Journal of Hydrology, 6(2), 60-69.

Jansen, T. J. (1985). Solar Engineering Technology, Prentice Hall, New Jersey.

Jiang, H., Fry, J. D., and Wiest, S. C. (1998) Variability in turfgrass water requirements on a golf course. HortScience 33[4], 689-691.

Jimenez, J. I. and Castro, Y. (1982). "Solar radiation on sloping surfaces with different orientations in Granada, Spain." Solar Energy, 28(3), 257-262.

Johansen, O. (1975). "Thermal conductivity of soils." University of Trondheim.

Jury, W. A. and Tanner, C. B. (1975). "Advection modification of the Priestly and Taylor evapotranspiration formula." Agrononmy Journal, 67, 840-842.

Khire, M. V., Benson, C. H., and Bosscher, P. J. (2000). "Capillary barriers: Design variables and water balance." Journal of Geotechnical and Geoenvironmental Engineering, 126(8), 695-708.

Klein, S. A. (1977). "Calculation of monthly average insolation on tilted surfaces." Solar Energy, 19, 325-329.

Klutcher, T. M. (1979). "Evaluation of models to predict insolation on tilted surfaces." Solar Energy, 23, 111-114.

Kondratyev, K. J. and Manolova, M. P. (1960). "The radiation balance of slopes." Solar Energy, 4(1), 14-19.

Kondratyev, K. Y. (1969). Radiation in the atmosphere, Academic Press, New York.

Kondratyev K. Y. (1965). Radiative heat exchange in the atmosphere, Pergamon Press, Oxford.

Kostiakov, A. N. (1932). "On the dynamics of the coefficient of water-percolation in soils and the necessity of studying it from a dynamic point of view for purposes of amelioration." Transactions of the Sixth Comm. of the International Society of Soil Science., Part A, 17-31.

Kowaleski, P. E. (1999). "Comparative reclamation soil cover modeling in an arid environment." Tailings and Mine Waste '99, Balkema, Rotterdam, 427-436.

Kumar, L., Skidmore, A. K., and Knowles, E. (1997). "Modelling topographic variation in solar radiation in a GIS environment." International Journal of Geographical Information Science, 11(5), 475-497.

Kuo, E. Y., Ritchie, A. I. M., and Timms, G. P. (2003). "Long-term monitoring of water infiltration through covers at White's waste rock dump at the Rum Jungle mine site using lysimeters." Proceedings Sixth International Conference on Acid Rock Drainage (ICARD), 703-710.

Kyriakidis, P. C., Kim, J., and Miller, N. L. (2001). "Geostatical mapping of precipitation from rain gauge data using atmospheric and terrain characteristics." Journal of Applied Meteorology, 40, 1855-1877.

Lee, R. (1963). "Evaluation of solar beam irradiation as a climatic parameter of mountain watersheds." Colorado State University Hydrology Paper, 2, 50.

Leij, F. J., Romano, N., Palladino, M., Schaap, M. G., and Coppola, A. (2004). "Topographical attributes to predict soil hydraulic properties along a hillslope transect." Water Resources Research, 40(2), art. no.W02407.

Lim, T. T., Rahardjo, H., Chang, M. F., and Fredlund, D. G. (1996). " Effect of rainfall on matric suctions in a residual soil slope ." Canadian Geotechnical Journal, 33, 618-628.

Linacre, E. T. (1968). " Estimating the net radiation flux." Agricultural Meteorology, 5, 49-63.

Liu, B. Y. and Jordan, R. C. (1960). "The interrelationship and characteristic distribution of direct, diffuse and total solar radiation." Solar Energy,(4), 1-19.

Ma, C. C. Y. and Iqbal, M. (1983). "Statistical comparison of models for estimating solar radiation on slopes." Solar Energy, 31(3), 313-317.

Manes, A. and Ianetz, A. (1983). "Solar irradiance on non-horizontal surfaces at the east-meditteranean costal plain of Israel." Solar Energy, 31(1), 3-19.

Matizinger, N., Andretta, M., Van Gorsel, E., Vogt, R., Ohmura A., and Rotach, M. W. (2003). "Surface radiation budget in an Alpine Valley." Quaterly Journal of the Royal Meteorological Society, 129, 877-895.

Maxwell, E. L. (1998). " METSTAT - The solar radiation model used in the production of the National Solar Radiation Data Base (NSRDB)." Solar Energy, 62(4), 263-279.

McKay, D. C. and Morris R. J. (1985). Solar Radiation Data Analyses For Canada 1967-1976. Volume 5: British Columbia, Envrionment Canada, Atmospheric Environmental Services, Ottawa, Canada.

Meriggi, R., Di Marco, C., and Pavoni, R. (2002). "A parametric analysis of colluvial slope stability during heavy rainfalls." Unsaturated Soils 2002, Balkema, 741-747.

Milczarek, M., Yao, T., Vinson, J., Word, J., Kiessling, S., Musser, B., and Mohr, R. (2003). "Performance of mono-layer evapotranspirative covers in response to high precipitation and extended drought periods in the Southwestern United States." Proceedings Sixth International Conference on Acid Rock Drainage (ICARD), 307-317.

Monteith, J. L. (1962). "Attenuation of solar radiation: a climatological study." Quarterly Journal of the Royal Meteorological Society, 88, 508-521.

Monteith, J. L. (1965). "Evaporation and environment." The State and Movement of Water in Living Organisms, XIX Symposium, Soc. Exp. Biol., Cambridge University Press.

Montgomery, D. C. and Runger, G. C. (2003). Applied Statistics and Probability for Engineers, John Wiley & Sons, Inc., New York.

Morris, C. E. and Stormont, J. C. (1998). "Evaluation of numerical simulations of capillary barrier field tests." Geotechnical-and-Geological-Engineering, 16(3 Se), 1998, P 201-213.

Morton, F. I. (1983). "Operational estimates of areal evapotranspiration and their significance to the science and practice of hydrology." Journal of Hydrology, 66, 1-66.

Munro, D. S. and Huang, L. J. (1997). "Rainfall, evaporation and runoff responses to hillslope aspect in the Shenchong Basin." Catena, 29, 131-144.

Nevilly, M. and CETAMA, (1999). Modelling and Estimation of Measurement Errors, Lavoisier Publishing, Paris, France.

Newman, G. P., Newman, L. L., and Krahn, J. (2003). "Two-dimensional, evaporative flux cover/cap analysis for prevention of acid mine drainage." Proceedings Sixth International Conference on Acid Rock Drainage (ICARD), 693-701.

Ng, C. W. W., Wang, B., and Tung, Y. K. (2001). "Three-dimensional numerical investigations of groundwater responses in an unsaturated slope subjected to various rainfall patterns." Canadian Geotechnical Journal, 38, 1049-1062.

Nichols, W. E. and Meyer, P. D. (1996). "Multidimensional water flow in a low-level waste isolation barrier." Ground Water, 34(4), 659-665.

Nicholson, R. V., Gillham, R. W. C. J. A., and Reardon, E. J. (1989). "Reduction of acid generation in mine tailings through the use of moisture retaining cover layers as oxygen barriers." Canadian Geotechnical Journal, 26, 1-8.

Noel, M. M. and Rykaart, E. M. (2003). "Comparative study of surface flux boundary models to design soil covers for mine waste facilities." Proceedings Sixth International Conference on Acid Rock Drainage (ICARD), 703-710.

Novak, M. D. and Black, T. A. (1985) Theoretical determination of the surface energy balance and thermal regimes of bare soils. Boundary-Layer Meteorology 33[4], 313-33.

Nunez, M. (1980). "The calculation of solar and net radiation in mountainous terrain." Journal of Biogeography, 7, 173-186.

Nyhan, J. W., Schofield, T. G., and Starmer, R. H. (1997). "A Water Balance Study of Four Landfill Cover Designs Varying in Slope for Semiarid Regions." Journal of Environmental Quality, 26(5), 1385-1392.

O'Kane, M. (1995). "Instrumentation and monitoring of an engineered soil cover system for an acid generating mine waste." M.Sc Thesis. University of Saskatchewan. Saskatoon, Saskatchewan.

O'Kane, M., Porterfield, D., Weir, A., and Watkins, L. (2000). "Cover system performance in a semi-arid climate on horizontal and sloped waste rock surfaces." ICARD 2000 Proceedings From the Fifth International Conference on Acid Rock Drainage, 1309-1318.

O'Kane, M. and Waters, P. (2003). "Dry cover trials at Mt Whaleback - A summary of overburden storage area cover systems performance." Proceedings Sixth International Conference on Acid Rock Drainage (ICARD), 147-153.

O'Kane, M., Wilson, G. W., and Barbour, S. L. (1998). "Instrumentation and monitoring of an engineered soil cover system for mine waste rock." Canadian Geotechnical Journal, 35, 828-846.

Oke, T. R. (1987). Boundary Layer Climates, Routledge, London and New York.

Oliphant, A. J., Spronken-Smith, R. A., Sturman, A. P., and Owens, I. F. (2003) Spatial variability of surface radiation fluxes in mountainous terrain. Journal of Applied Meteorology 42[1], 113-128. American Meteorological Society.

Olyphant, G. A. (1986) Longwave radiation in mountainous areas and its influence on the energy balance of alpine snowfields. Water Resources Research 22[1], 62-66.

Orgill, J. F. and Hollands, K. E. T. (1977). "Correlation equation for hourly diffuse radiation on a horizontal surface." Solar Energy, 19, 357-359.

Pachepsky, Y. A., Timlin, D. J., and Rawls, W. J. (2001). "Soil water retention as related to topographic variables." Soil Science Society of America Journal, 65(6), 1787-1795.

Paltridge, G. W. (1975). "Net radiation over the surface of Australia." Search, 6, 37-39.

Paltridge, G. W. and Platt, C. M. R. (1976). Radiative processes in meteorology and climatology, Elsevier Scientific Pub. Co, Amsterdam ; New York.

Pan, L. and Wierenga, P. J. (1995). "A transformed pressure head-based approach to solve Richards' equation for variably saturated soils." Water Resources Research, 31(4), 925-931.

Parent, S. E. and Cabral, A. (2004). "Procedure for the design of inclined covers with capillary barrier effects." 57th Canadian Geotechnical Conference, Session 2D:15-20.

Parlange, M. B., Eichinger, W. E., and Albertson, J. D. (1995). "Regional Scale Evaporation and the atmospheric boundary layer." Reviews of Geophysics, 33(1), 99-124.

Penman, H. L. (1948). "Natural evaporation from open water, bare soil and grass." Proceedings of the Royal Society of London Series A - Mathematical and Physical Sciences, 193, 120-145.

Pereira, L. S., Perrier, A., Allen, R. G., and Alves, I. (1999). "Evapotranspiration: Concepts and future trends." Journal of Irrigation and Drainage Engineering, 125(2), 45-51.

Philip, J. R. (1957). "The Theory of Infiltration 1: The infiltration equation and its solution." Soil Science, 83, 345-357.

Plüss, C. and Ohmura, A. (1997). Longwave radiation on snow-covered mountainous surfaces. Journal of Applied Meteorology 36[6], 824-818.

Pradel, D. and Raad, G. (1993). "Effect of permeability on surficial stability of homogenous slopes." Journal of Geotechnical Engineering, 119(2), 315-332.

Priestley, C. H. B. and Taylor, R. J. (1972). "On the assessment of the surface heat flux

and evaporation using large-scale parameters." Monthly Weather Review, 100, 81-92.

Qiu, G. Y., Yano, T., and Momii, K. (1998) An improved methodology to measure evaporation from bare soil based on comparison of surface temperature with a dry soil surface. J-hydrol 210[1/4], 93-105.

Qiu, Y., Fu, B. J., Wang, J., and Chen, L. D. (2001). "Spatial variability of soil moisture content and its relation to environmental indices in a semi-arid gully catchment of the Loess Plateau, China." Journal of Arid Environments, 49(4), 723-750.

Ragab, R., Bromley, J., Rosier, P., Cooper, J. D., and Gash, J. H. C. (2003). "Experimental study of water fluxes in a residential area: 1. Rainfall, roof runoff and evaporation: the effect of slope and aspect." Hydrological Processes, 17(12), 2409-2422.

Raupach, M. R. and Finnigan, J. J. (1997). "The influence of topography on meteorological variables and surface-atmosphere interactions." Journal of Hydrology, 190, 182-213.

Reddy, S. J. (1971). "An empirical method for the estimation of net radiation intensity." Solar Energy, 13, 291-292.

Reindl D.T., Beckman W.A., and Duffie J.A. (1990). "Diffuse fraction correlations." Solar Energy, 45, 1-7.

Rich, Paul M., Hetrick, William A., and Saving, Shawn C. (1994) SOLARFLUX. Los Alamos National Laboratory, Los Alamos, New Mexico.

Richards, L. A. (1931). "Capillary conduction of liquids through porous mediums." Physics, 1, 318-333.

Roderick, M. L. (1999). "Estimating the diffuse component from daily and monthly measurements of global radiation." Agricultural and Forest Meteorology, 95, 169-185.

Rosenberg, N. J., Blad, B. L., and Verma, S. B. (1983). Microclimate - the Biological Environments, John Wiley & Sons, New York.

Ross, B. (1990). "The diversionary capacity of capillary barriers." Water Resources Research, 26(10), 2625-2629.

Rouse, W. R. and Wilson, R. G. (1969). "Time and space variations in the radiant energy fluxes over sloping forrested terrain and their influence on seasonal heat and water balances at a middle latitude site." Geografiska annaler, 51A(3), 160-175.

Running S.W., Nemani R.R., and Hungerford R.D. (1987). "Extrapolation of synoptic meteorological data in mountainous terrain and its use for simulating forest evaporation and photosynthesis." Canadian Journal of Forest Research, 17(472-483).

Ruth, D. W. and Chant, R. E. (1976). "The relationship of diffuse radiation to total radiation in Canada." Solar Energy, 18, 153-154.

Rykaart, E. M., Wilson, G. W., Fredlund, D. G., and Currey, N. A. (2001). "A spatial flux boundary model for tailings dams." Proceedings of the 54th Annual Canadian Geotechnical Conferences, 1102-1109.

Salvucci, G. D. and Entekhabi, D. (1995). "Hillslope and climatic controls on hydrologic fluxes." Water Resources Research, 31(7), 1725-1739.

Samani, Z. (2000). "Estimating solar radiation and evapotranspiration using minimum climatological data." Journal of Irrigation and Drainage Engineering, 126(4), 265-267.

Scanlon, B. R., Christman, M., Reedy, R. C., Porro, I., Simunek, J., and Flerchinger, G. N. (2002). "Intercode comparisons for simulating water balance of surficial sediments in semiarid regions." Water Resources Research, 38(12), 59-1 to 59-16.

Schroeder, P. R., Lloyd C.M., Zappi P.A., and Aziz N.M. (1994). The Hydrologic Evaluation of Landfill Performance (HELP) Model, user's guide for version 3, EPA/600/168a, US Environmental Protection Agency Risk Reduction Engineering Lab, Cincinnati, Ohio.

Schroeder, P. R., Morgan, J. M., Walski, T. M., and Gibson, A. C. (1984). The Hydrologic Evaluation of Landfill Performance (HELP) Model: Vol. I. User's Guide for Version 1, Technical Resource Document EPA/530-SW-84-009, U.S. Environmental Protection Agency, Cincinnati, Ohio.

Segal, M., Mahrer, Y., Pielke, R. A., and Ookouchi, Y. (1985). "Modeling transpiration patterns of vegetation along south and north facing slopes during the subtropical dry season." Agricultural and Forest Meteorology, 36(1), 19-28.

Sellers, P. J., Heiser, M. D., Hall, F. G., Verma, S. B., Desjardins, R. L., Schuepp, P. M., and MacPherson, J. I. (1997). "The impact of using area-averaged land surface properties - topography, vegetation conditions, soil wetness - in calculations of intermediate scale (approximately 10 km2) surface-atmosphere heat and moisture fluxes." Journal of Hydrology, 190, 269-301.

Silvestri, V., Sarkis, G., Bekkouche, N., Soulie, M., and Tabib, C. (1991). "Laboratory and Field Calibration of a Neutron Depth Moisture Gauge for use in High Water Content Soils." Geotechnical Testing Journal, 14(1), 64-70.

Skartveit A. and Olseth J.A. (1987). "A model for the diffuse fraction of hourly global radiation." Solar Energy, 38, 271-274.

Smith, P. G. C., Addenbrooke, T. I., and Potts, D. M. (2002). "Coupled finite element analysis of infiltration into unsaturated soils." Unsaturated Soils 2002, Balkema, 3-7.

Snedecor, G. W. and Cochran, W. G. (1989). Statistical Methods, Iowa State University Press.

SoilVision Systems Ltd. (2005). SVFlux User's and Theory Guide. Version 5.55. Saskatoon, SK, Canada.

Stannard, D. I. (1993). "Comparison of Penman-Monteith, Shuttleworth-Wallace, and modified Priestly-Taylor evapotranspiration models for wildland vegetation in semi-arid rangeland." Water Resources Research, 29(5), 1379-1392.

Stormont, J. C. (1995). "The effect of constant anisotropy on capillary barrier performance." Water Resources Research, 31(3), 783-785.

Stormont, J. C. and Anderson, C. E. (1999). "Capillary barrier effect from underlying coarser soil layer. " Journal of Geotechnical and Geoenvironmental Engineering, 641-648.

Stormont, J. C. (1996). "Effectiveness of two capillary barriers on a 10% slope."

Geotechnical and Geological Engineering, 14(4), 243-267.

Suter, G. W. I., Luxmoore, R. J., and Smith, E. D. (1993). "Compacted soil barriers at abandoned landfill sites are likely to fail in the long term." Journal of Environmental Quality, 22, 217-226.

Swanson, D.A. (1995). Predictive modelling of moisture movement in engineered soil covers for acid generating mine waste. Ph.D. Thesis, University of Saskatchewan, Saskatoon, Saskatchewan.

Swanson, D. A., Barbour, S. L., and Wilson, G. W. (1997). "Dry-site versus wet-site cover design." Proceedings of the Fourth International Conference on Acid Rock Drainage, 1595-1609.

Swanson D.A., Barbour S.L., Wilson G.W., and O'Kane M. (2003). "Soil-atmosphere modelling of an engineered soil cover for acid generating mine waste in a humid, alpine climate." Canadian Geotechnical Journal, 40, 276-292.

Swift, L. W. (1976). "Algorithm for Solar Radiation on Mountain Slopes." Water Resources Research, 12(1), 108-112.

Swinbank, W. C. (1963). "Long-wave radiation from clear skies." Quarterly Journal of the Royal Meteorological Society, 89, 339-348.

Tami, D., Rahardjo, H., Leong, E.-C., and Fredlund, D. G. (2004). "Design and laboratory verification of a physical model of a sloping capillary barrier." Canadian Geotechnical Journal, 41, 814-830.

Taylor, G., Spain, A., Timms, G., Kuznetsov, V., and Bennett, J. (2003). "The medium-term performance of waste rock covers - Rum Jungle as a case study." Proceedings Sixth International Conference on Acid Rock Drainage (ICARD), 383-397.

Taylor, P. A. and Lee R.J. (1984). "Simple guidelines for estimating wind speed variations due to small scale topographic features." Climatological Bulletin, 18, 3-32.

Tchobanoglous, G., Theisen, H., and Eliassen, R. (1977). Solid Wastes. Engineering

Principles and Management Issues, McGraw-Hill, Inc., New York.

Tecplot, Version 9.2 (2002). Tecplot Inc, Bellevue Washington.

Temps, R. C. and Coulson, K. L. (1977). "Solar Radiation upon slopes of different orientations." Solar Energy, 19, 179-184.

The Mathworks. MATLAB Version 6.0 – Student Edition. 2001.

Thornthwaite, C. W. and Mather, J. R. (1955). The Water Balance. Publications in Climatology, Vol. 8 No. 1, Drexel Institute of Technology, Centerton, New Jersey.

Thornton, P. E., Running, S. W., and White, M. A. (1997). "Generating surfaces of daily meteorological variables over large regions of complex terrain." Journal of Hydrology, 190, 214-251.

Tian, Y. Q., Davies-Colley, R. J., Gong, P., and Thorrold, B. W. (2001). "Estimating solar radiation on slopes of arbitrary aspect." Agricultural and Forest Meteorology, 109, 67-74.

Timms, G. P. and Bennett, J. W. (2000). "The effectiveness of covers at Rum Jungle after 15 years." Proceedings of the Fifth International Conference on Acid Rock Drainage, 813-818.

Tindall, J. A. and Kunkel, J. R. (1999). Unsaturated Zone Hydrology for Scientists and Engineers, Prentice-Hall, Inc, New Jersey.

Torri, D. (1996). "Slope, aspect and surface storage." Soil erosion, conservation, and rehabilitation., Agassi-Menachem (editor), ed., Marcel Dekker., New York, United States, 77-106.

Tsaparas, I. and Toll, D. G. (2002). "Numerical analysis of infiltration into unsaturated residual soils." Unsaturated Soils 2002, Balkema, 755-761.

Tyler, S. W., Kranz, S., Parlange, M. B., Albertson, J., Katul, G. G., Cochran, G. F., Lyles, B. A., and Holder, G. (1997) Estimation of groundwater evaporation and salt flux from Owens Lake, California, USA. Journal of Hydrology 200[1-4], 110-135.

Unsaturated Soils Group. (1997). SoilCover. Unsaturated Soils Group, University of Saskatchewan. Saskatoon, Saskatchewan.

US Army Corps of Engineers (2001). Hydrologic Modeling System HEC-HMS User's Manual, Version 2.1, US Army Corps of Engineers, Hydrologic Engineering Center, Davis, CA.

van Asch, T. W. J., van Dijck, S. J. E., and Hendriks, M. R. (2001). "The role of overland flow and subsurface flow on the spatial distribution of soil moisture in the topsoil." Hydrological Processes, 15(12), 2325-2340.

Varghese, S., Murthy, A. S. V., and Narasimha, R. (2003). "A fast, accurate method of computing near-surface longwave fluxes and cooling rates in the atmosphere." Journal of the Atmospheric Sciences, 60, 2869-2886.

Varley, M. J., Beven K.J., and Oliver, H. R. (1996). "Modelling solar radiation in steeply sloping terrain." International Journal of Climatology, 16, 93-104.

Verberg, K., Ross, P. J., and Bristow, K. L. (1996). SWIM v2.1 User Manual Divisional Report No 130, CSIRO Division of Soils, Australia.

Vermaak, J. and Bezuidenhout, N. (2003). "The performance of trial cover used for the rehabilitation of acid generating coal reject dumps in Northern Kwazulu-Natal, South Africa." Proceedings Sixth International Conference on Acid Rock Drainage (ICARD), 399-410.

Wallach, R., Grigorin, G., and Rivlin, J. R. B. J. (1997). The errors in surface runoff prediction by neglecting the relationship between infiltration rate and overland flow depth. Journal of Hydrology. 200, 243-259.

Warren, S. D., Hohmann, M. G., Auerswald, K., and Mitasova, H. (2004). "An evaluation of methods to determine slope using digital elevation data." Catena, 58, 215-233.

Weast, R. C. Ed. (1985). CRC Handbook of Chemistry and Physics, CRC Press, Boca Raton, FL.

Webb S.W., McCord J.T., and Dwyer S.F. (1997). "Prediction of tilted capillary barrier performance." SAND. Sandia National Laboratories. Albuquerque, NM, United States.

Weeks, B. and Wilson G.Ward (2001). "Measurement methods for evaporative fluxes over the short term." Canadian Geotechnical Conference.

Weeks, B. and Wilson G. Ward (2006). "Variations in moisture content for a soil cover over a ten-year period." Canadian Geotechnical Journal. 42(6), 1615-1630.

Weeks, O. L., Mansell, R. S., and McCallister, S. W. (1992). "Evaluation of soil top-cover systems to minimize infiltration into a sanitary landfill: A case study." Environ Geol Water Sci, 20(2), 139-151.

Weiss, A. (1982). "An experimental study of net radiation, its components and prediction." Agron J., 74, 871-874.

Wels, C., O'Kane, M., Fortin, S., and Christensen, D. (2001). "Infiltration test plot study for waste rock at Questa Mine, New Mexico." 8th Annual National Meeting, American Society for Surface Mining and Reclamation.

Western, A. W., Grayson Rodger B., Bloschl Gunter, Willgoose Garry R, and McMahon Thomas A. (1999). "Observed spatial organization of soil moisture and its relation to terrrain indices." Water Resources Research, 35(3), 797-810.

Whiteman, C. D., Allwine, K. J., Fritschen, L. J., Orgill, M. M., and Simpson, J. R. (1989). "Deep valley radiation and surface energy budget microclimates. Part I: Radiation." Journal of Applied Meteorology, 25(5), 414-426.

Whiteman, C. D., Allwine, K. J., Fritschen, L. J., Orgill, M. M., and Simpson, J. R. (1989). "Deep valley radiation and surface energy budget microclimates. Part II: Energy budget." Journal of Applied Meteorology, 25(5), 427-437.

Williams, B., Neivandt, R., O'Kane, M., Browne, D., and White, C. (2003). "Demonstration of the application of a soil moisture monitoring system at the Mt. Leyshon tailings dam and waste rock cover system." Proceedings of 6th International Conference for Acid Rock Drainage.

Williams, D. J., Currey, N. A., Ritchie, P., and Wilson, G. W. (2003). "Kidston waste rock dump design and 'store and release' cover performance seven years on." Proceedings Sixth International Conference on Acid Rock Drainage (ICARD), 419-426.

Wilson, G. W., Fredlund D.G., and Barbour S.L. (1994). "Coupled soil-atmosphere modelling for soil evaporation." Canadian Geotechnical Journal, 31, 151-161.

Wilson, G. W. (1990). "Soil Evaporative Fluxes for Geotechnical Engineering Problems." University of Saskatchewan.

Wilson, G. W., Barbour S.L., Swanson, D., and O'Kane, M. (1995). "Instrumentation and modelling for saturated/unsaturated performance of soil covers for acid generating waste rock." Hydrogeologie, 4, 99-108.

Wilson, G. W., Williams, D. J., and Rykaart, E. M. (2003). "The integrity of cover systems - An update." Proceedings Sixth International Conference on Acid Rock Drainage (ICARD), 445-451.

Woo, M. K., Marsh, P., and Pomeroy, J. W. (2000). "Snow, frozen soils and permafrost hydrology in Canada 1995-1998." Hydrological Processes, 14(9), 1591-1611.

Wright, J. L. (1982). "New evapotranspiration crop coefficients." Journal of Irrigation and Drainage Engineering, 108(1), 57-74.

Yanful, E. K. (1993). "Oxygen diffusion through soil covers on sulphidic mill tailings ." Journal of Geotechnical Engineering, 119(8), 1207-1228.

Yanful, E. K., Bell, A. V., and Woyshner, M. R. (1993a). "Design of a composite soil cover for an experimental waste rock pile near Newcastle, New Brunswick, Canada." Canadian Geotechnical Journal, 30, 578-587.

Yanful, E. K., Riley, M. D., Woyshner, M. R., and Duncan, J. (1993b). "Construction and monitoring of a composite soil cover on an experimental waste rock pile near Newcastle, New Brunswick, Canada." Canadian Geotechnical Journal, 30, 588-599.

Yanful, E. K. and Mousavi, S. M. (2003). "Estimating falling rate evaporation from finite soil columns." The Science of the Total Environment,(313), 151-152.

Yanful, E. K., Mousavi, S. M., and Yang, M. (2003). "Modeling and measurement of evaporation in moisture retaining soil covers." Advances in Environmental Research, 7, 783-801.

Yang M. and Yanful E.K. (2002). "Water balance during evaporation and drainage in cover soils under different water table conditions." Advances in Environmental Research , 6, 505-521.

Young, K. L., Woo M.K., and Edlund S.A. (1997). "Influence of local topography soil and vegetation on microclimate and hydrology at a High Arctic site." Arctic and Alpine Research, 29, 270-284.

Zhang, L. L., Fredlund, D. G., Zhang, L. M., and Tang, W. H. (2004). " Numerical study of soil conditions under which matric suction can be maintained." Canadian Geotechnical Journal, 41, 569-582.

Zornberg, J. G., LaFountain, L., and Caldwell, J. A. (2003). "Analysis and design of evapotranspirative cover for hazardous waste landfill." Journal of Geotechnical and Geoenvironmental Engineering, 129(6), 427438.

Appendix A: Runoff and Infiltration for Slopes

A 1 Factors Affecting Infiltration and Runoff

Infiltration and runoff are interrelated processes. At the most simple level, the sum of the two can be considered equal to the applied precipitation. More advanced approaches can also account for precipitation temporarily stored on the surface, either through ponding or interception on vegetation. While infiltration and runoff theory are treated separately in the following sections, their interrelation should be kept in mind.

A 1.1 Basic Infiltration Theory

The calculation of infiltration into soils has been the subject of considerable research, and many alternative approaches to infiltration problem have been taken. The approaches can be grouped into empirical equations based on curve fitting to observed field data, and physically-based solutions developed from the processes that are thought to govern infiltration.

Some of the most well-known and commonly used empirical equations for infiltration include the approaches of Holtan (1961), Horton (1939) and Kostiakov (1932). The Holtan (1961) and Hortan (1939) approaches are both based on the concept that the infiltration capacity of the soil is a function of its initial capacity, and some final steady-

state infiltration rate. The Kostiakov (1932) approach relies on a power relationship between the cumulative infiltration, and the time since the start of the infiltration process.

A more sophisticated, and potentially more accurate treatment of infiltration problems is available through the application of Richards' (1931) equation. Richards developed the equation by combining Darcy's law with the continuity equation. The Richards' equation is commonly written in one of three forms, head (h) based, water content (θ_W) based, or the mixed form. The three forms are shown below:

Head Based:

$$C(h)\frac{\partial h}{\partial t} - \nabla \cdot K(h)\nabla h - \frac{\partial K}{\partial z} = 0$$

Water Content Based:

$$\frac{\partial \theta_w}{\partial t} - \nabla \cdot D(\theta_w)\nabla \theta_w - \frac{\partial K}{\partial z} = 0$$

Mixed:

$$\frac{\partial \theta_w}{\partial t} - \nabla \cdot K(h)\nabla h - \frac{\partial K}{\partial z} = 0$$

Where:

z = vertical dimension, positive upwards
h = pressure head
θ_W = volumetric water content
K(h) = unsaturated hydraulic conductivity function
C (h) = $\partial\theta_W/\partial h$; specific moisture capacity function
$D(\theta_W) = K(\theta_W)/C(\theta_W)$; unsaturated diffusivity

As can be seen from the above equations, Richards' equation is non-linear. As a result, analytical solutions to Richards' equation are only possible for certain, specific cases (Celia et. 1990). Many of the commonly used physically based solutions for infiltration problems can be considered closed-form solutions of the Richards' equation for cases where the soil is not layered and has a uniform initial water content (Tindall and Kunkel, 1999). Some of the common solutions that fall in this category include those of Green and Ampt (1911), and Philip (1957). For less restrictive conditions, numerical computer-based solutions have been developed, and are widely accepted (Dunin, 1976).

Each of the above forms of Richards' equation has advantages and disadvantages for numerical situations. As discussed by Pan and Wierenga (1995), solutions that are developed from the water content based formulation generally perform quite well for initially dry soil, but cannot handle saturated flow modeling and are limited in their ability to model multiple soil types in a single system. Head based solutions can cope with saturated/unsaturated flow, but are prone to mass balance errors and numerical instability in the solution of very dry soil problems.

From the application of Richards' equation to infiltration problems, it can be seen that that variations in the soils moisture content in the field will lead to variations in the infiltration rate. (Dunin, 1976). Dunin (1976) also stated that increases in the soil moisture content would increase the chance of overland flow. This view fails to account for the significant changes that may occur in unsaturated soil hydraulic conductivity as a result of low moisture contents. At very low moisture contents, the unsaturated hydraulic conductivity of a soil may be several orders of magnitude lower that its saturated value, resulting in higher runoff rates until significant moisture contents can develop in the soil (Fredlund and Rahardjo, 1993).

A 1.2 Runoff Theory

Hortonian overland flow, initially proposed in the 1930's by R.E. Horton (1939), is a well-known conceptual model for runoff. In the Hortonian model, runoff is a function of the precipitation rate and the infiltrative capacity of the soil. Where the precipitation rate exceeds the infiltration capacity of the soil, the excess will become runoff, or overland flow.

Dunne and Black (1970) proposed saturation excess runoff as an alternative runoff process. Under this process, the water content of the soil becomes an important factor, with runoff occurring when the soil surface is saturated, either through the presence of a perched water table, or through saturation of the entire soil column. Other researchers have found that the antecedent moisture content of soils are a significant factor in the runoff generated, including Barbour et al (1999), Allan and Roulet (1994), Dingman

(1994). Cabral et al (1992) considered saturated areas of soil to be effectively impermeable to precipitation, and to contribute fully to runoff. Barbour et al (1999) found that even when the soil profile was unsaturated and rainfall rates were less than the saturated conductivity of the soil, significant amounts of runoff were generated.

A 1.3 Modifications to Theory to account for Slope

Under sloping conditions, it is common to assume in slope stability studies that all of the precipitation that does not infiltrate will runoff from the slope. However, in the field of hydrology, where the researchers are concerned with the peak flows at some point of downstream runoff from hillslopes, the case where surface overland flow may infiltrate at some point downslope is also often considered. When water flows downslope, the depth of flow will affect the hydraulic gradient driving infiltration. Cabral et al (1992) showed that the depth of flow is relatively insensitive to the slope angle at shallow slopes. Further, while the infiltration rate can affect the depth of overland flow on the slope, Wallach et al (1997) showed in a theoretical study that neglecting this effect introduces only a small error in the solution (in the order of a few percent).

The assumption that all of the water that does not infiltrate will runoff, without infiltrating downslope has been termed the "cascade solution" by Gandolfi and Savi (2000). The authors compared the cascade solution to a fully coupled solution, using a one-dimensional solution of the Richards' equation coupled with a two-dimensional shallow water equation for overland flow for the coupled solution. The authors found

that there could be a significant difference between the coupled solution and the cascade solution, at least when dealing with deep soil profiles. Where the soil profile is relatively thin (such as for a soil cover), or the water table is relatively near the surface, the differences in the solutions were expected by the authors to become much smaller.

Ponding can be considered on both horizontal and sloping surfaces. For ponding to occur, there must be some local depression for water to accumulate. Depressions on sloping surfaces will have less storage capacity than equivalent depressions on horizontal surfaces (Torri, 1996).

One of the difficulties in fully defining the effect of slope on runoff is that the runoff from a sloping soil does not necessarily occur as a uniform sheet flow over the soil, as described in Horton's model. More typically, local variations in the topography will lead to flow concentration in rivulets down slope, in much more complex patterns than the model can handle (Bryan and Posen, 1989). Erosion and the development of rills can lead to local increases in the infiltration rate (Torri, 1996).

A 2 Past Research on the Effect of Slope on Infiltration and Runoff

Past research on the effect that slope has in infiltration and runoff includes both experimental studies (discussed in Section A 2.1) and numerical model studies (discussed in Section A 2.2).

A 2.1 Experimental Observations on Infiltration and Runoff

One of the most complete studies on the effect of soil cover slope on runoff and infiltration was conducted by Nyhan et al (1997), on east-facing soil covers with slopes of 5, 10, 15, and 25%. With a careful characterization of the water balance for several different cover designs, the authors found that for all of the soil covers evaluated, seepage was always greatest through the flattest plots. The authors also found that runoff tended to increase with surface slope, but that the results were not monotonically increasing with slope. For individual rainfall events, there was no clear correlation between slope angle and runoff.

The effect of slope on runoff was relatively insignificant in the study by Nyhan et al (1997). The precipitation losses measured during the study were 86 to 91% due to evaporation, and only 2 to 3% due to runoff, reflecting the effect of the semi-arid climate in which the study was conducted.

Weeks et. al (1992) conducted a study of soil covers on landfill covers. This study included a comparison of seepage through the soil cover following a series of irrigations,

ranging from 130 to 450 mm. In all cases, the steeper slope (20% surface slope) registered infiltration less than or equal to that observed on the shallower slope (7% surface). The cover soil used had a saturated hydraulic conductivity of 2.4 x 10^{-8} m/sec, and infiltration was calculated based on measured head gradients and the unsaturated hydraulic conductivity function for the soil.

Another field study, conducted by O'Kane et al. (2000) looked at the performance of a store-and-release cover placed over mining waste in a semi-arid environment. In comparing the soil suction measured in horizontal and sloping (36%) sections of the cover, it appeared that runoff was enhanced and infiltration reduced on the sloping section.

Fox et al (1997) conducted a rigorous laboratory study on the effect of slope angle on infiltration, using soil boxes filled with a sandy loam and sloped at angles between 2.6% and 40% degrees. They found that the infiltration rate decreased with increased slope angle. They did not feel that the higher infiltration on shallower slopes was due to greater pressure head driving infiltration. While greater flow depths were observed on the shallower slopes, the difference in the pressure head caused by the greater depth of flow was negligible. The authors suggest that on shallower slopes, the greater depth of flow may submerge areas of slightly higher permeability, resulting in an overall greater average permeability for the soil.

A study of steady-state runoff processes with soil boxes sloped at 2, 8 and 17% was conducted by Helming et. al. (1993). While looking at the effects of surface roughness,

the authors also noted that that the 17% slope generated steady state runoff amounts that were 10 to 20% greater than that observed on the 8 and 2% slopes.

Goczan (1972) conducted a laboratory study on sloping blocks of a forest soil (slope angles of 0, 8, 15, 21, 30 and 40%) under artificial rainfalls of 20 and 40 mm/hr. As shown on Figure A-2 (created from data presented in the paper), the greater rainfall rate produced runoff on all of the slopes, while the lower rate only produced runoff on the slopes of 21% or greater. For all of the cases where runoff was produced, the rate of runoff increased steadily with the slope.

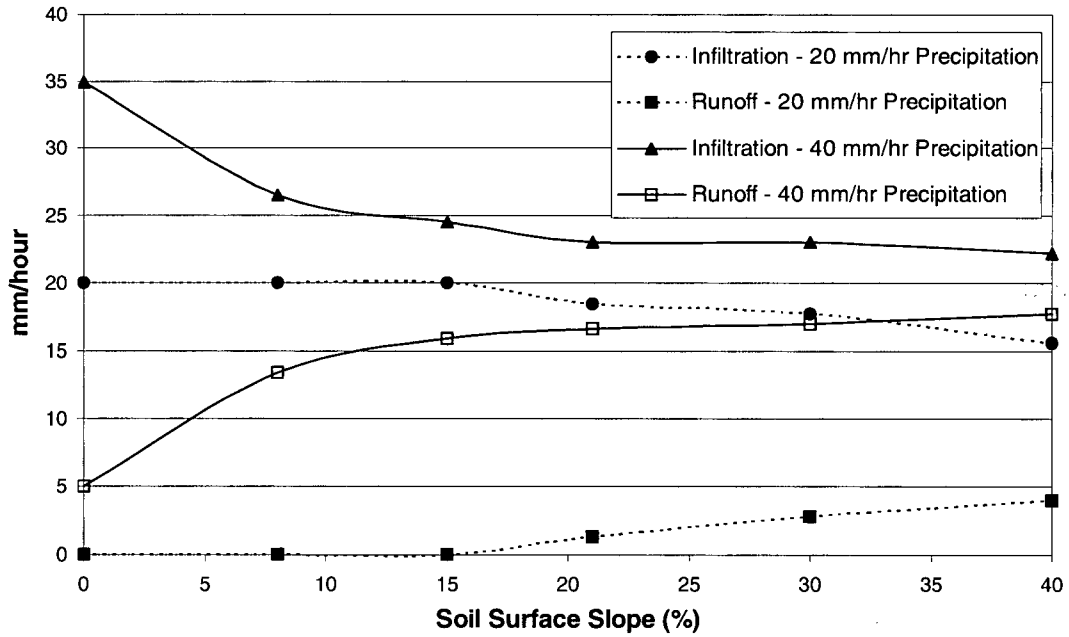

Figure A-2: Infiltration and Runoff from sloped soil (after Goczan, 1972)

El-Hassanin et al(1993) looked at the ratio of runoff to rainfall on a series of test plots in Burundi. Bare slopes were tested, along with those with natural and cultivated grasses,

and slope angles of 8, 12, 15, 20, and 30% were examined. In all cases, the amount of runoff observed increased with the slope angle. Runoff quantities were reduced by vegetation; the authors attribute this to the role of vegetation in preventing crust formation and maintaining the surface permeability of the soil.

Evett and Dutt (1985) conducted a study similar to that of El-Hassanin et. al (1993), looking at shallower slopes (1, 5, 10, and 15%). Evett and Dutt also found that runoff increased with slope, and developed the following empirical relationship to describe their results:

$$Q = B_1 (P - B_2)$$

Where

Q = runoff depth
P = Rainfall depth
B_2 = 'threshold rainfall depth' (0.34 for their soils)
B_1 = "runoff efficiency" = $S^{0.0453} X^{-0.183} + 0.183$
S = Slope
X = Slope length

This equation provided a close fit to the observed data, and suggests the relative effect of slope on the runoff observed. The importance of slope length is also suggested, a factor which the authors attribute to affecting the residence time of water on the slope.

Not all studies reported in the literature show that runoff rates increase with increases in slope. Cedra and Garcia-Fayos (1997) studied erosion and runoff from natural slopes of

2% to 55% under simulated rainfalls. In this study of dry, crusted slopes with minimal vegetation, the runoff coefficient was not affected by the slope angle. This does not necessarily mean that there was no effect of slope angle, as there were significant morphological differences between the steeper and shallower slopes studied. In particular, the authors noted that there was more surface cracking on the steeper slopes, which may have lead to higher infiltration rates at the start of the rainfall. In reviewing cases where infiltration increased with slope angle, Fox et al (1997) suggest that these cases "probably only arise where the [surface] seal is breached by rills and where there is a positive correlation between rill network development or depth and slope angle." Agassi et al (1990) also noted that a high rate of surface seal erosion on steep slopes could lead to a higher rate of infiltration on those slopes. Ben-Hur and Wakindiki (2004) also noted that there have been contradictory findings reported in the literature on the effect of slope on runoff.

A 2.2 Modeled Response to Surface Flux

The discussion of modeled responses to surface fluxes includes both a discussion of modeling techniques and results from model studies.

A 2.2.1 Modeling Techniques

The program SEEP/W (GEO-SLOPE International Ltd) has been used by many researchers in the geotechnical engineering field for the examination of infiltration into slopes. Gasmo et al (2000) and Tsaparas and Toll (2002) used the program to model

infiltration by setting a flux at the surface, with the condition that surface porewater pressures not exceed 0 kPa (water applied in excess of what was needed to maintain 0 kPa becomes runoff). Smith et al (2002) used a similar approach in the new finite element model that they had developed. In doing this, there is an implicit assumption that there is no ponding at the ground surface, as the ponding would result in porewater pressures at ground surface greater than zero (the porewater pressure would be proportional to the depth of water ponded). On steep or relatively smooth slopes, this may be a passable assumption.

In using this type of boundary condition, it is also important to carefully monitor the time steps used. Smith et. al. (2002) pointed out that it is otherwise possible for very high positive water pressures to develop during the time step before surface pressure is set to zero. This high porewater pressure timestep would then distort the porewater pressures in subsequent time steps.

Mesh size in the finite element grid is also important, especially near the soil surface where gradients can be large. Salvucci and Entekhabi (1995) recommended that a resolution on the order of centimetres is needed to depict infiltration fronts. Tsaparas and Toll (2002) used a mesh near the soil surface with elements 0.25 x 0.25 m.

A 2.2.2 Model Results

Tsaparas and Toll (2002) present a well-documented model, comparing the modeled and measured infiltration for an unsaturated soil slope. In order to accurately match the field

measured results, they found that they had to introduce a high permeability zone near the soil surface. The researchers felt that this zone simulated the effect of grass on the surface permeability of the site, a contention supported by Dunin (1976) and others.

Tsaparas and Toll found that for this slope (27 degrees, with a soil $k=6x10^{-7}$ m/sec), the high suctions that had developed near the soil surface disappeared rapidly with rainfall. . In general, there was a strong correlation between the amount of rainfall and the amount of runoff. They found that for this slope rainfall amounts of less than 8 mm failed to produce runoff. For all of the rainfalls observed and modeled, only small changes in the porewater pressure were evident at depth, while there was a major component of flow downslope in the shallow subsurface. Lim et al (1996) also found that the changes in matric suction following a rainfall were smaller at larger depths, and that small rainfalls had no effect on the suction at greater depths.

Gasmo et al (2000) studied the effect of applying a variety of fluxes to a sloping surface. Under steady state infiltration conditions, they found that a greater infiltration rate could be maintained at the crest of the hill, as downslope flow resulted in a saturation of the available moisture storage space at the toe of the slope, while freeing up storage at the crest. For the transient analysis, fluxes were applied at rates both above and below the saturated hydraulic conductivity of the slope soil. They found that applying a rainfall rate greater than K_{sat} resulted in an initially very high infiltration rate that decreased over time to less than K_{sat}. In contrast, at very low applied fluxes the initial infiltration rate

was very low, and increased gradually as the soil wetted as its hydraulic conductivity increased.

A 3 Infiltration and Runoff Summary

Experimental studies available in the literature have shown a general agreement that runoff tends to increase with increases in slope angle, while infiltration correspondingly decreases. Due to difficulties in solving the Richards' equation, variations in the infiltration excess approach, where water in excess of the soil's infiltrative capacity (however that is determined) is considered runoff, still appear to be the most common analytical approach for determining how rainfall is partitioned into runoff and infiltration.

Appendix B – Solar Geometry Calculations

The potential shortwave radiation on a horizontal surface under clear sky conditions, without considering atmospheric effects (S_o) is a function of the energy emitted by the sun, the distance between the earth and the sun, and the position on the earth of the location under consideration.

The solar constant represents the energy received by the earth from the sun under mean conditions, and measured on a surface perpendicular to the solar beam. The standard value of the constant as accepted by NASA is 1353 W/m^2 (Jansen, 1985), and is used in this thesis. Kumar et al (1997) show that there has been considerable debate over the value, with values of 1367 and 1373 W/m^2 also in the current literature. To account for variations in the distance between the earth an the sun throughout the year, the solar constant can be modified by the following relationship (Duffie, 1980):

$$G_{on} = (1+0.033 \cos (360\ t_j / 365))$$

Where:

G_{on} = extraterrestrial radiation, on a plane normal to the beam.

t_j = the day of the year (julian day)

To determine the potential radiation on a horizontal surface at a given location and for a specific day, it is necessary to calculate the solar declination for that day, and the length of the solar day.

The solar declination (δ) is taken at solar noon (when the sun is at its highest for the day), and is the angle formed between the sun and the plane of the equator. The declination can vary between +23.45° and –23.45°, with north taken as positive by convention.

Solar declination for any day of the year can be calculated as follows (Oke, 1987):

$$\delta = -23.45 \sin (360 (10 + t_j)/365)$$

Knowing the solar declination, it is then a simple matter to calculate the day length (or half-day length, h_S), as follows (Bristow, 1985):

$$h_S = \cos^{-1} (-\tan\phi \tan\delta)$$

Where:

ϕ = the latitude of the site (north positive).

Finally, S_O can then be calculated. For this work, a modified form of the equation for S_O given by Gates (1980) was used, incorporating the calculation of G_{on} shown previously:

$$S_o = 0.0864\ G_{on} \sin\phi \sin\delta\ (h_s - \tan h_s)(1/\pi)$$

This formulation gives S_o in MJ/m^2 for the day, assuming G_{on} is in W/m^2, and h_s is in radians.

Further Sun Angle Calculations

The solar zenith angle (θ_z) for a horizontal surface is the angle formed between a normal to the plane, and the location of the sun at any given time. It is a function of the site location (latitude), day of the year, and time of day. The angle will be at its minimum when the sun is highest in the sky (solar noon) and largest when the sun is near the horizon. It is given by (Duffie, 1980):

$$\theta_z = \cos^{-1}(\sin\varphi\sin\delta+\cos\varphi\cos\delta\cos\omega)$$

Where

ω = hour angle, the angular displacement of the sun through the sky at 15° per hour, zero at solar noon, positive in the afternoon, negative in the morning.

With the addition of the solar azimuth angle, the location the sun in the sky can be fully described. The solar azimuth angle is the location of the sun in the sky relative to true

north, measured in degrees clockwise from north (east = 90°). Before solar noon it is given by (Oke, 1987):

$$\Omega = \cos^{-1}(\sin\delta \cos\varphi - \cos\delta \sin\varphi \cos\omega)/\sin\theta_Z$$

And after solar noon, it is given by:

$$\Omega = 360^\circ - \cos^{-1}(\sin\delta \cos\varphi - \cos\delta \sin\varphi \cos\omega)/\sin\theta_Z$$

Finally, the angle between the solar beam and a normal to a plan with slope β and azimuth ψ (downslope direction) is given by (Oke, 1987):

$$\theta = \cos\text{-}1(\cos\beta \cos\theta_Z + \sin\beta \sin\theta_Z \cos(\Omega - \psi))$$

Appendix C – SunModel

The general form and theoretical development of the model for the prediction of net radiation on sloping surfaces was described in Chapter 4 of this thesis. The methodology described in Chapter 4 has been coded into a computer program called SunModel. The model was developed using MATLAB Release 12 (The MathWorks Inc. 2001), a high level programming language designed for technical applications. Programming in MATLAB allows a great deal of flexibility for handling data as matrices, and the matrix formulation of the language was well-suited to handling several years' worth of data for the anticipated analyses.

This appendix provides a brief description of SunModel program, including printout of the complete model code for an example problem. Also appended is the code for the analysis of data from a three-dimensional finite element mesh of the ground surface, such as can be developed in a plotting program like Tecplot (2002). The version printed includes routines for the calculation of both net radiation at all nodes in the mesh (using sunfunc) and the potential evaporation (using a data file with temperature, relative humidity and wind speed for each day). The program for the three-dimensional calculations is PEmodel.m. This program calls a short subroutine (PEfunc.m) for the calculation of daily potential evaporation by the Penman method. This subroutine could easily be altered if another method for the calculation of PE was desired.

The code for SunModel (MATLAB language)

The central code for SunModel consists of a function (sunfunc.m) that can be called to analyze data collected at a site. A shell program written for the analyses required calls the function (sunfunc.m), and passes to the function the specific site data (such as latitude, slope angle, slope azimuth, albedo, emissivity) for the analysis run.

The core function (sunfunc.m) then loads a user-specified data file, containing three columns, with the Julian date, the average daily air temperature, and the measured net radiation on the horizontal surface. This data file can be created in excel and exported as a tab-delimited .dat file.

For each day of data in the data file, the sunfunc.m routine performs the estimation of the net radiation on a horizontal surface. Two small functions (timecalc.m and radpot.m) are called by sunfunc.m in the process of the analysis.

The function sunfunc.m returns a single value for each day analyzed, equivalent to the estimated net solar radiation received by the analyzed slope. This returned value is a vector matrix, with a length equal to the number of days analyzed.

In the example code printed out, the shell program kidscall.m is used to repeatedly call sunfunc.m for the analysis of net radiation received on alternative slopes. The data set used by sunfunc.m is kids98.dat, a file containing 365 days of data (1998) for the Kidston Gold Mine site in Queensland, Australia. For each slope analyzed, the shell program

kidscall.m calculates the sum of the total energy received on the slope over the year, and creates a bar graph to illustrate the energy from the various scenarios.

For the three dimensional mapping, the program PEmodel.m is used to sort through the finite element mesh data for a 3D map of the site, such as could be generated in Tecplot (2002). A data input file with the locations of all nodes in the model space (xyz1.dat in the example shown) is required, as is a file containing the linkage data for the nodes (links1.dat in the example). Once the slope and azimuth at each node is calculated, the program calls sunfunc.m for the calculation of net radiation at each node. Once this is done, the program can also call PEfunc.m to calculate the potential evaporation at each node. This requires a supplemental weather data file with relative humidity (decimal fraction) and windspeed (km/hr) data corresponding to the daily temperature and net radiation data file that was called by sunfunc.m. Once the analysis is complete, the program PE model will generate a data file with net radiation and potential evaporation data for each day at each node. This data file can be imported to a plotting program, and used to prepare colour contour maps of the site.

Printout of Model Code:

Function kidscall.m

```
%Kidston Data setup and analysis
   %Slope at 45 degrees
   Slope45N = sunfunc(-16,45,0,0.2,0.2,.95);
   Slope45N = sum (Slope45N)
   Slope45E = sunfunc(-16,45,90,0.2,0.2,0.95);
   Slope45E = sum (Slope45E)
   Slope45S = sunfunc(-16,45,180,0.2,0.2,0.95);
   Slope45S = sum (Slope45S)
   Slope45W = sunfunc(-16,45,270,270,0.2,0.2,0.95);
   Slope45W = sum (Slope45W)
      %Slope at 20 degrees
   Slope20N = sunfunc(-16,20,0,0.2,0.2,0.95);
   Slope20N = sum (Slope20N)
   Slope20E = sunfunc(-16,20,90,0.2,0.2,0.95);
   Slope20E = sum (Slope20E)
   Slope20S = sunfunc(-16,20,180,0.2,0.2,0.95);
   Slope20S = sum (Slope20S)
   Slope20W = sunfunc(-16,20,270,0.2,0.2,0.95);
   Slope20W = sum (Slope20W)
% Get the data for radiation on a horizontal surface
   load kids98.dat
   data = kids98;
   Horiz = sum (data (:,3))
   Results = [Slope45N Slope20N;Slope45E Slope20E; Slope45S Slope20S; Slope45W Slope20W; Horiz
0];
   Locn = [0;90;180;270;360];
   bar (Locn,Results)
   xlabel ('Direction of Slope Orientation')
   ylabel ('Net Solar Energy Received by Slope over Year MJ/m2')
   legend ('Slope = 45 deg', 'Slope = 20 deg')
   title ('Net Solar Radiation on Various Slopes over the Year')
```

Function sunfunc.m

```
function Qnetslope = sunfunc (Lat,Slope,Azim,SlAlb,SurAlb,Emiss)

% A function to determine the Net Solar Energy recieved on a slope
   % with the above characteristics.  Function requires a data file with
   % the day, avg daily temp and Net Solar Rad on a horizontal surface
   % data should be in a tab delimited .dat file, exported from excel

load kids98.dat

% set data equal to the contents of the loaded file.
data = kids98;
Lat = Lat*pi/180;  %convert to radians
Slope = Slope*pi/180;
Azim = Azim* pi/180;
SolarCons=1353; %solar constant in W/m2

% Estimate Clearsky atmospheric Emissivity, based on the Swinbank formulae
Eac = 1.22-171./(((5.67e-8)*(data(:,2)+273).^4));

%  if eo is available, could use Brutsaert, remove % on next line to used if vapour pressure in mb is in 4th
col of data
%Eac = 1.24.*(data(:,4)./(data(:,2)+273)).^(1/7);
```

```
%or Idso formulation
%requires a0, 0.6 (ocean) to 0.7 (inland); 0.66 coastal value; remove % on next two lines to use
%a0=0.66;
%Eac = a0 + 5.95e-5 .* exp(1500./(data(:,2)+273));

% set difference between screen height and cloud temps (10 C from Novak)

dTcl = 10;
Tk = data(:,2)+273;  %temp in K between screen height and soil surface

% step through data set of length m, ie, m number of days

[m,n] = size(data);
for i=1:m
   fo = 1;  % initial estimate of f (fraction of sky that is clear)
   loopnum = 50;  % maximum number of iterations for a day
   for loop = 1:loopnum
      Ea(i,1)= fo*Eac(i,1) + (1-fo)*(Eac(i,1)+(1-Eac(i,1))*(1-4*dTcl/Tk(i,1)));
      %Estimate Net Downwards Longwave
      Ld(i,1) = 0.0864*Ea(i,1)*(5.67e-8)*((data(i,2)+273).^4);

       %Estimate Longwave Upwards
      Lu(i,1) = Emiss*0.0864*5.67e-8*(data(i,2)+273).^4;
      %Estimated Net Longwave
      Lnet(i,1)  = Ld(i,1) - Ld(i,1)*(1-Emiss)-Lu(i,1);
      %Estimated Net Shortwave
      Snet(i,1) = data(i,3)-Lnet(i,1);
      %Estimated Total Shortwave Downwards
      St(i,1) = Snet(i,1) /(1-SIAlb);
      %Estimated Upwards Shortwave
      Su(i,1) = St(i,1)*SIAlb;
      %Partitioning Shortwave into Beam and Diffuse Components
         %Calculate Solar Declination (ANSWER IN DEGREES)
         SolDec(i,1) = -23.45*cos((360*(data(i,1)+10)/365)*pi/180);
         %Estimated Solar Radiation on a surface perpendicular to the beam
         Kon(i,1) = SolarCons*(1+0.033*cos ((360*data(i,1)/365)*pi/180));
         %Calculate half daylength, in radians
          hs(i,1) = acos(-tan(Lat)*tan(SolDec(i,1)*pi/180));
         %Calculate the potential solar radiation on a Horizontal Surface
         So(i,1)= (86400/(pi*1000000))*Kon(i,1)*sin(Lat)*sin(SolDec(i,1)*pi/180)*(hs(i,1)-tan(hs(i,1)));
      if St(i,1) < 0
            St (i,1)= 0.5*So(i,1)
      end
         %Total Daily Transmittance  = St/So
         Tt(i,1)=St(i,1)/So(i,1);
      %recalculate fo
        %set constant a1
        a1=1.1;
        fc1=Tt(i,1)*a1+(1-a1);
        if fc1 >1   %simple trap to prevent fc1 from blowing up
           fc1=.37;
        end
        if fc1 <0  % second trap for negative fo values
           fc1= .37;
        end
        error = abs (fo-fc1);
        if error <= 0.001       %error tolerance
           solveinfo(i,2) = loop; %set second column in solveinfo = # of iterations
           solveinfo(i,3) = (fo-fc1); % set third to residual
           solveinfo(i,4) = fo; % set fourth to final value for fo
           break   % end the for loop for day m; should return to outer loop for day m+1
        else
```

```
        fo=fc1;  % if the difference is greater than the specified tolerance, set fo to the new calculated value
      end   % end of if statement

    end  % end of for loop stepping through 50 max iterations
    solveinfo(i,2) = loop; %set second column in solveinfo = # of iterations
    solveinfo(i,3) = (fo-fc1); % set third to residual
    solveinfo(i,4) = fo; % set fourth to final value for fo
 end % end of loop stepping through each day for calculations
 solveinfo(:,1) = data(:,1);
 solveinfo (:,2);  % remove semi-colon to display the iteration data (# of iterations and residual for each day)
 % B is the maximum clear sky transmisivity
  %  It should be estimated from site data; typically between 0.7 and 0.8
  B=0.74;
  % Daily diffuse transmitance (from eqn 6, Bristow et al 1985)
  Td = Tt.*(1-exp(0.6*(1-B./Tt)/(B-0.4)));
for i=1:m  % error trap to prevent negative Sd values
  if Td (i,1) < 0
     Td (i,1) = 0;
  end
end
  Td;
  % Final calculation of beam (Sb) and diffuse (Sd) components
  Sd = Td .* So;
  Sb = St - Sd;
%Calculation of factors to use in slope calculations
  %View Factor
  f= (cos(Slope/2))^2;
%Slope Factor F, Calculated based on the algorithm of Swift (1976)
%the full algorithm has been used, with corrections to account for all
%latitudes and all slopes
  %Latitude of Equivalent Slope, L1 (in radians)
  L1=asin (cos(Slope) * sin (Lat) + sin(Slope)*cos(Lat)*cos(Azim));
  %Time offset between actual and equiv slopes, hour angle (radians)
  D1=cos(Slope)*cos(Lat)-sin(Slope)*sin(Lat)*cos(Azim);
  if D1==0
     D1=1.0e-10;
  end
  L2 = atan(sin(Slope)*sin(Azim)/D1);
  if D1<0
     L2 = L2+pi;
  end
  % Calls timecalc function, which returns values in radians
  T=timecalc(L1,SolDec);
  T7=T-L2;
  T6=-T-L2;
  T = timecalc(Lat,SolDec);
  T1=T;
  T0=-T;
  %get the length of vector T7, and store it as variable i
  [i,j]=size(T7);
  %create a zero matrix for R4 of the appropriate length
  R4 = zeros(i,j);
  for n = 1:i
     T3(n,1)=T7 (n,1); % set T3 for the nth element to T7 as default
       if T7(n,1)>T1(n,1) %check if T7>T1 for given element
          T3(n,1) = T1 (n,1);  % set T3 for nth element to T1 for this case
       end
     T2 (n,1) = T6 (n,1); %set default
       if T6(n,1)<T0(n,1)
          T2 (n,1) = T0 (n,1);
       end
       %start loop for calculation of R4 (using call to radpot.m function)
```

```
        if T3(n,1)<T2(n,1)
           T2 (n,1)=0;
           T3 (n,1)=0;
        end
        T6 (n,1)=T6 (n,1)+2*pi;
        if T6 (n,1)<T1 (n,1)
           T8(n,1)=T6(n,1);
           T9(n,1)=T1(n,1);

R4(n,1)=radpot(L2,L1,T3(n,1),T2(n,1),SolDec(n,1),Kon(n,1))+radpot(L2,L1,T9(n,1),T8(n,1),SolDec(n,1),Kon(
n,1));
        else
           T7(n,1)=T7(n,1)-2*pi;
           if T7(n,1)>T0(n,1)
              T8(n,1)=T0(n,1);
              T9(n,1)=T7(n,1);

R4(n,1)=radpot(L2,L1,T3(n,1),T2(n,1),SolDec(n,1),Kon(n,1))+radpot(L2,L1,T9(n,1),T8(n,1),SolDec(n,1),Kon(
n,1));
           else
              R4(n,1)=radpot(L2,L1,T3(n,1),T2(n,1),SolDec(n,1),Kon(n,1));
           end
        end
     end
  %And finally, the slope factor is:
  F=R4./So;
%Total shortwave to slope
  Sts=Sb.*F + Sd.*f + St*(1-f)*SurAlb;
%Net shortwave to the slope
  Stsnet=Sts*(1-SIAlb);
%longwave downwards to slope
  Ldslp=Ld*f + Lu*(1-f);
%Net longwave to slope
  Lnetslp = Ldslp-(1-Emiss)*Ldslp-Lu;
%net total solar radiation to slope
  Qnetslope=Stsnet+Lnetslp;;
```

Function timecalc.m

```
function z=timecalc(y,SolDec)
%  Function called as subroutine for time calculation by sunmodel.m
z=acos(-tan(y).*tan(SolDec*pi/180));
z=real (z);
```

Function radpot.m

```
function z=radpot(v,w,x,y,SolDec,Kon)
%  Function called as subroutine for time calculation by sunmodel.m
%  Used for the calculation of potential solar energy on surfaces
z=(Kon*3600/(1000*1000)).*(sin(SolDec*pi/180).*sin(w).*(x-
y).*(12/pi)+cos(SolDec*pi/180).*cos(w).*(sin(x+v)-sin(y+v)).*(12/pi));
```

Function PEmodel.m

```
%program to analyze data from tecplot triagulated finite element mesh
% Requires two data files: xyz.dat, with xyz location of all nodes
% and links.dat, with all connectivity data
% NB- these files are generated as a single file in tecplot - need to split manually into two files
clear nodes
clear points
```

```
clear cnnx
load xyz1.dat;
nodes = xyz1;
[m,n]=size (nodes);
points = 1:m;
nodes = [points' nodes zeros(m,3)]
load links1.dat
cnnx = links1
abovonly = [];

%start of main loop to step through the matrix nodes, and evaluate connection/slopes for each point
for i = 1:m
   %search for points that are connected to node i in list cnnx
   clear set
   clear set1
   clear above
   below =[];
   clear fullset
   set = [];
   [x,y] = size (cnnx);
   for j=1:x
      if cnnx(j,1) == i
         set = [set cnnx(j,2) cnnx(j,3)];
      end
      if cnnx(j,2) == i
         set = [set cnnx(j,1) cnnx(j,3)];
      end
      if cnnx(j,3) == i
         set = [set cnnx(j,1) cnnx(j,2)];
      end
   end
   % create set1, a vector with an ascending list of all of the points that are connected to point i
   set1=sort(set);
   %find out how many elements are in set1
   q=numel(set1);
   %set duplicate entries in set1 to zero
   for j=1:q
      if j+1 <=q
         if set1(j) == set1(j+1)
            set1 (j+1)=0;
         end
      end
   end
   %eliminate nonzero entries
   set1=nonzeros (set1);
   set1 = set1';
   q=numel (set1);
   for j=1:q
      fullset (j,:) = [set1(j) nodes(set1(j),2) nodes(set1(j),3) nodes(set1(j),4)];
   end
   %clear any blank rows in fullset
   j=1;
   while j <= q
      if fullset(j,1)==0
         fullset(j,:) = [];
         [q,x]= size (fullset); %set q equal to the new size of fullset
         j=j-1; %bring back the step, so as not to skip the next line of the matrix
      end
      j=j+1;
   end
   %Area calculation - calculate the area associated with node i
   % this area assumes that the node i is enclosed
```

```
[a,b] = size(fullset);
clear doublearea
clear area
doublearea = fullset(1,2)*(fullset(2,3)-fullset(a,3))+ fullset(a,2)*(fullset(1,3)-fullset(a-1,3));
for j=2:(a-1)
   doublearea = doublearea+fullset(j,2)*(fullset((j+1),3)-fullset((j-1),3));
end
%check to see if the area would be larger if i is included in the perimeter (ie, i is a boundary node)
clear fullset1
fullset1 = [fullset; nodes(i,1) nodes(i,2) nodes(i,3) nodes(i,4)];
[a,b] = size(fullset1);
clear doublearea1
clear area1
doublearea1 = fullset1(1,2)*(fullset1(2,3)-fullset1(a,3))+ fullset1(a,2)*(fullset1(1,3)-fullset1(a-1,3));
for j=2:(a-1)
   doublearea1 = doublearea1+fullset1(j,2)*(fullset1((j+1),3)-fullset1((j-1),3));
end
if doublearea1>doublearea;
   doublearea=doublearea1;
end
%above calcs give double the planar area enclosed by the points
% tributary area for point i is calculated by dividing double area by two to get the enclosed area, and
dividing the
% enclosed area by the number of associated points
area = abs (doublearea/(2*a));
% place the calculated area for i in the last column of nodes
nodes(i,7) = area;
% now need to sort the values in fullset.  Those that have elevations greater or equal to that of i
% are placed in matrix 'above', while those with values below are placed in matrix 'below'
step = 1;
step1=1;
for j=1:q
   if fullset(j,4) >= nodes(i,4)
      above(step,:) = fullset (j,:);
      step = step+1;
   else below(step1,:) = fullset(j,:);
      step1= step1+1;
   end
end
% if the set 'below' is empty for node i, store null values (-6999) for the slope and azimuth of node i
% in the the matrix nodes
if isempty (below)
   nodes(i,5) = -6999;
   nodes(i,6) = -6999;
   % place the data from 'above' in matrix aboveonly that will collect all the data points associated
   %with nodes that have only points above.
   len = numel(above(:,1));  % how many nodes above
   col=i*ones(len,1);  % set a index colume to show that these nodes above are associated with element i
   above = [col above];
   abovonly = [abovonly; above]; % builds 'abovonly', the list of nodes above
else
   %if we reach this point, there are points below i, contained in 'below'
   %sum the vectors from i to the points in 'below'
   vectx = 0;
   vecty = 0;
   vectz = 0;
   clear slope
   clear azim
   [q,r]=size(below); % identify number of elements in 'below'
   for j=1:q
      vectx = vectx + below(j,2) - nodes(i,2);
      vecty = vecty + below(j,3) - nodes(i,3);
```

```
      vectz = vectz + below(j,4) - nodes(i,4);
    end
    % dy=vecty, dx = vectx, dz=vectz
    %calculate slope:
    if vectx ==0 & vecty ~=0
      slope = abs(atan(vectz/vecty));
    end
    if vecty ==0 & vectx ~=0
        slope =abs(atan(vectz/vectx));
    end
    if vectx~=0 & vecty~=0
        slope = atan(sqrt((vectz/vectx)^2 + (vectz/vecty)^2));
    end
    if vecty ==0 & vectx ==0
      slope =pi/2;
    end

    %convert from radians to degrees:
    slope = slope * 180/pi;
    % calculate Azimuth, where y = northing
    if vecty==0 & vectx > 0
      azim = pi/2;
    end
    if vecty == 0  & vectx<0
      azim = -pi/2;
    end
    if vecty ~=0
      azim = atan (vectx/vecty);
    end
    if vectx ==0 & vecty ==0
      azim = 0;
    end
    % convert azim from radians to degrees
    if vectx >= 0 & vecty >= 0
      azim = azim * 180/pi;
    else if vecty < 0
      azim = 180 + azim*180/pi;
    else %if vectx < 0 and vecty >=0 (the remaining condition)
      azim = 360 + azim*180/pi;
    end % end of azimuth correction to radians
    % insert slope and azimuth in appropriate spots within 'nodes'
  end
    nodes(i,5) = slope;
    nodes(i,6) = azim;
  end % end of routine that puts in dummy values if there are only points above i, and calcs slope and azim
if there are points below
end% ends the main loop - i is incremented for the next step through the data set


% now need to tidy up - evaluate the nodes that were not connected to lower data points
% clean up 'abovonly', which should have the node info for nodes with no points below
abovonly = sortrows (abovonly, [1,2]);  % sorts first by first column, then by second
[a,b]= size (abovonly);
j=1;
while j <= a
  vectorabove = [abovonly(j,1) abovonly(j,2)];
 while j+1 <=a & abovonly(j,1) == abovonly(j+1,1)
    vectorabove = [vectorabove abovonly(j+1,2)];
    j=j+1;
  end

  %have now produced 'vector above' which for the first node in the list, indictes all of the connected nodes
```

```
   %this is used to calculate the average slope for the first node, based on the slope and azimuth data
stored in
   %'nodes' for the above elements
   n=length (vectorabove);
   slopetot = 0;
   azimtot = 0;
   for i = 2:n   %start loop at 2, since 1 holds the node under consideration
      if nodes (vectorabove(i),5) == -6999 %make sure not to include any null values in the calculation
         slopetot = slopetot;
      else
         slopetot = slopetot + nodes(vectorabove(i),5);
      end
      if nodes (vectorabove (i),6) == -6999
         azimtot = azimtot;
      else
         azimtot = azimtot + nodes(vectorabove(i),6);
      end
   end
   %calculate averages for slope and azimuth.
   slopeavg = slopetot/(n-1);
   azimavg = azimtot/(n-1);
   %place averages in appropriate cells of 'nodes'
   nodes (vectorabove(1), 5) = slopeavg;
   nodes (vectorabove(1), 6) = azimavg;
   clear vectorabove
   j=j+1;
end
%matrix 'nodes' should now be a complete data file.
nodes

%SOLAR MODELLING OF TINSLOPE DATA

% Call sun2004final.m
[m,n] = size(nodes);
% Site data:
   Lat = 54.18
   Alb1=0.16
   Alb2 = 0.16
   Emiss = 0.9
% call sunfunc once for dummy variable, to get the new size for nodes
Qvalue = sun2004final (Lat, nodes(1,5), nodes(1,6),Alb1, Alb2,Emiss);
% expand nodes to have zero columns to hold Qvalues, total Qnet, and Qnet avg
n=numel(Qvalue);
nodes = [nodes zeros(m, n+2)];
for i = 1:m
   %Sunfunction requires (latitude, slope, azimuth, slope albedo, surrounding area albedo, Emissivity)
   Qvalue = sun2004final (Lat, nodes(i,5), nodes(i,6), Alb1, Alb2, Emiss);
   % calculate total qnet at the node
   % total is for whatever length of time (days) that the original data called by sunfunc is for.
   Qvaluetot = sum (Qvalue);
   %average is from total divided by the number of days in data set
   Qvalueavg = Qvaluetot/n;
   %build a matrix with Qnet total, and Daily Qnet data appended to the nodes matrix
   % nodes [node number, x,y,z,slope,azim, area, average Qnet, total Qnet, Qnet day 1, day 2, day 3, ...)
   % average Q value goes into column 8
   nodes(i,:) = [nodes(i,1:7) Qvalueavg Qvaluetot Qvalue'];
end
nodes
save EQ98.out nodes -ASCII -tabs

% CALCULATION OF POTENTIAL EVAPORATION FOR EACH NODE/DAY
clear PEdata weather weath1 weath2
```

```
[m,n] = size(nodes)
% load the basic weather data that is also called in sunfunc.m
load EQ98neg.dat
weath1 = EQ98neg

% Load the supplementary data file with {day, RH (fraction), windspeed (km/hr)}; daily averages in
% a tab delimited text file

load EQ98sup.dat
weath2 = EQ98sup

%Create a weather data file with [day, avg daily temp, RH, windspeed]

weather = [weath1(:,1) weath1(:,2) weath2(:,2) weath2(:,3)];

% from the number of columns in 'nodes', determine how many days of weather data there are
 days = n-9;
% set up a matrix for PE data, with 1 row for each node, an inital column of node index numbers, PE totals,
PE average
% and subsequent columns of PE data for each day
PEdata = zeros (m, days+3);

%Step through each node in the list
for i = 1:m
   %node elevation
   z= nodes (i,4);
   %put a node index number in the first column of PEdata
   PEdata(i,1)=i;
   %clear variables
   clear j day AvT RH Wind Qnode PEnode
   %step through each day
   for j=1:days
      day=j;
      AvT = weather (j,2);
      RH = weather (j,3);
      Wind = weather (j,4);
      Qnode = nodes (i, j+8);
      %call PEfunc.m to calculate PE at the node
      PEnode = PEfunc (day, AvT, RH, Wind, Qnode, z);
      %place the node data at the appropriate location in PEdata
      %PEdata is arranged [node#, PEtot, PEavg, PEday1, PEday2, etc . . ]
      PEdata (i, j+3)=PEnode;
      %End the day loop
   end
   % Insert the PE sum in column 2 of PEdata
   PEdata (i,2) = sum (PEdata(i,4:(days+3)));
   %Insert avg PE in column 3 of PEdata
   PEdata (i,3) = PEdata (i,2)/days;
   %end the node loop
end
PEdata
save PE98EQ.out PEdata -ASCII  -tabs
```

Function PEfunc.m

```
function PEnode = PEfunc (day, AvT, RH, wind, Qnode, z)

% a function to calculate PE, based on the weather data for that day
clear PB Psy fu HV ea ed slp
% Calculate the main parameters
   %Estimate barometric pressure
   PB = 101-0.0115*z+5.44e-7*z^2;
   %estimate psychrometric constant
   Psy = PB*6.6e-4;
   %mixing term f(u)
   fu= 0.35*(1+wind*0.146);
   %Latent heat of vapourization
   HV = 2.5-0.0022*AvT;
   %convert Qnet from MJ/m2 to mm/day
   Qnode = Qnode/HV;
   %saturated vapour pressure
   ea = 0.6108 * exp(17.27*AvT/(237.3+AvT));
   % Vapour Pressure
   ed = ea*RH;
   % Slope of the Saturation Vapour pressure curve
   slp = (ea/(AvT +273))*(-5.03+(6791/(AvT+273)));

   % Potential Evaporation, in mm

   PEnode = (slp/(slp+Psy))*(Qnode)+(Psy/(slp+Psy))*fu*(ea-ed);
   %reject negative values
   if PEnode < 0
      PEnode=0
   end
```

Appendix D: Equity Cover Moisture Monitoring Results

Monitoring of the cover moisture at the Equity site included monitoring with neutron probes and with TC sensors, as documented in the following sections.

D 1 Neutron Probe Moisture Monitoring Results

The neutron probe data collected at representative locations is shown on Figure D-1 through Figure D-8. Data collection at the neutron probe locations began in June, 1993 and has continued until present day. Figure D-1 shows a summary of neutron probe data for the upper, non-compacted till layer of the cover at select monitoring locations. Figure D-2 shows the data for the lower, compacted till layer of the cover at the same locations. Figures D-3 through D-8 show degree of saturation profiles at select locations, and the variations in those profiles over time. All neutron probe data is shown in terms of degree of saturation. For the uncompacted till near the surface, a 100% degree of saturation corresponds to a water content of approximately 22%, while for the compacted till at depth, a 100% saturation indicates a water content of 18%.

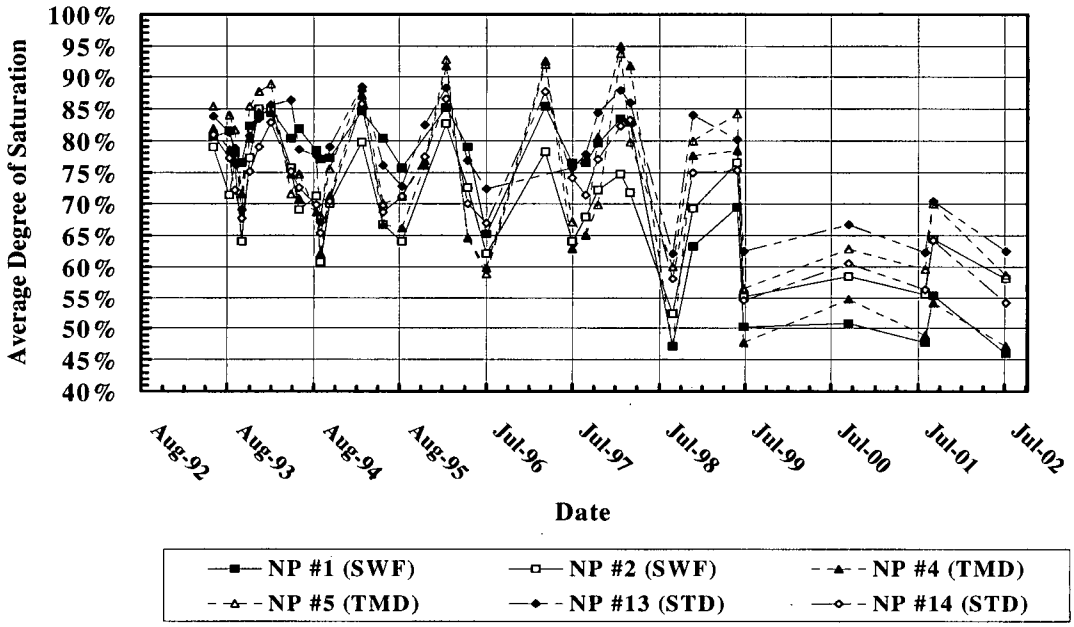

Figure D-1: Average degree of saturation in upper layer of cover soil at select neutron probe locations

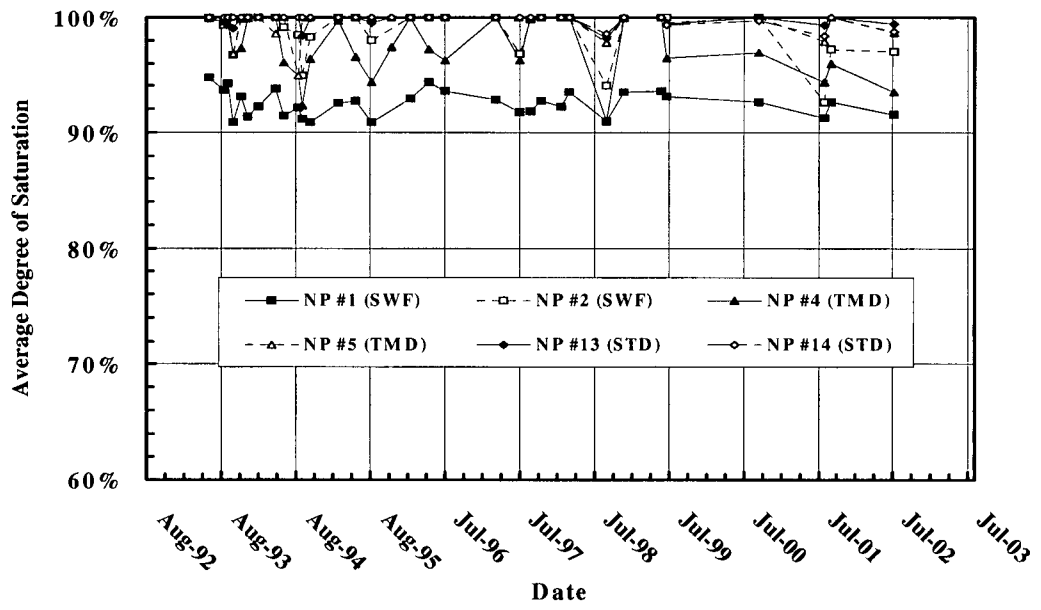

Figure D-2: Average degree of saturation in lower compacted layer of cover soil at select neutron probe locations

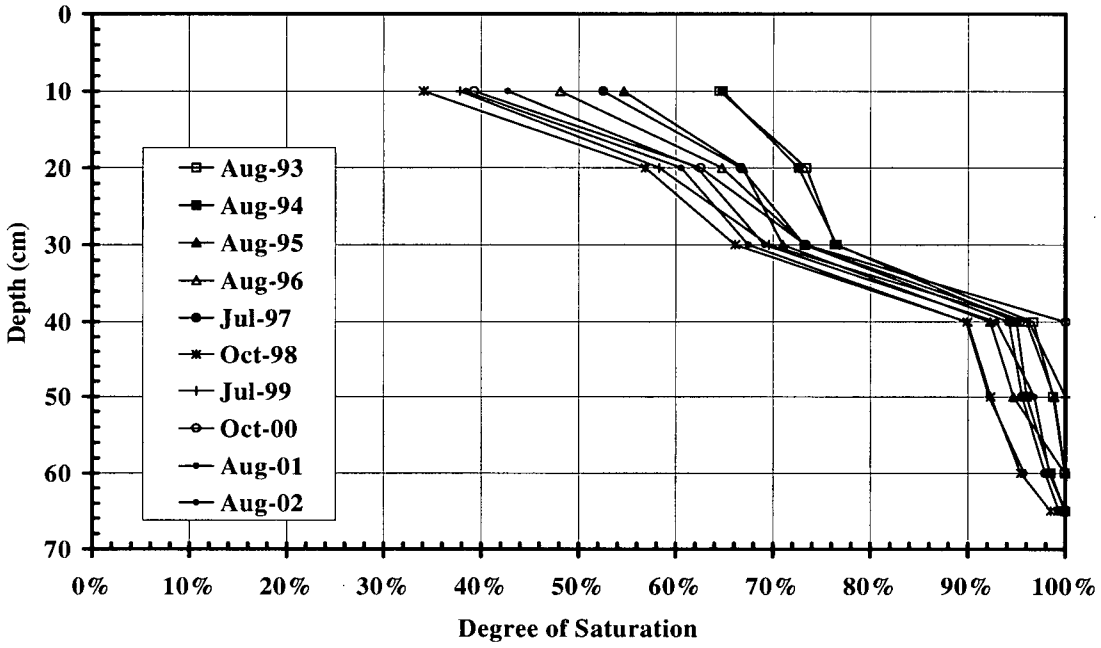

Figure D-3: Soil moisture profile at neutron probe NP2

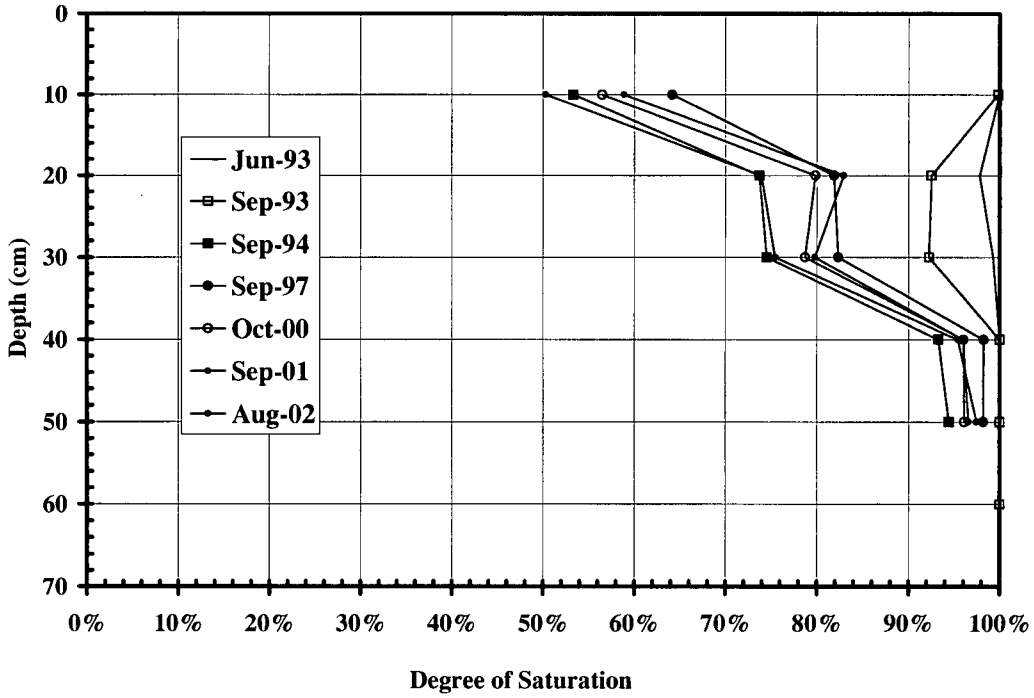

Figure D-4: Soil moisture profile at neutron probe NP3

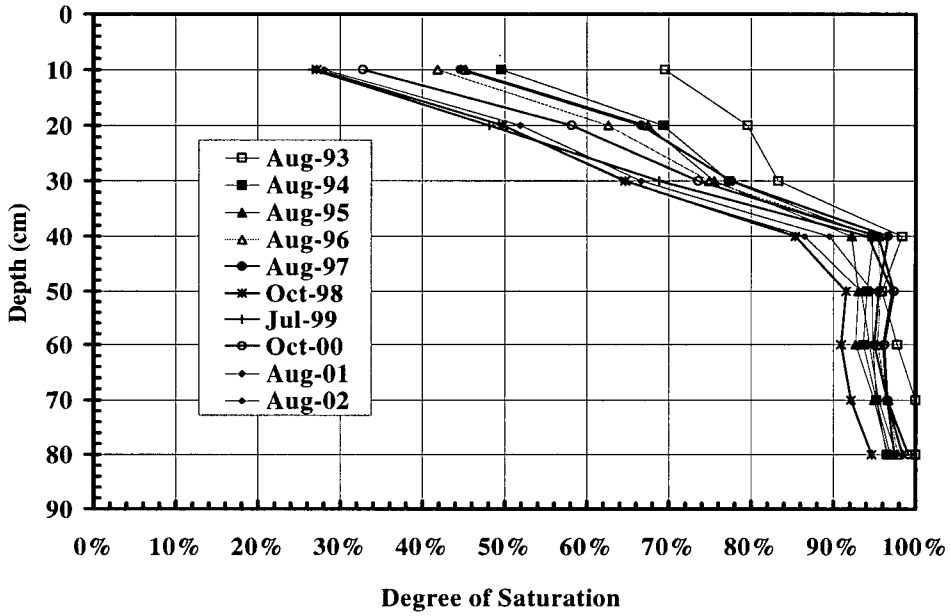

Figure D-5: Soil moisture profile at neutron probe NP4

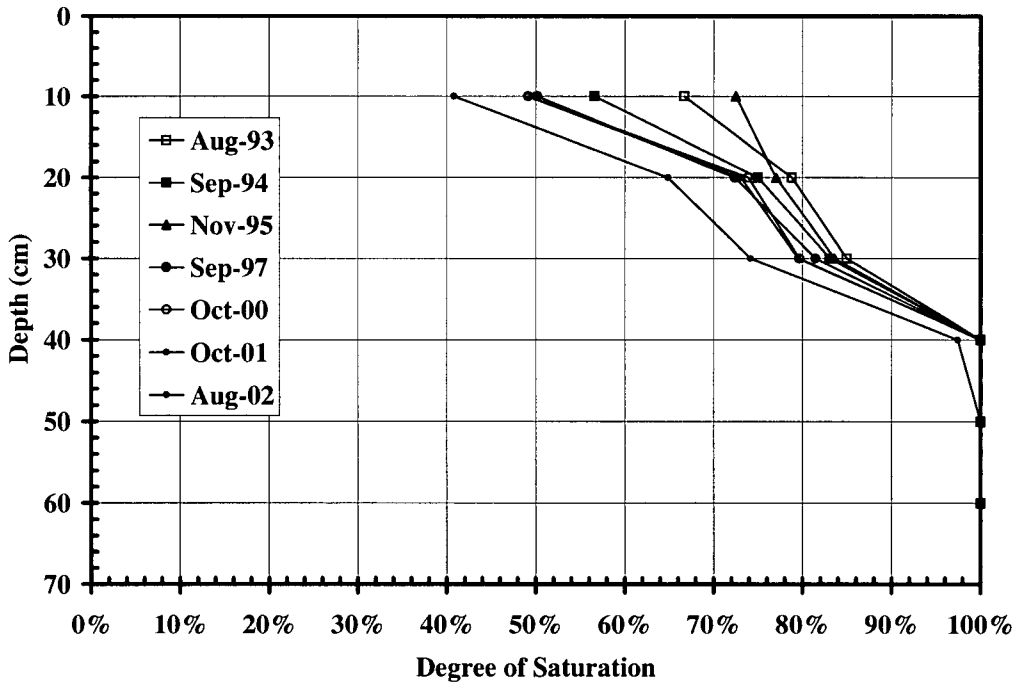

Figure D-6: Soil moisture profile at neutron probe NP6

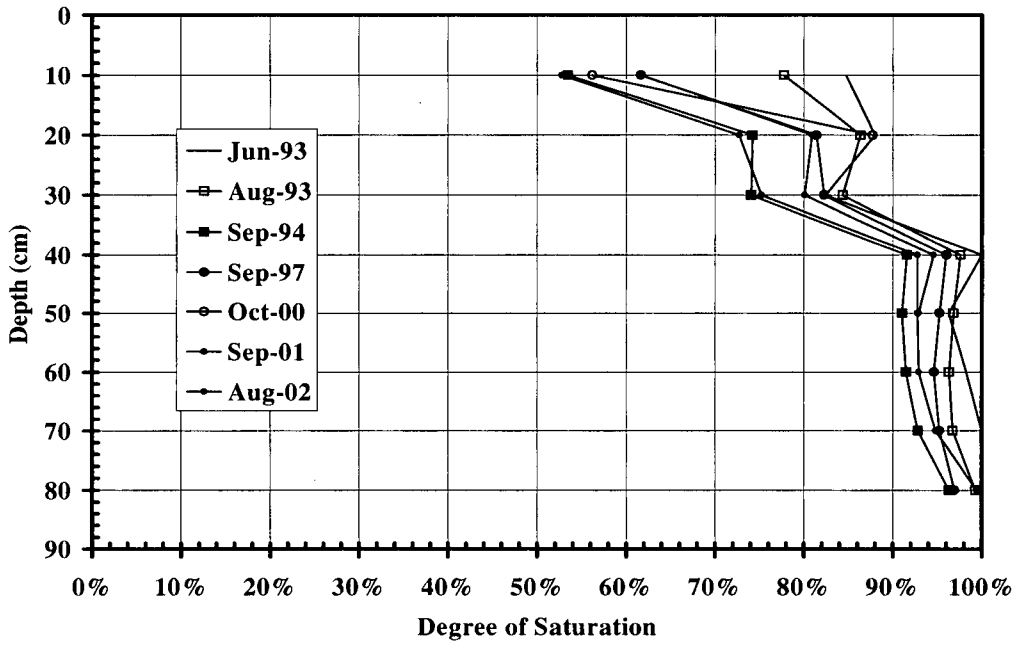

Figure D-7: Soil moisture profile at neutron probe NP7

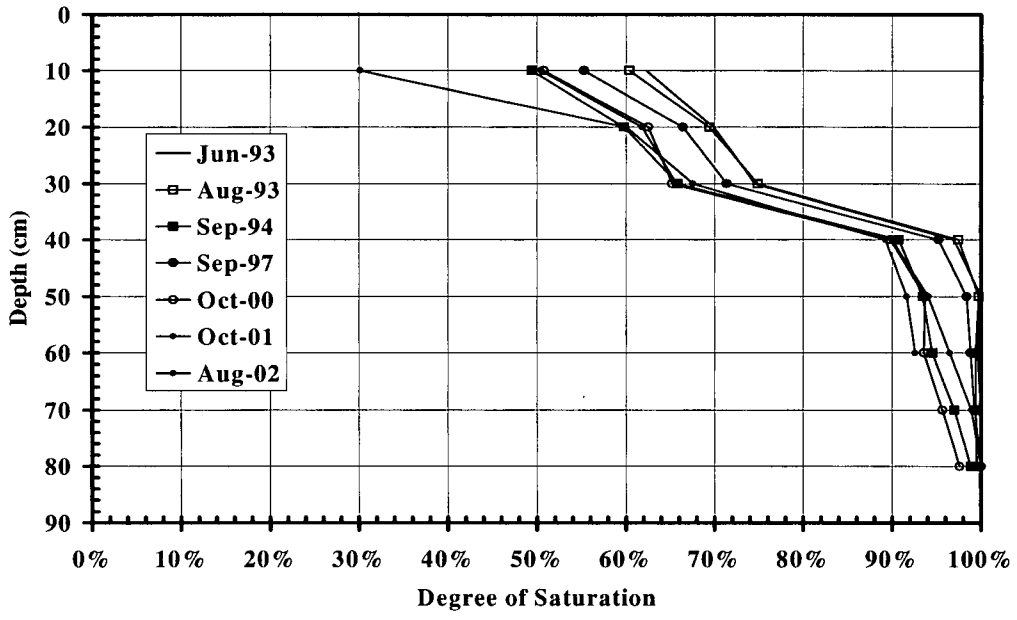

Figure D-8: Soil moisture profile at neutron probe NP8

D 2 TC Sensor Moisture Monitoring Results

TC Sensor data was collected throughout the soil profile at three different locations. Representative data is shown on Figure D-9 and Figure D-10 for the TMD location at depths of 18 cm and 87 cm depth respectively, and on Figure D-11 and Figure D-12 for the STD location at depths of 13 cm and 58 cm respectively. Readings at the sensors were collected twice daily, starting in January 1993 (TMD), May 1993 (STD), and November 1993 (SWF). Reliability of the sensors was an issue, with data collected at sensors approximately 67% of the time (comparing actual measurements collected at the dataloggers to the number of measurements attempted).

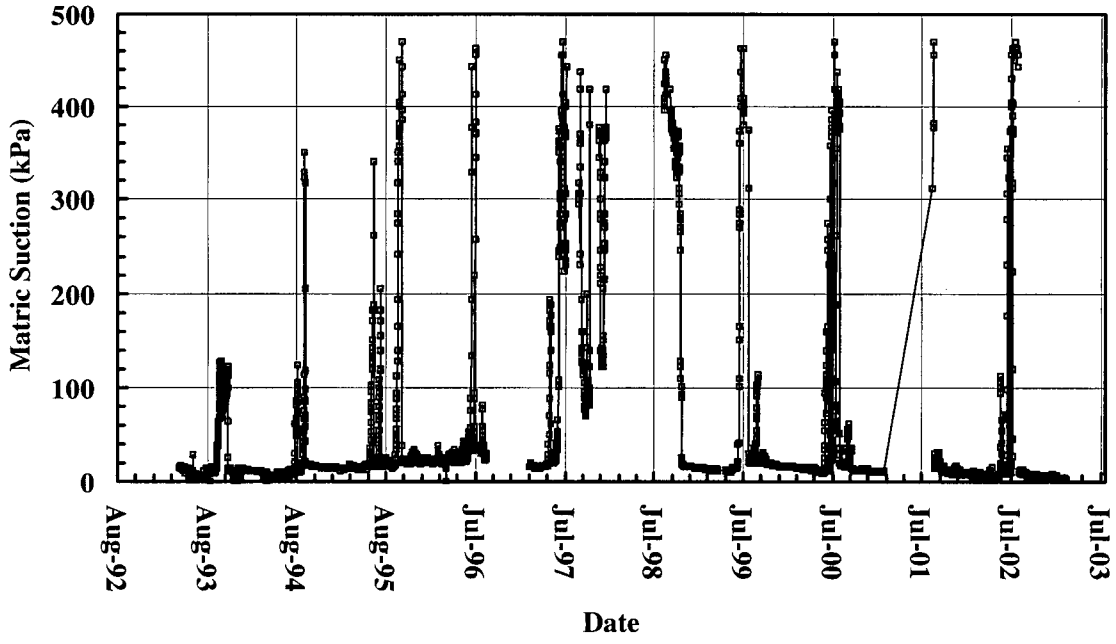

Figure D-9: Soil suction at 18 cm depth, TMD location

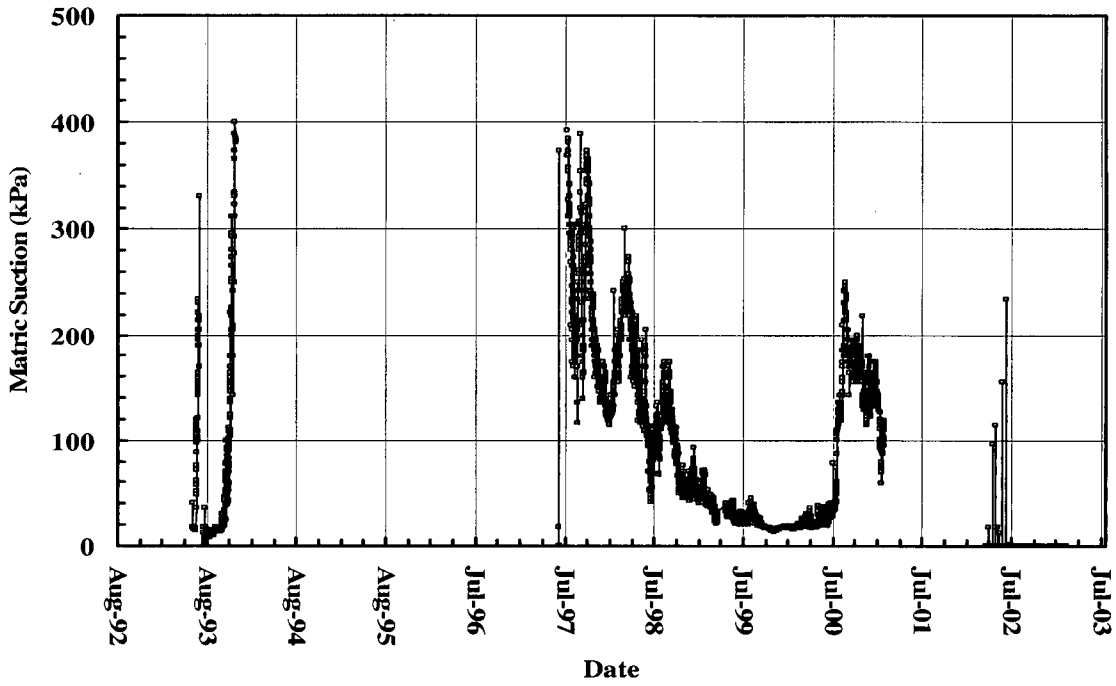

Figure D-10 : Soil suction at 87 cm depth, TMD location

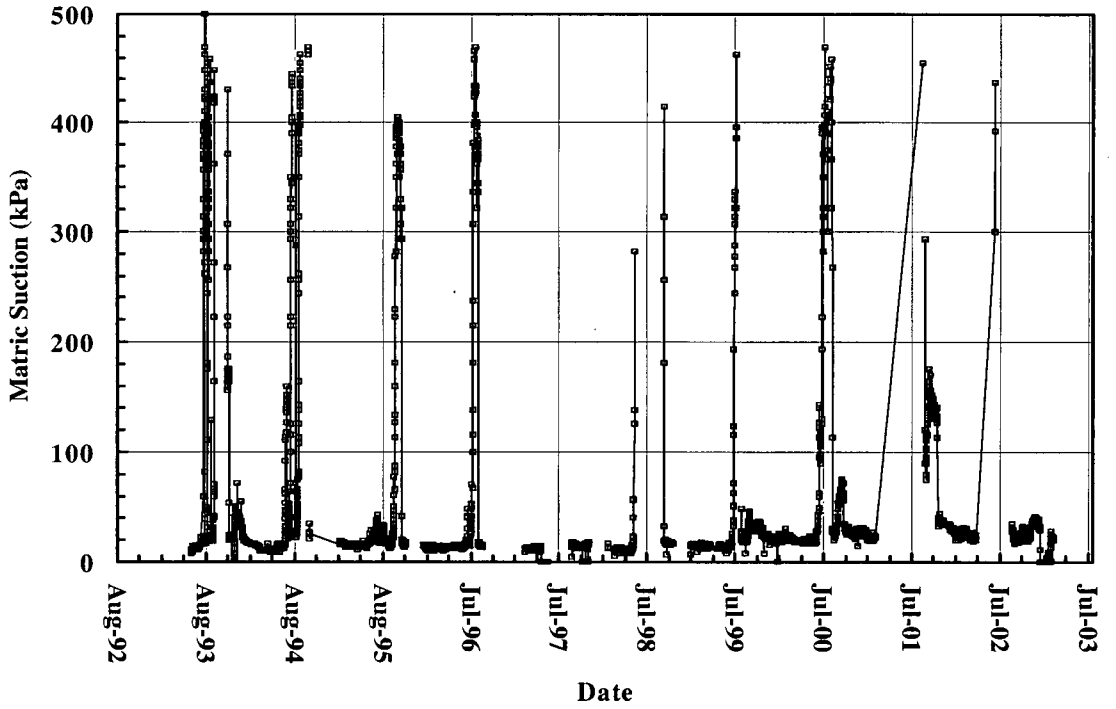

Figure D-11: Soil suction at 13 cm depth, STD location

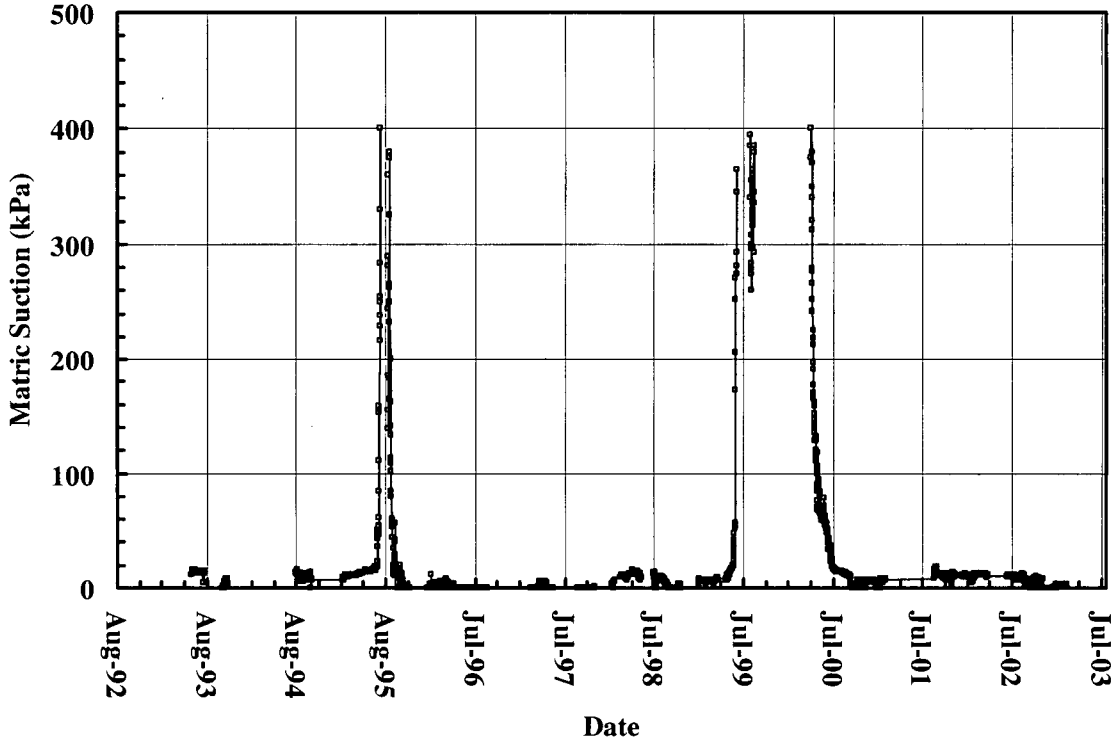

Figure D-12: Soil suction at 58 cm depth, STD location

Appendix E – Summary of Equity Sensitivity Runs

Table E.1 Summary of Sensitivity Study for Equity 2002/2003 Data

Parameter Varied	Albedo α	Emissivity ε	Maximum clear sky transmissivity B_c	Clear sky factor a_1	Absolute Residual Error		Absolute Percent Error (%)	
					Mean	95% CI (±)	Mean	95% CI (±)
Base Case	0.16	0.9	0.74	1.1	0.661	0.12	15.6	3.1
Albedo	0.11	0.9	0.74	1.1	0.657	0.12	14.4	2.7
	0.14	0.9	0.74	1.1	0.631	0.13	13.8	2.7
	0.18	0.9	0.74	1.1	0.698	0.13	17.6	3.8
	0.21	0.9	0.74	1.1	0.761	0.13	20.1	5.0
Emissivity	0.16	0.87	0.74	1.1	0.630	0.12	13.8	2.7
	0.16	0.92	0.74	1.1	0.685	0.13	17.0	3.5
	0.16	0.94	0.74	1.1	0.709	0.13	18.2	4.0
B	0.16	0.9	0.7	1.1	0.689	0.13	16.8	3.5
	0.16	0.9	0.72	1.1	0.676	0.13	16.4	3.3
	0.16	0.9	0.77	1.1	0.638	0.12	14.5	2.9
	0.16	0.9	0.8	1.1	0.622	0.12	13.7	2.8
a1	0.16	0.9	0.74	1.05	0.682	0.12	17.1	3.6
	0.16	0.9	0.74	1.15	0.645	0.13	14.4	2.8
	0.16	0.9	0.74	1.2	0.644	0.13	14.1	2.7
	0.16	0.9	0.74	1.3	0.662	0.13	14.6	2.9
Latitude (-0.1°)	0.16	0.9	0.74	1.1	0.654	0.12	15.3	3.0
Latitude (+ 0.1°)	0.16	0.9	0.74	1.1	0.668	0.12	16.0	3.2

Note:
All solutions calculated using the Swinbank (1963) formula for E_{ac}.

Appendix F – Net radiation maps for Equity Surface

The following maps show the net radiation distribution for the Equity Site for select days in the 1998 data set.

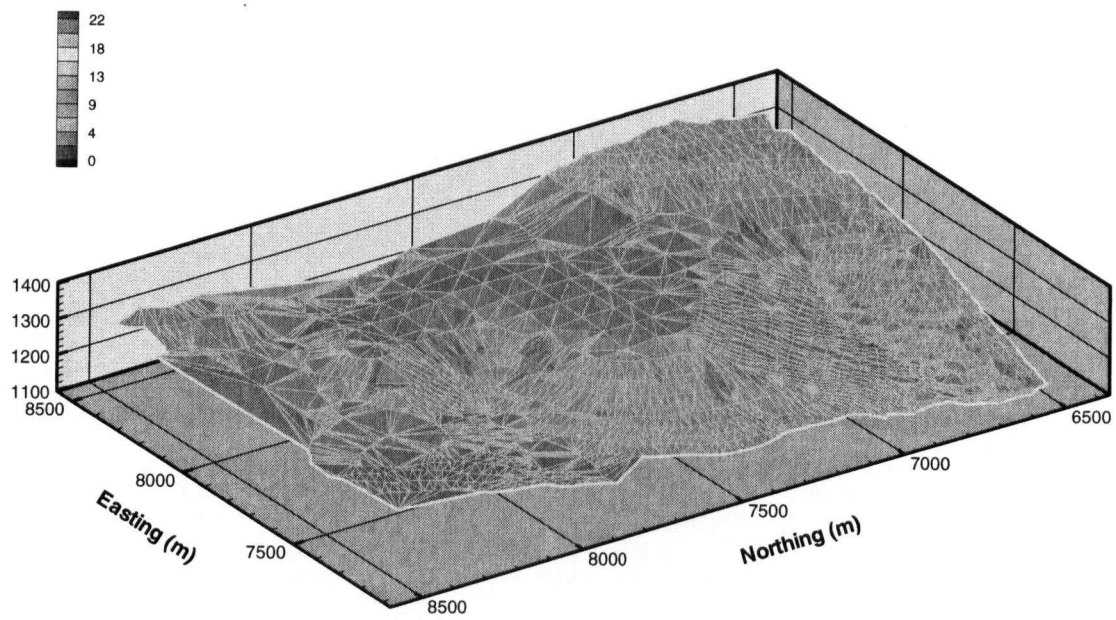

Figure F-1: Day 116 (April 26, 1998)

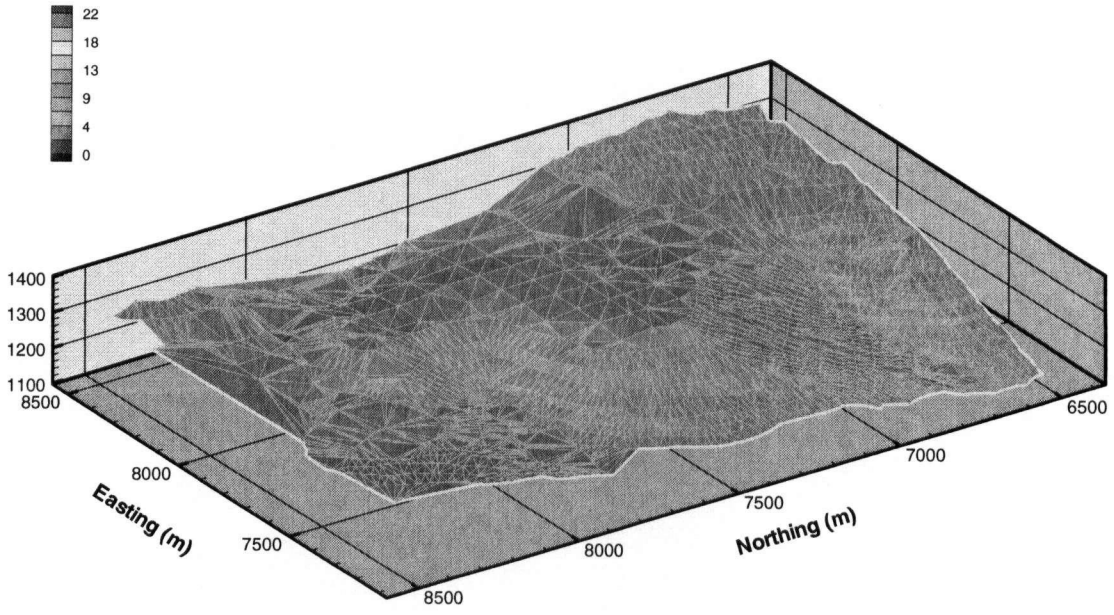

Figure F-2: Day 126

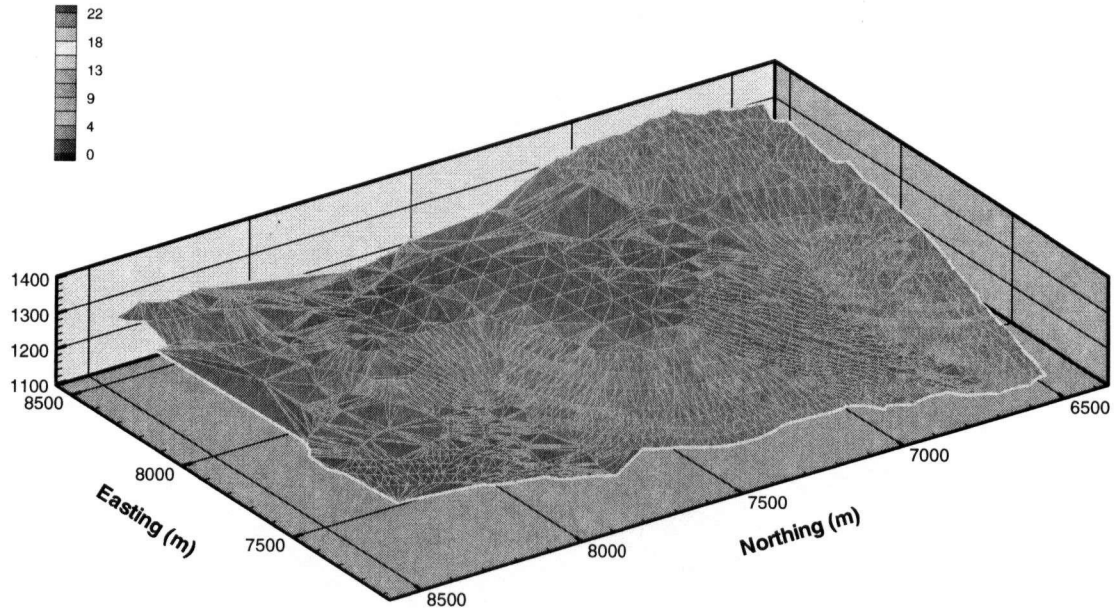

Figure F-3: Day 136

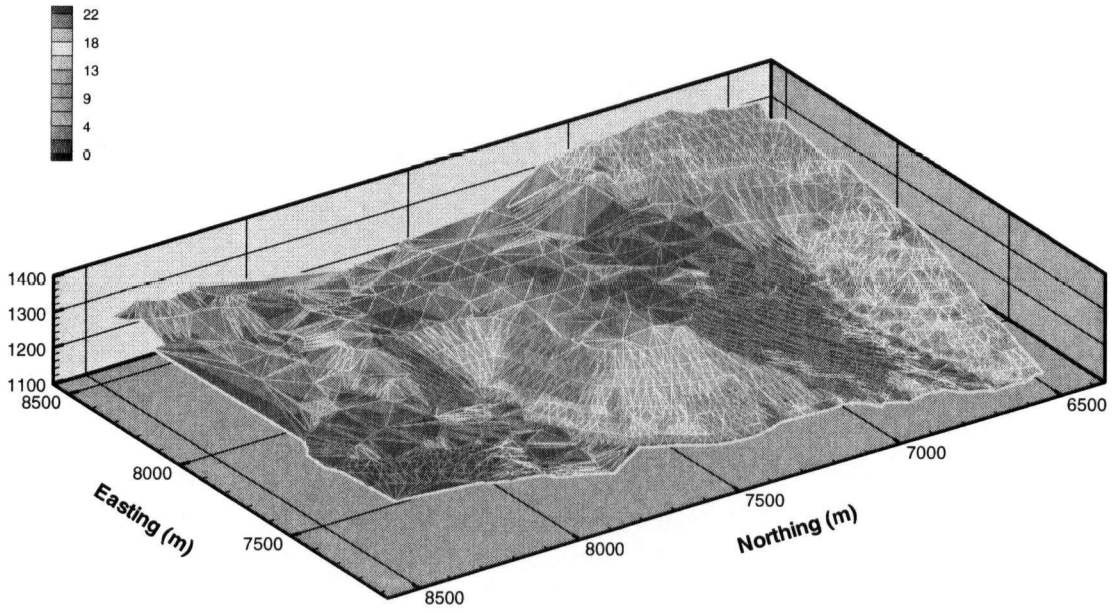

Figure F-4: Day 146

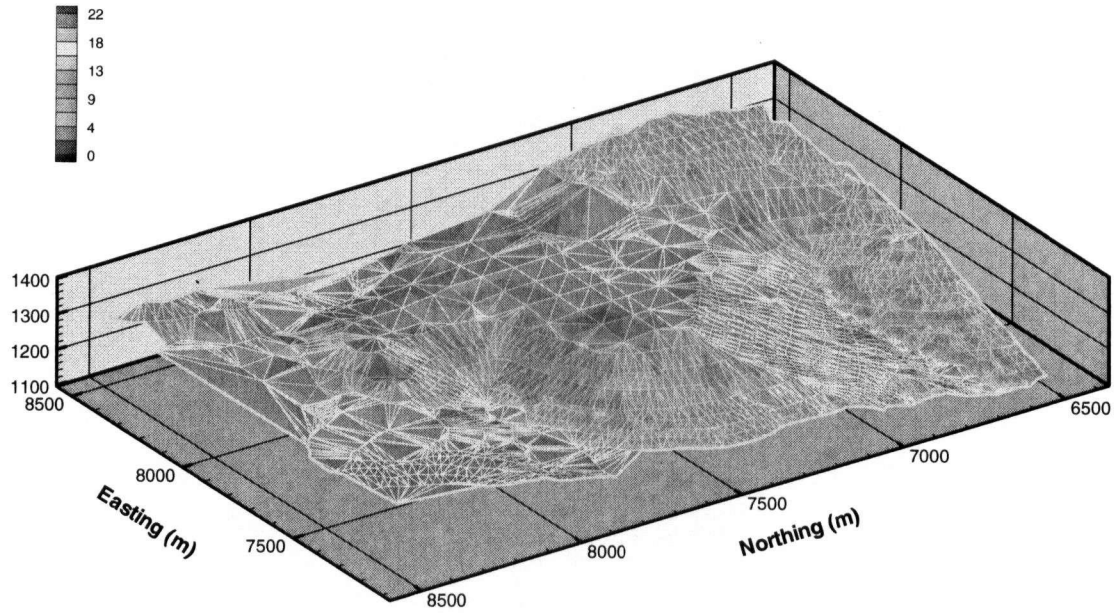

Figure F-5: Day 156

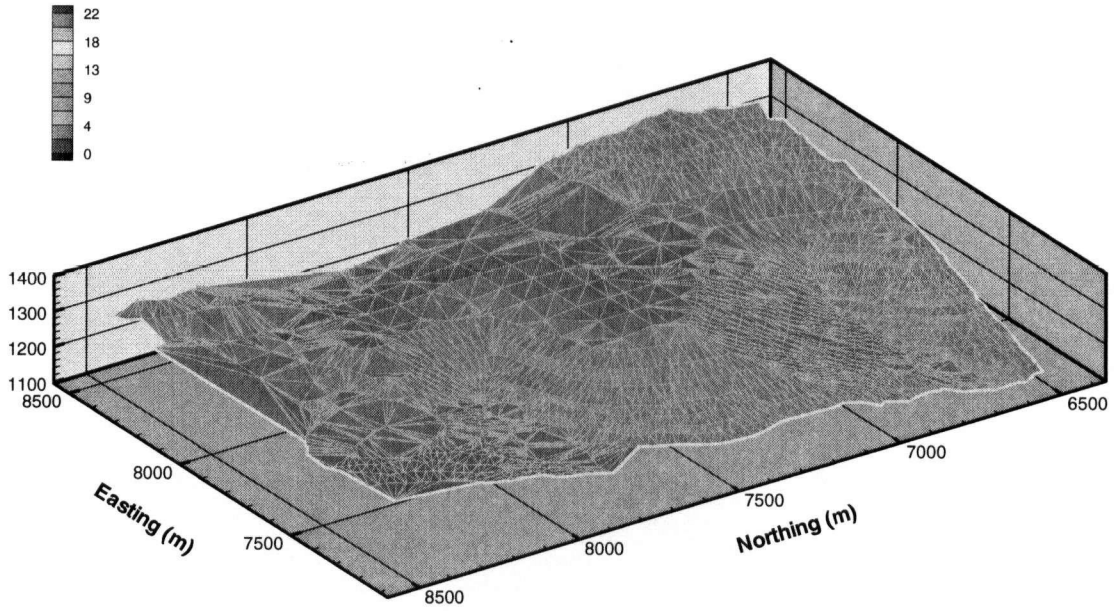

Figure F-6: Day 166

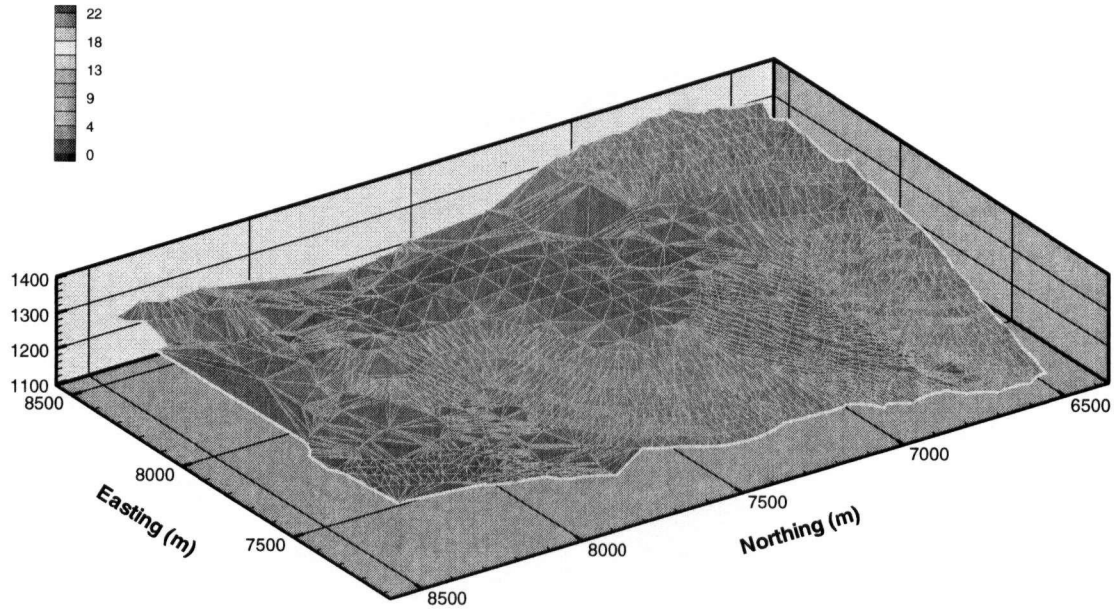

Figure F-7: Day 176

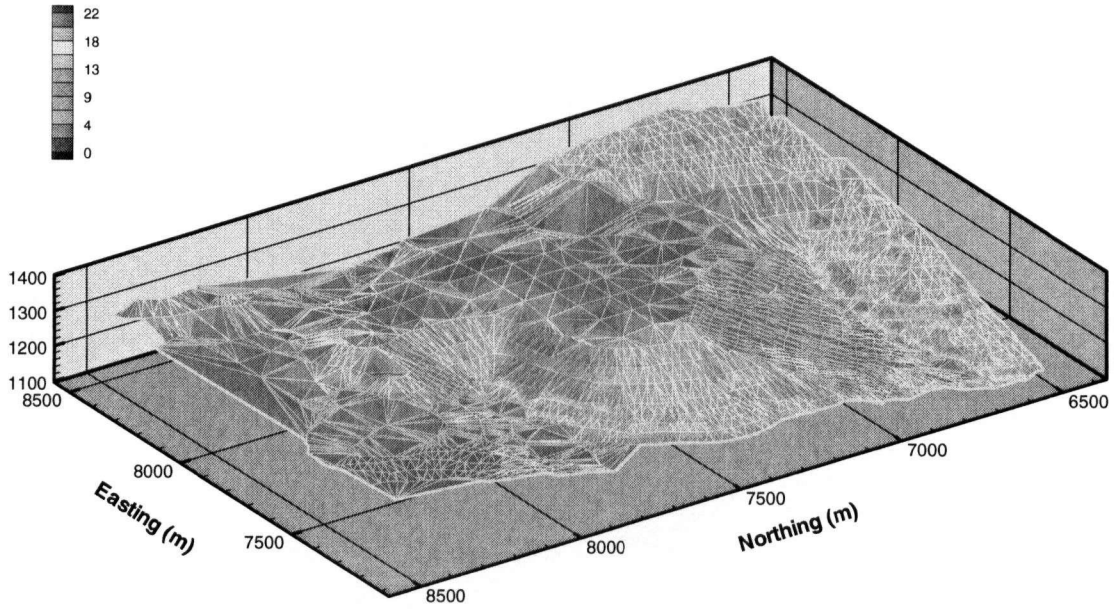

Figure F-8: Day 186 (July)

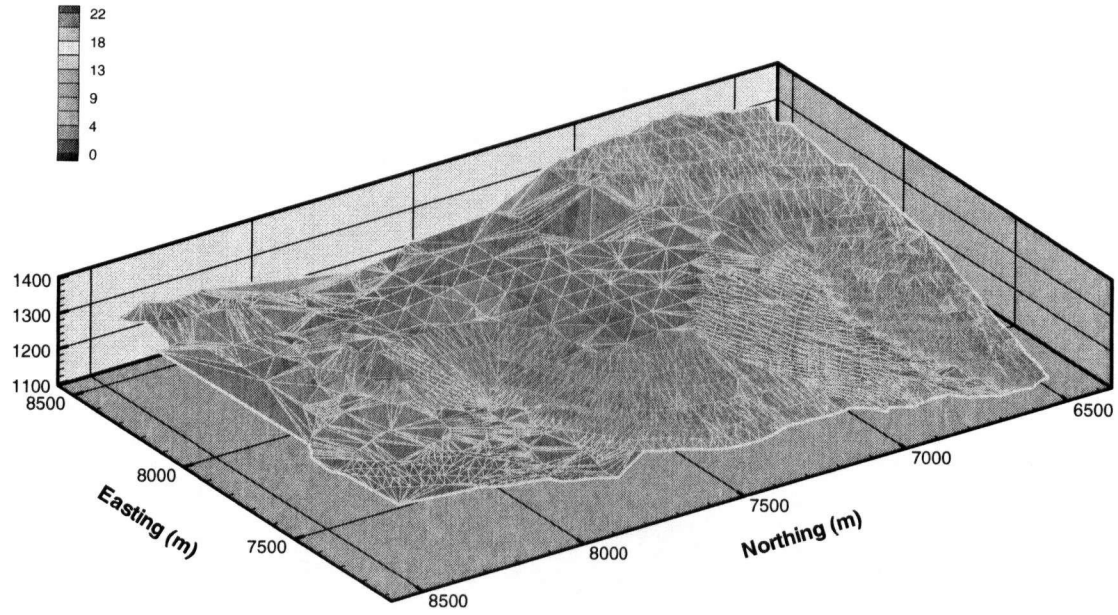

Figure F-9: Day 196

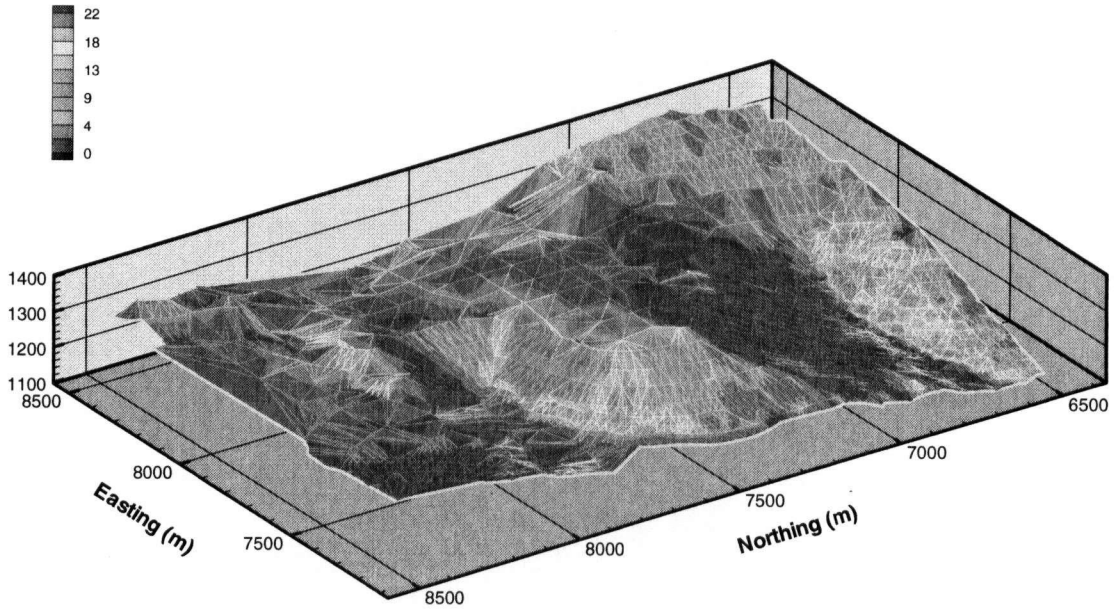

Figure F-10: Day 206

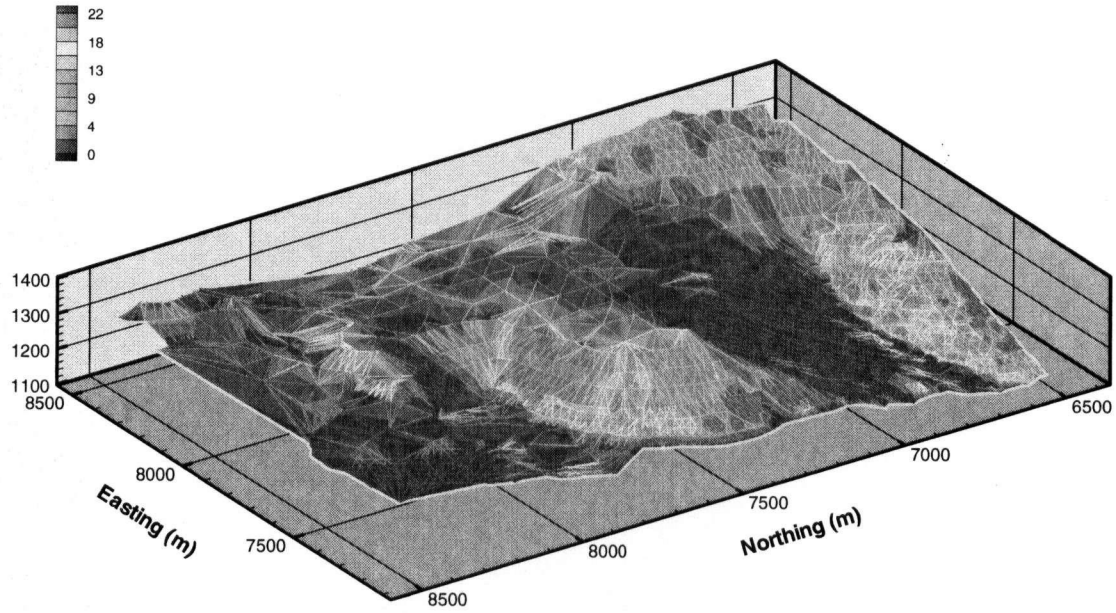

Figure F-11: Day 207

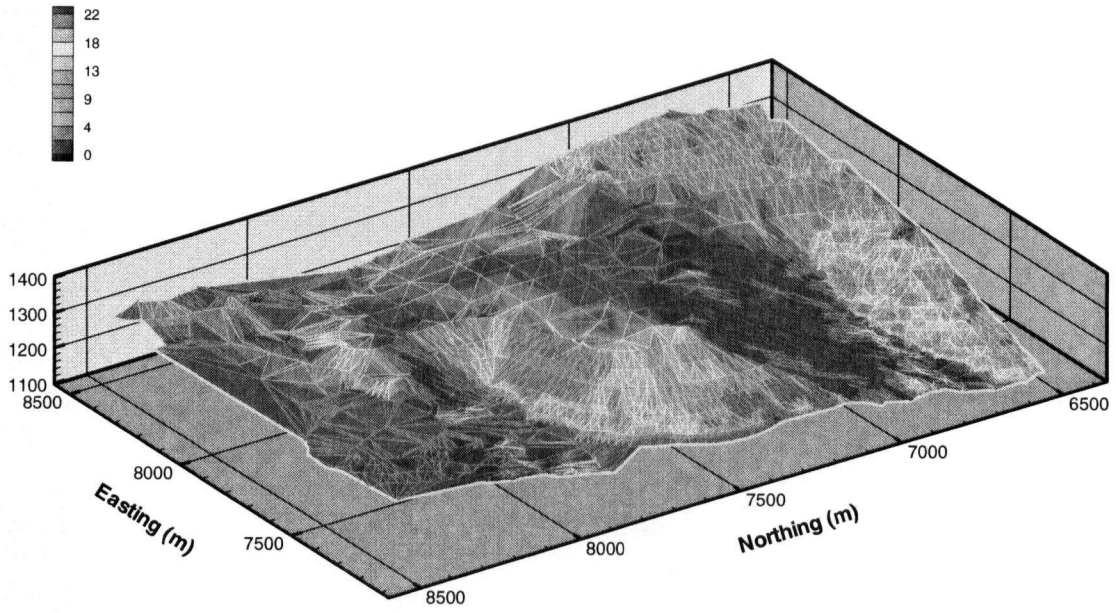

Figure F-12: Day 208

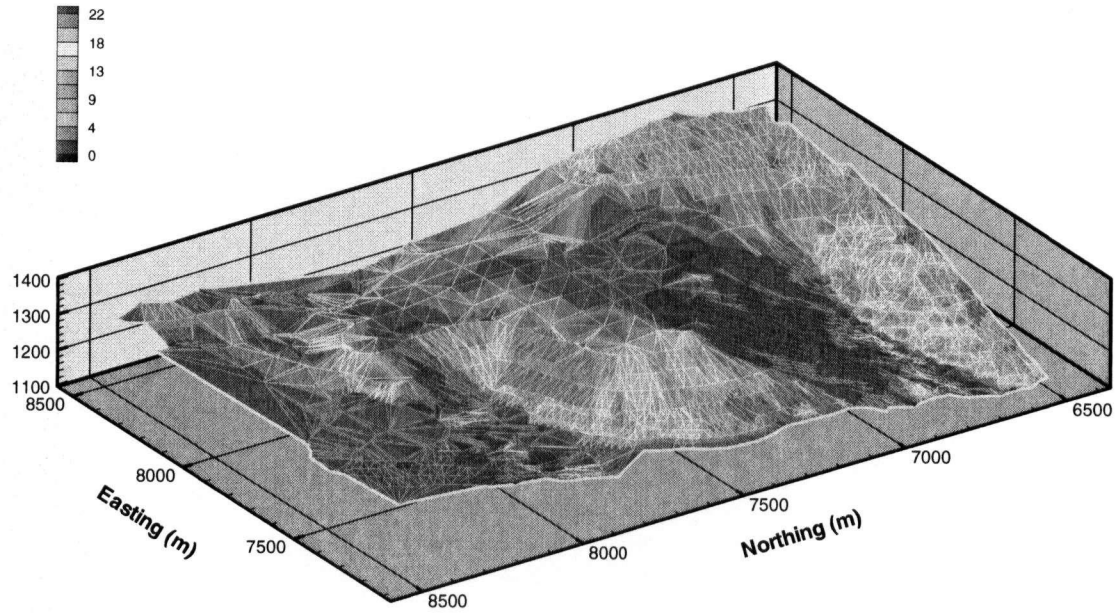

Figure F-13: Day 209

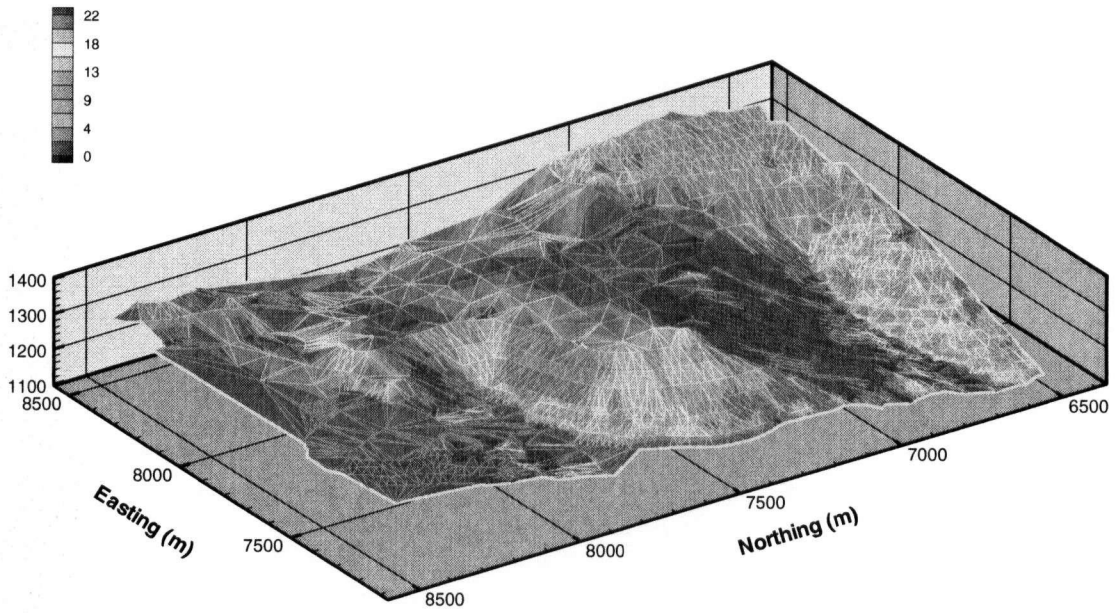

Figure F-14: Day 210

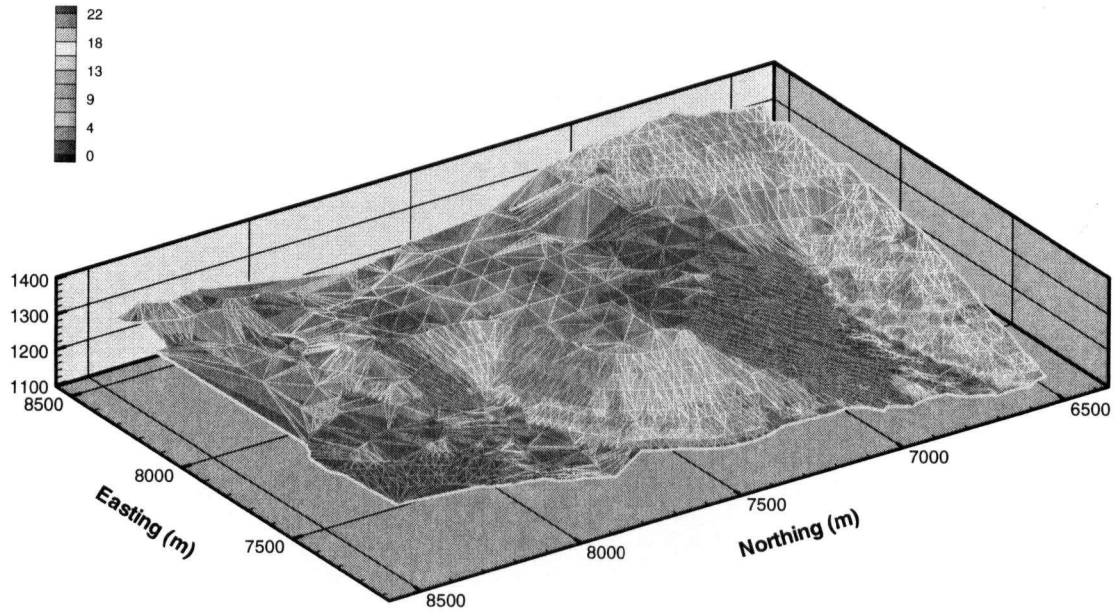

Figure F-15: Day 211

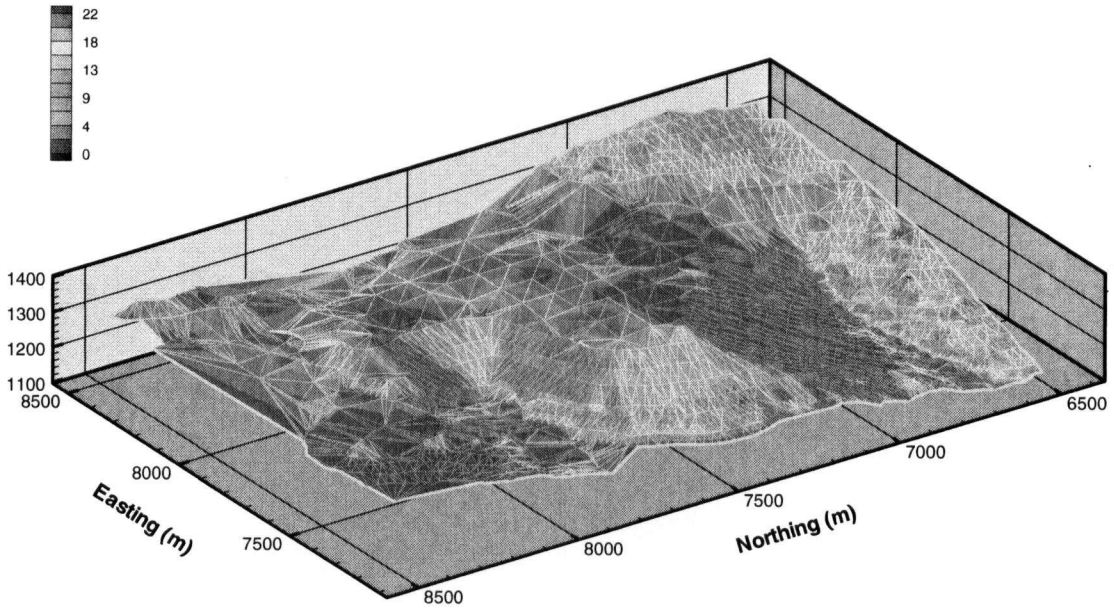

Figure F-16: Day 212

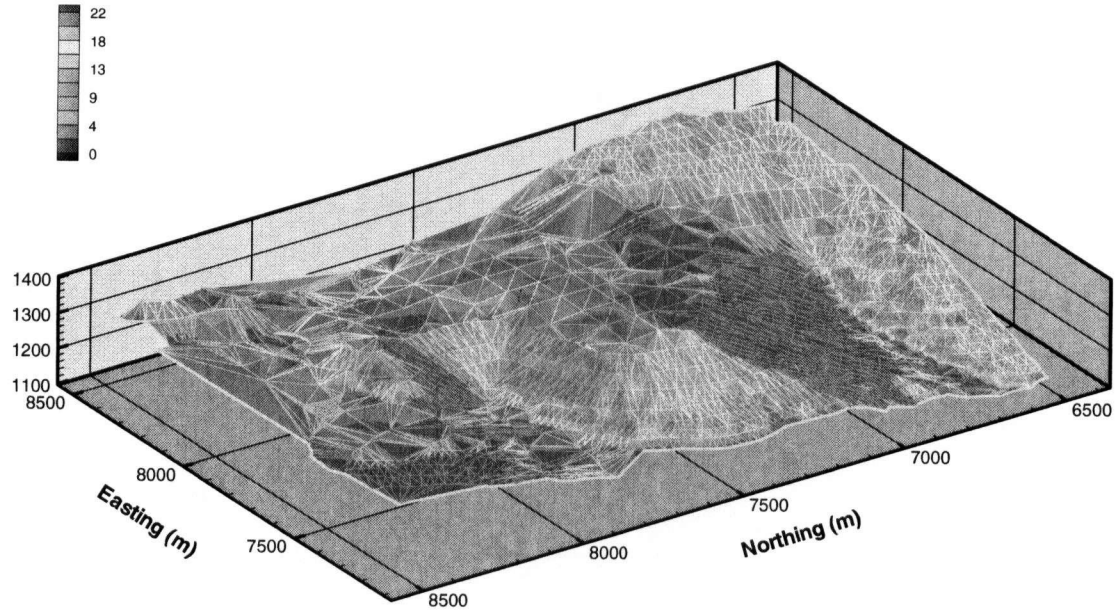

Figure F-17: Day 213

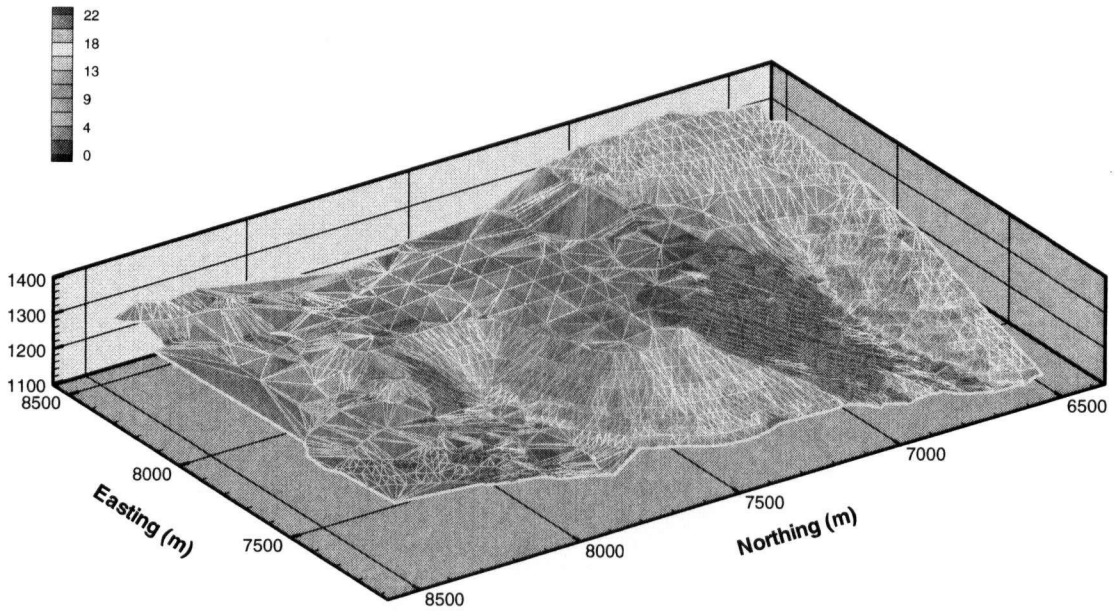

Figure F-18: Day 214

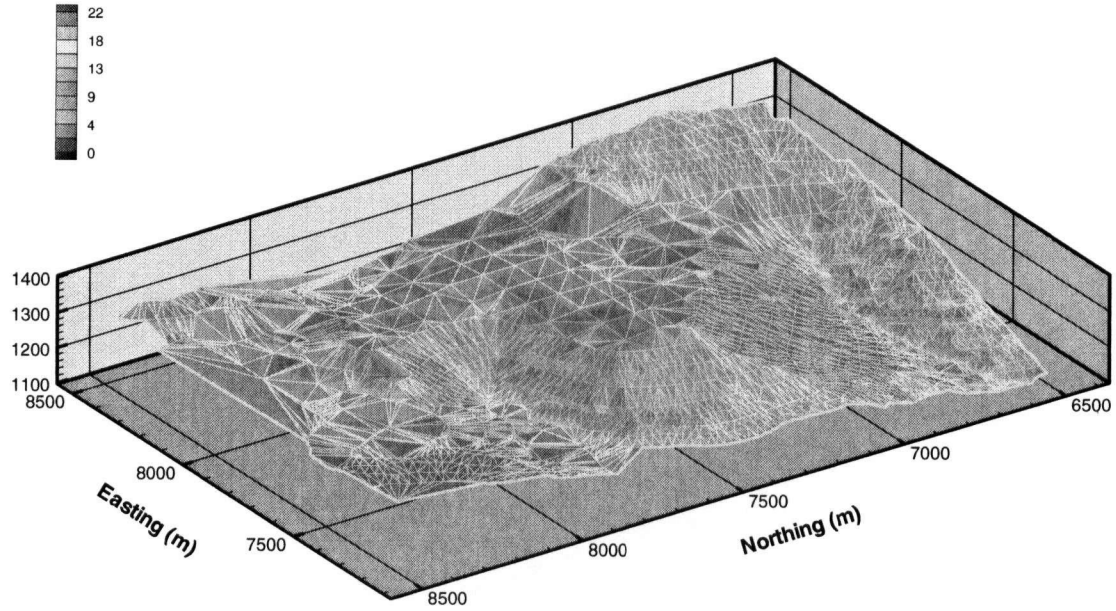

Figure F-19: Day 215

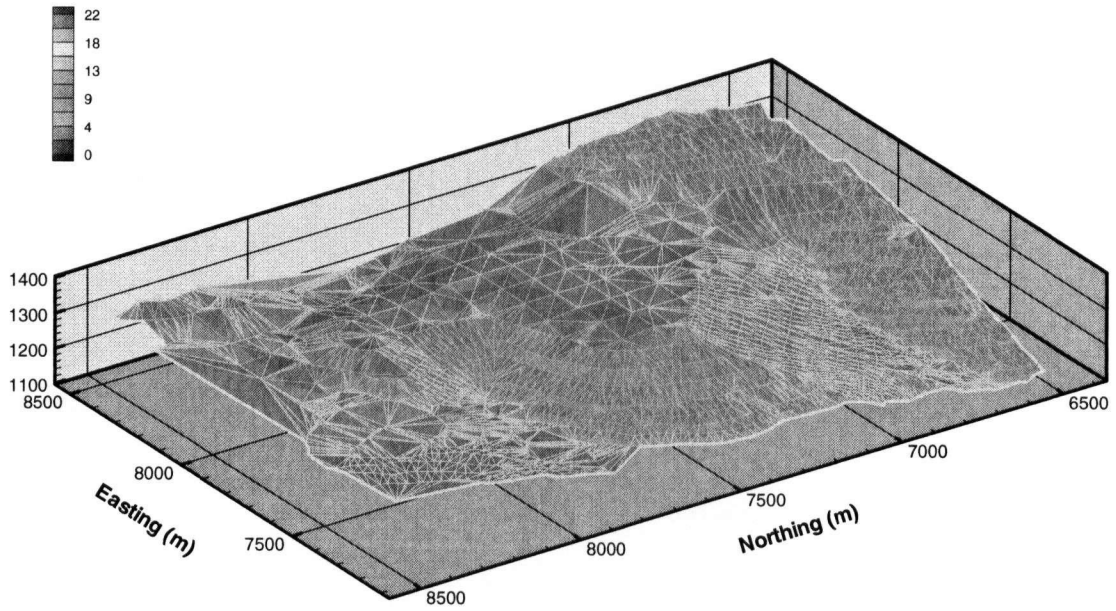

Figure F-20: Day 216 (August)

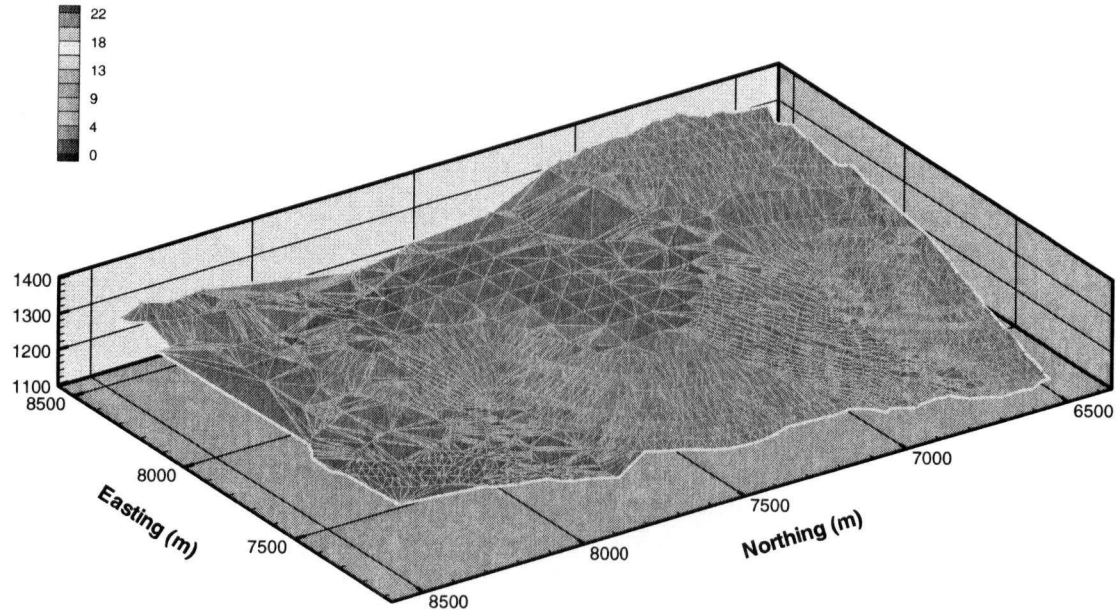

Figure F-21: Day 226

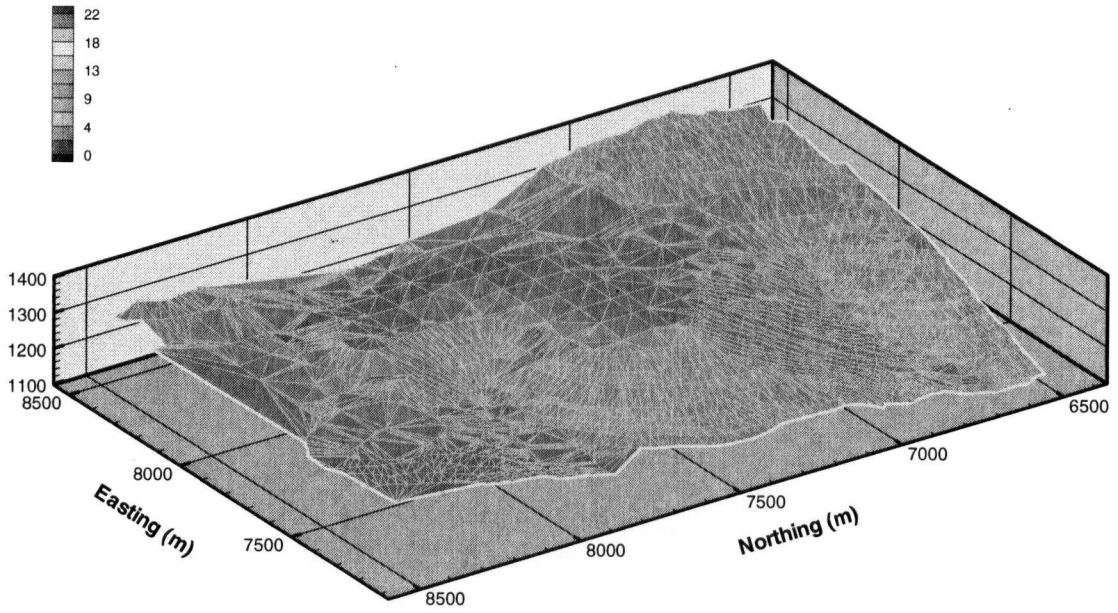

Figure F-22: Day 236

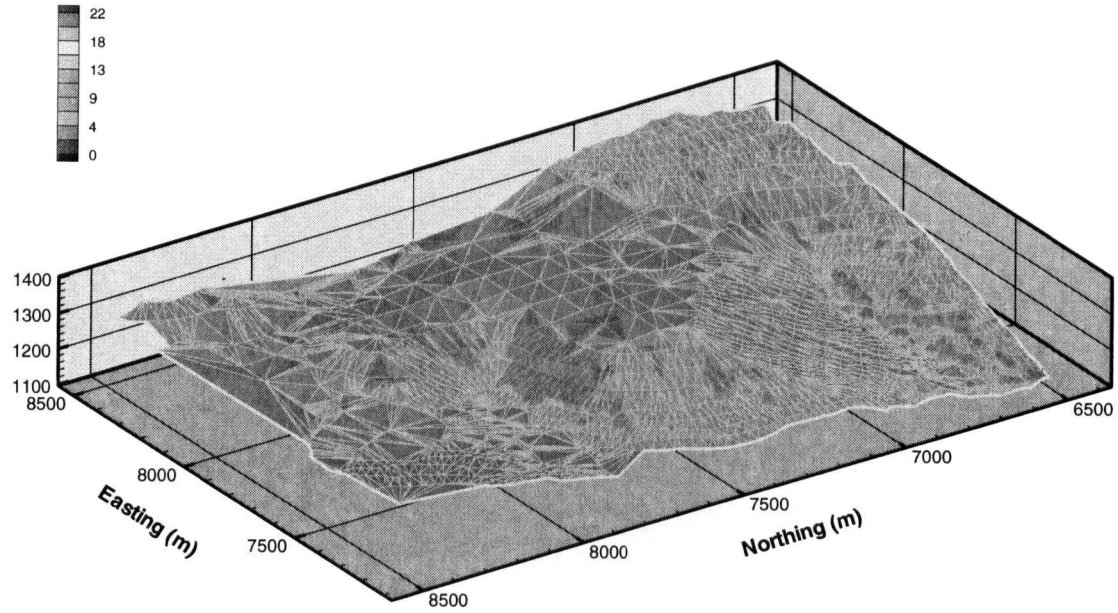

Figure F-23: Day 246

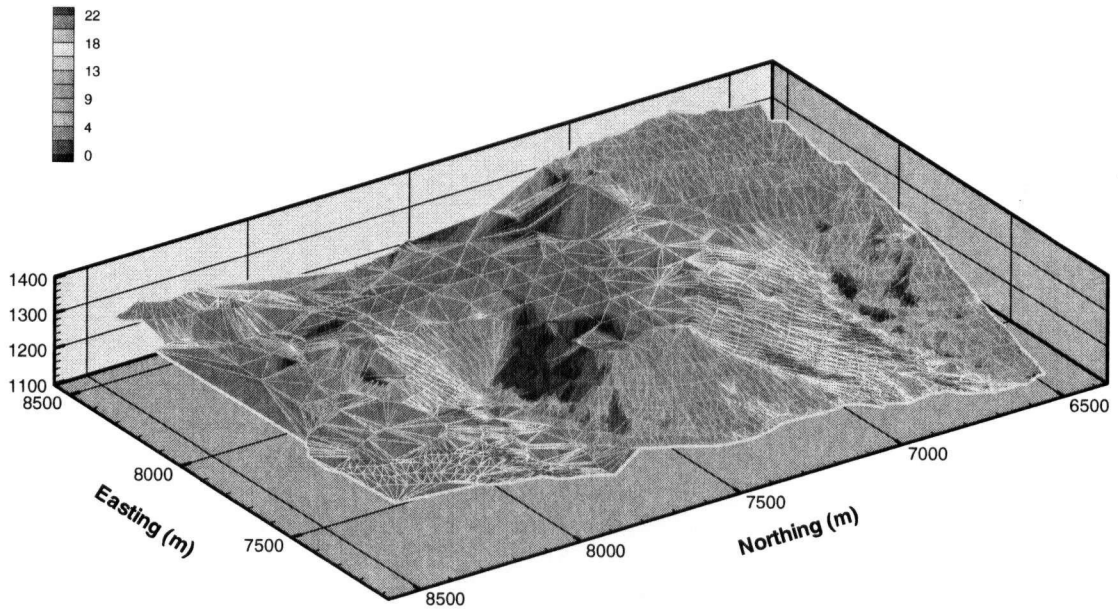

Figure F-24: Day 256

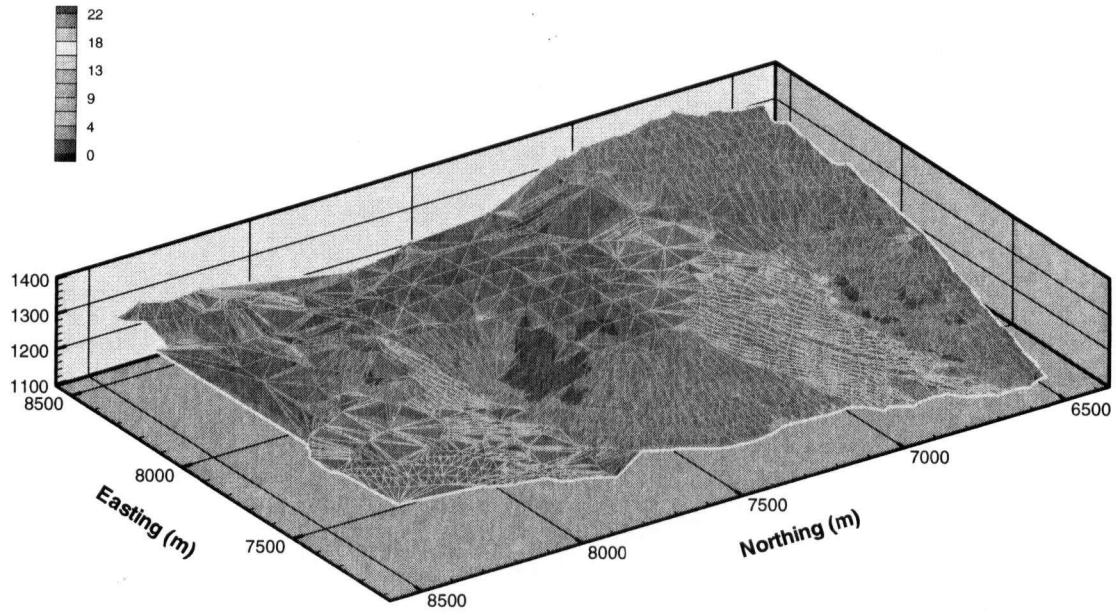

Figure F-25: Day 266

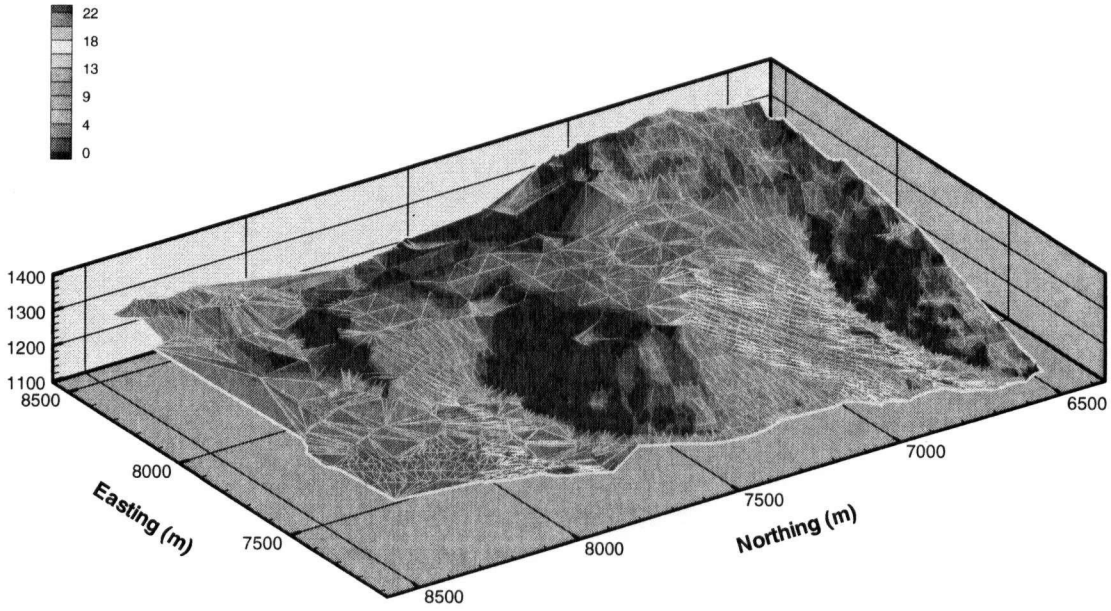

Figure F-26: Day 276

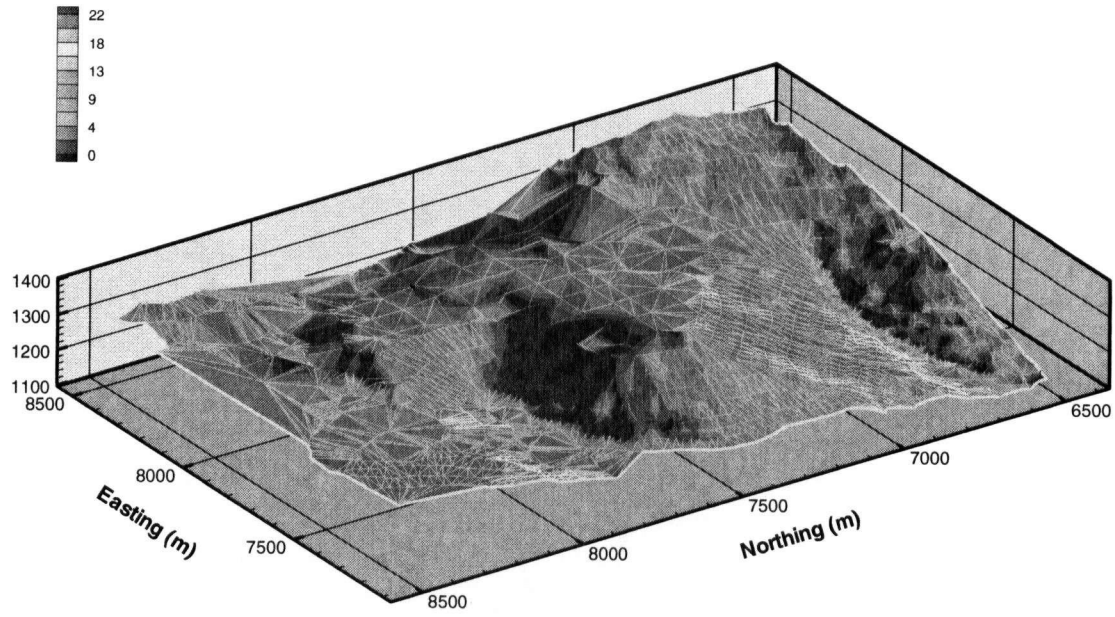

Figure F-27: Day 286

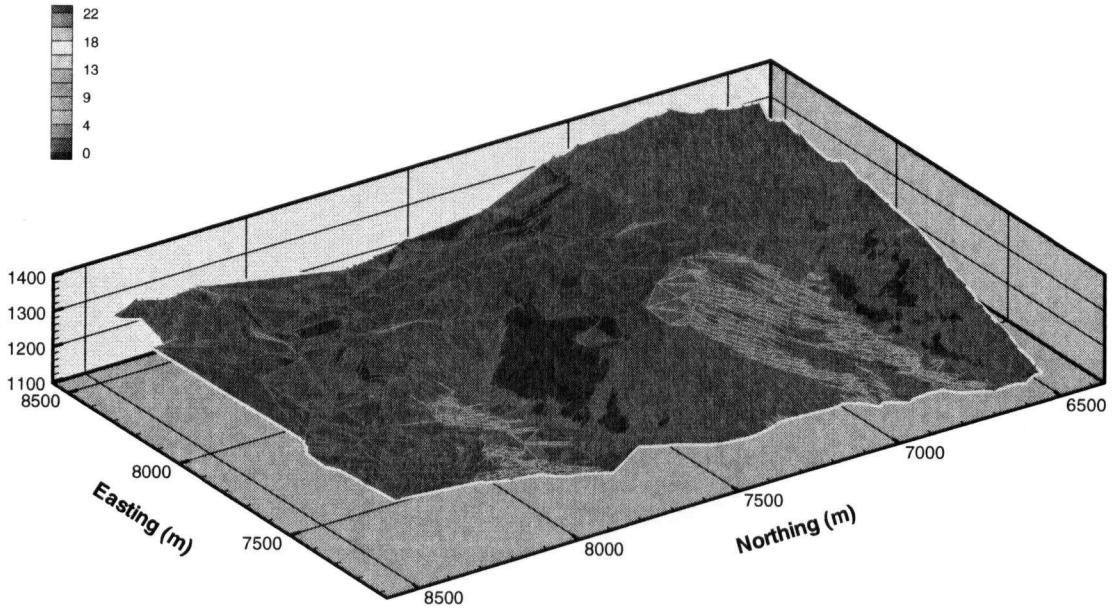

Figure F-28: Day 296

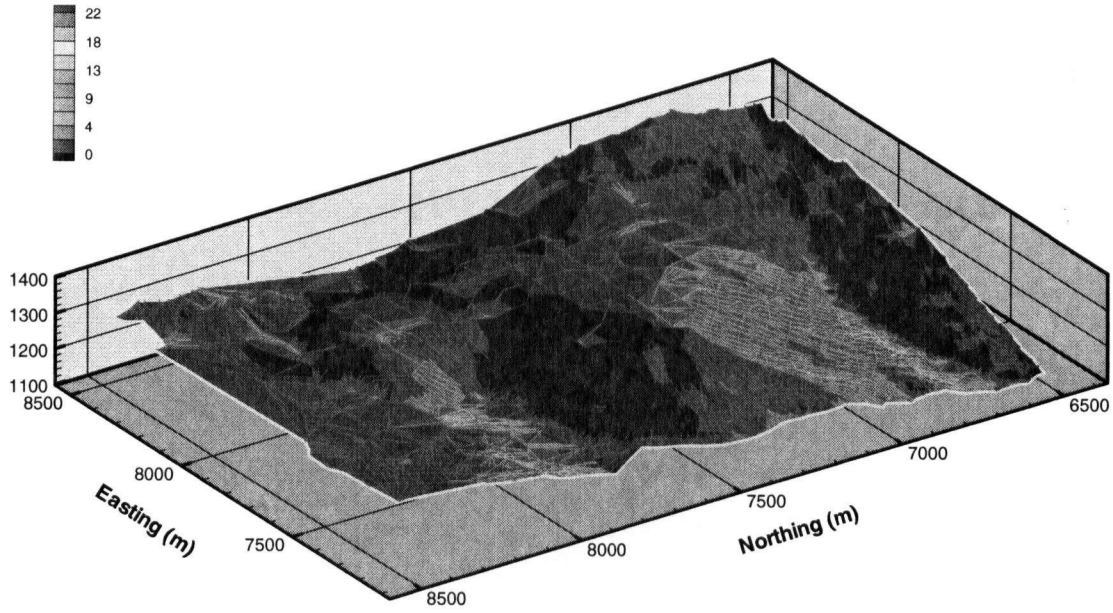

Figure F-29: Day 306